Quantum Aspects of Black Holes: From Microstates to Echoes and Somewhere In-Between

by

Krishan Saraswat

A thesis
presented to the University of Waterloo
in fulfillment of the
thesis requirement for the degree of
Doctor of Philosophy
in
Physics

Waterloo, Ontario, Canada, 2023

Examining Committee Membership

The following served on the Examining Committee for this thesis. The decision of the Examining Committee is by majority vote.

External Examiner:	Samir Mathur Professor, Dept. of Physics, Ohio State University
Supervisor(s):	Niayesh Afshordi Professor, Dept. of Physics and and Astronomy, University of Waterloo Associate Faculty, Perimeter Institute for Theoretical Physics
Internal Member:	Avery Broderick Associate Professor, Dept. of Physics and and Astronomy, University of Waterloo
Internal-External Member:	Achim Kempf Professor, Dept. Applied Mathematics, University of Waterloo
Other Member(s):	Robert Myers Professor, Perimeter Institute for Theoretical Physics Director, Perimeter Institute for Theoretical Physics Adjunct Faculty, Dept. of Physics and and Astronomy, University of Waterloo

Author's Declaration

This thesis consists of material all of which I authored or co-authored: see Statement of Contributions included in the thesis. This is a true copy of the thesis, including any required final revisions, as accepted by my examiners.

I understand that my thesis may be made electronically available to the public.

Statement of Contributions

This thesis is based on the following published and ongoing/unpublished works:

- Chapter 1: is a review typed by the author of the known body of relevant literature and textbooks which frame the topics covered in this thesis.
- Chapter 2: is the published work:
  Saraswat, K., Afshordi, N. Quantum nature of black holes: fast scrambling versus echoes. J. High Energ. Phys. 2020, 136 (2020). https://doi.org/10.1007/JHEP04(2020)136.
  I am the primary author of this work and my supervisor is the coauthor. I typed up the manuscript and did all calculations under the guidance of my advisor.
- Chapter 3: is the published work:
  Saraswat, K., Afshordi, N. Spacing statistics of energy spectra: random matrices, black hole thermalization, and echoes. J. High Energ. Phys. 2022, 17 (2022).
  I am the primary author of this work and my supervisor is the coauthor. I typed up the manuscript and did all calculations under the guidance of my advisor.
- Chapter 4: is the published work:
  Saraswat, K., Afshordi, N. Extracting Hawking radiation near the horizon of AdS black holes. J. High Energ. Phys. 2021, 77 (2021). https://doi.org/10.1007/JHEP02(2021)077
  I am the primary author of this work and my supervisor is the coauthor. I typed up the manuscript and did all calculations under the guidance of my advisor.
- Chapter 5: is ongoing and unpublished work which the author is working on in collaboration with Dominik Neuenfeld (Postdoctoral Fellow at the University of Amsterdam). The material presented in the chapter was written by the author and the calculations were done by the author and later checked (for consistency) independently by Dominik Neuenfeld. The ideas investigated in this chapter are guided by questions and ideas posed by Dominik Neuenfeld and the author has express permission from Dominik Neuenfeld to add the calculations/work in this thesis.
- Chapter 6 is the conclusion of the thesis and is written by the author

All parts of this thesis were written (typed out) by the author.

Abstract

In this thesis we explore quantum aspects of black holes from a variety of perspectives. In part I of this thesis we are motivated by the black hole information paradox to explore the idea of gravitational wave echoes from the perspective of black hole microstate statistics. We adopt the idea that a UV complete description of a black hole should involve $e^{S_{BH}}$ microstates in a thermal ensemble, where $S_{BH} = \frac{A}{4G_N}$, is the Bekenstein Hawking entropy of the black hole. Furthermore, we take the stance that issues about the existence of echoes and black hole microstructure might be understood in terms of thermal correlators in the ensemble of microstates. We make use of the spectral form factor as a proxy for a thermal 2-point correlator calculation. We study how spacing statistics between microstates affects the thermalization behaviour of the black hole at late and early times. We find "echoes" in cases where there is substantial eigenvalue repulsion between individual microstates or if there are regularly spaced clusters of microstates. In part II of the thesis we analyze the process of information recovery and unitarity in black hole/gravity systems coupled to non-gravitational baths. In the first work of part II we study how the evaporation rate of a black hole changes when radiation is extracted near the horizon and apply our results to study how long it takes to recover information thrown into a black hole after the Page time. In the last work of part II we study entanglement wedge nesting in 3D AdS spacetimes cut off by an end-of-the-world brane. Finally, in part III we summarize the main results of the research works.

Acknowledgements

First and foremost I must thank my PhD advisor, Prof. Niayesh Afshordi, for giving me the opportunity to work with him in his research group and for giving me the freedom to pursue my own evolving research interests. Without his constant support and advice this thesis would have never have come to fruition. His guidance not only helped me grow as a researcher but also as a human being.

I would also like to thank Matthew Robbins, Naritaka Oshita, Ramit Dey, Qingwen Wang, Rafael Sorkin, Jahed Abedi, Alice Chen, Tianyi Yang, Elizabeth Gould, Conner Dailey, Johanna N. Borissova, Luís Longo, Ghazal Geshnizjani, and everyone else I have met through Niayesh's weekly group meetings, I have learned a great deal from all of you.

I want to thank the members of my PhD committee, Niayesh Afshordi, Robert Myers, Robert Mann, and Achim Kempf for their feedback and guidance on my thesis work during my PhD program.

I thank Dominik Neuenfeld, Bin Guo, and Luca Iliesiu who took the time collaborate with me in the last few years of my PhD program. I learned a great deal about black holes and gravity from the collaborations and discussions I had with them.

Thanks to Beni Yoshida, Julian Sonner, Alexander Maloney, Geoffrey Pennington, Adam Brown, Steve Giddings, Simon Ross, Mark Van Raamsdonk, and Douglas Stanford for their comments and discussions when I was preparing the manuscripts of the works that have been compiled in this thesis.

I thank all the administration and IT staff members at Perimeter Institute and the University of Waterloo for their help and guidance during my PhD program.

I would also like to give a special thanks to Mr. Daniel Towne, who was a teacher I had in junior high school who helped foster my interest in physics at a young age through the countless discussions we had about popular physics books.

Last but not least, I would like to thank my family; Mom, Dad, Ganesh, Manisha, and Ruby for all the support and encouragement you gave me throughout the ups and downs of my degree program especially during the pandemic.

The works in this thesis were supported by the University of Waterloo, Natural Sciences and Engineering Research Council of Canada (NSERC), and the Perimeter Institute for Theoretical Physics. Research at Perimeter Institute is supported in part by the Government of Canada through the Department of Innovation, Science and Economic Development Canada and by the Province of Ontario through the Ministry of Colleges and Universities.

Dedication

This thesis is dedicated to my mother (Nirmal Saraswat) and my father (Shiv Saraswat). This thesis is a testament to their support and encouragement. It is as much an achievement for them as it has been for me.

Table of Contents

List of Figures

List of Tables

Chapter 1

Thesis Introduction

In this section of the thesis we will begin by giving a basic review of some useful concepts and equations in the subjects of General Relativity, Quantum Theory, and black hole physics which may aid in the understanding of the topics covered in this thesis. Followed by these reviews we will give an overview of recent advancements in our understanding of the quantum nature of black holes and then conclude the introduction by giving an overview of the main works complied in this thesis and the types of questions they are attempting to investigate/address.

1.1 Basic Review of General Relativity

Alongside the formalism of Quantum Theory, Einstein's General Theory of Relativity serves as one of the great pillars of modern theoretical physics. It formulates our familiar notions of space and time as one entity called spacetime and formulates the force of gravity in terms of quantities that characterize the curvature of spacetime.

In the following subsections we will go over some aspects of General Relativity that will be useful to know in the reading of this thesis. For a more thorough treatment of the subject we refer the reader to the following textbooks which cover the ideas we will review [36, 154, 120, 15].

1.1.1 Manifolds, Tensor Fields, and the Metric

The rich mathematical theory of differential geometry and tensor analysis lies at the heart of the mathematical formulation of spacetime and its curvature. A spacetime in $d+1$-dimensions is described by a manifold, denoted $\mathcal{M}_{d+1}$, which is essentially a space that resembles flat space in a sufficiently small open neighborhood of any point $p \in \mathcal{M}_{d+1}$. This aspect of the manifold is very important because it allows one to generalize the familiar notion of vector spaces in Euclidean/Lorentzian flat spaces to curved manifolds through the introduction of a tangent space to a point on the manifold.

The tangent space is a way by which one can associate a vector space to any point $p \in \mathcal{M}_{d+1}$. We denote the tangent space to the point p as $T_p(\mathcal{M}_{d+1})$. The dimension of the tangent space is equal to the dimension of the manifold (in our case here it is $d+1$-dimensional). Like any vector space, it will be spanned by $d+1$ basis vectors, a particularly useful basis for the tangent space is the so called "coordinate-basis" which is the set of partials, $\{\partial_\mu\}_{\mu=0}^d$. Along with the tangent space one can define the cotangent space $T_p^*(\mathcal{M}_{d+1})$ which is a vector space of equal dimension to the tangent space and is spanned by $d+1$ "dual basis vectors." We denote the dual basis vectors (in coordinate basis), as $\{dx^\mu\}_{\mu=0}^d$, which will satisfy the identity $\partial_\nu(dx^\mu) = dx^\mu(\partial_\nu) = \delta^\mu_\nu$. Under general invertible coordinate transformations of the form $\tilde{x} = \tilde{x}(x)$ the basis and dual basis vectors transform as follows:

$$\begin{aligned} \partial_\mu &= \frac{\partial \tilde{x}^{\mu'}}{\partial x^\mu}\tilde{\partial}_{\mu'} \\ d\tilde{x}^{\mu'} &= \frac{\partial \tilde{x}^{\mu'}}{\partial x^\mu}dx^\mu. \end{aligned} \tag{1.1}$$

Note that throughout this thesis we use Einstein summation convention where repeated indices are summed over (e.g. $A^\mu B_\mu = \sum_{\mu=0}^d A^\mu B_\mu$). One can define a general (n,m)-tensor field T over the manifold $\mathcal{M}_{d+1}$. It is a multi-linear map $T : T_p^* \times \cdots \times T_p^* \times T_p \times \cdots \times T_p \to \mathbb{R}$. In the coordinate basis it can be expressed as follows:

$$T = T^{\mu_1\mu_2\cdots\mu_n}{}_{\nu_1\nu_2\cdots\nu_m}\partial_{\mu_1} \otimes \partial_{\mu_2} \otimes \cdots \otimes \partial_{\mu_n} \otimes dx^{\nu_1} \otimes dx^{\nu_2} \otimes \cdots \otimes dx^{\nu_m}, \tag{1.2}$$

where $T^{\mu_1\mu_2\cdots\mu_n}{}_{\nu_1\nu_2\cdots\nu_m}$ are the components of T in the coordinate basis. The tensor T represents a physically meaningful quantity over the manifold and should be invariant under general coordinate transformations. In particular, we define the coordinate transformed tensor as follows:

$$\tilde{T} = \tilde{T}^{\mu'_1\mu'_2\cdots\mu'_n}{}_{\nu'_1\nu'_2\cdots\nu'_m}\tilde{\partial}_{\mu'_1} \otimes \tilde{\partial}_{\mu'_2} \otimes \cdots \otimes \tilde{\partial}_{\mu'_n} \otimes d\tilde{x}^{\nu'_1} \otimes d\tilde{x}^{\nu'_2} \otimes \cdots \otimes d\tilde{x}^{\nu'_m}. \tag{1.3}$$

Using the transformation law for the basis vectors and their dual we will find that the components of the transformed tensor (i.e. $\tilde{T}^{\mu'_1\mu'_2\cdots\mu'_n}{}_{\nu'_1\nu'_2\cdots\nu'_m}$) must transform in a specific way to ensure that $\tilde{T} = T$. In particular, the components of a (n, m)-tensor, T, should transform according to the identity below:

$$\tilde{T}^{\mu'_1\cdots\mu'_n}{}_{\nu'_1\cdots\nu'_m}(\tilde{x}) = \frac{\partial \tilde{x}^{\mu'_1}}{\partial x^{\alpha_1}} \cdots \frac{\partial \tilde{x}^{\mu'_n}}{\partial x^{\alpha_n}} \frac{\partial x^{\sigma_1}}{\partial \tilde{x}^{\nu'_1}} \cdots \frac{\partial x^{\sigma_m}}{\partial \tilde{x}^{\nu'_m}} T^{\alpha_1\cdots\alpha_n}{}_{\sigma_1\cdots\sigma_m}(x(\tilde{x})). \tag{1.4}$$

Some common examples of tensor fields are:

- Scalar field, ϕ, which transforms as $(0, 0)$-tensor field.
- Vector field, $V = V^\mu \partial_\mu$, whose components, V^μ, transform as $(1, 0)$-tensor fields. For example, if we parameterize a line using some parameter λ then the tangent to the curve $\frac{dx^\mu}{d\lambda}$ describes the components of a vector field.
- One-form field, $\omega_\mu dx^\mu$, whose components, ω_μ, transform as $(0, 1)$-tensor fields. For example, the gradient of a scalar field $\partial_\mu \phi$ describes the components of a one-form.

More often than not we will work in a prescribed coordinate system and manipulations of tensors will reduce to the manipulation of tensor components. Therefore, from this point forward (unless otherwise specified) we will identify tensors with their components in the natural coordinate basis. If we ever need the full physical tensor object we can "tack-on" the necessary basis vectors and one-forms after the manipulations are complete.

Now that we have reviewed some basic facts about tensors and how they transform under coordinate transformations, we will define some operations which allow us build new tensors from old ones. Lets suppose we have a (n, m)-tensor T and a (p, q)-tensor U. We can define a $(n + p, m + q)$-tensor by taking the tensor product. The new tensor, denoted $T \otimes U$, will have the following components:

$$(T \otimes U)^{\mu_1\cdot\cdot\mu_n\alpha_1\cdot\cdot\alpha_p}{}_{\nu_1\cdot\cdot\nu_m\sigma_1\cdot\cdot\sigma_q} = \left(T^{\mu_1\cdot\cdot\mu_n}{}_{\nu_1\cdot\cdot\nu_m}\right)\left(U^{\alpha_1\cdot\cdot\alpha_p}{}_{\sigma_1\cdot\cdot\sigma_q}\right). \tag{1.5}$$

We can also do an operation between tensor components called "index contraction." This amounts to taking an upper index and lower index and setting them equal to each other (i.e. summing over the indices). For example, lets consider an (n, m)-tensor T we can apply the operation of index contraction to the k-th upper index and p-th lower index

(where $1 \leq k \leq n$ and $1 \leq p \leq m$) shown below[1]:

$$\delta^{\nu_p}_{\mu_k} T^{\mu_1 \cdots \mu_k \cdots \mu_n}{}_{\nu_1 \cdots \nu_p \cdots \nu_m} = \sum_{\mu_k=0}^{d} T^{\mu_1 \cdots \mu_{k-1} \mu_k \mu_{k+1} \cdots \mu_n}{}_{\nu_1 \cdots \nu_{p-1} \mu_k \nu_{p+1} \cdots \nu_m}. \tag{1.6}$$

The resulting object is a $(n-1, m-1)$ tensor field. This also extends to tensors that are built from a tensor product of multiple tensors. As long as we contract one upper and one lower index the result will transform as a tensor. We can see that in certain cases index contraction can be used to define coordinate invariant quantities. A simple example is to contract a one-form with a vector we will obtain a scalar field which is invariant under coordinate transformations.

Now that we have defined basic operations that allow us to build up tensors from other tensors through the use of tensor products and index contraction we move on and define the metric. The metric is a special object which allows one to measure distances and angles on a manifold. More specifically it maps a pair vectors in $T_p(\mathcal{M}_{d+1})$ to real numbers. We denote this map, $\mathbf{g}$, and it has the following properties for $V, W, Z \in T_p(\mathcal{M}_{d+1})$ and $a \in \mathbb{R}$:

- It is symmetric: $\mathbf{g}(V, W) = \mathbf{g}(W, V)$.
- It is linear: $\mathbf{g}(aV + W, Z) = a\mathbf{g}(V, Z) + \mathbf{g}(W, Z)$.
- It is non-degenerate: There is no $V \neq 0$, such that $\mathbf{g}(V, W) = 0$ for any possible choice of $W \Rightarrow \det(\mathbf{g}) \neq 0$.

The metric allows us to distinguish the difference between three types of non-degenerate manifolds through the signature. The signature is essentially the number of positive and negative eigenvalues of the metric. We have the following classification:

1. Riemannian (Euclidean) manifold: All eigenvalues of metric are of one sign (usually we take convention that they are all positive). The short-hand is to say the signature is $(+, +, +, ..., +)$
2. Lorentzian manifold: All eigenvalues except one are of the same sign. The short-hand is to say signature is $(-, +, +, ..., +)$, this is the convention we adopt in this thesis.

[1] Although, it is computational clear why the appearance of the Kronecker delta symbol is necessary in the process of index contraction it has a much deeper meaning when we consider the basis and dual basis vectors. If we recall that the basis and dual basis satisfy $dx^\mu \partial_\nu = \delta^\mu_\nu$ we can view index contraction as making use of this identity we are actually contracting the k-th basis with the p-th dual basis vector to get the Kronecker delta symbol.

3. Indefinite manifold: A non-degenerate manifold that is neither Euclidean nor Lorentzian.

The statement we made before, that spacetime is a manifold, can be refined further by stating that spacetime is a Lorentzian manifold. Unlike Euclidean manifolds, which will always have a non-negative inner product between vectors, a Lorentizan manifold can have an inner product which can be positive, negative, or zero. In particular, we have three types of vectors in a Lorentzian manifold:

- A vector $V \in T_p(\mathcal{M}_{d+1})$ is timelike if $\mathbf{g}(V,V) < 0$.
- A vector $V \in T_p(\mathcal{M}_{d+1})$ is lightlike (null) if $\mathbf{g}(V,V) = 0$ (also we assume $V \neq 0$).
- A vector $V \in T_p(\mathcal{M}_{d+1})$ is spacelike if $\mathbf{g}(V,V) > 0$.

This adds additional structure to the manifold which is not present in an Euclidean manifold namely the notion of causality and lightcones[2].

Now that we have introduced the notion of a metric and how it defines the type of manifold we deal with we will connect it to our discussion of tensor fields. In particular, the metric is also tensor due to the fact that it is a linear map. We can express the metric in the coordinate basis by writing:

$$\mathbf{g}(V,W) = \mathbf{g}(V^\mu \partial_\mu, W^\nu \partial_\nu) = \mathbf{g}(\partial_\mu, \partial_\nu) V^\mu W^\nu. \tag{1.7}$$

We identify $\mathbf{g}(\partial_\mu, \partial_\nu) = g_{\mu\nu}$ as the components of the metric in the coordinate basis. So the metric now becomes a symmetric $(0,2)$-tensor. Using it, we can define the invariant spacetime infinitesimal length element:

$$ds^2 = g_{\mu\nu} dx^\mu \otimes dx^\mu = g_{\mu\nu} dx^\mu dx^\mu. \tag{1.8}$$

Beyond just defining a length element, the metric tensor also serves as a way to lower the indices of other tensors defined on the manifold. In particular for a given tensor (n,m) we can obtain a $(n-1, m+1)$ tensor as follows:

$$g_{\alpha\mu_k} T^{\mu_1 \cdots \mu_{k-1} \mu_k \mu_{k+1} \cdots \mu_n}{}_{\nu_1 \cdots \nu_m} = T^{\mu_1 \cdots \mu_{k-1}}{}_{\alpha}{}^{\mu_{k+1} \cdots \mu_n}{}_{\nu_1 \cdots \nu_m}. \tag{1.9}$$

We can see that one of the indices of the metric tensor is contracting with an upper index of the T. This is usually called "lowering the index" of T. The inverse metric denoted $g^{\mu\nu}$ is a (2,0)-tensor which satisfies the following identity:

$$g^{\mu\alpha} g_{\alpha\nu} = \delta^\mu_\nu. \tag{1.10}$$

[2]The discussion of causality is quite rich and plays a central role in understanding the propagation of matter field in various spacetime backgrounds and in the discussion of horizons.

In a similar way by which one can lower the index of a tensor with the metric the inverse metric can be used to "raise the index" of a tensor. In other words, we can use the inverse metric and get a $(n+1, m-1)$-tensor from a (n, m)-tensor as follows:

$$g^{\alpha\nu_p} T^{\mu_1 \cdots \mu_n}{}_{\nu_1 \cdots \nu_{p-1} \nu_p \nu_{p+1} \cdots \nu_m} = T^{\mu_1 \cdots \mu_n}{}_{\nu_1 \cdots \nu_{p-1}}{}^{\alpha}{}_{\nu_{p+1} \cdots \nu_m}. \tag{1.11}$$

Now that we have gone over the basics of a manifold and how to define tensor quantities over the manifold, we proceed to the next subsection and define the notion of a geodesic, derivatives of tensors, and how to quantify and compute the curvature of a manifold given the metric tensor.

1.1.2 Geodesics, Derivatives, and Curvature

The familiar fact that the shortest distance between two points in Euclidean flat space is a straight line can be generalized to curved manifolds through the concept of a geodesic. We fix two points on the manifold $p_1, p_2 \in \mathcal{M}_{d+1}$ and define a line segment in the manifold which connects the two points. We parameterize this line through some arbitrary parameter $\lambda \in [\lambda_1, \lambda_2]$ and write it as $x^\mu = x^\mu(\lambda)$, where $p_1 = x^\mu(\lambda_1)$ and $p_2 = x^\mu(\lambda_2)$. Then the length of this line can be expressed in terms of the following coordinate invariant length functional involving the metric and the tangent vector to the curve:

$$s[x, \dot{x}] = \int_{\lambda_1}^{\lambda_2} \sqrt{g_{\mu\nu} \dot{x}^\mu \dot{x}^\nu} d\lambda = \int_{\lambda_1}^{\lambda_2} \sqrt{g_{\mu\nu} \frac{dx^\mu}{d\lambda} \frac{dx^\nu}{d\lambda}} d\lambda. \tag{1.12}$$

The geodesic connecting the two points will be stationary under variations of the form $x^\mu \to x^\mu + \delta x^\mu$. In particular we have that:

$$\delta s[x, \dot{x}] = -\int_{\lambda_1}^{\lambda_2} \left[\frac{g_{\sigma\nu} \ddot{x}^\nu + \frac{1}{2} \left(\partial_\mu g_{\nu\sigma} + \partial_\nu g_{\mu\sigma} - \partial_\sigma g_{\mu\nu} \right) \dot{x}^\mu \dot{x}^\nu}{\sqrt{g_{\mu\nu} \dot{x}^\mu \dot{x}^\nu}} \right] \delta x^\sigma = 0. \tag{1.13}$$

Setting the terms in the numerator in the square brackets to zero gives the following equation of motion:

$$\begin{aligned} &\frac{d^2 x^\mu}{d\lambda^2} + \Gamma^\mu_{\alpha\beta} \frac{dx^\alpha}{d\lambda} \frac{dx^\beta}{d\lambda} = 0 \\ &\Gamma^\mu_{\alpha\beta} = \frac{1}{2} g^{\mu\sigma} \left(\partial_\alpha g_{\beta\sigma} + \partial_\beta g_{\alpha\sigma} - \partial_\sigma g_{\alpha\beta} \right). \end{aligned} \tag{1.14}$$

The equation above is called the "geodesic equation" and solving it gives the trajectory of a geodesic connecting two fixed points in a spacetime. The three index object, $\Gamma^\mu_{\alpha\beta}$,

is called a Christoffel symbol (sometimes called the metric-compatible connection) and is not a tensor. However, it plays a central role in quantifying the curvature of a spacetime. Before discussing this it is worth mentioning that are three types of geodesics in spacetime which are distinguished by the inner product of the tangent vector to the geodesic:

- Timelike geodesics: $g_{\mu\nu}\frac{dx^\mu}{d\lambda}\frac{dx^\nu}{d\lambda} < 0$.
- Lightlike (null) geodesics: $g_{\mu\nu}\frac{dx^\mu}{d\lambda}\frac{dx^\nu}{d\lambda} = 0$.
- Spacelike geodesics: $g_{\mu\nu}\frac{dx^\mu}{d\lambda}\frac{dx^\nu}{d\lambda} > 0$.

Now that we have discussed geodesics which generalize the notion of straight lines to curved manifolds we will discuss how to compute rates of change of tensor fields defined on a manifold. In general given a (n, m)-tensor the partial derivative of a tensor will not result in a tensor quantity. Instead, one must introduce the notion of a covariant derivative, denoted ∇_μ, which acts on an (n, m)-tensor, T, as follows:

$$\begin{aligned}\nabla_\mu T^{\mu_1\cdots\mu_n}{}_{\nu_1\cdots\nu_m} &= \partial_\mu T^{\mu_1\cdots\mu_n}{}_{\nu_1\cdots\nu_m} + \Gamma^{\mu_1}_{\mu\alpha}T^{\alpha\cdots\mu_n}{}_{\nu_1\cdots\nu_m} + \cdots + \Gamma^{\mu_n}_{\mu\alpha}T^{\mu_1\cdots\alpha}{}_{\nu_1\cdots\nu_m} \\ &- \Gamma^{\alpha}_{\mu\nu_1}T^{\mu_1\cdots\mu_n}{}_{\alpha\cdots\nu_m} - \cdots - \Gamma^{\alpha}_{\mu\nu_m}T^{\mu_1\cdots\mu_n}{}_{\nu_1\cdots\alpha}.\end{aligned} \tag{1.15}$$

Unlike the derivative of a tensor which in general is not a tensor the covariant derivative of a (n, m) tensor results in a $(n, m + 1)$-tensor. Some useful identities/properties involving the covariant derivative are as follows:

- It acts linearly: $\nabla_\mu\left[T^{\mu_1\cdots\mu_n}{}_{\nu_1\cdots\nu_m} + Q^{\mu_1\cdots\mu_n}{}_{\nu_1\cdots\nu_m}\right] = \nabla_\mu T^{\mu_1\cdots\mu_n}{}_{\nu_1\cdots\nu_m} + \nabla_\mu Q^{\mu_1\cdots\mu_n}{}_{\nu_1\cdots\nu_m}$.
- It obeys a product rule:
  $\nabla_\mu\left[T^{\mu_1\cdots\mu_n}{}_{\nu_1\cdots\nu_m}Q^{\alpha_1\cdots\alpha_p}{}_{\beta_1\cdots\beta_l}\right] = \nabla_\mu T^{\mu_1\cdots\mu_n}{}_{\nu_1\cdots\nu_m}Q^{\alpha_1\cdots\alpha_p}{}_{\beta_1\cdots\beta_l} + T^{\mu_1\cdots\mu_n}{}_{\nu_1\cdots\nu_m}\nabla_\mu Q^{\alpha_1\cdots\alpha_p}{}_{\beta_1\cdots\beta_l}$.
- The covariant derivative of the metric and inverse metric vanish: $\nabla_\alpha g_{\mu\nu} = 0$ and $\nabla_\alpha g^{\mu\nu} = 0$.
- If ϕ is a scalar (i.e. (0,0)-tensor) then, $\nabla_\mu\phi = \partial_\mu\phi$.

Now that we have defined the notion of a covariant derivative of a tensor we can proceed to quantify the curvature of a manifold through the definition of the Riemann curvature tensor. It is given by:

$$R^\rho{}_{\sigma\mu\nu} = \partial_\mu\Gamma^\rho_{\nu\sigma} - \partial_\nu\Gamma^\rho_{\mu\sigma} + \Gamma^\rho_{\mu\lambda}\Gamma^\lambda_{\nu\sigma} - \Gamma^\rho_{\nu\lambda}\Gamma^\lambda_{\mu\sigma}. \tag{1.16}$$

Although Christoffel symbols by themselves are not tensors, the Riemann curvature tensor defined above really is a $(1,3)$-tensor. It defines the curvature of a manifold at any point in terms of the first and second derivatives of the metric tensor. In particular, one says a manifold is flat exactly when all components of the Riemann tensor vanish at all points on the manifold. If this does not hold then the manifold is not flat and has curvature quantified by the Riemann tensor. The Riemann tensor has a number of symmetries involving the placement of indices. To discuss these symmetries it is useful to lower the upper index and talk about $R_{\rho\sigma\mu\nu} = g_{\rho\lambda}R^{\lambda}{}_{\sigma\mu\nu}$. With this we have the following identities:

- Antisymmetric in first two indices: $R_{\rho\sigma\mu\nu} = -R_{\sigma\rho\mu\nu}$.
- Antisymmetric in last two indices: $R_{\rho\sigma\mu\nu} = -R_{\rho\sigma\nu\mu}$.
- Invariant under first and last pair interchange: $R_{\rho\sigma\mu\nu} = R_{\mu\nu\rho\sigma}$.
- Sum of cyclic permutation of last three indices vanish: $R_{\rho\sigma\mu\nu} + R_{\rho\nu\sigma\mu} + R_{\rho\mu\nu\sigma} = 0$.

These index symmetries imply that the Riemann tensor in $d+1$ dimensions has $\frac{d(d+2)(d+1)^2}{12}$ independent components.

From the Riemann tensor there are a number of other tensors on can define which often show up in the context of gravity. In particular, the Ricci tensor is a $(0,2)$-tensor which is defined as follows:

$$R_{\mu\nu} = R^{\lambda}{}_{\mu\lambda\nu}. \tag{1.17}$$

The Ricci tensor is symmetric under the interchange of its indices. Using the Ricci tensor we can define the Ricci scalar as follows:

$$R = R^{\mu}_{\mu} = g^{\mu\nu}R_{\mu\nu}. \tag{1.18}$$

Both the Ricci scalar and Ricci tensor are used to define the Einstein tensor:

$$G_{\mu\nu} = R_{\mu\nu} - \frac{1}{2}Rg_{\mu\nu}. \tag{1.19}$$

It has the property that:

$$\nabla^{\mu}G_{\mu\nu} = 0. \tag{1.20}$$

The Einstein tensor plays the role of encoding the geometry and curvature in the Einstein field equations which describes the dynamics of the spacetime manifold in the presence of matter and energy.

1.1.3 Einstein Hilbert Action and Field Equations

Thus far we have discussed the idea of manifolds and tensor fields. In this subsection we will briefly discuss the Einstein field equations. These encode the dynamics of the spacetime manifold itself. In particular, the central idea behind the Einstein field equations is that matter and energy generate spacetime curvature. Mathematically, the idea is made precise through the Einstein field equations (with cosmological constant):

$$G_{\mu\nu} + \Lambda g_{\mu\nu} = R_{\mu\nu} - \frac{1}{2} R g_{\mu\nu} + \Lambda g_{\mu\nu} = 8\pi G_N T_{\mu\nu}. \tag{1.21}$$

The left hand side contains information about spacetime geometry and its curvature which can be written in terms of the metric tensor, $g_{\mu\nu}$, and its derivatives. The constant Λ is called the "cosmological constant" and is an additional term that is added in the field equations which gives rise to a non-trivial energy density in spacetime even in the absence of matter (i.e. related to the energy density of quantum fields in the vacuum state).

The right-hand side is the stress-energy tensor of matter fields that propagate in the spacetime. Since any spacetime can arise through an appropriate choice of $T_{\mu\nu}$ it is possible to construct pathological spacetimes with closed time-like curves or naked singularities. For this reason, it is useful to constrain the kind of matter field configurations. What we deem as physically allowable configurations of matter are motivated by our current understanding of matter and is summarized in terms of mathematical relations called energy conditions.

Einstein's Field equations (with cosmological constant) can also be derived from the principle of least action through the Einstein-Hilbert action with cosmological constant, denoted $I_{EH}[g]$ (with an appropriate boundary term), plus some covariant matter action denoted $I_{\text{matter}}[g, \Psi]$ and often serves as a useful starting point when discussing quantum aspects of gravity and the dynamics of the propagation of matter fields on spacetime. Explicitly, the action of interest is given by:

$$\begin{aligned}
I_{grav+\text{matter}}[g, \Psi] &= I_{EH}[g] + I_B[g] + I_{\text{matter}}[g, \Psi] \\
I_{EH}[g] &= \frac{1}{16\pi G_N} \int_{\mathcal{M}_{d+1}} d^{d+1}x \sqrt{-g}\, [R - 2\Lambda] \\
I_B[g] &= \frac{\sigma}{8\pi G_N} \int_{\partial\mathcal{M}_{d+1}} d^d y |h|^{1/2} K \\
I_{\text{matter}}[g, \Psi] &= \int_{\mathcal{M}_{d+1}} d^{d+1}x \sqrt{-g} \mathcal{L}(\Psi),
\end{aligned} \tag{1.22}$$

where $I_B[g]$ is a boundary term which allows us to obtain a well defined variational problem when varying the metric ($\sigma = \pm 1$ depending on if the boundary is timelike or spacelike).

Note that there actually two dynamical fields one involves the matter fields Ψ and the other involves the metric g. Varying the gravity plus matter action with respect to the inverse metric $g^{\mu\nu}$ will give rise to the Einstein field equation given in Eq. (1.21) with:

$$T_{\mu\nu} = -2\frac{1}{\sqrt{-g}}\frac{\delta I_{matter}}{\delta g^{\mu\nu}}. \tag{1.23}$$

Note that the action also contains matter fields which we should also treat dynamically. So we also have another set of equations of motion beyond the Einstein equations field equations which are given by requiring:

$$\frac{\delta I_{matter}}{\delta \Psi} = 0. \tag{1.24}$$

A common example of I_{matter} is for a minimally coupled massive scalar Ψ where:

$$I_{matter}[g, \Psi] = \int_{\mathcal{M}_{d+1}} d^{d+1}x\sqrt{-g}\left[-\frac{1}{2}g^{\mu\nu}\nabla_\mu\Psi\nabla_\nu\Psi - \frac{1}{2}m^2\Psi^2\right]. \tag{1.25}$$

In this case the equation of motion for the scalar is the wave equation (Klein-Gordon equation in curved spacetime):

$$\begin{aligned} &\Box\Psi - m^2\Psi = 0 \\ &\Box = g^{\mu\nu}\nabla_\mu\nabla_\nu. \end{aligned} \tag{1.26}$$

The stress energy tensor for the scalar field becomes:

$$T^{\Psi}_{\mu\nu} = -2\frac{1}{\sqrt{-g}}\frac{\delta I_{matter}}{\delta g^{\mu\nu}} = \nabla_\mu\Psi\nabla_\nu\Psi - \frac{1}{2}g_{\mu\nu}\nabla^\lambda\Psi\nabla_\lambda\Psi - \frac{1}{2}m^2 g_{\mu\nu} \tag{1.27}$$

So the issue of fully solving the classical problem of a scalar field propagating on a fully dynamical spacetime involves finding a simultaneous solution to both Ψ and g in the following equations:

$$\begin{aligned} &R_{\mu\nu} - \frac{1}{2}Rg_{\mu\nu} + \Lambda g_{\mu\nu} = 8\pi G_N\left[\nabla_\mu\Psi\nabla_\nu\Psi - \frac{1}{2}g_{\mu\nu}\nabla^\lambda\Psi\nabla_\lambda\Psi - \frac{1}{2}m^2 g_{\mu\nu}\right] \\ &\Box\Psi - m^2\Psi = 0. \end{aligned} \tag{1.28}$$

Even for this simple example the full dynamical problem is very difficult to solve exactly and often certain assumptions are made. For example a common approach, is to treat G_N as a perturbative parameter. One begins by trying to find a solution in the regime where $G_N \to$

0 (in this limit we can think of approximating spacetime as a fixed curved background with fields propagating on it, not changing the overall geometry too much). In this case the right-hand side of the Einstein field equations vanish and one can study solutions of the scalar wave equation on a fixed curved background. Once such a solution is found then a more general solution might be built up around this background as perturbative series in G_N. Even this leading order solution serves as a useful effective tool to study wave phenomena on curved backgrounds. For this reason as well others, it is often quite useful to simply study the Einstein equations when $T_{\mu\nu} = 0$ (i.e. the Einstein field equation in a vacuum).

When we set $T_{\mu\nu} = 0$ the Einstein field equations reduce to what are called the Einstein vacuum equations which read ($d \geq 2$):

$$R_{\mu\nu} - \frac{2\Lambda}{d-1} g_{\mu\nu} = 0. \tag{1.29}$$

In the case when $\Lambda = 0$ one solution to the vacuum equation is flat Minkowski spacetime (the manifold over which special relativity is formulated), $\mathbb{R}^{1,d}$, and has the following line element in Cartesian-like coordinates:

$$ds^2 = -(dx^0)^2 + (dx^1)^2 + (dx^2)^2 + \cdots + (dx^d)^2. \tag{1.30}$$

One interesting aspect about this solution is that it is a maximally symmetric spacetime it has the $\frac{(d+1)(d+2)}{2}$ Killing vectors (the maximal number you can possibly have in $d+1$-dimensions)[3]. A useful fact of maximally symmetric spacetimes is that the Riemann tensor of the spacetime is completely determined by the Ricci scalar. In particular, we have the following formula for the Riemann tensor of a maximally symmetric manifold:

$$R_{\rho\sigma\mu\nu} = \frac{R}{d(d+1)} \left(g_{\rho\mu} g_{\sigma\nu} - g_{\rho\nu} g_{\sigma\mu} \right). \tag{1.31}$$

The maximally symmetric analogue of Minkowski spacetime for $\Lambda < 0$ is called Anti-de Sitter spacetime (or pure AdS). In global coordinates the spacetime has the following metric:

$$ds^2 = L^2 \left(-\cosh^2 \rho d\tau^2 + d\rho^2 + \sinh^2 \rho d\Omega_{d-1}^2 \right). \tag{1.32}$$

[3]We say that a vector ξ^μ is a Killing vector if the Lie derivative of the metric along the integral curves generated by ξ^μ vanishes. This condition corresponds to solving Killing's equation $\nabla_\mu \xi_\nu + \nabla_\nu \xi_\mu = 0$. Physically, it means that if I move along the integral curves generated by the vector Killing vector field the way I measure distances (i.e. the metric) will not change. Maximally symmetric spacetimes in $d+1$ dimensions have the maximal number of Killing vectors corresponding to $d+1$ translations, d boosts, and $d(d-1)/2$ spatial rotations for a grand total of $\frac{(d+1)(d+2)}{2}$ Killing vectors.

One can check that this constitutes a solution to the vacuum equations with the AdS radius, L, identified with the cosmological constant through the following relation:

$$\Lambda_{AdS} = -\frac{d(d-1)}{2L^2}. \tag{1.33}$$

Such negatively curved spacetimes are of central importance in the discussion of the AdS/CFT correspondence which we will discuss in later sections.

For $\Lambda > 0$ the maximally symmetric analogue of Minkowski spacetime is de-Sitter spacetime (or dS). In global coordinates the spacetime has the following line element:

$$ds^2_{dS} = -d\tau^2 + L^2 \cosh^2\left(\frac{\tau}{L}\right) d\Omega_d^2. \tag{1.34}$$

This spacetime serves as a useful starting point when discussing cosmological spacetimes (which we will not discuss in this thesis).

In this thesis we will mainly concern ourselves with spacetimes with $\Lambda \leq 0$ (i.e. asymptotically flat or AdS).

Of course, the maximally symmetric solutions are but one example of solutions to the Einstein vacuum equations. Black holes (the primary concern of this thesis) are another example of spacetimes that are solutions to the equations. We will discuss these solutions in more depth in later sections.

1.2 Basic Review of Quantum Theory

Alongside the formalism of General Relativity, Quantum Theory serves as one of the great pillars of modern theoretical physics. It serves as the fundamental formalism to study the quantum nature of matter and its interactions with the electromagnetic, weak nuclear force, and strong nuclear force. All of which can be understood in a unified framework called the "Standard Model." At the heart of quantum theory lies the idea that a physical system can be described in terms of a state vector living in a Hilbert space. This state vector evolves according to deterministic laws but the predictions we extract from measuring a quantum state are of a probabilistic/statistical nature.

In the following subsections, we will go over some aspects of quantum theory that will be useful to know in the reading of this thesis. For a more thorough treatment of the subject we refer the reader to the following textbooks which cover the ideas we will review [109, 118, 15].

1.2.1 Hilbert Spaces, States Vectors, and Operators

In quantum mechanics physical systems are described by a state vectors $|\psi\rangle$ and the state vector lives in a Hilbert space, $\mathcal{H}$, which is a vector space over the complex field, $\mathbb{C}$. The vector space has an inner product, which maps two state vectors to a complex number and has the following properties for any three $|\psi\rangle, |\phi\rangle, |\chi\rangle \in \mathcal{H}$ and any $a, b \in \mathbb{C}$:

1. Positivity : $\langle\psi|\psi\rangle \geq 0$ and is saturated iff $|\psi\rangle = 0$.
2. Linearity: $\langle\psi| (a|\phi\rangle + b|\chi\rangle) = a\langle\psi|\phi\rangle + b\langle\psi|\chi\rangle$.
3. Complex conjugation: $\langle\psi|\phi\rangle = \langle\phi|\psi\rangle^*$.

Using this inner product we require that the state vector, $|\psi\rangle$, of a physical system to be of unit norm (i.e. $\langle\psi|\psi\rangle = 1$). Any state vector can be decomposed into basis vectors that span the Hilbert space. In particular, we can choose a set of orthonormal basis vectors, $\{|n\rangle\}$, which span $\mathcal{H}$. Then we can write any state, ψ, in the basis $\{|n\rangle\}$:

$$|\psi\rangle = \mathcal{I}|\psi\rangle = \sum_n |n\rangle\langle n|\psi\rangle = \sum_n \langle n|\psi\rangle |n\rangle = \sum_n \psi_n |n\rangle, \tag{1.35}$$

where we used the fact that the identity operator, $\mathcal{I} = \sum_n |n\rangle\langle n|$, and defined expansion coefficients, $\psi_n = \langle n|\psi\rangle \in \mathbb{C}$. The dual to the state $|\psi\rangle$ is $\langle\psi|$ and this can be written in the dual basis $\{\langle n|\}$ as follows:

$$\langle\psi| = \sum_n \psi_n^* \langle n|. \tag{1.36}$$

Due to the fact that the state has a unit norm we obtain the following identity for the sum over the modulus square of the expansion coefficients:

$$\sum_n \psi_n^* \psi_n = \sum_n |\psi_n|^2 = 1. \tag{1.37}$$

We can also describe a composite quantum system. Suppose $|\psi_1\rangle \in \mathcal{H}_1$ and $|\psi_2\rangle \in \mathcal{H}_2$, then we can describe the joint quantum state as a tensor product of the two state vectors $|\psi_1\rangle \otimes |\psi_2\rangle$ in a larger Hilbert space $\mathcal{H}_1 \otimes \mathcal{H}_2$. If $\{e_n^{(1)}\}$ and $\{e_{n'}^{(2)}\}$ constitute a complete basis for $\mathcal{H}_1$ and $\mathcal{H}_2$ respectively, then $\{e_n^{(1)} \otimes e_{n'}^{(2)}\}$ forms a complete basis for $\mathcal{H}_1 \otimes \mathcal{H}_2$.

Now that we have defined the mathematical language by which we define states and subsystems of a physical system we can discuss the issue of physical processes. In quantum

mechanics a physical process is represented by a some operator. The operator is a linear map that takes state vectors to other state vectors. For example, if A is operator then we can act on some state vector $|\psi\rangle$ to get another state vector $|\phi\rangle$. We write:

$$|\phi\rangle = A\,|\psi\rangle\,. \tag{1.38}$$

In this thesis we will primarily be interested in unitary and hermitian operators. A unitary operator, U, is a map from $\mathcal{H}$ to itself which has the following property:

$$U^{-1} = U^{\dagger}. \tag{1.39}$$

These types of operators usually implement time evolution or dynamics of a closed quantum system. Another class of operators that are of particular interest in quantum mechanics are Hermitian operators which satisfy $A = A^{\dagger}$. These operators are usually used to represent observables (i.e. quantities which can be measured). We can always write an observable A in a diagonal form given by:

$$A = \sum_n a_n\,|A_n\rangle\,\langle A_n|\,, \tag{1.40}$$

where $|A_n\rangle$ forms a complete orthonormal basis for the Hilbert space over which it acts. Furthermore, since the operator is Hermitian $a_n \in \mathbb{R}$.

When we measure an observable A the possible outcomes of the measurement are given by the eigenvalues of the spectral decomposition of A (i.e. $\{a_n\}$). The probability of obtaining the particular outcome with eigenvalue a_n (assuming no degeneracies) when the system is in a state ψ is:

$$p(a_n) = |\,\langle A_n|\psi\rangle\,|^2. \tag{1.41}$$

If we do indeed measure a_n then immediately after the measurement the state of the system is given by.

$$|\psi'\rangle = \frac{\langle A_n|\psi\rangle}{|\,\langle A_n|\psi\rangle\,|}\,|A_n\rangle\,. \tag{1.42}$$

So up to a phase the new state after obtaining the outcome a_n is $|A_n\rangle$.

We are also often interested in the expectation value of an observable, A, when a system is in a particular state $|\psi\rangle$. This is given by:

$$\langle A\rangle_{\psi} = \langle\psi|A|\psi\rangle\,. \tag{1.43}$$

We can expand this quantity in the basis where A is diagonal to obtain:

$$\langle A\rangle_{\psi} = \sum_n a_n|\,\langle A_n|\psi\rangle\,|^2 = \sum_n a_n p(a_n). \tag{1.44}$$

It is the the weighted average over the possible outcomes. An important aspect of operators is that they generally do not commute. This leads to the notion that there are certain observables that cannot be simultaneously measured to arbitrary accuracy. The prime example being the position and momentum operators which have a commutator of the form:

$$[x, p] = xp - px = i\hbar. \tag{1.45}$$

Since the two operators do not commute they cannot be simultaneously diagonalized and therefore eigenstates of one operator are not eigenstates of the other. Such commutation relations often serve as starting points for the the canonical quantization of fields in quantum field theory and generally are the origin of the "weird" and counter-intuitive aspects of quantum theory.

1.2.2 Unitary Time Evolution and the Hamiltonian

In this subsection, we will briefly discuss the role that the Hamiltonian plays in the time evolution of states in the Schrodinger picture and operators in the Heisenberg picture. In the Schrodinger picture, states are defined to evolve with time and operators are thought to be fixed. The dynamics of a system is captured by the Schrodinger equation given by:

$$i\hbar\frac{\partial}{\partial t}\left|\psi(t)\right\rangle = H\left|\psi(t)\right\rangle, \tag{1.46}$$

where H is a hermitian operator and is the quantum analogue of the total energy of a system. Recall that earlier in this subsection we mentioned that time evolution of a closed quantum system is generally governed by a unitary operator, $U(t, t_0)$ which takes a state vector at time t_0, denoted $|\psi(t_0)\rangle$ to another state vector at a later time t, denoted $|\psi(t)\rangle$. More explicitly, we have:

$$\left|\psi(t)\right\rangle = U(t, t_0)\left|\psi(t_0)\right\rangle. \tag{1.47}$$

With some work one can show that H and U are related by the following equation:

$$i\hbar\frac{\partial U}{\partial t} = HU. \tag{1.48}$$

In the special case where the Hamiltonian is time independent one can obtain the following expression for U in terms of H:

$$U(t, t_0) = e^{-\frac{i}{\hbar}H(t-t_0)}. \tag{1.49}$$

With these results in mind lets consider how the expectation value of an observable evolves in time. As we already reviewed in the Schrodinger picture, state vectors evolve according to Schrodinger's equation, given in Eq. (1.46). The expectation value of an operator A, which is taken to be time independent in this picture, will satisfy the following equation:

$$\frac{\partial}{\partial t}\langle A\rangle_\psi = \partial_t \langle\psi(t)|A|\psi(t)\rangle = \frac{i}{\hbar}\langle\psi(t)|[H,A]|\psi(t)\rangle\,. \tag{1.50}$$

We can see that observables that commute with the Hamiltonian will have expectation values that remain constant with time.

An alternate approach to computing expectation values of hermitian operators is to take the state vectors as being time independent and writing the operators as time dependent. This approach is called the Heisenberg picture. In this picture we can rewrite the expectation values of the hermitian operator A as follows:

$$\langle A\rangle_\psi = \langle\psi(t)|A|\psi(t)\rangle = \langle\psi(t_0)|U^\dagger(t,t_0)AU(t,t_0)|\psi(t_0)\rangle\,. \tag{1.51}$$

We define the following time dependent Heisenberg operators by conjugating with the unitary responsible for time evolution:

$$\begin{aligned} H(t) &= U^\dagger(t,t_0)H(t_0)U(t,t_0) \\ A(t) &= U^\dagger(t,t_0)A(t_0)U(t,t_0). \end{aligned} \tag{1.52}$$

With some work these operators can be shown to satisfy the following equation of motion:

$$\frac{\partial}{\partial t}A(t) = \frac{i}{\hbar}[H(t),A(t)]. \tag{1.53}$$

Usually in the area of AdS/CFT and quantum field theory (and throughout this thesis) we will find it most convenient to use the Heisenberg picture where states are fixed and operators are time dependent. In particular, in the special case where H is time independent we have a very simple prescription for computing expectation values of observables:

$$\langle A(t)\rangle_\psi = \langle\psi|A(t)|\psi\rangle = \langle\psi|e^{\frac{i}{\hbar}Ht}Ae^{-\frac{i}{\hbar}Ht}|\psi\rangle\,, \tag{1.54}$$

where $|\psi\rangle = |\psi(0)\rangle$ and $A = A(0)$.

1.2.3 Density Matrices and Von Neumann/Entanglement Entropy

In this subsection we will give a basic overview of quantum information theory focusing on the concept of entanglement entropy. Our discussion begins with the density matrix

formalism of quantum mechanics which can be thought of as an extension of the state vector formalism we described in Section 1.2.1. In the density matrix formalism we are given an ensemble of quantum states $\{|\psi_k\rangle\}_{k=1}^N$. Each state is weighed by a probability $0 \leq p_k \leq 1$ and $\sum_{k=1}^N p_k = 1$. Now the state of a physical system is given by the density matrix (operator):

$$\rho = \sum_{k=1}^{N} p_k \left|\psi_k\right\rangle \left\langle\psi_k\right| . \tag{1.55}$$

As we can see from the definition above the density matrix has the following properties:

- Unit trace: $Tr(\rho) = 1$.
- Positive Hermitian operator: $\rho = \rho^\dagger$ and eigenvalues are non-negative.

The expectation value of an observable A when the quantum system is described by ρ is now given by the following:

$$\begin{aligned} \left\langle A\right\rangle_\rho &= Tr(A\rho) = Tr(\rho A) = \sum_{k=1}^{N} p_k \left\langle A\right\rangle_{\psi_k} \\ \left\langle A\right\rangle_{\psi_k} &= \sum_n a_n |\left\langle A_n|\psi_k\right\rangle|^2. \end{aligned} \tag{1.56}$$

Unitary evolution of a quantum system described by a density matrix ρ is given by conjugation of a unitary operator U shown below:

$$\rho(t) = U(t, t_0)\rho(t_0)U^\dagger(t, t_0). \tag{1.57}$$

The time evolved density matrix is still a density matrix (i.e. a positive unit trace Hermitian operator). The possible set of outcomes that we measure for an observable A is still given by the eigenvalues of A (where $A\left|A_n\right\rangle = a_n \left|A_n\right\rangle$) except now the probability that we obtain a particular eigenvalue a_n is given by:

$$p(a_n) = Tr\left(\left|A_n\right\rangle \left\langle A_n|\rho|A_n\right\rangle \left\langle A_n\right|\right) = \left\langle A_n|\rho|A_n\right\rangle = \sum_{k=1}^{N} p_k |\left\langle A_n|\psi_k\right\rangle|^2. \tag{1.58}$$

If one does obtain a value a_n after the measurement of the system then immediately after the measurement the system is described by the following density matrix:

$$\rho' = \left|A_n\right\rangle \left\langle A_n\right| . \tag{1.59}$$

In the density matrix formalism we generally distinguish between two kinds of states. A pure state is one in which the density matrix after being diagonalized contains only one non-zero eigenvalue equal to 1. Otherwise we call the state a mixed state. When the state is pure it is straightforward to check that one recovers the state vector formalism. An important fact about pure states is that a pure state undergoing unitary evolution will remain pure this fact will be important in the discussion the black hole information paradox.

A particularly important quantity which one can compute using a density matrix is the Von- Neumann entropy it is given by taking the following trace of a density matrix ρ:

$$S_{VN}(\rho) = -Tr\left[\rho \ln \rho\right]. \tag{1.60}$$

To concretely compute the quantity above it is useful to express the density matrix in a particular orthonormal basis so that it is diagonal:

$$\rho = \sum_{i=1}^{dim(\mathcal{H})} p_i \left|i\right\rangle \left\langle i\right|. \tag{1.61}$$

The Von-Neumann entropy becomes:

$$S_{VN}(\rho) = -\sum_{i=1}^{dim(\mathcal{H})} p_i \ln p_i. \tag{1.62}$$

Where we take "$0 \ln 0 = 0$." From this we can immediately see that if ρ describes a pure state the Von-Neumann entropy is exactly zero. The Von-Neumann entropy is maximized when $p_i = \frac{1}{dim(\mathcal{H})}$ for all i's and the Von-Neumann entropy is $\ln\left[dim(\mathcal{H})\right]$. Sometimes one refers to states in which $\rho \propto \mathcal{I}$ as "maximally mixed states."

Now that we have discussed the basics of density matrices and the Von-Neumann entropy associated with a density matrix we can discuss the idea of entanglement entropy. Before doing this however, we need to discuss the taking the partial trace of density matrices describing composite systems.

Suppose we have a density matrix, ρ_{AB}, describing a composite system in a joint Hilbert space $\mathcal{H}_A \otimes \mathcal{H}_B$. We define the reduced density matrix for subsystem A through an operation called the partial trace. Taking the partial trace of ρ_{AB} can be accomplished by choosing a normalized basis for $\mathcal{H}_B$, lets say it is given by the set of vectors $\{|i\rangle\}$, and computing:

$$\rho_A = Tr_B(\rho_{AB}) = \sum_i \left\langle i|\rho_{AB}|i\right\rangle. \tag{1.63}$$

In a similar manner we can also find the reduced density matrix for subsystem B by taking a partial trace over subsystem A:

$$\rho_B = Tr_A(\rho_{AB}). \tag{1.64}$$

In the special case where ρ_{AB} describes a pure state in the composite system (i.e. $\rho = |\Psi\rangle\langle\Psi|$) we can define a quantity called the "entanglement entropy" which is the Von-Neumann entropy of the reduced density matrices.

$$S_{EE}(\rho_A) = -Tr(\rho_A \ln \rho_A) = -Tr(\rho_B \ln \rho_B) = S_{EE}(\rho_B). \tag{1.65}$$

The reason it is called an "entanglement entropy" is because it can be used to diagnose the existence of quantum entanglement between the subsystem A and B (we must stress that the state of the composite system must be pure). In particular, we have:

- $S_{EE}(\rho_A) = 0$ iff $|\Psi\rangle$ can be written as a product of two states in each subsystem (i.e. a non-entangled state).
- $S_{EE}(\rho_A) > 0$ iff $|\Psi\rangle$ cannot be written as a product of two states in each subsystem (i.e. an entangled state).

This concludes our overview of the basics ideas involved in the discussion of entanglement entropy.

1.2.4 Quantum Statistical Mechanics in Canonical Ensemble

In this subsection we will go over the basics of quantum statistical mechanics and the computation of partition functions in the canonical ensemble.

We start with a quantum system with a Hamiltonian, H, which governs its dynamics. When we place such a quantum system in contact with a thermal bath of fixed temperature $T = \frac{1}{\beta}$ we are considering the system in the so called "canonical ensemble." The system in equilibrium is described by the following density matrix:

$$\rho_{can.} = \frac{e^{-\beta H}}{Z(\beta)}. \tag{1.66}$$

The normalization constant in the denominator is the canonical partition function and can be computed through the following trace:

$$Z(\beta) = Tr\left[e^{-\beta H}\right] = \sum_k \langle E_k|e^{-\beta H}|E_k\rangle = \sum_k e^{-\beta E_k}, \tag{1.67}$$

where we evaluated the trace using the eigenstates of the Hamiltonian to get a more familiar expression of the canonical partition function. With the help of the partition function one can construct the "free energy" of the system given by:

$$F = -T \ln Z(\beta). \tag{1.68}$$

One can then use this to compute thermodynamic quantities like entropy given by:

$$S = -\frac{\partial F}{\partial T}. \tag{1.69}$$

We can compute the thermal average of an observable O in the ensemble, denoted $\langle O \rangle_\beta$, as follows:

$$\langle O \rangle_\beta = Tr\left[\rho_{can.} O\right] = \frac{Tr[e^{-\beta H} O]}{Z(\beta)}. \tag{1.70}$$

More generally one might consider a set of observables in the Heisenberg picture $O_i(t_i)$ and compute n-point thermal correlators in the thermal ensemble as follows:

$$\langle O_1(t_1) O_2(t_2) \cdots O_n(t_n) \rangle_\beta = \frac{Tr\left[e^{-\beta H} O_1(t_1) O_2(t_2) \cdots O_n(t_n)\right]}{Z(\beta)}. \tag{1.71}$$

One can also generalize these notions to more general kinds of thermodynamic ensembles.

1.3 Black Holes

Classical black holes are solutions to the Einstein field equations. However, for the past half a century they have served as systems where the conflict between gravity and quantum theory becomes apparent. In the discussion of in information paradox the need to enforce unitarity in black hole evolution appears to challenge fundamental assumptions about the quantum nature of black hole horizons and whether they should really exist in a UV complete description of gravity.

In the following subsections we will go over some aspects of black holes that will be useful to know in the reading of this thesis. For a more thorough treatment of the subject we refer the reader to the following textbooks/notes which cover the ideas we will review [36, 15, 65, 154, 99, 153].

1.3.1 Black Holes and Black Hole Thermodynamics

Black holes in Einstein's theory of General Relativity represent solutions of the Einstein field equations, given by Eq. (1.21). The most simple class of black holes are spherically symmetric. In particular, a spherically symmetric black hole solution will have a line element of the following form:

$$ds^2 = -f(r)dt^2 + \frac{dr^2}{f(r)} + r^2 d\Omega_{d-1}^2. \tag{1.72}$$

The precise kind of black hole we are dealing with as well as its asymptotic properties are determined by specific choices of the function $f(r)$. In this thesis the most general kind of black hole we will be dealing with is the AdS Reisener-Nordstrom black hole. The line element of the black hole takes the form of Eq. (1.72) with $f(r)$ being:

$$\begin{aligned} f(r) &= 1 - \frac{2m}{r^{d-2}} + \frac{q^2}{r^{2(d-2)}} + \frac{r^2}{L^2} \\ m &= \frac{8\pi G_N M}{(d-1)\left(\frac{2\pi^{d/2}}{\Gamma(d/2)}\right)} \\ q^2 &= \frac{8\pi G_N Q^2}{(d-1)(d-2)\left(\frac{2\pi^{d/2}}{\Gamma(d/2)}\right)}, \end{aligned} \tag{1.73}$$

where M is the mass and Q is the charge of the black hole. If we set $Q = 0$ we will recover the AdS Schwarzschild black hole and we can also discuss asymptotically flat RN black holes by sending the AdS radius $L \to \infty$. The horizon, $r = r_H$, is the largest real root of the $f(r)$ (i.e. $f(r_H) = 0$). The apparent occurrence of the singularity at the horizon, $r = r_H$, is simply an artifact of the coordinate system and can be removed by choosing a different coordinate system. A famous example are the in-going Eddington-Finkelstein coordinates (v, r) where we define $v = t + r_*$ and then write the metric as follows[4]:

$$ds^2 = -f(r)dv^2 + 2dvdr + r^2 d\Omega_{d-1}^2. \tag{1.74}$$

We can see that even though $f(r)$ vanishes at the horizon the metric is well defined. Another useful coordinate transformation (assuming that $f'(r_H) \neq 0$) which leaves the

[4]The coordinate r_* is called the tortoise coordinate. It is related to the radial coordinate r through the following relation $dr_* = dr/f(r)$. In this redefinition of the radial coordinate the horizon is pushed to $r_* \to -\infty$ and radial infinity is at $r_* \to \infty$ for asymptotically flat black holes or $r_* < \infty$ for asymptotically AdS black holes.

horizon regular can be defined as follows:

$$\begin{aligned}\tilde{u} &= -e^{-\frac{1}{2}f'(r_H)(t-r_*)} \\ \tilde{v} &= e^{\frac{1}{2}f'(r_H)(t+r_*)}.\end{aligned} \tag{1.75}$$

With some work one will arrive at the following expression for the Schwarzschild metric:

$$ds^2 = \frac{4f(\tilde{u},\tilde{v})}{\tilde{u}\tilde{v}}\frac{d\tilde{u}d\tilde{v}}{f'(r_H)^2} + r(\tilde{u},\tilde{v})^2 d\Omega_{d-1}^2. \tag{1.76}$$

Near the horizon one can expand the tortoise coordinate (assuming that $f'(r_H) \neq 0$ and well defined) to find that:

$$\lim_{r\to r_H} \frac{f(\tilde{u}\tilde{v})}{\tilde{v}\tilde{u}} = -e^{cf'(r_H)}f'(r_H), \tag{1.77}$$

where c is some integration constant associated to the integral to get the tortoise coordinate and we can see that the expression is completely well defined and non-zero at the horizon. Note that the exterior spacetime outside the horizon was specifically given by $\tilde{u} < 0$ and $\tilde{v} > 0$ but we can also have three other sign combinations for $\tilde{u}, \tilde{v}$. In particular we can have a second exterior region with $\tilde{u} > 0$ and $\tilde{v} < 0$, the future interior when $\tilde{u}, \tilde{v} > 0$ and the past interior for $\tilde{u}, \tilde{v} < 0$. The horizon(s) are at $uv = 0$. The coordinates in which we have the maximally extended solution is often called Kruskal coordinates.

A particularly important coordinate system when discussing the near horizon physics of non-extremal black holes (i.e. black holes with $f'(r_H) > 0$) are Rindler coordinates. These can be obtained by expanding the the metric given in 1.72 near the horizon $r = r_H$, we obtain:

$$ds^2 = -\left[f'(r_H)(r-r_H)\right]dt^2 + \frac{dr^2}{f'(r_H)(r-r_H)} + r^2 d\Omega_{d-1}^2. \tag{1.78}$$

We redefine the radial coordinate using the following relation $d\rho = \frac{dr}{\sqrt{f'(r_H)(r-r_H)}} \Rightarrow \rho = \frac{2\sqrt{r-r_H}}{\sqrt{f'(r_H)}}$ and obtain the following near horizon metric:

$$ds^2 = -\left(\frac{\rho f'(r_H)}{2}\right)^2 dt^2 + d\rho^2 + r(\rho)^2 d\Omega_{d-1}^2. \tag{1.79}$$

The (t, ρ) part of the metric describes a Rindler space which also appears in the discussion of constantly accelerated observers. In particular, an observer with a constant proper

acceleration (in a spacetime with no black hole) will experience very similar physics to an observer which is sitting at a constant radial distance near the horizon of a black hole.

At this stage it is interesting to recall that the black hole solutions are solutions to the Einstein field equations. Furthermore, the Einstein field equations can be obtained through the principle of stationary action using the Einstein Hilbert Action. In standard quantum field theory one can define statistical systems using the action by Wick rotating to imaginary time on a circle whose periodicity defines the temperature and using periodic boundary conditions on the fields[15, 118]. This motivated the quantum gravity community to define a statistical system associated with the Einstein Hilbert action whose partition function is schematically written as (up to counter terms and boundary terms)[57, 15]:

$$Z = \int_{\text{fix}\partial V} [Dg] e^{-S_{EH}^{Euc.}[g]}. \tag{1.80}$$

We use the Euclidean version of the Einstein Hilbert action $S_{EH}^{Euc.}[g]$ and fix the asymptotic metric and sum over possible geometries (metric) consistent with the fixed boundary condition. In general, such a path integral is not well defined and it is not even clear how to evaluate such an object. However, it has been suggested that one might understand/approximate such a path integral in terms of a sum of smooth Euclidean geometries which are saddles of the Euclidean action. In particular, one might suggest an approximation scheme of the form:

$$Z \approx \sum_i e^{-S_{EH}^{Euc.}[g_i]}, \tag{1.81}$$

where g_i are solutions to the equations of motion of the Euclidean action. By carefully including counter and boundary terms this object is expected to be well defined and can also be explicitly computed in simple examples and then treated as a partition function from which thermodynamic quantities can be computed.

As a simple example, one can consider the saddle corresponding to the Euclidean Schwarzschild black hole. To obtain the Euclidean black hole saddle one can start with the Lorentzian saddle metric of the form given in Eq. (1.72) and take $t \to it_E$ which is periodic and its period defines a temperature for the statistical system we defined in terms of the action. The Euclidean metric takes the form:

$$ds^2 = f(r)dt_E^2 + \frac{dr^2}{f(r)} + r^2 d\Omega_{d-1}^2. \tag{1.82}$$

The metric above is regular everywhere in the exterior of the black hole except possibly near the horizon. Using the discussion of Rindler coordinates as a description of the near

horizon geometry we will find the following metric near the horizon:

$$ds^2 = \left(\frac{f'(r_H)}{2}\right)^2 \rho^2 dt_E^2 + d\rho^2 + r^2 d\Omega_{d-1}^2. \tag{1.83}$$

Now we redefine the $dt_E = \frac{2d\phi}{f'(r_H)}$ so that we have:

$$ds^2 = \rho^2 d\phi^2 + d\rho^2 + r^2 d\Omega_{d-1}^2. \tag{1.84}$$

The (ρ, ϕ) part of the metric will contain a conical singularity unless we require $\phi \sim \phi + 2\pi$. Therefore, the smoothness condition requires us to fix the periodicity of t_E which we set to the temperature β. We get the relation between the temperature and f:

$$\beta = \frac{4\pi}{f'(r_H)}. \tag{1.85}$$

So the Euclidean black hole saddle takes the shape of a cigar in (t_E, ρ) coordinates. The tip of the cigar, which is smooth by the identification between temperature and the $f'(r_H)$, is what the horizon becomes in the Euclidean description. Miraculously when we evaluate the regulated value of the Euclidean action on the black hole saddle and take that as defining a partition function for the black hole and compute its entropy we will obtain the famous Bekenstein Hawking formula for the entropy of the black hole [20]:

$$S_{BH} = \frac{A}{4G_N}. \tag{1.86}$$

Associated with the black hole is also a temperature which is often referred to as the Hawking temperature:

$$T_H = \frac{1}{\beta} = \frac{f'(r_H)}{4\pi}. \tag{1.87}$$

It is unclear why the computations above should really give a correct answer. After all, we only approximated the full partition function via a saddle point approximation (which we really just took a functioning definition of the sum of metrics for a lack of a better approach). We only included the black hole saddle and there might be other ones (as we will see in the discussion of the Hawking-Page transition in AdS/CFT). It ultimately forces us to ask if this just a happy coincidence or is there something more deeper involved?

There are some interesting semi-classical computations which seem to clarify and also deepen some questions about the thermodynamic nature of black holes. In particular, Hawking's application of quantum field theory on Lorentzian black hole backgrounds predicts the existence of Hawking radiation [68]. The black hole, due to near horizon quantum

effects, losses its energy by emitting Hawking radiation at a temperature which given by Eq. (1.87). So at least physically it seems there might be reasons why the black hole might have a temperature because it really does radiate like a thermal body. The entropy is still quite mysterious however. Nonetheless, there are a large number of approaches and computations that one can do to motivate the idea that black holes are thermodynamic systems which obey analogues of the conventional 4 laws of thermodynamics [18]:

- Zeroth Law of BH thermodynamics: A stationary black hole as constant surface gravity κ[5].
- First Law of BH thermodynamics: $dE = \frac{\kappa}{8\pi} dA + \Omega dJ + \Phi dQ$. Changes in total energy of black hole arise from changes in charge Q, angular momentum J, and area A.
- Second Law of BH thermodynamics: $S_{gen.} = S_{BH} + S_{out} \geq 0$. Entropy of black hole plus fields outside of black hole will not decrease.
- Third Law of BH thermodynamics: Black hole cannot be made to have $\kappa = 0$ after a finite number of processes.

1.3.2 Black Holes and AdS/CFT

A great deal of progress has been made in clarifying the origins of black hole entropy and temperature since the formulation of the AdS/CFT correspondence. The AdS/CFT correspondence was first formulated in Maldacena's work [96]. With its formulation, emerged a central idea, that quantum gravitational systems in asymptotically AdS_{d+1} spacetimes are dual to conformal field theories in in one less dimension which live on the d-dimensional boundary of asymptotically AdS_{d+1} spacetime. The correspondence represented a concrete/controlled realization of the "holographic principle" which stated that gravity in an enclosed volume $\mathcal{V}$ has an equivalent description in terms of some theory that lives on the boundary of the enclosed space $\partial\mathcal{V}$ [142, 146].

In its most non-restrictive incarnation the basic idea behind the study of quantum gravity via AdS/CFT is that there is a gravitational system (String Theory, Supergravity, Einstein gravity, etc..) in a $d+1$-dimensional asymptotically AdS spacetime called the "bulk". For this gravitational system there exists a holographic CFT system on the boundary which will be equivalent to the bulk gravity system. In particular, the CFT system, if understood well enough provides a complete UV description of quantum gravity

[5]Note that the surface gravity is related to the Hawking temperature of the black hole via $\kappa = 2\pi T_H$.

effects in the bulk. In this framework, one views states in the CFT descriptions as dual to some bulk configuration[6]. In particular the most simple examples of this duality between states and geometries is the relation between the vacuum state of the a holographic CFT, $|0\rangle$, and the geometry of empty AdS.

$$|0\rangle \leftrightarrow \text{Vacuum AdS}. \tag{1.88}$$

Within this framework we one can introduce fields in the bulk, $\phi(x, z)$, which are dual to certain to certain gauge-invariant operators on the boundary CFT $O(x)$.

$$O \leftrightarrow \phi. \tag{1.89}$$

Then computation of correlators in the vacuum state of the CFT is dual to describing scattering of dual fields in the bulk:

$$\langle 0|O(x_1)O(x_2)\cdots O(x_n)|0\rangle \leftrightarrow \text{Scattering processes of dual } \phi \text{ fields in AdS}. \tag{1.90}$$

More generally we have an equivalence between the full quantum gravity partition function in the bulk and the boundary CFT partition function:

$$Z_{bulk} = Z_{CFT}. \tag{1.91}$$

We can apply this to AdS black holes and connect it to our previous discussion of the Euclidean path integral for gravity and the entropy and temprature of a black hole. Recall that one does the path integral by fixing the asymptotics of the Euclidean bulk geometry. In AdS/CFT the CFT lives on the asymptotic boundary. We can consider the thermal CFT by compactifying the time direction and then go through the standard procedure to compute the partition function as well as thermal correlators. Due to the AdS/CFT correspondence this has a dual interpretation of finding the partition function using the Euclidean path integral. In such a setup one sees that by fixing the boundary CFT and then filling out the bulk geometry with the smooth cigar results in the following identifications:

- The Hawking temperature of the black hole is the temperature of the thermal CFT (with some caveats which we will shortly discuss).

[6]It is not necessarily expected that all choices of CFT states correspond to "nice" geometries. There are special states within the CFT which have been demonstrated to be dual to some smooth bulk geometries (at least in certain regimes) the most well understood probably being the vacuum state of a holographic CFT being identified with vacuum AdS.

- The entropy of the black hole can be interpreted as arising from the entropy of the CFT living on a sphere (assuming the horizon is spherical). In particular, aspects of the microstates involved in the sourcing the black hole entropy can be studied by studying the CFT spectrum of states.

Now lets discuss the caveat for the first point. The point about AdS/CFT is that the gravitational partition function in the bulk (with fixed asymptotics) can be defined in terms of a CFT partition function. But note that Z_{bulk} is usually difficult to define and compute explicitly. We simply opted to approximate/define Z_{bulk} as a sum over on-shell bulk geometries that are consistent with the prescribed boundary conditions. If we consider the cigar geometry as corresponding to the black hole there is also another bulk Euclidean geometry which looks like a cylinder which is thermal AdS (can be though of as empty AdS with a thermal gas) which can also be made to satisfy the boundary conditions. So we actually have a competition between two saddles. The black hole saddle and the thermal AdS saddle. Both these saddles should be included in the Z_{bulk} calculation i.e.:

$$Z_{CFT} = Z_{bulk} \approx e^{-S_{EH}[g_{BH}]} + e^{-S_{EH}[g_{ThermalAdS}]}. \tag{1.92}$$

One can compute the free energy associated with each of the saddles and determine which is thermodynamically favoured. One will find that at temperatures:

$$T \leq \frac{d-1}{2\pi L}. \tag{1.93}$$

Thermal AdS is more favored than the black hole saddle and for:

$$T > \frac{d-1}{2\pi L}. \tag{1.94}$$

the AdS black hole is favoured. The transition between these two saddles is called the Hawking-Page transition. So when we say that in AdS/CFT the CFT in a thermal ensemble is describing a black hole we really mean that it should describe an AdS black hole well beyond the Hawking Page transition such black holes will have $r_H/L \gg 1$ and are sometimes referred to as large AdS black holes. These are thermodynamically stable (have positive heat capacity) and can be understood as being in equilibrium with the Hawking radiation they emit. The reason for this is that AdS has a confining potential which essentially puts the black hole in a box. For very large AdS black holes the black hole is large enough that Hawking radiation emitted from the black hole will bounce off the conformal boundary and be reabsorbed by the black hole sufficiently quickly preventing it from completely evaporating. This is in contrast to very small AdS black holes, which will

have $r_H/L \ll 1$ which are not thermodynamically stable and eventually evaporate away similar to black holes in asymptotically flat space. So at sufficiently high temperatures a holographic CFT in a thermal ensemble should describe a large AdS black hole ($r_H \gg L$). Correlators evaluated in the CFT will primarily get contributions from studying the propagation of the dual fields in the black hole background. Now that we have discussed some basic ideas of how black holes are described in AdS/CFT we can continue and describe the black hole information paradox. Again, for a more comprehensive review of the subject we recommend [65, 15].

1.3.3 The Information/Firewall Paradox and the need for Microstructure

The black hole information paradox arises from the realization that Hawking's computation of black hole evaporation via Hawking radiation emission allows for a mechanism by which pure states can evolve into mixed states. In particular, suppose we have some matter in a pure state $|\psi\rangle$ and then we allow the matter to collapse to a black hole. Immediately after collapse, according to Hawking's calculation the black hole will start to emit Hawking radiation. The Hawking radiation is going to be thermal and hence in a mixed state. If we trust/assume that the process of Hawking radiation continues until the black hole completely evaporates we will be led to a troubling conclusion. Namely that matter that started in a pure state has evolved, through the formation of a black hole and its subsequent evaporation, into a mixed state of thermal Hawking radiation. This raises questions about the nature of quantum gravity and makes one question whether it should be unitary as all other quantum theories of nature are. In particular, Hawking's computations that unitarity is violated through the process of black hole evaporation is problematic from the perspective of the AdS/CFT conjecture which postulates the even black hole evaporation at least in AdS should be dual to some unitary CFT description. This has led many to take the stance that:

1. There is something wrong with Hawking's calculation and should not be trusted to the end of the evaporation process.

2. Black hole evaporation is a unitary process (especially if you believe in AdS/CFT).

Now the first point is fairly reasonable since Hawking's calculation is based on semi-classical principles there are valid reasons to distrust Hawking's computation all the way to the end of the process. Now one might suggest that there is not actually a problem then Hawking's

calculation is incomplete at the end of evaporation and nothing can be said. However, as we will discuss shortly, if we do insist that unitary be respected (which we should if AdS/CFT is correct) then the information paradox is actually much worse. As we will see issues begin even before the black hole has a chance to become Planck sized in a regime where Hawking's calculation might be expected to go through without issue. So lets now discuss what should happen if the black hole evolves unitarily.

Our discussion starts with the quantity known as the entanglement entropy of Hawking radiation. This quantity is motivated by the idea that each Hawking quanta has a partner behind the horizon which it is entangled with it so that the joint system of the radiation and black hole is pure (the reason for this entanglement to exist is because it is important if we want to have a drama-free horizon and if Einstein's equivalence principle is respected at the horizon). In particular, if one takes the joint system which is thought to be pure, and traces out the black hole then the entanglement entropy of the Hawking radiation will follow the Page curve[115, 8] (if the process is unitary) depicted in Figure 1.1.

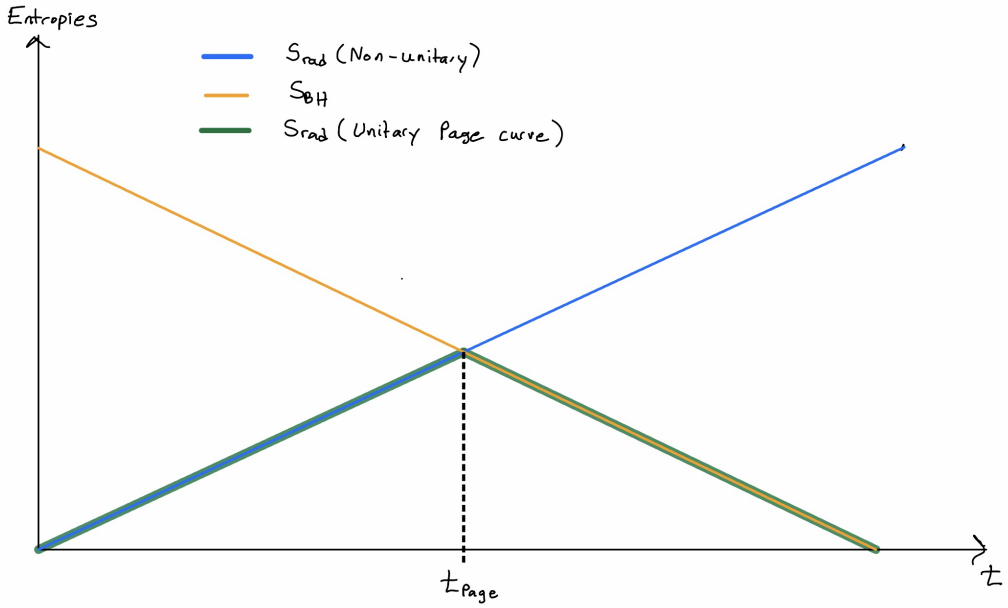

Figure 1.1: Above is a depiction of the entropies involved during the evaporation process as a function of time. The yellow line is the Bekenstein-Hawking entropy of the evaporating black hole, it decays with time. The blue line is the entanglement entropy of Hawking radiation according to Hawking's calculation which violates unitary expectations. Finally the green line is the Page curve. Before the Page time it coincides with Hawking's calculation and after the Page time it coincides with the Bekenstein Hawking entropy of the black hole and should go to zero indicating purity of the final state of radiation.

The explanation for this is fairly simple. Initially there is no Hawking radiation so the entanglement entropy of Hawking radiation is zero. In the early stages of evaporation the black hole will emit Hawking radiation and each quanta is entangled with another partner mode behind the horizon so entanglement entropy of the black hole will gradually increase. Roughly after the black hole emits half its initial entropy one should expect the entanglement entropy of the radiation to reach a peak. The time which this occurs is referred to as the Page time. After the Page time the subsequent radiation that is emitted from the black hole should start to purify the earlier radiation and the entanglement entropy should begin a downward slope and go to zero signifying that the final state is pure (of course we know that Hawking's calculation does not predict this even though the black hole is macroscopic and not Planckian but this is what we should expect if black hole evolution is truly unitary). Now we can see why the insistence of unitarity poses an

interesting puzzle. It is not the case that the issue begins when the black hole becomes Planckian; the real issue begins as soon as the Page time when the black hole is macroscopic and spacetime near the horizon is weakly curved so we expect Hawking's calculation to be perfectly fine. So if we insist to preserve unitarity then we must figure out why Hawking's calculation should not go through (i.e. what assumptions go into Hawking's calculations which may not be satisfied after a Page time).

To understand what goes wrong it is important to more carefully discuss the role that entanglement plays in discussing the smoothness of the horizon and how the monogamy of entanglement suggests the development of firewalls after the Page time[65, 99]. In particular as we already stated the entanglement between the modes in the interior and the Hawking quanta serve as a method by which the spacetime at the horizon remains in a vacuum state. However, in order to begin the process of purification of the radiation after the Page time, the new Hawking quanta must also be entangled with the older Hawking quanta the black hole emitted. This requires a single Hawking quanta to be maximally entangled with two subsystems which is not possible due to the monogamy of entanglement (i.e. a system can only be entangled so much to two other systems). This has led to the idea that in order to save unitary evolution one must "cut" the entanglement between modes inside the horizon and the Hawking quanta outside. This will lead to a disruption in the entanglement between the interior and exterior fields and lead to a divergence called the "firewall" [10]. Basically it is believed that after the Page time a very high energy curtain of energy would form near the horizon which would violate Einstein's equivalence principle and our hopes of have a smooth drama free horizon (this may also explain why Hawking's calculation should not match the Page curve after the Page time since smoothness of the horizon needs to be thrown out due to the presence of a firewall). This marked the beginning of the realization that unitary evolution might require us to throw out the notion of a black hole having a smooth horizon with no microstructure.

Since the formulation of these problems it has been realized that a proper resolution to the information problem will require the abandonment of at least one of the three assumptions listed below [21]:

1. Unitary evolution for black holes.

2. Smooth horizon for black holes.

3. Locality of quantum theory in the presence of black holes.

We want to keep unitarity so we must either give up on locality (e.g. Giddings' non-violent unitarization[58, 59, 60] and quite possibly the recent islands proposal[8]) or we must give

up on the notion of a horizon (e.g. in the discussion of fuzzballs[99, 100]). **The main point here is that if unitarity is to be held sacred then there is the need for new physics/microstructure near the horizon.**

Before concluding our discussion of the information paradox and how it motivates the need for microstructure near the horizon it is worth pointing out that there is also another version of the information paradox which was actually discussed by Maldacena in the early days of the AdS/CFT correspondence when he introduced the the thermofield double state, $|TFD\rangle$, as the the holographic dual of the eternal two-sided AdS black hole[97]. Here we give a brief overview of Maldacena's version of the information paradox. The main points of Maldacena's version of the information problem is as follows:

- Large AdS black holes with spherical horizons are dual to a thermal ensemble of holographic CFT states of a CFT living on a sphere (i.e. a compact space).
- Since the CFT lives on a compact space the spectrum of states will be discrete.
- Initially thermal correlators of CFT operators are expected to decrease.
- At late times discreteness of spectrum of states becomes important and correlators should not decay to zero but instead fluctuate with average amplitude that is exponentially small in entropy.
- Computation of quasi-normal modes in bulk (which would be dual to to computation of two point correlator on CFT) will also decay at early time consistent with the CFT.
- Quasi-normal modes continue to decay forever and there will be mismatch between thermalization behaviour in bulk and CFT.
- Absence of decay to zero in CFT calculation is signature of unitary evolution.
- Decay to zero of perturbation in quasi-normal mode decay calculation signal that information of perturbation is lost and violates unitarity.

Maldacena has suggested that a way forward was to include the thermal AdS saddle in the calculation as well to prevent the decay, since the partition function of the CFT is really a sum over saddles in the bulk and after a long time the thermal AdS saddle would dominate the behaviour and prevent decay. Since Maldacena pointed this out there were a number of papers that investigated this in more detail from the Lorentzian perspective[17, 138, 147]. These works concluded that the horizon was the primary culprit which caused correlators

in the bulk to decay to zero and it was suggested that modifications to the near horizon geometry may be necessary to restore unitary evolution. So even well before the discussion of the firewall problem, nearly a decade later, there were reasons to suspect the notion of horizon smoothness in a unitary bulk description of a black hole. In the past 5-10 years, a great deal of interest has been sparked in the discussion of both versions of the information paradox (i.e. the Page curve version and late time correlator version). In the next subsection we will briefly describe these efforts as well as experimental efforts to detect signatures of horizon modifications.

1.4 Recent Frontiers of Exploration for Black Holes

The assumption that black holes should evolve in a unitary manner seems to require some new physics near the horizon well before the black hole becomes Planck sized. This has been suggested both by the firewall problem (and the discussion of the Page curve) as well as the subsequent analysis of Maldacena's version of the information problem involving the late time behaviour of correlators. In the past 5-10 years a great deal of theoretical progress has been made in understanding how to reproduce a Page curve [8, 117, 7] as well as some expected features of the late behaviour of correlators which are intimately connected to the discussion of quantum chaos and random matrix theory. Parallel to these developments there have been interests in trying to experimentally determine if there are modifications to the near horizon physics of black holes. In particular, if the modifications to the near horizon physics of black holes result in the partial reflection of perturbations then one might detect signatures of such near horizon microstructure in gravity waves that are emitted after a binary system coalesces and forms a black hole.

1.4.1 Connections between Black Holes, Quantum Chaos, and Random Matrix Theories

Lets begin our discussion with the developments that have found black holes to be dual to quantum chaotic systems [78]. The discussion of classical chaos can be traced back to the idea of having a system with two initial conditions that are "close" which evolve to configurations that are very far away from from each other in the state space. As an example one can consider a one dimensional system with phase space variables (q, p), where q is a position and p is a momentum. The system is said to be chaotic if the following

Poisson bracket grows exponentially with time:

$$\{q(t), p(0)\}_{P.B.} \sim e^{\lambda_L t}. \tag{1.95}$$

This is essentially saying that initial conditions that are close in phase space will have trajectories that evolve away from each other exponentially fast (the essence of chaos). The quantum analogue of this statement is involves replacing the Poisson bracket with commutator and promote q and p to operators. So we say a quantum system with a large number of degrees of freedom, N, in a thermal ensemble is quantum chaotic if the square of the commutator of two generic unitary hermitian operators, W, V, also grows exponentially:

$$C(t) = -\langle [W(t), V(0)]^2 \rangle \sim e^{2\lambda_L t}. \tag{1.96}$$

The rate of growth in the exponent, λ_L, is often called the Lyapunov exponent and is used to characterize the degree of chaos (i.e. the larger λ_L is the more chaotic the system is said to be). If we expand out the commutator squared we will get an expression of the form:

$$C(t) = 2\langle W(t)W(t)V(0)V(0)\rangle_\beta - 2\langle W(t)V(0)W(t)V(0)\rangle_\beta . \tag{1.97}$$

The first term in the above equation is a time ordered correlator and the last term is called the out-of-time-order correlator (OTOC). At $t = 0$ the two terms cancel and $C(0) = 0$. Due to the unitary condition the second term evaluates to 1 so we have:

$$C(t) = 2\left[1 - \langle W(t)V(0)W(t)V(0)\rangle_\beta\right]. \tag{1.98}$$

If we assume that the system is chaotic then we should have:

$$C(t) = 2\left[1 - \langle W(t)V(0)W(t)V(0)\rangle_\beta\right] \sim e^{2\lambda_L t}. \tag{1.99}$$

So saying that the commutator squared is exponentially increasing is a statement that the OTOC exponentially decreases. This diagnosis (i.e. the exponential decay of OTOCs is often used rather than the commutator squared which has natural analogue to the classical Poisson bracket diagnosing chaos).

So why is this important for our discussion of black holes as quantum chaotic systems? The answer is because a holographic CFT in a thermal ensemble at very high temperatures describes the exterior of a large AdS black hole in the bulk. This realization motivated the works [135, 136] that gave a bulk interpretation to the computation of OTOC and used the bulk computations to argue that the holographic CFT should have thermal correlators

that decay exponentially fast at a rate with a Lyapunov exponent characterized by the bulk black hole's Hawking temperature:

$$\lambda_L = 2\pi T_H = \frac{2\pi}{\beta}. \tag{1.100}$$

In particular, the phase of exponential decay was shown to occur at times much earlier than the so-called scrambling time, $t_{scr} \sim \beta \ln(N)$, but later than the time scale set by the inverse temperature, β. This result connected the chaotic aspects of black holes to older ideas that black holes acted as the fastest scramblers of information. In particular, the results suggested that the chaotic dynamics were connected to the fast scrambling of quantum information thrown into a black hole. Along with the notion that black holes were unitary systems that had the fastest scrambling rates [134] it was conjectured that the Lyapunov exponent for black holes formed an upper bound on the set of possible values of the Lyapunov exponent for large N quantum thermal systems (i.e. black holes are maximally chaotic systems)[94].

Up to that point the notion that black holes were quantum chaotic systems was mostly understood from a bulk perspective these ideas were difficult to explore directly in the boundary CFT system (this is because the usual examples of the duality involved strongly coupled gauge theories which are difficult to treat analytically). This changed with the realization that the SYK model saturated the Lyapunov bound and exhibited some emergent conformal symmetries (suggesting a possible AdS_2 gravity description) at low energies in the infinite N regime[123, 55, 56, 145]. The SYK model is a quantum mechanical model (0+1-dimensional QFT) which consists of N Majorana fermions whose dynamics are governed by the following Hamiltonian:

$$H_{SYK} = \sum_{i,j,k,l=1}^{N} J_{ijkl}\chi_i\chi_j\chi_k\chi_l, \tag{1.101}$$

where N is even and J_{ijkl} is a random coupling parameter which is Gaussian distributed. The Majorana fermions obey the following anti-commutation relations $\{\chi_i\chi_j\} = \delta_{ij}$. The reason this was exciting was because the SYK model represented a concrete quantum system which not only saturated the Lyapunov bound for black holes but was simple enough to analyze analytically in large N regimes. It was also relatively simple to do more exact numerical computations at finite N and diagonalize the Hamiltonian given in Eq. (1.101) discrete spectrum of states. In particular, numerical computations of correlators at finite N made it possible to now understand the late time behaviour of correlators and how they fluctuate (note that this was not an easy task directly from the bulk perspective).

With the study of the SYK model it was noted that the late time behaviour of correlators immediately after the initial decay would exhibit a linear ramp followed by a plateau. This behaviour was also found in the closely related computation of the spectral form factor for the SYK model given by:

$$\langle Z_{SYK}(\beta + it) Z_{SYK}(\beta - it) \rangle = \langle \sum_{n,m} e^{-\beta(E_m + E_n)} e^{i(E_n - E_m)t} \rangle \,, \tag{1.102}$$

where the braket means to average over many numerical samples (recall that the SYK Hamiltonian involves a random coupling J_{ijkl}) and E_n are the eigenvalues of the diagonalized SYK Hamiltonian. In the work [42] the late time ramp was traced back to the spectral statistics of the spacing between eigenvalues. In particular, it was demonstrated that the spacing statistics between eigenvalues exhibited "repulsion" which is a key feature found in the study of random matrix theories. This connected the spectrum statistics of black holes to the spectrum statistics of random matrix theories involving classical Gaussian ensembles.

Lets conclude this subsection with a brief overview of "classical" random matrix theory i.e. the theory of random matrices belonging to the following ensembles:

- Gaussian Orthogonal Ensembles (GOE): The set of real symmetric square matrices whose elements are Gaussian distributed random variables.
- Gaussian Unitary Ensembles (GUE): The set of square hermitian matrices whose whose elements are Gaussian distributed random variables.
- Gaussian Symplectic Ensemble (GSE): The set of square matrices whose elements are defined by quaternions which Gaussian distributed.

Lets suppose we take an $N \times N$ matrix from any one of the three ensembles above and diagonalize it we will have a set of of randomly distributed eigenvalues $\{\lambda_1, \lambda_2, ..., \lambda_N\}$. The study of random matrix theory is the study of the statistical properties of the random eigenvalues we get. In particular, a very important result for the three ensembles listed above is that the eigenvalues exhibit eigenvalue "repulsion." This repulsion can be quantified by studying the spacing statistics between an adjacent pair of eigenvalues. It is a well known fact in random matrix theory that the probability of having two adjacent eigenvalues a distance s away from each other is well approximated by the Wigner surmise which is a probability distribution which takes on the following form (in the equation below we set s to be a dimensionless distance and did not write a normalization):

$$\mathcal{P}_\alpha(s) \sim s^\alpha e^{-s^2}. \tag{1.103}$$

The label α is sometimes referred to as the Dyson index and is equal to 1,2, and 4 for the GOE, GUE, and GSE respectively. There are many other facts about these ensembles but we will not heavily rely on them in this thesis (if the reader is interested in learning more about the mathematical details of random matrix theory a good introduction is [93]).

1.4.2 Echoes as Signatures of Near Horizon Microstructure

In this subsection we will give a brief overview of the main conceptual aspects of the experimental search for echoes and why they are thought to be a smoking-gun signature of non-trivial near horizon modifications to a black hole (see [3] for a more comprehensive review.) .

The discussion of echoes begins with the discussion of how they might be formed. Aside from the commonly known matter collapse to a black hole, a black hole may also form when two sufficiently large massive bodies (e.g. two black holes, two neutron stars, etc..) in a binary system orbit into each other and form a black hole. After the initial merging of the two bodies it is expected that the black hole will settle to an equilibrium state by emitting gravitational waves. The precise physics of the ringdown after the merge event is widely regarded as being controlled by a set of quasi-normal modes of the resulting black hole.

Quasi-normal modes are obtained by studying wave phenomena in black hole backgrounds. Schematically, one solves a wave equation of the form $\Box\Psi = 0$, where $\Box$ is the given by $\Box = g^{\mu\nu}\nabla_\mu\nabla_\nu$ and g is the metric for the black hole. The quasi-normal modes are obtained by finding solutions that obey specific boundary conditions, namely:

- The perturbation at the horizon obeys "in-going" boundary conditions.
- The perturbation at infinity is obeys "out-going" boundary conditions.

When one uses these modes to model the ringdown one gets a smooth decay profile for the decay of the amplitude of the perturbation which is what one would expect (eventually the black hole absorbs everything or things are sent off to infinity and never come back).

The discussion of echoes involves changing the boundary condition near the horizon from a purely ingoing boundary condition to a partially reflective (mixed) boundary condition. The physical motivation is that there are some unknown quantum gravity effects near the horizon which come together and effectively behave like a cutoff near the horizon with some non-standard boundary conditions which allow for the partial reflection of perturbations near the horizon. When such modes are used to model the ringdown

of the modified black hole one initially obtains a smooth decay not unlike the standard quasi-normal mode decay. However, after some time scale t_{dev} there are deviations away from the standard signal these deviations manifest as repeating echoes (i.e. a resurgence in the amplitude of the perturbation as measured by a distant observer). The physical explanation for the repeating echoes is that there are modes trapped between the modified horizon and the angular momentum barrier which bounce back and fourth as they slowly leak out. In the geometric optics approximation the time delay between the echoes for a spherically symmetric black hole would be approximated by:

$$t_{echo} = \int_{r_H+\delta r}^{r_0} \frac{2}{f(r)} dr, \tag{1.104}$$

where δr is the radial coordinate distance away from the horizon where the semi-reflective boundary condition is enforced and r_0 is the position of the angular momentum barrier. It is easy to see that this is just the length of time it takes for a null radial geodesic to go from the point $r_H + \delta r$ to the angular momentum barrier at r_0 and back again.

A particularly interesting choice for δr corresponds to fixing the boundary conditions a proper Planck length away from the horizon. In such a case it was noted that the echo time was comparable to the scrambling time of the black hole:

$$t_{echo} \sim \beta \ln(S_{BH}). \tag{1.105}$$

So it was suggested that if echoes did show up in the gravitational wave data collected by the Laser Interferometer Gravitational-wave Observatory (LIGO) in the aftermath of a binary merger and they were delayed from each other by a scrambling time scale, that such echoes would be smoking gun signatures of near horizon modifications localized within a Planck length of the horizon.

1.5 Overview of Thesis

1.5.1 Central Ideas and Motivations of Part I

Part I of this thesis will primarily be motivated by the recent advancements discussed in Sections 1.4.1 and 1.4.2.

In Chapter 2, we set out with the idea that in AdS/CFT all possible information about how a black hole relaxes in a manner consistent with unitarity is governed by the calculation of correlators in the state we believe the black hole geometry is dual to. We suggest that if

black holes really did have microstructure near the horizon then a CFT calculation would be able to determine their existence. In this chapter, we explore this idea by noting the resemblance of the echo time with the scrambling time and try to understand how echoes would manifest in a dual CFT calculation. The guiding questions of the chapter are:

- To what extent can the Echo time scale mimic the Scrambling time scale for AdS black holes?
- If the Echo time scale can be identified with the scrambling time scale of AdS black holes, is there a holographic interpretation?
- What would it mean if a correlator in a holographic CFT state exhibited echoes?

In Chapter 3, we take some of the ideas and results in Chapter 2 and explore the phenomena of echoes from a more quantum perspective. We are guided by the idea that the discreteness of the spectrum of microstates of a Large AdS black hole with a spherical horizon is responsible for the absence of the decay of correlators at late times. We entertain the idea that perhaps echoes can be directly attributed to the discrete nature of black hole microstates and explore this idea. The basic idea is that from the CFT perspective the black hole in the bulk is a thermal ensemble of e^S_{BH} microstates. The unitary ringdown of the black hole in the bulk would be described by a thermal correlator calculation in the thermal ensemble of microstates and that would in turn depend on the precise statistics of the microstates in the ensemble (see Figure 1.2 for a depiction).

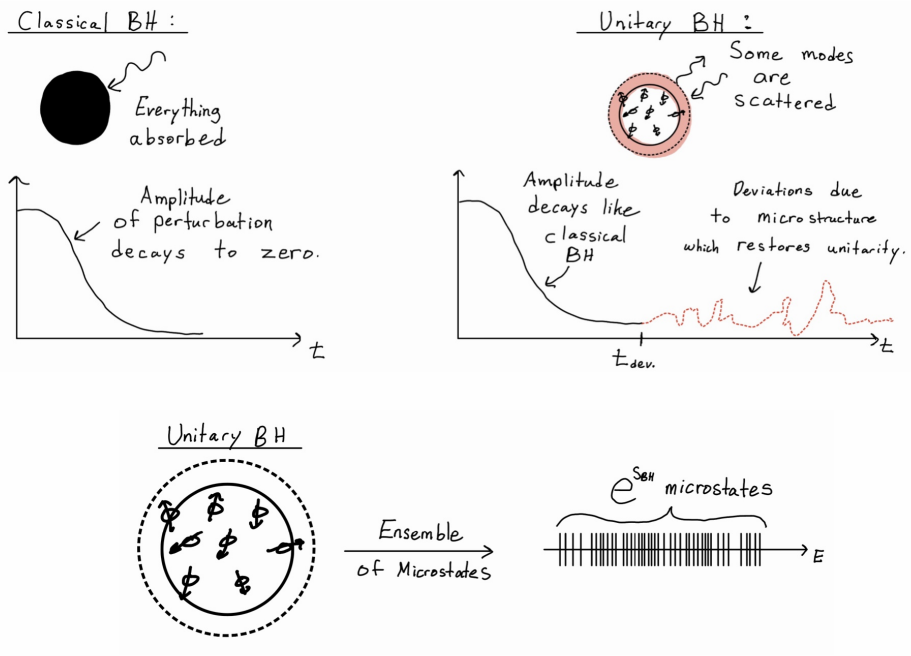

Figure 1.2: Depicted above is a diagram showing the differences between a non-unitary classical black hole on the left and a unitary (quantum black hole) one on the right. The classical black hole absorbs all modes of a perturbation and this results in the smooth decay of the perturbation to zero. The unitary black hole has a discrete spectrum of microstates so only certain modes can be absorbed and other are reflected. In particular, at early times the perturbation has not been able to resolve the discrete nature of the spectrum of the black hole so the amplitude decays in a manner similar to the non-unitary black hole. After a time scale t_{dev} the microstructure is probed and deviations manifest. Precise nature of deviations depends on specifics of the ensemble of microstates depicted at the very bottom of the figure.

With this picture we set out to investigate the following questions:

- Can the existence of echoes be attributed to the discreteness of the spectrum of black hole microstates?
- What would the existence of echoes imply about the microstate spectrum statistics of a black hole?

- Are echoes compatible with the notion of black holes being quantum chaotic systems?
- If we do not find echoes does this mean there is no microstructure near the horizon?
- Does the issue of a black hole having a smooth horizon depend on the microstate statistics?

1.5.2 Central Ideas and Motivation of Part II

Part II of this thesis is loosely based/motivated by the recent advancements in reproducing the Page curve for evaporating black holes coupled to baths [117, 7, 8, 38, 37, 107, 90].

Chapter 4, is primarily motivated by the work of Pennington who computed the information recovery time in a system involving a black hole coupled to a bath[117]. He assumed that radiation is extracted near the horizon (with some kind of un-specified extraction method) so that greybody factors could be ignored and used a certain expression for the evaporation rate of a black hole. With that he computed that information thrown into a black hole after the Page time could be recovered in a scrambling time scale. The guiding questions in Chapter 4 are:

- Can we model Pennington's non-specific extraction method near the horizon with a concrete model involving a absorptive screen placed near the horizon?
- How does the evaporation rate change as a function of how close and absorptive the screen is?
- If the evaporation rate changes how does it affect Pennington's computation of the scrambling time?
- What is the physics of the absorptive screen and can it be understood in terms of a coarse grained boundary CFT?
- Will the screen violate energy conditions?

Chapter 5, is primarily motivated by the works [38, 37, 107, 90]. We set out to investigate when entanglement wedge nesting is violated in three dimensional AdS spacetimes that are cut off by an end-of-the-world brane. Our investigations were and are continued to be guided by the questions:

- Can we define an entanglement wedge associated with a subregion on a brane?

- Are there non-trivial constraints on the gravity theory living on the brane which can be obtained by studying the violation of entanglement wedge nesting in the island/connected phase?
- What is the interpretation of the constraints and are they correct (i.e. are they just sufficient conditions or necessary)?
- What is the nature of the apparent non-local identifications between subregions in non-gravitating regions and gravitating regions on the brane in the connected/island phase?
- Can the results we obtained in 3D be extended to higher dimensions?
- What will our results mean for black holes coupled to bath setups in double holography?

Part I

Echoes and Near Horizon Microstructure from Black Hole Microstate Statistics

Chapter 2

Quantum Nature of Black Holes: Fast Scrambling versus Echoes

Two seemingly distinct notions regarding black holes have captured the imagination of theoretical physicists over the past decade: First, black holes are conjectured to be fast scramblers of information, a notion that is further supported through connections to quantum chaos and decay of mutual information via AdS/CFT holography. Second, black hole information paradox has motivated exotic quantum structure near horizons of black holes (e.g., gravastars, fuzzballs, or firewalls) that may manifest themselves through delayed gravitational wave echoes in the aftermath of black hole formation or mergers, and are potentially observable by LIGO/Virgo observatories. By studying various limits of charged AdS/Schwarzschild black holes we show that, if properly defined, the two seemingly distinct phenomena happen on an identical timescale of $\log(\text{Radius})/(\pi \times \text{Temperature})$. We further comment on the physical interpretation of this coincidence and the corresponding holographic interpretation of black hole echoes.

2.1 Introduction

Recent studies of black holes from the point of view of string theory and quantum information suggest that the horizon of a black hole may be modified. Most notably, modified horizons appear in the context of the black hole information paradox in the form of a firewall [10, 122, 140] and also within string theory in the tight fuzzball paradigm [99, 100, 64]. These descriptions usually suggest modifications within a Planck length of the horizon, we

refer to these as "hard" modifications. These are in contrast to studies which suggest "soft" modifications which can manifest as soon as one gets within a black hole radius of the horizon [58, 59, 30]. Furthermore, recent experimental results from the detection of gravitational waves have provided tentative (albeit controversial) evidence of modified horizons [4, 40, 1] (see [156] and [5], for counterpoint and rebuttal). A particularly interesting property of black holes with modified horizons comes from the study of its quasi-normal modes. Typically, quasi-normal modes of a black hole are found by requiring in-going boundary conditions at the horizon [75, 23]. However, for black holes with modified horizons, it is believed that such boundary conditions will be altered. One way to model such changes is to introduce boundary conditions on a surface which exists within a proper Planck length of the horizon[1]. This surface or membrane allows for the partial reflection of perturbations. Studies using this approach have shown that the quasi-normal modes exhibit "echoes"[31, 32, 98, 33, 34, 155, 35]. The term "echoes" is used to refer to a feature of the late time decay behaviour of the quasi-normal modes. For typical black holes (i.e. black holes with smooth horizons) the decay is exponential. For black holes with modified horizons the late time behaviour is accompanied by small repeating peaks in the amplitude. The physical reason why one sees repeating peaks in the amplitude is because perturbations will bounce back and fourth between the modified horizon and angular momentum barrier (similar to echoes created using sound waves). The time delay between adjacent peaks is referred to as the *echo time*. The echo time, in the geometric optics approximation, is twice the tortoise coordinate distance between the modified horizon/membrane and angular momentum barrier [4, 155]:

$$t_{echo} \simeq 2|r_*|_{\text{membrane}}. \tag{2.1}$$

It was first noted in [4] that the echo time was comparable to the scrambling time scale for black holes.

The scrambling time scale appears when black holes are studied from an information theoretic point of view [2]. In the context of quantum information recovery, the scrambling time scale can be viewed as a lower bound on the time it takes between throwing information into a black hole and being able to recover it, with small error from the subsequent Hawking radiation [73, 134, 158]. It has also been described as the amount of time it takes for a qubit of information thrown into a black hole to become thoroughly "mixed" [134, 86]. There are many methodologies in the current literature to calculate the scrambling time scale for black holes [134, 86, 136, 91, 29]. Depending on the particular approach one takes

[1] Since these modifications are localized within a Planck length of the horizon we would classify these as "hard" modifications.

[2] Usually these types of studies assume that black hole evaporation is unitary.

the exact mathematical expression for the scrambling time scale may vary. However, as diverse as they may be, it seems that the approaches described in [134, 86, 136, 47, 91, 29] give a time scale that can be roughly quantified by the following expression[3]:

$$t_{scr} \sim \beta \ln(S). \tag{2.2}$$

Here, β is the inverse temperature of the system and S can be viewed as the number of microscopic degrees of freedom in the system which take part in the fast scrambling process. The reason we do not explicitly identify S with entropy of the black hole is because this is not generally true. For example, in [134] the scrambling time scale for very small AdS black holes[4] is given by setting $S \sim r_H/\ell_p$, where r_H is the horizon radius and ℓ_p is the Planck length. However, for very large AdS black holes (i.e. the ones that are thought to be dual to large N CFTs) the scrambling time scale is given by setting $S \sim L/\ell_p$, where L is the AdS radius. From this it follows that, for very small AdS black holes (or asymptotically flat black holes) it is reasonable to identify S with the full Bekenstein-Hawking entropy of the black hole. However, for very large AdS black holes S is really given by the Bekenstein-Hawking entropy of a small cell on the horizon whose characteristic length is given by the AdS radius. Indeed, this seems to be consistent with the scrambling time scale given by analyzing the behaviour of out of time order correlators [94] for large N CFTs which states that the scrambling time scale is given by $t_{scr} \sim \beta \ln(N^2)$[5].

In this work, we will do a detailed analysis of the time scale set by the echo time for asymptotically AdS_{d+1} black holes in various regimes. The main reason for analyzing the echo time scale for AdS black holes is because, we want to understand exactly how accurately the echo time scale can mimic the scrambling time scale.

In Section 2.2, we introduce the definition for the echo time of a spherically static black hole and define the location of the membrane in relation to the mathematical horizon. We introduce the Planck length scale by requiring the membrane is within a proper Planck length of the horizon. This enables us to expand the echo time integral as a series in the Planck length with a leading order Log term that will later be compared with the scrambling time scale. In Sections 2.3 and 2.4, we explicitly calculate the echo time for different types of AdS black holes and verify the validity of the series expansion defined in Section 2.2. A central aspect of of the calculations done in Sections 2.3 and 2.4 is to do a detailed analysis of the $\mathcal{O}(1)$ sub-leading term in the series expansion to see how large it

[3]This is not to say that every approach to compute scrambling time gives a time scale similar to Eq. (2.2). A notable exception is suggested by Peter Shor in [137], which we will comment on in Section 2.7.

[4]Such black holes are good approximations to asymptotically flat black holes as long as we consider processes occurring close to the horizon, fast scrambling is one such process.

[5]Where we identify $(L/\ell_p)^{d-1} \sim N^2$ for large N CFTs.

gets in various regimes. In Section 2.5, we compare the echo time scale and the scrambling time scale. More specifically, in Section 2.5.1 we review the scrambling time scale in [134] and find that the scrambling time scale and echo time scale agree up to a factor of two. In Section 2.5.2 we review the results of [91, 29] and discuss how the scrambling time scale in [91, 29] is related to the scrambling time scale given in [134]. Furthermore, we review how the results of [91, 29] suggest that there are modifications to Eq. (2.2) for near extremal Reissener-Nordstrom (RN) black holes. We find that the modifications, suggested by [91], to the scrambling time scale initially appears to be inconsistent with the echo time scale. We show that the discrepancy can be traced back to how one defines the smallest "reasonable" perturbation to a black hole. In Leichenauer's work, the smallest reasonable semi-classical perturbation is defined such that the entropy of a the black hole changes by one. We argue that this is too restrictive and propose a different definition (see Appendix A.5) which results in an agreement between the echo and scrambling time scales in the near extremal regime. In Section 2.6 we pose the question of whether echoes can exist within the framework of AdS/CFT. Based on the results of the previous sections, we give a heuristic picture of how the phenomena of echoes may be related to the phenomena of fast scrambling and what they tell us about the evolution of the Planck scale structure of the horizon. In Section 2.7, we conclude by summarizing the major findings of this chapter and discuss what they imply for future studies into the connection between echoes and fast scrambling.

2.2 Universal Features of Echo Time for Spherically Static Black Holes

2.2.1 Defining Echo Time

In this section, we will introduce the exact definition of the echo time we will be using in this chapter. To simplify our calculations we will restrict our discussions to spherically symmetric $d+1$-dimensional black hole metrics of the form:

$$ds^2 = -f(r)dt^2 + \frac{dr^2}{f(r)} + r^2 d\Omega_{d-1}^2, \tag{2.3}$$

with $d \geq 3$. The echo time, in the geometric optics approximation is [4, 155]:

$$t_{echo} = 2\int_{r_H+\delta r}^{r_t} \frac{dr}{f(r)}, \tag{2.4}$$

which is the coordinate time it takes for a radial null geodesic to go from r_t to $r_H + \delta r$ and back (hence the factor of two). Here, $r = r_H + \delta r$ is the location of the semi-reflective membrane, with r_H being the location of the event horizon, i.e. $f(r_H) = 0$. The upper bound of the integral, r_t, can be understood as a turning point of the effective potential that our perturbations are subject to. To understand exactly what this means we will consider a minimally coupled scalar field in a background defined by Eq. (4.68). In this case, the equation of motion for the scalar field can be simplified to a radial equation of the form:

$$\frac{d^2\mathcal{R}}{dr_*^2} + \left(\omega^2 - V_{\text{eff}}(r)\right)\mathcal{R} = 0. \tag{2.5}$$

The details of the derivation of Eq. (2.5) as well as the exact form of the effective potential, V_{eff}, is given in the Appendix A.1. We define r_t as:

$$r_t = \min\{r : \omega^2 - V_{\text{eff}}(r) = 0\}. \tag{2.6}$$

With this definition, it is clear that the turning point depends on the frequency, ω, of the scalar perturbation. In this chapter we will be focusing on the echo time for "low" frequency perturbations[6]. Exactly what is meant by "low" frequency will be explained later and made more clear when we calculate the echo time in explicit examples. We shall see that, for our purposes, the exact value of r_t will not be important in the "low" frequency regime. Finally, we will relate δr to the Planck length, ℓ_p, through the following integral expression:

$$\ell_p = \int_{r_H}^{r_H+\delta r} \frac{dr}{\sqrt{f(r)}}. \tag{2.7}$$

Physically this means that the membrane is a *proper* Planck length away from the horizon.

2.2.2 Near Horizon Expansion of Echo Time

Now that we have defined what the echo time is, we will expand Eq. (2.4) in terms of ℓ_p. To do this we will make the following assumptions on $f(r)$[7]:

1. $f(r_H) = 0$

[6]Recent studies [113, 114] involving echoes has suggested that the reflection probability off the membrane for high frequency perturbations is exponential suppressed.

[7]All the assumptions we make are true for the black holes considered in this work.

2. $f'(r_H) \neq 0$

3. $f(r)$ is non zero and non-singular for $r > r_H$

With these assumptions, we will split the echo integral into two parts:

$$t_{echo} = \int_{r_H+\delta r}^{r_0} \frac{2}{f(r)} + \int_{r_0}^{r_t} \frac{2}{f(r)}. \tag{2.8}$$

Roughly speaking r_0 is to be chosen such that we can do the first integral by retaining only the leading order terms in the near horizon expansion of $f(r)$. In general $r_0 \sim r_H$. This is deduced by considering the length scale set by the ratio of derivatives $|f^{(n)}(r_H)/f^{(n+1)}(r_H)| \sim r_H$. Therefore, we will write the upper limit as $r_0 = Cr_H$ with $C > 1$. With this we can calculate the first integral in Eq. (2.8):

$$\begin{aligned} \int_{r_H+\delta r}^{Cr_H} \frac{2dr}{f(r)} &\approx \int_{r_H+\delta r}^{Cr_H} \frac{2dr}{f'(r_H)(r-r_H) + \frac{1}{2}f''(r_H)(r-r_H)^2} \\ &= \frac{\beta}{2\pi} \ln\left[\frac{(C-1)r_H}{\delta r}\left(\frac{1+\frac{c_2}{c_1}\delta r}{1+(C-1)\frac{c_2}{c_1}r_H}\right)\right], \end{aligned} \tag{2.9}$$

where $c_n = f^{(n)}(r_H)/n!$. It is straightforward to calculate the leading order relation between the Planck length and δr. Using Eq. (2.7) we find that:

$$\ell_p = \sqrt{\frac{\beta\delta r}{\pi}} \Rightarrow \delta r = \frac{\pi\ell_p^2}{\beta}, \tag{2.10}$$

where $\beta = T^{-1} = 4\pi/f'(r_H)$. To simplify the final result for the leading order term we will set $C = \pi + 1$[8]. Any error this introduces will be finite and of $\mathcal{O}(1)$. The $\mathcal{O}(1)$ error will be absorbed into the sub-leading terms in the Planck length expansion. With this choice of C, we find that:

$$\int_{r_H+\delta r}^{(\pi+1)r_H} \frac{2dr}{f(r)} \approx \frac{\beta}{2\pi}\left[\ln\left(\frac{\beta r_H}{\ell_p^2}\right) - \ln\left(1+\frac{f''(r_H)}{8}\beta r_H\right) + \mathcal{O}(\ell_p)\right]. \tag{2.11}$$

Therefore, in general we can write the series expansion for the echo time as:

$$\begin{aligned} t_{echo} &= \frac{\beta}{2\pi}\left[\ln\left(\frac{\beta r_H}{\ell_p^2}\right) + \chi + \mathcal{O}(\ell_p)\right], \\ \chi &= -\ln\left(1+\frac{f''(r_H)}{8}\beta r_H\right) + \chi_0. \end{aligned} \tag{2.12}$$

[8]This is simply a convention that fixes the form of the leading order Log term in the series expansion.

In Eq. (2.12) χ_0 is roughly given by the second integral term in Eq. (2.8) plus any small errors we introduce by fixing $C = \pi + 1$ and doing integral in Eq. (2.11). Consequently, the way we defined χ_0 makes it impossible to know its exact value without explicitly doing the echo integral and expanding it as a series. However, we can give a sufficient condition on it being finite. In particular, we are guaranteed that χ_0 is finite as long as the second integral in Eq. (2.8) converges. This is guaranteed if r_t is finite which brings us to a more precise definition of what is meant by a "low" frequency perturbation. For the black holes we will be considering the effective potential will vanish at the horizon and slowly increase. Depending on the kind of black hole, the effective potential may continue to increase (for very large AdS BH as shown in Fig. 2.1) or reach a local maximum at some point, r_c, (for very small AdS shown in Fig. 2.1 or asymptotically flat BH). In the case where a local maximum is achieved we will only allow $r_t \leq r_c$. This will naturally place an upper bound Ω on the set of frequencies we are dealing with. We will define "low" frequency as $\omega < \Omega$. So we see that the low frequency criterion is needed to ensure that the size of χ_0 is controlled[9].

However, note that even if χ_0 is finite this does not imply that the entire sub-leading term χ is going to be finite. This is why we decompose χ in Eq. (2.12) into two pieces. The Log term will be finite far from the extremal regime, but as we approach the extremal regime the Log term will become uncontrollably large. Therefore, we should combine the the Log term in the definition of χ with the leading order Log term to get the following leading order contribution to the echo time for a near extremal BH:

$$t_{echo}^{ext} \simeq \frac{\beta}{2\pi}\left[\ln\left(\frac{8}{\ell_p^2 f''_{ext}(r_H)}\right) + \mathcal{O}\left(\frac{1}{\beta r_H}\right)\right]. \tag{2.13}$$

Together, Eqs. (2.12 - 2.13) completely characterize the behaviour of the leading order terms in the series expansion of the echo time in various important regimes. Furthermore, we are guaranteed that sub-leading terms are either finite or suppressed by the Planck length ℓ_p. In the next section, we will explicitly calculate the echo time for various types of black holes and show that the echo time can be arranged as a series given by Eq. (2.12). We will give explicit expressions for χ in these examples. In particular, we will show that χ is finite for non-extremal black holes and diverges logarithmically in β in the near extremal regime.

[9]We intentionally did not provide a definition of low frequency for large black holes whose effective potential has no local max. This is because χ_0 is always finite and does not change a great deal as we increase the turning point.

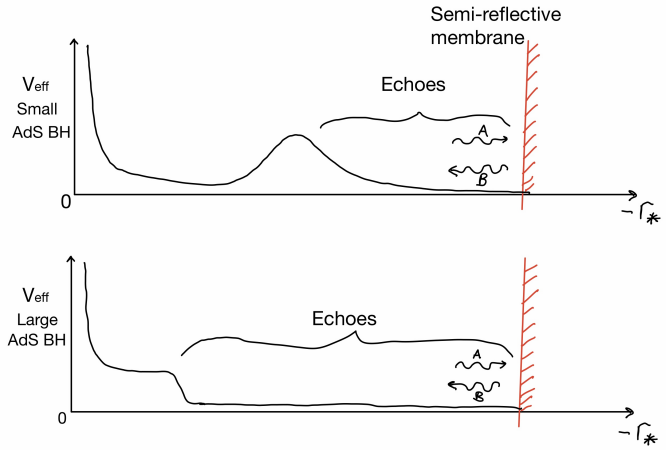

Figure 2.1: Above is a depiction of how echoes are generated for very large ($r_H/L \gg 1$) and very small ($r_H/L \ll 1$) AdS black holes. The event horizon in these coordinates is at $r_* = -\infty$ and the conformal boundary is at $r_* = 0$. The general solution to the massless scalar wave equation near the horizon takes the form $\psi \sim Ae^{-i\omega(t+r_*)} + Be^{-i\omega(t-r_*)}$. The semi-reflective membrane, depicted by the vertical read line, allows for the partial reflection of scalar perturbations with a reflectivity of $|(B/A)e^{2i\omega r_*}|^2$. After the perturbation is partially reflected off the membrane it will head towards the conformal boundary and encounter the effective potential causing reflection back towards the membrane. The process repeats until the perturbation dissipates. For very small black holes the effective potential contains a local max before diverging near the boundary. This is in contrast to very large black holes whose effective potential continues to increase. For asymptotically flat black holes the local maximum is still present. However, there is no conformal boundary and the potential does not diverge.

2.3 Echo Time For AdS Schwarzschild Black Holes

2.3.1 Overview of AdS Schwarzschild Solution

The line element of a $d+1$-dimensional AdS Schwarzschild black hole is given by Eq. (4.68) with $f(r)$ given by:

$$f(r) = 1 - \frac{2M}{r^{d-2}} + \frac{r^2}{L^2}, \tag{2.14}$$

where L is a constant called the AdS radius and M is a measure of the mass of the black hole. The largest real root of $f(r)$ is the location of the event horizon and will be denoted as r_H. Using this fact it is useful to rewrite $f(r)$ in terms of the horizon radius to get:

$$f(r) = 1 + \frac{r^2}{L^2} - \left(\frac{r_H}{r}\right)^{d-2}\left(1 + \frac{r_H^2}{L^2}\right). \tag{2.15}$$

We can then easily write down an expression for the temperature of the black hole:

$$T = \frac{1}{4\pi}\frac{df}{dr}\bigg|_{r=r_H} = \frac{dr_H^2 + (d-2)L^2}{4\pi r_H L^2}. \tag{2.16}$$

Analyzing the sign of dT/dr_H gives us insight about the heat capacity of AdS black holes. In particular, black holes with $r_H^2/L^2 < (d-2)/d$ will have a negative heat capacity and black holes with $r_H^2/L^2 > (d-2)/d$ will have a positive heat capacity. The black holes with positive heat capacity are commonly referred to as large black holes and ones with negative heat capacity are referred to as small black holes.

2.3.2 Echo Time in the Planar Limit

Since very large AdS Schwarzschild black holes at high temperature are well approximated by planar black holes it will be useful to calculate the echo time for a planar black hole. The planar black hole metric is given by Eq. (4.68) with[10]:

$$f(r) = \frac{r^d - r_H^d}{L^2 r^{d-2}}. \tag{2.17}$$

The temperature is given by:

$$T = \frac{dr_H}{4\pi L^2}. \tag{2.18}$$

[10]This not exactly correct. Technically we have to replace $d\Omega_{d-1}$ with the metric on a $d-1$ plane. Now the solutions to the scalar wave equation will be decomposed into plane waves instead of hyper-spherical harmonics. The large angular momentum modes maps to large linear momentum modes along the horizon.

In this case the echo time integral can be expressed in terms of the hyper-geometric function for $d \geq 3$ and is given by:

$$\begin{aligned} t_{echo} &= \int_{r_H+\delta r}^{r_t} \frac{2L^2 r^{d-2}}{r^d - r_H^d} \\ &= \frac{2L^2}{r}\left[{}_2F_1\left(1, -\frac{1}{d}, \frac{d-1}{d}, \frac{r^d}{r_H^d}\right) - 1\right]\Bigg|_{r_H+\delta r}^{r_t} \\ &= \frac{\beta}{2\pi}\left[\frac{dr_H}{r}{}_2F_1\left(1, -\frac{1}{d}, \frac{d-1}{d}, \frac{r^d}{r_H^d}\right) - \frac{dr_H}{r}\right]\Bigg|_{r_H+\delta r}^{r_t}. \end{aligned} \tag{2.19}$$

With some work, we can write the echo time above as a series given by Eq. (2.12) with $\chi(r_t, r_H)$ given by:

$$\begin{aligned} \chi(r_t, r_H) &= \frac{dr_H}{r_t}{}_2F_1\left(1, -\frac{1}{d}, \frac{d-1}{d}, \frac{r_t^d}{r_H^d}\right) + d\left(1 - \frac{r_H}{r_t}\right) - i\pi - \alpha_d \\ \alpha_d &= \gamma + \ln(\pi d) + \psi\left(-\frac{1}{d}\right), \end{aligned} \tag{2.20}$$

where $\gamma \approx 0.577$ is the Euler-Mascheroni constant and ψ is the digamma function. We define χ_∞ as the value of χ when we take the turning point $r_t = \infty$. For the planar black hole we get a finite result:

$$\lim_{r_t \to \infty} \chi\left(r_t, r_H\right) = \chi_\infty = -\gamma - \ln(\pi d) - \psi\left(\frac{1}{d}\right). \tag{2.21}$$

Here, χ_∞ represents an upper bound on the set of all possible values of χ. In other words if we find that χ_∞ is finite, it puts a non-trivial upper bound on χ in the series expansion given by Eq. (2.12). In Fig. 2.2 we plot χ as a function of the ratio r_t/r_H in different dimensions. We see that in general, χ is a strictly increasing function of the turning point. This makes sense because the further the turning point is the longer it takes for the echo to go from the membrane to the turning point. Furthermore, we see that for large values of the turning point χ is approaching χ_∞. We can ignore the divergence in the plot as $r_t \to r_H$ because we always consider our turning points to be far away from the horizon[11]. Most importantly the plot shows that $\chi \leq \chi_\infty < \infty$.

[11] Actually the divergence we see is necessary. The echo time should go to zero if we approach the horizon and indeed the divergence in χ will cancel with the divergence in the leading order term as we send $\ell_p \to 0$ to give an echo time of zero.

Now that we have verified that χ is finite we can safely ignore it and focus our attention to the leading order term. We can use the expression for the temperature given by Eq. (2.18) to write down the leading order contribution to the echo time:

$$t_{echo} \simeq \frac{\beta}{2\pi} \ln\left(\frac{\beta r_H}{\ell_p^2}\right) = \frac{\beta}{2\pi} \ln\left(\frac{4\pi}{d}\frac{L^2}{\ell_p^2}\right). \tag{2.22}$$

This expression will be useful when we start comparing scrambling time to echo time for very large AdS black holes.

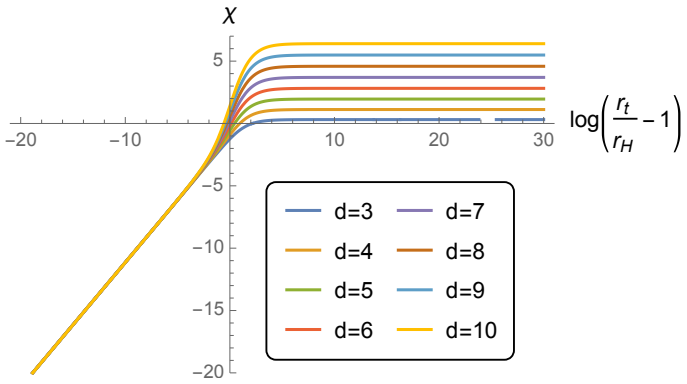

Figure 2.2: Correction to the echo-Log, χ (defined in Eq. (2.12)) as a function of the upper bound on echo integral (Eq. (2.4)) for a $d+1$-dimensional planar (or large spherical) black hole. We see that χ asymptotes to a finite value given by Eq. (2.21) for χ_∞.

2.3.3 Echo Time for Asymptotically Flat Schwarzschild Black Hole

In this subsection, we will compute the echo time for asymptotically flat Schwarzschild black holes. The reason this is interesting is because, we expect the effective potential close to the horizon of a small AdS black hole to be well approximated by the effective potential of an asymptotically flat black hole. Due to this fact, we should expect the low frequency echo time for a small AdS black hole to approximately match with echo time of an asymptotically flat black hole.

To begin, we recall that for an asymptotically flat Schwarzschild black hole in $d+1$-dimensions $f(r)$ is given by:

$$f(r) = 1 - \left(\frac{r_H}{r}\right)^{d-2}, \tag{2.23}$$

and the temperature is given by:

$$T = \frac{d-2}{4\pi r_H}. \tag{2.24}$$

It follows that the echo time is given by [12]:

$$\begin{aligned} t_{echo} &= \frac{\beta}{2\pi}\int_{r_H+\delta r}^{r_t} \frac{(d-2)}{r_H\left(1-\left(\frac{r_H}{r}\right)^{d-2}\right)}dr \\ &= \frac{\beta}{2\pi}\left[(d-2)\frac{r}{r_H}{}_2F_1\left(1,-\frac{1}{d-2},\frac{d-3}{d-2},\left(\frac{r_H}{r}\right)^{d-2}\right)\right]\Bigg|_{r_H+\delta r}^{r_t}. \end{aligned} \tag{2.25}$$

With some work we can eventually write the echo time in the prescribed form given by Eq. (2.12) with χ given by:

$$\begin{aligned} \chi(r_t, r_H) &= \frac{(d-2)r_t}{r_H}{}_2F_1\left(1,\frac{1}{2-d},\frac{d-3}{d-2},\left(\frac{r_H}{r_t}\right)^{d-2}\right) - \alpha_{d-2} \\ \alpha_{d-2} &= \gamma + \psi\left(\frac{-1}{d-2}\right) + \ln\left(\pi(d-2)\right). \end{aligned} \tag{2.26}$$

Just like for the planar black hole we can plot χ as a function r_t/r_H in Fig. 2.3.

Once again we find a strictly increasing function. However this time we find its not bounded and diverges as the turning point gets larger. The reason for this is because the point $r \to \infty$ is mapped to infinity in tortoise coordinates. To get finite results we have to restrict r_t to something finite. A natural choice of the turning point is the location of the local maximum of the effective potential. It will represent the upper bound on the set of possible turning points that leave χ finite. In this case, it turns out that in the large l regime we can analytically solve for the location of the local maximum. It is located at:

$$r_c = \left(\frac{d}{2}\right)^{\frac{1}{d-2}} r_H. \tag{2.27}$$

Using this we can calculate $\chi(r_c, r_H) = \chi_{max}$ and find that:

$$\chi_{max} = (d-2)\left(\frac{d}{2}\right)^{\frac{1}{d-2}}{}_2F_1\left(1,\frac{1}{2-d},\frac{d-3}{d-2},\frac{2}{d}\right) - \alpha_{d-2}. \tag{2.28}$$

[12] It should be noted that taking the limit of the above expression as $d \to 3$ is ill defined. The formula above only works for $d \geq 4$. The $d = 3$ case will be calculated separately in the next subsection.

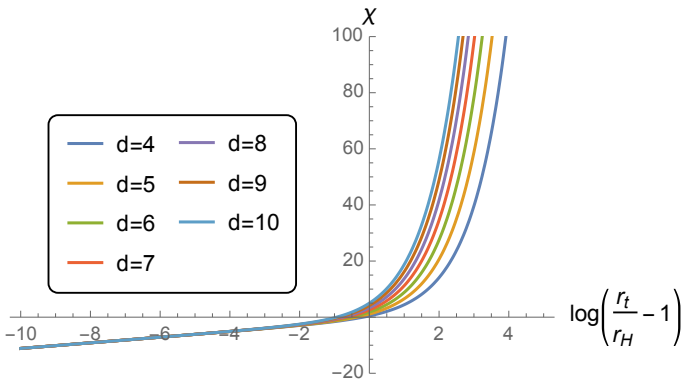

Figure 2.3: Same as Fig. 2.2, but for a $d+1$-dimensional asymptotically flat Schwarzschild black hole. The divergent behaviour implies we must impose a cutoff to control the how large χ becomes. The cutoff is implemented using the low frequency criterion discussed in Section 2.2.

By definition we know $\chi < \chi_{max} < \infty$ and therefore finite. At this point the reader may be worried about the fact that $r_c < r_0 = (\pi + 1)r_H$. In Section 2.2 we split the echo integral into two parts and made an implicit assumption that $r_t > r_0$ we can see that this assumption is not true here. Even so, this fact will not change the conclusion that χ is finite. However, it will change the sign of χ and make $\chi < 0$. More generally, when we plot χ as a function of the turning point there will always be a set of turning points in which $\chi < 0$. This will roughly correspond to when $r_t < r_0$. We say roughly because χ is not exactly given by the second integral in Eq. (2.8) it also contains other small errors which we discussed in Section 2.2.

Now that we have addressed the subtleties that go into making χ finite for asymptotically flat Schwarzschild black holes we can analyze what the leading order term looks like. We can use the expression for temperature given by Eq. (2.24) to get:

$$t_{echo} \simeq \frac{\beta}{2\pi} \ln\left(\frac{\beta r_H}{\ell_p^2}\right) = \frac{\beta}{2\pi} \ln\left(\frac{4\pi}{d-2}\frac{r_H^2}{\ell_p^2}\right). \tag{2.29}$$

This expression will also be useful when we start comparing scrambling time to echo time for very small AdS black holes.

2.3.4 Echo Time for 4D AdS Black Hole

So far we have only done calculations that will give the echo time for for very large or very small AdS black holes in arbitrary dimensions. Now, we want to fix the dimension of spacetime and do the integrals without making assumptions on the size of the AdS black hole. In 4D the echo time is given by an integral of the form:

$$\begin{aligned} t_{echo} &= \int_{r_H+\delta r}^{r_t} \frac{2rL^2}{L^2(r-r_H)+(r^3-r_H^3)}dr \\ &= \frac{\beta}{2\pi}\left[\frac{2+3x_H^2}{x_H\sqrt{4+3x_H^2}}\arctan\left(\frac{2x+x_H}{\sqrt{4+3x_H^2}}\right)+\ln\left(\frac{x-x_H}{\sqrt{1+x^2+xx_H+x_H^2}}\right)\right]\Bigg|_{x_H+\delta x}^{x_t}, \end{aligned} \tag{2.30}$$

where $x_H = r_H/L$, $x = r/L$, $\delta x = \delta r/L$, and $x_t = r_t/L$. We can express the result as a series expansion given by Eq. (2.12) with χ given by:

$$\begin{aligned} \chi(x_t, x_H) =& \frac{2+3x_H^2}{x_H\sqrt{4+3x_H^2}}\left[\arctan\left(\frac{2x_t+x_H}{\sqrt{4+3x_H^2}}\right)-\arctan\left(\frac{3x_H}{\sqrt{4+3x_H^2}}\right)\right] \\ &+\ln\left(\frac{x_t-x_H}{\pi x_H}\sqrt{\frac{1+3x_H^2}{1+x_t^2+x_tx_H+x_H^2}}\right). \end{aligned} \tag{2.31}$$

We can use this result to compute χ for $d = 3$ asymptotically flat black hole by taking the limit as $L \to \infty$ we find:

$$\chi(r_t, r_H) = \frac{r_t}{r_H} - 1 + \ln\left(\frac{r_t}{r_H} - 1\right) - \ln(\pi). \tag{2.32}$$

It is easy to see that χ is strictly increasing with the turning point and diverges with r_t as expected. We can compute χ_{max} by setting $r_t = r_c = 3r_H/2$ this gives:

$$\chi_{max} = \frac{1}{2} - \ln(2\pi) \approx -1.34. \tag{2.33}$$

This completes our $d = 3$ calculation for asymptotically flat black holes.

Next we calculate χ_∞ by taking r_t to infinity this will result in the following expression:

$$\chi_\infty(x_H) = \frac{(2+3x_H^2)\left[\pi - 2\arctan\left(\frac{3x_H}{\sqrt{4+3x_H^2}}\right)\right]}{2x_H\sqrt{4+3x_H^2}} + \ln\left(\frac{\sqrt{1+3x_H^2}}{\pi x_H}\right). \tag{2.34}$$

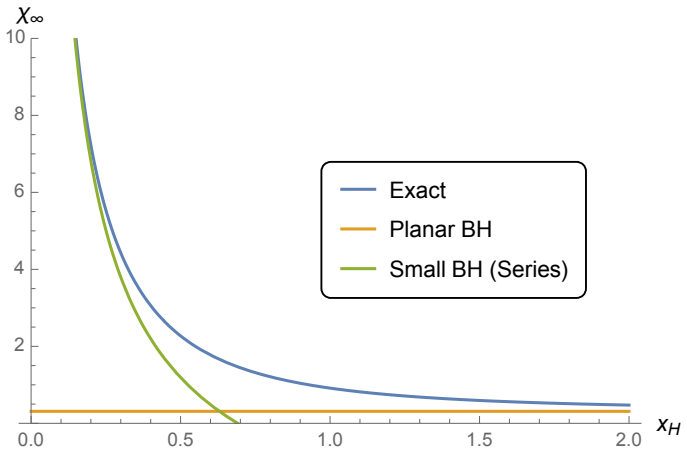

Figure 2.4: The blue line plots χ_∞, the yellow line represents the planar black hole result, and the green line plots the truncated series of χ_∞ near $x_H = 0$ given in Eq. (2.35).

We plot χ_∞ as a function of $x_H = r_H/L$ to get the blue line in Fig. 2.4. We see that χ_∞ strictly decreases and approaches the value of χ_∞ for the planar black hole represented by the horizontal yellow line. The reason that χ_∞ is strictly decreasing is because the horizon of a larger black hole will be closer to the conformal boundary at infinity. If we analyze the behaviour of χ_∞ for small values of x_H we will find that it diverges as $x_H \to 0$. The divergent behaviour can by deduced by analyzing the series expansion of χ_∞ near $x_H = 0$:

$$\chi_\infty \approx \frac{\pi}{2x_H} - \ln(\pi x_H) - \frac{3}{2} + \mathcal{O}(x_H). \tag{2.35}$$

The green line in Fig. 2.4 shows that the series expansion above describes χ_∞ accurately for $x_H \lesssim 0.3$. This means that for very small black holes even though χ_∞ is finite it can become arbitrarily large for an arbitrarily small AdS black hole. However, we recall from our discussions in Section 2.2 that we only want to consider low frequency modes. In such a case, the "low" frequency modes will encounter a local maximum in the effective potential, similar to the asymptotically flat case, before they have a chance of getting to the conformal boundary. Therefore, for low frequency modes we can ignore the fact that χ_∞ is unbounded for very small AdS black holes. This means that χ will always be bounded and much smaller compared to the leading order Log term in the series expansion.

Finally, we can make the following statement about the leading order contribution to

the echo time for a d+1 -dimensional AdS black hole for low frequency perturbations::

$$t_{echo} \simeq \frac{\beta}{2\pi} \ln\left(\frac{4\pi}{d(x_H^2+1)-2}\frac{r_H^2}{\ell_p^2}\right) = \begin{cases} \frac{\beta}{2\pi}\left[\ln\left(\frac{4\pi L^2}{\ell_p^2 d}\right) + \mathcal{O}(1/x_H^2)\right] & x_H \gg 1 \\ \frac{\beta}{2\pi}\left[\ln\left(\frac{4\pi r_H^2}{\ell_p^2(d-2)}\right) + \mathcal{O}(x_H^2)\right] & x_H \ll 1 \text{ and } r_t \leq r_c. \end{cases} \tag{2.36}$$

Unsurprisingly, we see that up to small corrections the leading order term for very large and very small AdS Schwarzschild black holes will match the planar black hole, Eq. (2.22), and Schwarzschild black hole, Eq. (2.29), at the same temprature respectively. Similar calculations can be done in higher dimensions to verify similar results that have been explored for 4D AdS Schwarzschild black holes. Through these calculations we have explicitly checked that for non-extremal black holes χ is always finite[13].

2.4 Echo Time for Reissner-Nordstrom Black Holes

2.4.1 Overview of RN Solution

In this section, we want to understand what happens to the echo time for a Reissner-Nordstrom (RN) black hole in the near extremal regime. The RN black hole in $d+1$-spacetime dimensions is given by Eq. (4.68) with:

$$f(r) = 1 - \frac{2M}{r^{d-2}} + \frac{Q^2}{r^{2(d-2)}}. \tag{2.37}$$

The event horizon is given by the largest root of f we can explicitly write down the roots as:

$$y_\pm = r_\pm^{d-2} = M\left[1 \pm \sqrt{1 - \frac{Q^2}{M^2}}\right], \tag{2.38}$$

where the event horizon is at r_+ and r_- is the inner horizon. We can rewrite everything in terms of $r_\pm$:

$$\begin{aligned} Q^2 &= y_+ y_- \\ M &= \frac{1}{2}(y_+ + y_-) \\ f(r) &= \frac{(r^{d-2} - r_+^{d-2})(r^{d-2} - r_-^{d-2})}{r^{2(d-2)}}. \end{aligned} \tag{2.39}$$

[13]With the additional assumption that for very small black holes we only consider echo time for modes of sufficiently small frequency such that $r_t \leq r_c$.

The temperature of the black hole is given by:

$$T = \frac{d-2}{4\pi r_+}\left[1 - \left(\frac{r_-}{r_+}\right)^{d-2}\right]. \tag{2.40}$$

The extremal limit of the black hole occurs when $r_- = r_+$. Since we are dealing with an asymptotically flat black hole solution we should use the position of the local maximum as the turning point to get finite results. In the large l regime we can find the local maximum at:

$$r_c = \left[\frac{d(r_+^{d-2} + r_-^{d-2})}{4}\left(1 + \sqrt{1 - \frac{4(d-1)}{d^2}\frac{4r_-^{d-2}r_+^{d-2}}{(r_+^{d-2} + r_-^{d-2})^2}}\right)\right]^{\frac{1}{d-2}}. \tag{2.41}$$

It can be checked that as long as $Q^2 \leq M^2$ then r_c is real.

2.4.2 Echo Time for Non-Extremal RN Black Hole

To calculate the echo time we need to calculate the following integral:

$$t_{echo} = \int_{r_+ + \delta r}^{r_c} \frac{2}{\left[1 - \left(\frac{r_+}{r}\right)^{d-2}\right]\left[1 - \left(\frac{r_-}{r}\right)^{d-2}\right]} dr. \tag{2.42}$$

Unfortunately, there does not appear to be a closed form for the integral unless we fix $d \geq 3$ to some particular value. As an example we can fix $d = 3$. When we do this we find that:

$$t_{echo}^{(d=3)} = \frac{\beta}{2\pi}\left[\frac{r(r_+ - r_-) + r_+^2 \ln(r - r_+) - r_-^2 \ln(r - r_-)}{r_+^2}\right]\Bigg|_{r_+ + \delta r}^{r_c}. \tag{2.43}$$

The expression for r_c when $d = 3$ is:

$$r_c = \frac{3}{4}(r_+ + r_-)\left(1 + \sqrt{1 - \frac{32}{9}\frac{r_+ r_-}{(r_+ + r_-)^2}}\right). \tag{2.44}$$

We expand the echo time in terms of the Planck length and get it into the form given by Eq. (2.12), where χ is given by:

$$\begin{aligned}\chi = & \frac{1-x}{4}\left[3x-1+\sqrt{9+x(9x-14)}\right] \\ & + x^2 \ln\left[\frac{4(1-x)}{3-x+\sqrt{9+x(9x-14)}}\right] \\ & + \ln\left[\frac{-1+3x+\sqrt{9+x(9x-14)}}{4\pi}\right],\end{aligned} \tag{2.45}$$

where $x = r_-/r_+$. It is not difficult to see that χ is well defined and finite away from the extremal regime. However, as we approach the extremal regime there is a divergence of the form:

$$\chi = \ln\left(\frac{1-x}{\pi}\right) + \mathcal{O}(1-x). \tag{2.46}$$

As expected, χ will diverge logarithmically as $x \to 1$. We will address this divergence in more detail in the next section. Assuming we are far from the extremal regime, we can write down the leading order contribution to the echo time for a d+1 -dimensional RN black hole as:

$$t_{echo} \simeq \frac{\beta}{2\pi} \ln\left(\frac{\beta r_+}{\ell_p^2}\right) = \frac{\beta}{2\pi} \ln\left(\frac{4\pi}{(d-2)(1-x^{d-2})} \frac{r_+^2}{\ell_p^2}\right). \tag{2.47}$$

Looking at the expression above it is clear that the expression in the log is also diverging in the extremal limit.

2.4.3 Echo Time for Near Extremal RN Black Hole

In the previous section, we calculated the echo time for an RN black hole in 4D and showed that χ was divergent in the near extremal limit. If we now go towards the extremal limit and combine the result for χ given in Eq. (2.46) with Eq. (2.47) the echo time for a 4D RN black hole is given by:

$$t_{echo}^{(d=3)} = \frac{\beta}{2\pi}\left[\ln\left(\frac{4r_+^2}{\ell_p^2}\right) + \mathcal{O}(1-x) + \mathcal{O}(\ell_p)\right]. \tag{2.48}$$

We see that the divergence in χ canceled with the divergence in β leading to a finite expression for the Log. Moreover, we can check that the leading order term in the expansion

of echo time in the near extremal limit is exactly given by Eq. (2.13). To do this we recall that:

$$f_{ext}(r) = \frac{\left(r^{d-2} - r_+^{d-2}\right)^2}{r^{2(d-2)}} \Rightarrow f''_{ext}(r_+) = \frac{2(d-2)^2}{r_+^2}. \tag{2.49}$$

Plugging this into Eq. (2.13) we find:

$$t_{echo}^{ext} \simeq \frac{\beta}{2\pi} \ln\left(\frac{4r_+^2}{(d-2)^2\ell_p^2}\right). \tag{2.50}$$

Which correctly reproduces the leading order term in the echo time in the near extremal limit for $d = 3$. One can also check this formula also works for any $d \geq 3$. This corroborates our claim that the leading order term in the echo time should look like Eq. (2.13) for near extremal black holes.

We can also apply Eq. (2.13) for very large near extremal AdS RN black holes to find:

$$t_{echo}^{ext} \simeq \frac{\beta}{2\pi} \ln\left(\frac{4L^2}{d(d-1)\ell_p^2}\right). \tag{2.51}$$

For very small near extremal AdS RN black holes we will get the same leading order term as in the the asymptotically flat case, assuming $r_t \leq r_c$, which is given in Eq. (2.50). The details of how to calculate $f''_{ext}(r_+)$ for AdS RN black holes is given in Appendix A.2.

We can summarize the results of Section 2.3 and Section 2.4 as follows. We found that the leading order term for the echo time for very large AdS black holes in both near extremal and non-extremal regimes is given by[14]:

$$t_{echo}^{(Large)} \simeq \frac{\beta}{2\pi} \ln\left(\frac{L^2}{\ell_p^2}\right) \simeq \frac{2}{d-1}\frac{\beta}{2\pi} \ln(N^2). \tag{2.52}$$

For very small or asymptotically flat black holes in both near extremal and non-extremal regimes the echo time is given by:

$$t_{echo}^{(Small)} \simeq \frac{\beta}{2\pi} \ln\left(\frac{r_H^2}{\ell_p^2}\right) \simeq \frac{2}{d-1}\frac{\beta}{2\pi} \ln(S_{BH}), \tag{2.53}$$

where S_{BH} is the Bekenstein-Hawking entropy of the black hole. The important fact to note here is that the echo time scale for large black holes is set by the the AdS radius and

[14]Note that in the context of AdS/CFT the ratio L/ℓ_p is a measure of the effective degrees of freedom of the dual CFT state [126]. In particular, for large black holes dual to large N CFTs we know $N^2 \sim L^{d-1}/\ell_p^{d-1}$.

for small AdS (or asymptotically flat) black holes it is set by the horizon radius. This is consistent with the way the scrambling time scale differs for large and small AdS black holes discussed in Section 2.2.

In the next section we will do a more detailed comparison of the time scales given by Eqs.(2.52 - 2.53) to the scrambling time scales given in [134, 91, 29].

2.5 Echoes vs Scrambling

2.5.1 Comparison to Charge Spreading Time Scale

In this section, we will compare the echo time scales given by Eqs. (2.52 - 2.53) with the scrambling time scale conjectured in [134]. We will focus on the charge spreading derivation which is done in the stretched horizon framework [143]. In the derivation it is assumed that the amount of time it takes for charge from a point source to spread uniformly throughout the black hole horizon can be identified with the scrambling time scale. In [134] the true horizon was replaced by a Rindler horizon and the charge spreading calculation was done for the Rindler horizon. With some work, which is detailed in [134, 141], the following expression was derived:

$$t_{sp} = \frac{\beta}{2\pi} \ln\left(\frac{\Delta x}{\ell_s}\right), \tag{2.54}$$

where t_{sp} is the Schwarzschild time it takes for the charge density to spread a distance Δx along the horizon and ℓ_s is the string length[15]. The length scale Δx, in general, cannot be identified with the horizon radius of a black hole. In particular, depending on the size of the AdS black hole, one will naturally choose either r_H or L length scales for Δx. In [134] for asymptotically flat black holes $\Delta x \sim r_H$ and for large AdS black holes $\Delta x \sim L$. Let us now discuss why these choices make sense [16].

In the charge spreading calculation the true black hole horizon is replaced by a Rindler horizon. Such a replacement can only be valid within a small patch on the horizon. The size of this patch should be identified with Δx. We can estimate the length scale of the patch by calculating the Kretschmann invariant, at the horizon of the AdS black hole. To

[15] In this chapter we will simply assume $\ell_s = \ell_p$ and use the two interchangeably.

[16] The argument we present is not explicitly contained in [134]. The authors simply identified Δx with r_H for the asymptotically flat black holes without explicitly explaining why such a choice is valid. With our argument we hope to fill in this gap.

understand why the Kretschmann invariant is important one can consider Riemann normal coordinates at a point on or near the horizon. At the point of choice one is free to choose a flat metric, up to corrections second order in displacement. In other words, we are free to use use a Rindler patch. However, as we move away from this point along the horizon corrections will arise that can be written in terms of the Riemann tensor. The Riemann tensor will set an inverse length scale which should roughly be given by (the fourth root of) the Kretschmann invariant. Therefore, to suppress higher order corrections, the size of the neighborhood should be no bigger than this length scale. Now that we have an understanding of this point, let us consider the example of a 4D AdS black hole. The Kretschmann invariant is given by [74]:

$$R_{\mu\nu\rho\sigma}R^{\mu\nu\rho\sigma}|_{r=r_H} = 12\left(\frac{2}{L^4} + \frac{\left(1+\frac{r_H^2}{L^2}\right)^2}{r_H^4}\right) \simeq \begin{cases} \frac{36}{L^4}\left[1+\mathcal{O}(1/x_H^2)\right] & r_H \gg L \\ \frac{12}{r_H^4}\left[1+\mathcal{O}(x_H^2)\right] & r_H \ll L, \end{cases} \tag{2.55}$$

where $x_H = r_H/L$. We see that the curvature invariant sets different length scales for large and small or asymptotically flat black holes. This means that $\Delta x \sim r_H$ for small black holes and for large black holes $\Delta x \sim L$. This is consistent with the scrambling time scales suggested in [134].

Comparing to the echo time scales in Eqs. (2.52 - 2.53), we find agreement (up to a factor of two) between the leading order echo time scale with the charge spreading time scales for both small and large AdS black holes. Therefore, if it is reasonable to identify scrambling time scale with charge spreading then, it is also valid to identify the echo time with the scrambling time scale defined in [134].

2.5.2 Comparison to Mutual Information Disruption Timescale

In the previous subsection, we showed that the leading order contribution to the echo time reproduces the scrambling time scale as defined by charge spreading in [134] (at least for non-extremal black holes). In this section, we will review how the scrambling time scale appears in Leichenauer's calculation [91] of mutual information disruption. After this review, we will compare with the echo time scale that we calculated.

In [91] one considers a two sided RN black hole in AdS. It is known that the holographic dual to the two sided RN geometry is a charged thermofield double state of the form:

$$|\text{cTFD}\rangle = \frac{1}{\sqrt{Z}}\sum_{n,\sigma} e^{-\frac{\beta}{2}(E_n-\phi Q_\sigma)}\,|n,Q_\sigma\rangle_L \otimes |n,-Q_\sigma\rangle_R\,, \tag{2.56}$$

where $|n, Q_\sigma\rangle_L$ and $|n, Q_\sigma\rangle_R$ are energy and charge eigenstates that live on the left and right conformal boundaries respectively. One can then consider two sub-regions A and B on the left and right field theories respectively and ask how much entanglement there is between the two sub-regions. One way of quantifying the entanglement is to calculate the mutual information which is given by:

$$I(A, B) = S(A) + S(B) - S(A \cup B) \geq 0, \tag{2.57}$$

where S is the standard von Neumann entropy of the reduced density matrix of each sub-region. In general, for sufficiently large sub-regions one can show that the mutual information is non-vanishing. With these quantities in mind, one can then consider a small perturbation to the field theory on one side. This will change or disrupt the mutual information between regions A and B. More specifically, Leichenauer shows that the mutual information goes to zero after a time t_* given by [91]:

$$t_* \sim \frac{\beta}{2\pi} \ln\left(\frac{\Delta E}{\delta E}\right), \tag{2.58}$$

where $\Delta E = E_{tot} - E_{ext}$, is the excess energy above the extremal energy and δE is the energy of the perturbation[17]. The calculation was not directly carried out on the field theory side but instead calculated in the bulk. This was done using the Ryu-Takayanagi conjecture [129, 111, 126] which relates the quantities $S(A)$, $S(B)$, and $S(A \cup B)$ to the area of the extremal surfaces that extend into the bulk. The perturbation on the boundary is dual to the introduction of a shock wave that travels towards the event horizon and lengthens the wormhole connecting the two sides of the RN black hole. The disruption of mutual information occurs because the extremal surface that extends through the lengthened wormhole represents the term $S(A \cup B)$, which will also increase and cause an overall decrease in the mutual information. By considering the non-extremal regime (i.e. $\Delta E \approx E_{tot}$), it was shown that the scrambling time scale, given by Eq. (2.2), is obtained by identifying $\delta E \sim E_{tot}/S$, where S is the entropy of the black hole. Using this fact it was suggested that the scrambling time scale for a near-extremal black holes should be modified to $t_{scr} \sim \beta \ln(S - S_{ext})$, where $S - S_{ext}$ is the excess entropy above the extremal black hole of the same charge.

More recently, the same time scale has been discussed in [29]. In [29] the time scale derived by Leichenauer is recast completely in terms of black hole entropy rather than energy quantities on the boundary:

[17]The energy above extremality of the field theory corresponds to taking the total energy E_{tot} and subtracting off the energy of the field theory in the zero temperature limit, E_{ext}, keeping the charge fixed.

$$t_* \sim \frac{\beta}{2\pi} \ln\left(\frac{S - S_{ext}}{\delta S}\right), \tag{2.59}$$

where S is the entropy of the black hole, S_{ext} is the entropy of the extremal black hole with same charge, and δS is how much the entropy of the black hole has changed after begin perturbed. Note that, by setting $\delta S = 1$ one will recover Leichenauer's modified scrambling time scale. Furthermore, we can use the first law for black hole thermodynamics and easily see that setting $\delta S = 1$ corresponds to $\delta E = T_H$, where T_H is the Hawking temperature of the black hole. Usually the absorption or emission of a single Hawking quantum is regarded as the smallest "natural" choice of perturbation to a black hole in the semi-classical regime. However, we should note that this condition might be too restrictive. For example, explicit string theory constructions of near-extremal black holes can have $\delta S \ll 1$ (e.g., see chapter 11.3 of textbook [19]). Moreover, the statistical interpretation of entropy suggests that the number of microstates is given by e^S, implying that $\delta S_{min} \sim e^{-S} \ll 1$ (in lieu of significant degeneracies)[18].

Of course, perturbations with $\delta S < 1$ will not admit to a Hawking quanta (with characteristic energy T_H) interpretation. However, we suggest that this may not be enough reason to disregard such perturbations in the semi-classical regime. To understand why consider the following. Suppose we have a static spherically symmetric black hole and we perturb [19] it to another static spherical black hole of a different radius. Since one cannot resolve proper distances smaller than a proper Planck length it is reasonable to require that any "measurable" perturbation should shift the horizon by an amount larger than a proper Planck length. (We give a precise definition of what it means to shift the horizon of a black hole by a certain proper length in Appendix A.5). For our purposes, we require that for a given δR which corresponds to a coordinate shift in the horizon radius:

$$\int_{R_H}^{R_H+\delta R} \frac{dr}{\sqrt{f(r)}} \gtrsim \ell_p. \tag{2.60}$$

The minimal observable perturbation will saturate the constraint above and will be denoted as $\delta R_{obs} \sim \ell_p^2 T_H$. Recall that the entropy of a spherically symmetric black hole in $(d+1)$ dimensions is given by:

[18] One way to think about this is to consider the black hole of as a collection of qubits (as is done in many considerations of scrambling in black holes) with a number of micro states equal to $W = e^S$. The smallest change in micro-states (or bits) should be larger than one. So this implies that $\delta W = e^S \delta S > 1$. This in turn implies $\delta S_{min} > e^{-S}$. So even in the context of scrambling it is not necessary that $\delta S > 1$.

[19] Assume the perturbation only changes energy and not charge or angular momentum.

$$S_{BH} = \frac{C_d R_H^{d-1}}{\ell_p^{d-1}}$$
$$C_d = \frac{S_{d-1}}{4} = \frac{\pi^{d/2}}{2\Gamma\left(\frac{d}{2}\right)}, \tag{2.61}$$

where S_{d-1} is the area of a $(d-1)$ unit sphere. We can take the first order variation of the entropy with respect to the horizon radius and plug in $\delta R_{obs} \sim \ell_p^2 T_H$ to find:

$$\delta S_{obs} \sim \frac{R_H^{d-2} T_H}{\ell_p^{d-3}}, \tag{2.62}$$

where we dropped order one factors such as C_d. The expression above gives the smallest change in entropy that results in a measurable change in the horizon radius. When we deal with AdS RN black holes it is possible to have $\delta S_{obs} \ll 1$ when sufficiently close to the extremal regime (See appendix A.4). So proper Planck shifts in the near extremal regime do not have to admit to a description of perturbing by Hawking quanta with characteristic energy T_H. Nonetheless, you can still detect the effect of such perturbations by measuring the proper shift in the horizon. This is why it is not always necessary to discard perturbations that have $\delta S < 1$ since there are alternate ways to detect a perturbation other than counting Hawking quanta.

Going back to Eq. (2.59) and using the choice $\delta S = \delta S_{obs}$ we will obtain time scales consistent with the echo time given by Eqs. (2.52 - 2.53) (see Appendix A.3 for details of calculations).

To summarize, we find that the mutual information disruption time scale defined by Eq. (2.59) is connected to the scrambling time scale by making a choice of the smallest reasonable δS. If one chooses $\delta S = 1$ one obtains Leichenauer's modified scrambling time scale for near extremal black holes. However if one instead insists that the smallest semi-classical perturbation results in observable shifts in the horizon by a proper Planck length then one will get a different time scale for scrambling consistent with the echo time. The usual choice of setting $\delta S = 1$ or some other constant that is independent of any parameters specific to the black hole will always give some kind of $S - S_{ext}$ dependence inside the Log. However, as we argued these may not be the only perturbations of physical interest. One may choose perturbations that depend on parameters of the black hole. Our example of choosing perturbations that shift the horizon by a proper Planck length is one example where δS has non-trivial β dependence (of the form $\delta S \sim r_s/\beta$).

More recently the scrambling time scale has also been calculated in holographic contexts that use entanglement wedge reconstruction [117, 7]. In particular, Pennington's work [117] applies to the types of black holes we have been studying in this chapter. The scrambling time in his work is given by:

$$t_{scr} \sim \frac{\beta}{2\pi} \ln\left(\frac{R_H}{c_{evap}\beta}\frac{R_H^{d-1}}{\ell_p^{d-1}}\right) \sim \frac{\beta}{2\pi} \ln\left(\frac{S - S_{ext}}{c_{evap}}\right). \tag{2.63}$$

In his expressions for the scrambling time there is a parameter, c_{evap}, which depends on where the Hawking radiation is being extracted near the horizon. In our recent work [132] we have shown that c_{evap} will generally have non-trival dependence on β. Depending on how one chooses to extract radiation near the horizon c_{evap} can have different β dependence. This freedom/ambiguity on how we choose the β dependence of c_{evap} is similar to the freedom/ambiguity we have in choosing the β dependence of δS in Eq. (2.59).

2.6 Discussion: A Holographic Description of Echoes?

Thus far, we have motivated a mere mathematical relationship between that echo and scrambling time scales. In this section, we want to speculate on the physical consequences of being able to identify the scrambling time scale with the echo time scale in the context of AdS/CFT.

For the sake of argument, we will assume that echoes really do exist in nature and that they owe their existence to a modification of the event horizon at Planck scales due to quantum gravity effects. Under these assumptions, it is natural to ask whether there is a holographic description of echoes within the framework of AdS/CFT. This is because the AdS/CFT correspondence claims to provide a complete description of quantum gravity in the bulk in terms of a CFT. If echoes exist in nature they should somehow also show up in the CFT description of quantum gravity.

To get an idea of how echoes might manifest themselves in a CFT calculation. It is useful to assume the existence of a state $|\psi\rangle$ which resembles a large one-sided black hole with a modified horizon. More specifically, we want the bulk dual to have a smooth geometrical description of a black hole when far away from the horizon. However, within a Planck length of the horizon the smooth geometrical picture of spacetime should break down. This is similar to the tight fuzzball proposal discussed [64]. This will result in an interface between a smooth geometric exterior and a non-geometric interior as depicted in Fig. 2.5. We will assume that the interface will effectively behave like the membrane that

generates echoes in the bulk. We will denote this bulk spacetime as $\mathcal{M}_\psi$. Based on this bulk model of the CFT state $|\psi\rangle$ we will speculate how echoes in the bulk would manifest in a CFT calculation involving $|\psi\rangle$.

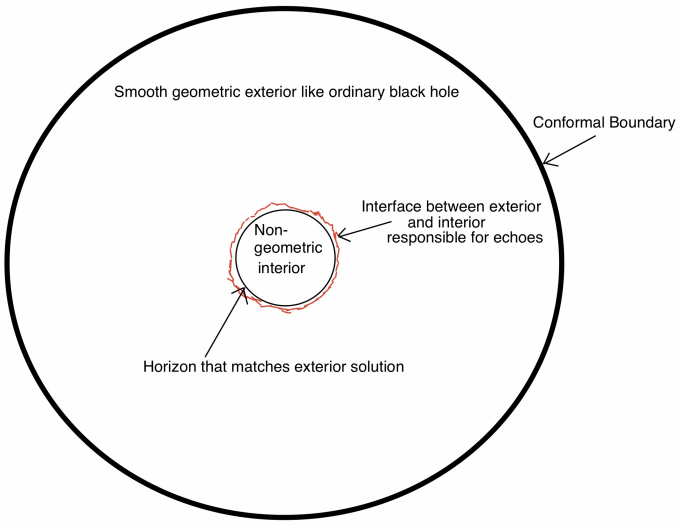

Figure 2.5: A diagram depicting the bulk dual of a particular CFT state that exhibits echoes. The exterior far from the horizon resembles a standard black hole geometry. Within a Planck length of the horizon one expects the smooth geometrical description of spacetime to breakdown at the jagged surface colored in red. Effectively the interface between the smooth exterior and non-geometric interior generates echoes.

To start we know that if we want to "see" echoes we need to perturb the bulk in some way. This can be done by introducing a small perturbation near the conformal boundary in the bulk at time t_0. We can then consider the following quantity $\Delta \langle \hat{O}(t) \rangle = \langle \psi | \hat{O}(t) | \psi \rangle - \langle BH | \hat{O}(t) | BH \rangle$. Where $|BH\rangle$ is the CFT dual state to a black hole with a smooth horizon (i.e. same bulk as Fig. 2.5 without jagged red interface) and $\hat{O}(t)$ is the dual field theory operator to the perturbation in the bulk. We will refer to the smooth horizon spacetime as $\mathcal{M}_{BH}$. The time evolution of the expectation value of the operator $\hat{O}(t)$ in $|\psi\rangle$ and $|BH\rangle$ should be dual to the time evolution of the bulk perturbation around a background $\mathcal{M}_\psi$ and $\mathcal{M}_{BH}$ respectively. Based on the bulk geometry we should roughly expect the following behaviour:

$$\Delta \langle \hat{O}(t) \rangle = \langle \psi | \hat{O}(t) | \psi \rangle - \langle BH | \hat{O}(t) | BH \rangle \approx \begin{cases} 0 & 0 < t - t_0 < t_{echo} \\ \mathcal{O}[\langle \psi | \hat{O}(t_0) | \psi \rangle] & t - t_0 \simeq t_{echo}, \end{cases} \tag{2.64}$$

To understand why this should be the case we consider what is happening in the bulk as time evolves. Initially, at $t = t_0$ the perturbation is close boundary and far from the horizon. Since $\mathcal{M}_\psi$ and $\mathcal{M}_{BH}$ are the same in such a region we also expect time evolution of the perturbation to be the same. However, once the perturbation gets close to the horizon it will behave differently in the two bulk spacetimes we are considering. In $\mathcal{M}_{BH}$ the perturbation will be unhindered and eventually pass through the horizon. However, in $\mathcal{M}_\psi$ the perturbation will encounter a reflective surface and get partially reflected back towards the conformal boundary. Information of this reflection will not arrive back at the conformal boundary until $t - t_0 \simeq t_{echo}$. This is why we should expect $\Delta \langle \hat{O}(t) \rangle \approx 0$ when $0 < t - t_0 < t_{echo}$. Once the reflected perturbation hits the boundary there should be a big difference between $\langle \psi | \hat{O}(t) | \psi \rangle$ and $\langle BH | \hat{O}(t) | BH \rangle$ roughly of the order $\mathcal{O}[\langle \psi | \hat{O}(t_0) | \psi \rangle]$. After this time we expect the perturbation to bounce off the conformal boundary and go back towards the horizon and repeat the same process we outlined above until the perturbation dissipates entirely. If we were to plot $\Delta \langle \hat{O}(t - t_0) \rangle$ we would expect a result resembling Fig. 2.6.

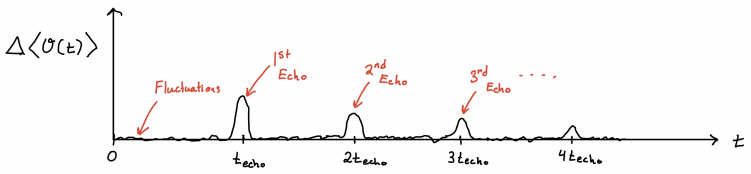

Figure 2.6: A diagram depicting how echoes will manifest themselves in a calculation involving $\Delta \langle \hat{O}(t - t_0) \rangle$. Initially, the difference in the expectation value of the operator is subject to small fluctuations around zero. After one echo time scale, one would find a distinct signal above the usual fluctuations represented by the first peak. This signals the first echo in the bulk. This would reflect off the boundary and go back towards horizon and the process would repeat except subsequent echoes would gradually weaken (depicted by subsequent peaks with smaller amplitude).

Now that we have discussed how echoes in the bulk would manifest themselves in a dual CFT calculation we will discuss how we can use this picture to argue how echoes and fast scrambling can be physically related. To begin, we recall that by perturbing a black hole we can deduce the structure of the horizon by analyzing how the perturbation decays. If the decay is accompanied by echoes then it suggests the existence of a modified horizon. On the other hand, perturbing a black hole can also be regarded as the introduction of information into the black hole. As the information approaches the horizon it will become scrambled within a scrambling time scale. The process of scrambling the newly added

information should gradually destroy the finely tuned entanglement between degrees of freedom close to the horizon and lead to the development of modified horizons similar to the scenarios discussed in [152, 135, 136]. Eventually, the bulk geometry should evolve into configurations depicted in Fig. 2.5 and these types of bulk geometries would give us echoes. In other words, we believe fast scrambling to be a mechanism by which bulk geometries with smooth horizons can develop modified horizons which result in echoes. The findings of this chapter which suggest that echoes and fast scrambling occur within time scales that can be reasonably identified with each other seems to be consistent with this idea.

Another interesting proposal we have on how echoes may manifest in CFT calculations is based on the work [94]. It was shown that for large N CFTs, with a holographic Einstein dual, the following quantity has the following $1/N$ perturbative expansion:

$$\begin{aligned} F(t) &= Tr[yV(0)yW(t)yV(0)yW(t)] = f_0 - \frac{f_1}{N^2} e^{\frac{2\pi t}{\beta}} + \mathcal{O}(N^{-4}) \\ y^4 &= \frac{1}{Z} e^{-\beta H}, \end{aligned} \tag{2.65}$$

where $f_0, f_1 > 0$ and depend on the choice of the operators V and W. The calculation of the sub-leading term above is done by doing a gravity calculation similar to the type of calculations done using shock wave geometries in [136, 135, 91]. In such calculations the shock waves are perturbations to the horizon and the function $F(t)$, we suggest, should be viewed as a kind of response function which can diagnose the existence of a modified horizon. In particular, we see that the echo time for very large black holes is consistent with the scrambling time set by $\frac{\beta}{2\pi} \ln(N^2)$[20] which is also when the sub-leading term in Eq. (2.65) becomes of order one. This means that the perturbative calculation after such a time scale breaks down and one needs to include higher order terms. By including all the higher order terms one might see echoes in the function $F(t)$. If this was indeed the case, it would help corroborate the claim that probing the horizon (via shock waves) will cause the horizon to develop some modified structure, which would be responsible for the echoes in $F(t)$.

2.7 Conclusion

As we already stated in the introduction of this work the existence of echoes from an experimental point of view is still tentative and controversial [4, 40, 1, 156, 5]. On the

[20] Recall that $(L/\ell_p)^{d-1} \sim N^2$.

theoretical side, there are reasons to think that General Relativity does not tell the whole story of the nature of spacetime near the horizon of a black hole [10, 122, 140, 99, 100, 64, 137, 152, 59, 58].

In this chapter, we explored the potential connection between the echo and fast scrambling time scales. We began by defining the echo time scale and explored whether it was capable of reproducing the scrambling time scale in various regimes for AdS black holes. In non-extremal regimes, we found agreement between the echo and scrambling time scales.

For near extremal black holes, we showed that the echo and scrambling time agree with each other for perturbations that shift the horizon by a proper Planck length. We argued in in Section 2.5.2 that the usual choice of setting $\delta S = 1$ in Eq. (2.59) as the smallest perturbation to a black hole is too restrictive. In light of this, we proposed that the smallest semi-classical perturbation should shift the horizon by a proper Planck length. The consequences of this alternate proposal is explored in depth in Appendix A.4 and Appendix A.5. Depending on the exact value of the ratios R_{ext}/R_H and R_H/L, one will see a proper Planck shift results in different changes in the entropy (details in Appendix A.4). In general, the farther one is from the extremal regime, the larger the entropy change is for a proper Planck shift in the horizon. Furthermore, in the limit where R_H/L becomes arbitrarily large, one can get arbitrarily close to an extremal black hole before $\delta S < 1$.

In Section 2.6, we speculated on how echoes might manifest themselves in the context of AdS/CFT. We postulated the existence of a state $|\psi\rangle$ whose dual geometry, $\mathcal{M}_\psi$, resembled the bulk depicted in Fig. 2.5. With this correspondence we argued that the echo time represented the amount of time it takes to determine whether a bulk geometry has a smooth or modified horizon based on the time evolution of the expectation value of some operator on the boundary. We then conjectured that the phenomena of fast scrambling and echoes are related to each other in the sense that one is a precursor for the other. More specifically we argued that fast scrambling would provide a mechanism by which black holes would develop modified horizons when perturbed. The development of modified horizons would be accompanied by echoes in the thermalization behaviour of certain CFT observables. We went further and speculated that echoes may actually be found in non-perturbative calculations of quantities similar to the ones explored in [94] given by Eq. (2.65). It would be interesting to see if it is possible to perform such non-perturbative calculations.

As interesting as the proposals in Section 2.6 are there is one major problem. The problem lies in our assumption that states that resemble black holes with modified horizons actually exist. Such an assumption is critical for the discussions in Section 2.6 to be valid. In order for our arguments to be convincing one should try to explicitly find or construct a CFT state and show it exhibits echoes when perturbed. At the moment we do

not have a concrete way of constructing such a state. However, it is interesting to draw upon the work of Shenker and Stanford [136] which discusses the holographic dual of the thermofield double state begin perturbed by strings of operators referred to as "thermal-scale operators." The bulk interpretation of such a state is that of a two sided black hole with a smooth horizon connected by a very long wormhole. Perhaps in a similar way if one acts with more generic operators on the thermofield double one might transition from a black hole with a smooth horizon to a black hole with a modified horizon. If so, such states may exhibit echoes in the way we discussed in Section 2.6.

A recent paper [114], investigating the reflectivity of modified black hole horizons, was able to show that Boltzmann reflectivity[21] can be derived by considering perturbations on an $\mathbb{R}P^3$ geon. This is interesting because it provides a connection between the Boltzmann reflectivity of a modified black hole to the $\mathbb{R}P^n$ geons which have also been discussed in the context holography. In particular, work done in [63] which discussed the construction CFT_2 states dual to the $\mathbb{R}P^2$ geon may provide ways to construct CFT states that have horizons with Boltzmann reflectivity.

Finally, it is worth noting that not all notions of scrambling give a time scale comparable to Eq. (2.2). A recent paper by Shor [137] suggests that in order for scrambling to occur as fast as the time scale given by Eq. (2.2), via causal processes outside the stretched horizon, one needs information to leave the stretched horizon at a rate greater than what would be allowed by conventional Hawking radiation. To arrive at this conclusion, Shor used a definition of scrambling which is stronger than the definitions used in [134, 86, 136, 91, 29]. In particular, Shor identifies the scrambling time scale as the amount of time it takes for two unentangled hemispheres of a black hole to become maximally entangled. Naively, it seems that echoes would allow for information to escape the stretched horizon at a non-conventional rate and provide a mechanism to speed up the generation of entanglement between the two hemispheres. Therefore, it would be interesting to see if echoes can be used to speed up scrambling and make Shor's scrambling time scale consistent with Eq. (2.2).

[21] This model assumes that the reflectivity of a modified black hole horizon depends on the frequencies of perturbations. In particular, different frequencies are weighted by a Boltzmann factor $e^{-\beta\omega}$. This means that for very high frequencies the modified horizon behaves very similar to a smooth horizon (reflectivity is approximately zero).

Chapter 3

Spacing Statistics of Energy Spectra: Random Matrices, Black Hole Thermalization, and Echoes

Recent advances in AdS/CFT holography have suggested that the near-horizon dynamics of black holes can be described by random matrix systems. We study how the energy spectrum of a system with a generic random Hamiltonian matrix affects its early and late time thermalization behaviour using the spectral form factor (which captures the time-dependence of two-point correlation functions). We introduce a simple statistical framework for generating random spectra in terms of the nearest neighbor spacing statistics of energy eigenvalues, enabling us to compute the averaged spectral form factor in a closed form. This helps to easily illustrate how the spectral form factor changes with different choices of nearest neighbor statistics ranging from the Poisson to Wigner surmise statistics. We suggest that it is possible to have late time oscillations in random matrix models involving β-ensembles (generalizing classical Gaussian ensembles). We also study the form factor of randomly coupled oscillator systems and show that at weak coupling, such systems exhibit regular decaying oscillations in the spectral form factor making them interesting toy models for gravitational wave echoes. We speculate on the holographic interpretation of a system of coupled oscillators, and suggest that they describe the thermalization behaviour of a black hole geometry with a membrane that cuts off the geometry at the stretched horizon.

3.1 Introduction

3.1.1 Background and Context

Black holes serve as an important testing ground and challenge for our understanding of the quantum nature of gravity. The application of quantum field theory on black hole backgrounds leads to the conclusion that pure states can evolve into mixed states through the mechanism of Hawking radiation [68, 69]. On the other hand, theoretical developments in string theory and AdS/CFT suggest that quantum gravity should be a unitary theory. The conflict with the expectation that quantum gravity should be a unitary theory and the apparent violation of unitarity by Hawking's calculation has given rise to the black hole information problem [99, 65, 140]. Explorations into the information problem have led to the idea of quantum gravity effects modifying the near horizon description of black holes, most notably in the form of some kind of microstructure near the horizon (e.g. fuzzballs, firewalls, non-locality etc.) [10, 122, 140, 99, 100, 72, 107, 60].

The idea of quantum effects modifying the near horizon physics of a black hole have recently also been considered from an experimental perspective. If quantum effects near the horizon give rise to the possibility of partial reflection rather than complete absorption of a perturbation then it could give rise to "echoes" in the ringdown behaviour of a black hole after being perturbed. In particular, such echoes may be detected by LIGO in gravitational waves emitted during black hole binary merger events [4, 32, 31, 40, 156, 113, 5, 1, 35, 3, 2]. In most studies, these modifications are modelled by cutting off the black hole geometry near the horizon. At the cutoff, semi-reflective boundary conditions are enforced and perturbations on the cutoff background are studied[1] [98, 155, 133, 45, 44, 124]. Studies that do this make an implicit assumption that the quantum effects that encode the unitary nature of black holes are "localized" near the horizon and that they effectively manifest themselves as a cutoff near the horizon with non-standard boundary conditions. Although such models are completely classical, they highlight the interesting possibility of finding observable imprints of horizon scale quantum gravity effects in the ringdown behaviour of black holes.

In this chapter, we will explore the idea of echoes in the context of the thermalization behaviour of quantum chaotic systems. The motivation behind this study is the idea that

[1] In these studies the time scale over which the echoes manifest after the black hole is perturbed is called the "echo time scale." It depends on how close the cutoff is placed relative to the horizon. For a cutoff placed a proper radial Planck length from a Schwarzschild black hole it can be shown the echo time takes the form of the scrambling time $\beta \ln(S_{BH})$ [133] (e.g. for a 10 solar mass Schwarzschild black hole the scrambling or echo time is of the order of 0.2 secs.).

the near horizon dynamics of a black hole is generally captured by quantum chaotic degrees of freedom. When a perturbation begins to probe and excite the microstructure near the horizon, it could lead to observable deviations from the standard ringdown as predicted by quasi-normal mode decay. If the microstructure effectively behaves as a semi-reflective cutoff near the horizon, then one would get echoes in the unitary description of the black hole. The goal of this chapter is to explore the properties a quantum chaotic system, if it were to exhibit echoes in its thermalization behaviour. To aid in this exploration, we will make use of recent advances and tools in AdS/CFT that have placed interesting constraints on the energy spectrum of black holes. In the next subsection, we will give a brief overview of these developments and tools.

3.1.2 Black Holes as Quantum Chaotic Systems

The AdS/CFT correspondence, which was first formulated by Maldacena [96] suggests that (quantum) gravitational systems in AdS have a non-perturbative formulation in terms of a strongly coupled CFT [121, 125, 153]. This in turn provides a way to explore various aspects of the quantum nature of black holes from the perspective of a thermal CFT [97, 75, 99, 140, 122].

One of the earliest explorations into the quantum spectrum of a black hole from the perspective of AdS/CFT involved the thermofield double (TFD) state [97]. The TFD is a state which is conjectured to describe a two sided eternal black hole in AdS and is written as:

$$|TFD\rangle = \frac{1}{\sqrt{\mathcal{Z}(\beta)}} \sum_n e^{-\beta E_n/2} |n\rangle_L \otimes |n\rangle_R \,, \tag{3.1}$$

the state above describes two identical systems (one living on the left boundary and the other on the right) which are entangled. The states $|n\rangle_{L,R}$ are eigenstates of a Hamiltonian with eigenvalues E_n, and the quantity $\mathcal{Z}(\beta)$ is the partition function. Using this, one should expect the decay of quasi-normal modes of the dual black hole to be consistent with the decay of two-point thermal correlators.

It was noted in [97], that the spectrum of a CFT which is dual to a black hole (with a spherical horizon) lives on a compact space and as a result its spectrum will be discrete. The discreteness of the spectrum implies that correlation functions cannot decay to zero which is an indication of unitary evolution in the bulk [97, 65, 17, 138]. The inability for correlators to decay to zero comes as a surprise from the bulk perspective because quasi-normal modes for an AdS black hole decay exponentially to zero [75]. It was argued in [97] that correlators will decay in a manner consistent with the semi-classical calculation of

quasi-normal modes of the black hole until the correlator roughly becomes of the order e^{-S}, where S is the entropy. Afterwards, the discreteness of the spectrum will become important and the semi-classical calculation will no longer agree with the boundary calculation of the two-point function. In a semi-classical context, it was shown that to prevent the continual decay in the bulk, one can include other saddle point geometries in the Euclidean path integral approach [97]. It was also demonstrated that one can avoid continual decay of the two-point function and make the spectrum discrete by cutting off the spacetime near the horizon [147, 17, 138].

Quantum chaos is another important feature of thermal CFT systems that are dual to black holes. In particular, CFT systems that are dual to black holes are conjectured to be maximally chaotic[2] [94]. Quantum chaos manifests itself in the spectrum of a quantum system through nearest neighbor eigenvalue "repulsion." In particular, it is conjectured that many statistical properties of the spectrum of a quantum chaotic system follow the spectrum statistics of random matrices drawn from a suitably chosen ensemble [27, 49, 93]. The connection between gravity and random matrix theory has been further explored in the context of 2D Jackiw-Teitelboim (JT) gravity by showing the partition function of JT gravity can be expressed as a random matrix integral [130, 131, 139, 26]. These recent results corroborate the conjecture that random matrix theories are capable of describing the statistical properties of the spectrum of quantum chaotic systems such as black holes.

A particularly useful observable that has been computed in the context of quantum chaos, is the normalized spectral form factor which is defined by:

$$\frac{\mathcal{Z}(\beta+it)\mathcal{Z}(\beta-it)}{\mathcal{Z}(\beta)^2} = \frac{\sum_{n,m} e^{-\beta(E_m+E_n)} e^{i(E_n-E_m)t}}{\sum_{n,m} e^{-\beta(E_m+E_n)}}, \tag{3.2}$$

where $\mathcal{Z}(\beta)$ is the partition function in the canonical ensemble with inverse temperature β. It is a useful quantity since it can be used to diagnose the discreteness of a spectrum. In the context of the TFD state, if one considers the two point function of a Hermitian operator of the form $\mathcal{I}_R \otimes A$ (where $\mathcal{I}_R$ is the identity on the right boundary and A is a Hermitian operator living on the left boundary) we have:

$$\begin{aligned} \langle TFD|[\mathcal{I}_R \otimes A(t)][\mathcal{I}_R \otimes A(0)]|TFD\rangle &= \frac{1}{\mathcal{Z}(\beta)} \sum_{n,m} e^{-\beta E_n} e^{i(E_n-E_m)t} \left|\langle n|A|m\rangle\right|^2 \\ &= \frac{1}{\mathcal{Z}(\beta)} \left[\sum_n e^{-\beta E_n} \left|\langle n|A|n\rangle\right|^2 + \sum_{n,m;n\neq m} e^{-\beta E_n} e^{i(E_n-E_m)t} \left|\langle n|A|m\rangle\right|^2 \right], \end{aligned} \tag{3.3}$$

[2]The SYK model is an example of a maximally chaotic system which has been of recent interest [123, 55, 56, 145].

we can see the time dependence (up to matrix elements which will depend on the energy) of the form factor and the two point function are governed by the details in the energy differences in the spectrum. If the matrix elements are smooth functions of energy that vary slowly, we can use the form factor as a proxy for understanding how a perturbation thermalizes for a TFD state. This is interesting because by identifying a Hamiltonian and its spectrum of states we can construct the associated TFD state. If we conjecture that the TFD is dual to a two-sided black hole geometry, then we can roughly interpret the early time behaviour of the spectral form factor as a description of the ringdown of the black hole after being perturbed (i.e. the quasi-normal modes). From this perspective, different choices of Hamiltonian give different types of ringdowns of the conjectured dual black hole. Usually, at early times, the discrete spectrum can be replaced by a coarse grained smooth density - and one initially sees decay in the form factor (controlled by the decay of quasi-normal modes of the black hole). At very late times, the behaviour of the spectral form factor is governed primarily by the small energy differences between nearby eigenvalues - and in general it produces very erratic oscillations which never decay to zero.

In the context of a random matrix ensemble (RME), one is interested in the normalized averaged spectral form factor (throughout this chapter we shorten the name and call it the "form factor" unless otherwise stated) given by:

$$\frac{\langle \mathcal{Z}(\beta+it)\mathcal{Z}(\beta-it)\rangle_{RME}}{\langle \mathcal{Z}(\beta)^2\rangle_{RME}}, \tag{3.4}$$

where $\langle\cdot\rangle_{RME}$ is an average over a random matrix ensemble[3]. One can compute this numerically, by taking an average over many samples of the form factor which is constructed using the eigenvalues of sample matrices drawn from the ensemble. In the context of a random spectrum, the early time behaviour of the form factor has the property of being "self-averaging" which means that the form factor of a single sample is close to the average over many samples. However, at late times the form factor of a single sample will deviate significantly from the average and will no longer be self-averaging. In the case of classical Gaussian ensembles whose averaged form factor was studied in [42], it was shown that the averaged late time behaviour after the initial decay took the form of a ramp followed by a plateau(e.g., see Figure 3.1). The existence of the ramp can be attributed to the nearest neighbor spacing statistics of the eigenvalues of the matrices drawn from the classical Gaussian ensembles. Furthermore, the spectrum of the SYK model (which is a toy model

[3]Note that we are taking the average over the numerator and denominator separately. This particular way of averaging is called "annelled" disorder averaging and this is in contrast to "quench" disorder average which is obtained by doing an average of the entire normalized expression for the form factor. At infinite temperature annealed and quenched averages are the same.

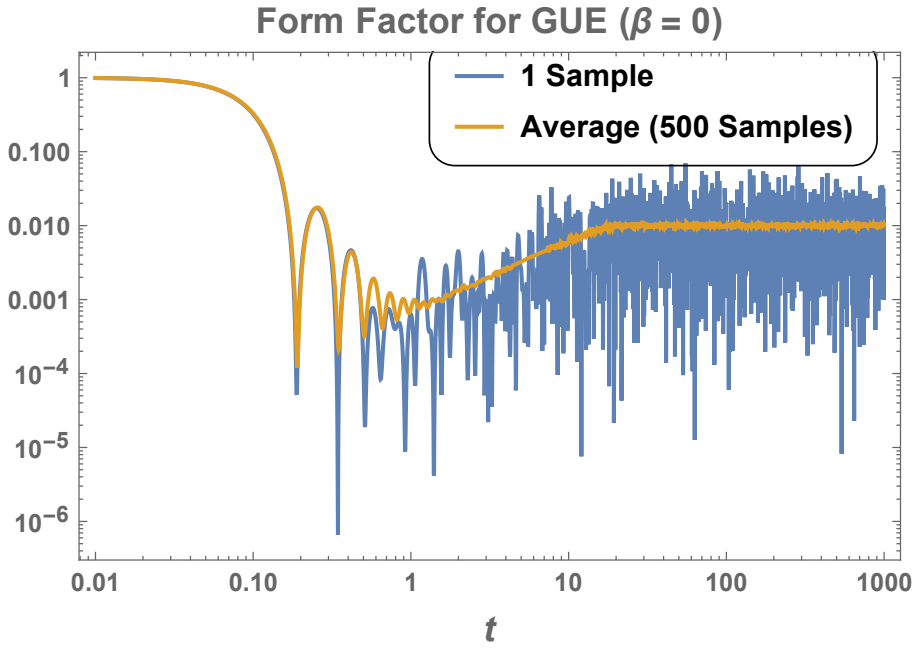

Figure 3.1: We plot the infinite temperature form factor for a spectrum generated by 100×100 matrices pulled from the Gaussian unitary ensemble (GUE). The blue line is the form factor for a single sample matrix from the GUE and the yellow line is the 500 sample average. One can see that at late times, the averaged form factor exhibits a linear ramp followed by a plateau.

for near extremal black hole physics) had similar features to the spectrum of random matrices belonging to classical Gaussian ensembles[4]. These findings led to the idea that large AdS black holes are described by theories that have a spectrum resembling the spectrum of random matrix theories.

In particular, the results reviewed in this subsection suggest that black holes are dual to quantum systems that have a discrete and chaotic energy spectrum[5]. In light of this, it is natural to ask if it is possible for a quantum chaotic system to exhibit echoes in its thermalization behaviour. If the answer is yes, then one might view such a system as

[4]In Section 3.3.3 we will discuss how the SYK model form factor is differs in certain details with the form factor associated with matrices pulled from classical Gaussian ensembles.

[5]It should also be noted that there is an additional constraint that the system should saturate the Lyapunov bound discussed in [94]. We will address this point in the discussion of echoes in quantum chaotic systems at the end of the chapter.

potential candidate for describing black holes with microstructure near the horizon[6]. In our exploration we will primarily be interested in how various aspects of the spectrum of a system manifest in the early and late time behaviour of the form factor and use this as a way to understand how perturbations to such systems thermalize. In the context of black hole echoes, we will be interested in finding a system with a quantum chaotic spectrum that gives rise to regular but decaying oscillations in the form factor which might be interpreted as echoes being generated by some microstructure near the horizon of a black hole in the bulk.

3.1.3 Overview

In Section 3.2, we will introduce a model for a random spectrum and derive closed form expressions for the averaged spectral form factor in terms of the nearest neighbor spacing statistics. In particular, Section 3.2.1, will go over the details of the model we adopt to describe a random spectrum and also go over the basics of computing various averaged quantities in such a model. In Section 3.2.2, we use our model to derive a closed form expression for the averaged spectral form factor in terms of integrals which involve the nearest neighbor spacing (NNS) distribution.

In Section 3.3, we consider various common NNS distributions and compute the associated averaged form factor using the formulas we derived in Section 3.2. In Section 3.3.1, we analyze the form factor of a non-random evenly spaced spectrum and show the form factor is periodic with a period that is inversely proportional to the spacing between the energy levels. In Section 3.3.2, we analyze the form factor associated with having a Poisson NNS distribution (which would serve as a model for the spectrum of a generic quantum integrable system). We show that the averaged form factor monotonically decreases and saturates to a non-zero value at late times. In Section 3.3.3, we compute the averaged form factor of a system which has NNS statistics following the Wigner surmise (which serve as a model for the spectrum of a quantum chaotic system that follows the statistics of classical Gaussian ensembles). We find that the form factor has an initial dip followed by a ramp and plateau, which is consistent with expectations from the studies of classical Gaussian ensembles, as shown in Figure 3.1. In Section 3.3.4, we introduce the gamma distribution as a simpler alternative to the Wigner surmise NNS distribution. We show that, in the appropriate regimes, the form factor associated with the gamma distribution

[6]Here we are specifically referring to microstructure that gives rise to echoes. It is possible that a black hole could have microstructure near its horizon but not exhibit echoes when perturbed. We will discuss this possibility in more detail at the end of the chapter.

will still have a ramp and plateau. We also show that there are other regimes in which the NNS distribution contains a large "gap." We show the existence of the gap results in regular decaying oscillations in the averaged form factor after the initial dip. We argue that similar oscillations in the form factor will occur for large values of the Dyson index in the Wigner surmise distribution (Equation 3.30). These larger values of the Dyson index can be obtained from generalizations of classical Gaussian ensembles and are commonly refereed to as "β-ensembles," which are know to arise from tri-diagonal random matrices [46].

In Section 3.4, we study the spectrum of a many-body system composed of identical oscillators coupled to each other by a matrix belonging to a classical Gaussian ensemble. In the weak coupling regime, we study the role the chaotic interactions play in the splitting of degenerate energy states. We show that within each degenerate sector, the splitting of the energy levels will generally give rise to chaotic spectrum statistics within each sector. We verify this by numerically studying the form factor and spectral density in the weak and strongly coupled regime. We show that the averaged spectral form factor of such systems at weak coupling exhibit regular decaying oscillations at early times followed by a ramp and plateau at late times - which is consistent with random matrix theory models that describe black holes. We then propose such systems of weakly coupled oscillators as toy models for describing a membrane which gives rise to decaying echoes. The echoes repeat at approximately the fundamental frequency of the oscillators. We identify the parameters in the oscillator system with those of the bulk geometry+membrane system. Through this identification, we show that the question of whether the oscillator system is strongly or weakly coupled depends on how far the membrane is placed from the horizon.

In Section 3.5, we conclude by summarizing the major findings and discuss future research directions.

3.2 A Simple Model for Random Spectra

As stated in the introduction, quantum chaotic systems are generally conjectured to have spectrums that follow the statistics of random matrix theories (most notably Gaussian ensembles). One of the most important pieces of statistical data in the spectrum of a random matrix ensemble is the NNS statistics between eigenvalues. The NNS statistics encode non-trivial correlations between eigenvalues that give rise to quantum chaotic or integrable dynamics. In the following subsections, we will introduce a simple model for a random spectrum which allows us to specify the NNS statistics of the system we are trying to model. Such an approach is unorthodox from the perspective of random matrix

theory. Usually, one specifies an ensemble of random matrices and then derives the spectral statistics of the ensemble. Here, we take a different approach and generate a random spectrum by specifying the NNS statistics. The choice of NNS statistics is then assumed to correspond to some choice of random matrix ensemble (for example, by using the Wigner surmise for the NNS distribution, our model should approximately describe the statistical behaviour of eigenvalues pulled from a Gaussian ensemble). In Section 3.3 we will address the issue of how well these models reproduce various aspects of the spectral form factor of certain matrix ensembles.

3.2.1 Random Spectrum with Fixed NNS ("i.i.d Model")

We begin the construction of our random spectrum model by expressing its energy levels as follows:

$$E_n = E_{gs} + \sum_{k=1}^{n} \delta E_k, \tag{3.5}$$

where E_{gs} is the ground state energy, which we assume is fixed to a constant $E_{gs} = E_0$, and δE_k are independent-identically-distributed (i.i.d) random variables which follow a probability distribution $\mathcal{P}$. By assuming that $\mathcal{P}$ is a distribution with non-zero support for $\delta E_k \in \mathbb{R}^+$ we get an ordered set of energy levels in the spectrum $E_0 \leq E_1 \leq E_2 \leq \cdots \leq E_N$. Throughout the rest of this chapter we will refer to this model as the **i.i.d model**.

Since we choose δE_k to be i.i.d random variables we can express the joint probability density of the energy levels $\{E_k\}_{k=1}^N$ of the spectrum as[7]:

$$P(E_1, E_2, ..., E_N) = \prod_{k=1}^{N} \mathcal{P}(E_k - E_{k-1}). \tag{3.6}$$

Using this, we can define the average of some function, $f(E_1, .., E_N)$, associated with the random spectrum:

$$\langle f \rangle = \int_{-\infty}^{\infty} dE_1 \cdots dE_N f(E_1, .., E_N) P(E_1, .., E_N). \tag{3.7}$$

For example, the spacing distribution between two eigenvalues E_i and E_j in terms of the joint probability distribution function is given by the following integral expression:

$$p_{i,j}(s) = \int_{-\infty}^{\infty} dE_1 \cdots dE_N P(E_1, .., E_N) \delta\left(s - |E_i - E_{j-1}|\right). \tag{3.8}$$

[7]Note that under the change of variables $\delta E_k = E_k - E_{k-1}$ we have the equivalence of probability measures $dE_1 \cdots dE_N = d\delta E_1 \cdots d\delta E_N$. This is due to the Jacobian being a lower(or upper) triangular matrix filled with 1's.

Using the formula for the spectrum defined by Eq. (3.5), we can see that the spacing distribution between the adjacent energy levels E_m and E_{m+1} is[8]:

$$\begin{aligned} p_{m,m-1}(s) &= \int_{-\infty}^{\infty} dE_1 \cdots dE_N P(E_1, .., E_N) \delta\left(s - (E_m - E_{m-1})\right) \\ &= \int_{-\infty}^{\infty} d\delta E_1 \cdots d\delta E_N \prod_{k=1}^{N} \mathcal{P}(\delta E_k) \delta(s - \delta E_m) = \mathcal{P}(\delta E_m). \end{aligned} \tag{3.9}$$

This proves that the NNS distribution between any nearest neighbor pair is given by $\mathcal{P}$ in the i.i.d model.

We can also define the average spectral density by doing the following integral:

$$\begin{aligned} \langle \rho(E) \rangle &= \int_{-\infty}^{\infty} dE_1 \cdots dE_N P(E_1, .., E_N) \sum_{m=0}^{N} \delta(E - E_m) \\ &= \delta(E - E_0) + \sum_{m=1}^{N} \int_{-\infty}^{\infty} dE_1 \cdots dE_N \prod_{k=1}^{N} \mathcal{P}(E_k - E_{k-1}) \delta(E - E_m). \end{aligned} \tag{3.10}$$

The averaged double spectral density is also another useful quantity defined by:

$$\begin{aligned} &\langle \rho(E)\rho(E') \rangle = \sum_{m=0}^{N} \sum_{p=0}^{N} \int_{-\infty}^{\infty} dE_1 \cdots dE_N P(E_1, .., E_N) \delta(E - E_m) \delta(E' - E_p) \\ &= \delta(E - E_0)\delta(E' - E_0) + \delta(E - E_0) \sum_{p=1}^{N} \int_{-\infty}^{\infty} dE_1 \cdots dE_N P(E_1, ..., E_N) \delta(E' - E_p) \\ &+ \delta(E' - E_0) \sum_{m=1}^{N} \int_{-\infty}^{\infty} dE_1 \cdots dE_N P(E_1, ..., E_N) \delta(E - E_m) \\ &+ \sum_{m=1}^{N} \sum_{p=1}^{N} \int_{-\infty}^{\infty} dE_1 \cdots dE_N P(E_1, ..., E_N) \delta(E - E_m) \delta(E' - E_p). \end{aligned} \tag{3.11}$$

[8]The result that the NNS distribution is equal to $\mathcal{P}$ relies on the assumption that $\mathcal{P}(x) = \Theta(x)\mathcal{P}(x)$ i.e. the probability distribution can only have non-zero support for non-negative x values, this allows us to know the ordering of the variables $E_0 \leq E_1 \leq \cdots \leq E_N$.

Using this we can also define the connected double spectral density given by:

$$\begin{aligned}
&\langle \rho(E)\rho(E')\rangle_{conn.} = \langle \rho(E)\rho(E')\rangle - \langle \rho(E)\rangle \langle \rho(E')\rangle \\
&= \sum_{m,p=1}^{N} \int_{-\infty}^{\infty} dE_1 \cdots dE_N P(E_1,..,E_N)\delta(E-E_m)\delta(E'-E_p) \\
&- \left[\sum_{m=1}^{N} \int_{-\infty}^{\infty} dE_1 \cdots dE_N P(E_1,..,E_N)\delta(E-E_m)\right]\left[\sum_{p=1}^{N} \int_{-\infty}^{\infty} dE_1 \cdots dE_N P(E_1,..,E_N)\delta(E'-E_p)\right].
\end{aligned} \tag{3.12}$$

3.2.2 Averaged Spectral Form Factor in the i.i.d Model

In this subsection, we will derive a closed form expression for the annealed averaged normalized spectral form factor associated with the type of spectrum we discussed in subsection 3.2.1. The normalized annealed averaged spectral form factor is given by the following expression:

$$\begin{aligned}
g(\beta,t) &= \frac{\langle \mathcal{Z}(\beta+it)\mathcal{Z}(\beta-it)\rangle}{\langle \mathcal{Z}(\beta)^2\rangle} \\
\mathcal{Z}(\beta \pm it) &= \sum_{n=0}^{N} e^{-(\beta \pm it)E_n}.
\end{aligned} \tag{3.13}$$

Following the derivation provided in Appendix B.1, we will find the following expression for the averaged spectral form factor[9]:

$$\begin{aligned}
&\langle \mathcal{Z}(\beta+it)\mathcal{Z}(\beta-it)\rangle = e^{-2\beta E_0}\left(1+\frac{b(1-b^N)}{1-b}+\frac{b^*(1-(b^*)^N)}{1-b^*}+B_1\right)\\
&= e^{-2\beta E_0}\left(\frac{1-a^{N+1}}{1-a}+\frac{b}{1-b}\left[\frac{a-b+a^{N+1}(b-1)+b^{N+1}(1-a)}{(1-a)(a-b)}\right]\right)\\
&+ e^{-2\beta E_0}\frac{b^*}{1-b^*}\left[\frac{a-b^*+a^{N+1}(b^*-1)+(b^*)^{N+1}(1-a)}{(1-a)(a-b^*)}\right]\\
&a = \langle e^{-2\beta\delta E}\rangle = \int_0^\infty \mathcal{P}(x)e^{-2\beta x}dx\\
&b = \langle e^{-(\beta+it)\delta E}\rangle = \int_0^\infty \mathcal{P}(x)e^{-(\beta+it)x}dx\\
&b^* = \langle e^{-(\beta-it)\delta E}\rangle = \int_0^\infty \mathcal{P}(x)e^{-(\beta-it)x}dx.
\end{aligned} \tag{3.14}$$

We can simplify the complicated expression under the assumption that $|a|<1$, $|b|<1$, and $N \gg 1$ (thermodynamic regime). In this case, at leading order, we ignore terms of the order $\mathcal{O}(a^N)$ and $\mathcal{O}(b^N)$ to obtain the following approximation for the normalized form factor:

$$\begin{aligned}
g(\beta,t) &\approx \frac{1+\frac{b}{1-b}+\frac{b^*}{1-b^*}}{1+\frac{2b_0}{1-b_0}}\\
b &= \int_0^\infty \mathcal{P}(x)e^{-(\beta+it)x}dx\\
b_0 &= \int_0^\infty \mathcal{P}(x)e^{-\beta x}.
\end{aligned} \tag{3.15}$$

Note that the approximation given in Eq. (3.15) is only expected to be useful at finite temperatures for sufficiently large values of N. It is expected to fail when $\beta = 0$. When $\beta = 0$ we formally take the limit of Eq. (3.14) above as $a \to 1$ to get the following

[9]Note, the expression for the form factor does not rely on the assumption of $\mathcal{P}$ begin zero for negative arguments. So in principle one could actually have $\mathcal{P}$ with support at negative values (you will just extend the lower limit of integration to $-\infty$ for the expressions describing the form factor) but then the interpretation of $\mathcal{P}$ being the NNS distribution is not as transparent. Although, we suspect that as long as $\mathcal{P}$ is an even function then it can still roughly be interpreted as the NNS distribution between eigenvalues in this model.

normalized average form factor at $\beta = 0$:

$$g(\beta = 0, t) = \frac{N + 1 + \left[\frac{b}{(1-b)^2}\left(b^{N+1} + N - b(N+1)\right) + \frac{b^*}{(1-b^*)^2}\left((b^*)^{N+1} + N - b^*(N+1)\right)\right]}{(N+1)^2}$$
$$b = \int_0^\infty \mathcal{P}(x) e^{-itx} dx$$
$$b^* = \int_0^\infty \mathcal{P}(x) e^{itx} dx. \tag{3.16}$$

In cases where b and b^* go to zero as $t \to \infty$ it is easy to see that[10]:

$$\lim_{t\to\infty} g(\beta = 0, t) = \frac{1}{N+1}. \tag{3.17}$$

At infinite temperature we identify the entropy as $S = \ln(N+1)$ and conclude that after a sufficiently long time, the infinite temperature averaged form factor will plateau toward a value e^{-S}. In a similar manner, we can approximate the expression for the large time value of the form factor (again we assume b and b^* vanish in the $t \to \infty$ limit) at finite temperature for large values of N using the approximation given in Eq. (3.15):

$$\lim_{t,N\to\infty} g(\beta, t) \approx \frac{1 - b_0}{1 + b_0} = \frac{1 - \int_0^\infty \mathcal{P}(x) e^{-\beta x} dx}{1 + \int_0^\infty \mathcal{P}(x) e^{-\beta x} dx}. \tag{3.18}$$

3.3 Spectral Form Factor of Common NNS Distributions

Thus far, we have proposed the i.i.d model for a random spectrum which involves specifying the NNS statistics of the system we are interested in modelling. In the following sections we will use the i.i.d model to compute the averaged spectral form factor associated with various choices of NNS statistics. In particular, we will investigate how well the i.i.d model (with a Wigner surmise NNS distribution) reproduces the features of the spectral form factor for Gaussian ensembles in Section 3.3.3. Aside from the more common NNS statistics that are found in integrable and quantum chaotic systems, we will also study generalizations of these statistics in Section 3.3.4 and explore how the behaviour of the form factor changes.

[10] In many of the examples we consider the assumption that b and b^* vanish in the large t limit will be valid. However, there are examples where the assumption fails. In Sec. 3.3.1 we have $\mathcal{P}(x)$ equal to a delta function, which results in an oscillating form factor that does not settle any particular value in the large t limit.

3.3.1 Delta Function (Non-Random Evenly Spaced Spectrum)

The most trivial spectrum that one can generate using the i.i.d model is an evenly spaced spectrum (with no degeneracy) where the NNS distribution is given by the Dirac delta distribution below:

$$\mathcal{P}(x = \delta E) = \delta(x - \Delta E), \tag{3.19}$$

where $\Delta E \geq 0$, in this case the integrals in Eq. (3.14) are simply given by[11]:

$$\begin{aligned} a &= e^{-2\beta\Delta E} \\ b &= e^{-\Delta E(\beta+it)} \\ b^* &= e^{-\Delta E(\beta-it)}. \end{aligned} \tag{3.20}$$

The normalized averaged spectral form factor equals:

$$\begin{aligned} g(\beta,t) &= \mathcal{N}\left[\frac{e^{2\beta\Delta E} + e^{-2N\beta\Delta E} - 2e^{-\beta(N-1)\Delta E}\cos((N+1)\Delta E t)}{1 + e^{2\beta\Delta E} - 2e^{\beta\Delta E}\cos(\Delta E t)}\right] \\ \mathcal{N} &= \frac{1 + e^{2\beta\Delta E} - 2e^{\beta\Delta E}}{e^{2\beta\Delta E} + e^{-2N\beta\Delta E} - 2e^{-\beta(N-1)\Delta E}}. \end{aligned} \tag{3.21}$$

In this case we can see from the expression above that the form factor is periodic with a period:

$$\tau = \frac{2\pi}{\Delta E}. \tag{3.22}$$

3.3.2 Poisson Distribution (Quantum Integrable Systems)

For sufficiently large diagonal matrices whose diagonal elements are i.i.d random variables, it is known that the NNS distribution of eigenvalues follows a Poisson distribution [6, 93]. Furthermore, the Poisson distribution also appears when studying the energy spacing statistics of a wide variety of integrable systems [22, 62, 16]. This gives us reason to consider the spectral form factor of a spectrum generated by the i.i.d model whose NNS distribution is given by the Poisson distribution[12]:

$$\mathcal{P}(x = \delta E) = \Theta(x)\frac{e^{-x/\sigma}}{\sigma}. \tag{3.23}$$

[11] It is clear from this that b and b^* do not go to zero in the large t limit this is an example in which the form factor does not plateau towards a fixed value.

[12] Usually one defines a dimensionless spacing $s = \delta E/\sigma$ and discusses NNS in terms of s rather than δE, but here we will work directly with δE and σ.

The average spacing between adjacent eigenvalues is given by $\langle \delta E \rangle = \sigma$.

We compute the integral expressions for a, b, b^*, they are given by:

$$\begin{aligned} a &= \frac{1}{1+2\beta\sigma} \\ b &= \frac{1}{1+\sigma\left(\beta+it\right)} \\ b^* &= \frac{1}{1+\sigma\left(\beta-it\right)}. \end{aligned} \tag{3.24}$$

Notice that, in this case b and b^* do go to zero in the limit as $t \to \infty$, this means that the normalized average spectral form factor at infinite temperature goes to $(N+1)^{-1}$. At infinite temperature the form factor is given as:

$$\begin{aligned} g(\beta = 0, t) &= \frac{1}{N+1} + \frac{2 - (1+ix)^{-N} - (1-ix)^{-N}}{(1+N)^2 x^2} \\ x &= t\sigma. \end{aligned} \tag{3.25}$$

For finite temperature, the expression for the form factor is not as simple - so we will not explicitly write it here. However, because $|b| < 1$ and $|a| < 1$ we can use the approximated form factor in the large N regime given by Eq. (3.15) to give a simple approximation for the form factor:

$$g(\beta, t) \approx \frac{1 + \frac{2\beta\sigma}{\sigma^2(\beta^2+t^2)}}{1+\frac{2}{\beta\sigma}}. \tag{3.26}$$

We compare the approximated expression for the form factor given in Eq. (3.26) to the full expression we have in Eq. (3.14) in Figure 3.2. We can see that for sufficiently large N the approximated expression converges toward the exact expression for the form factor. At lower temperatures, convergence will occur at smaller values of N. We also consider the averaged spectral form factor at various temperatures for a fixed value of $N = 100$ in Figure 3.3 [13]. The expression for the asymptotic value of the form factor is given by the

[13] One can check that similar looking plots can be made for higher and lower values of N.

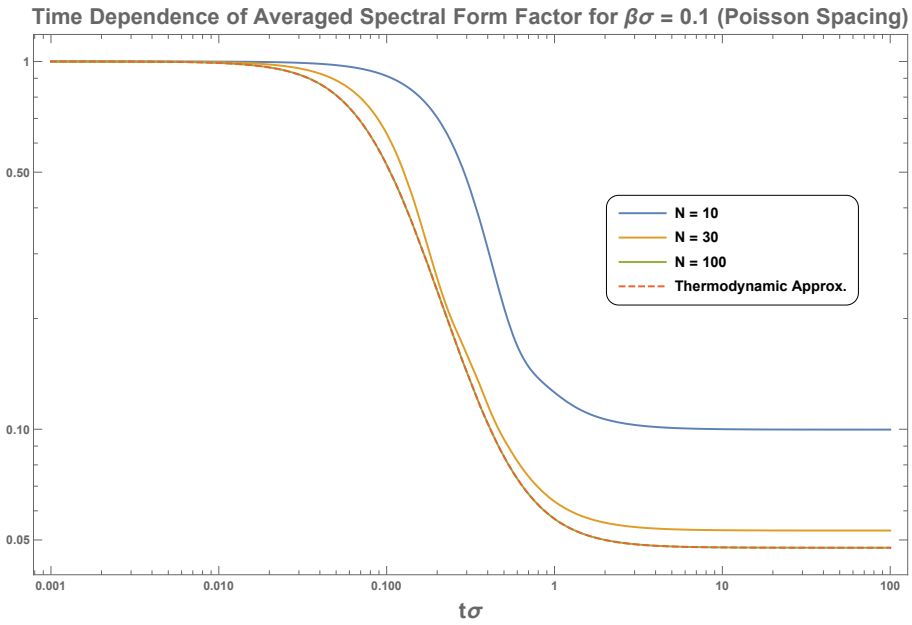

Figure 3.2: Above is a Log-Log plot of the averaged spectral form factor of a spectrum generated by the i.i.d model with Poisson NNS distribution given by Eq. (3.23). The temperature is fixed at $\beta\sigma = 0.1$ and we vary N. The plot illustrates how the form factors for larger values of N converge towards the thermodynamic approximation given in Eq. (3.26).

following expression:

$$\begin{aligned}\lim_{t\to\infty} g(\beta,t) &= \lim_{t\to\infty} \frac{\langle \mathcal{Z}(\beta+it)\mathcal{Z}(\beta-it)\rangle}{\langle \mathcal{Z}(\beta)^2\rangle} \\ &= \frac{\tilde{\beta}(1+\tilde{\beta})^N\left(\left(1+2\tilde{\beta}\right)^{N+1}-1\right)}{\left(1+\tilde{\beta}\right)^N\left(2+3\tilde{\beta}\right)+\left(1+2\tilde{\beta}\right)^{N+1}\left[\left(1+\tilde{\beta}\right)^N\left(2+\tilde{\beta}\right)-4\right]} \\ \tilde{\beta} &= \beta\sigma.\end{aligned} \tag{3.27}$$

We can see that the form factor decays from its initial normalized value towards a non-zero value given by Eq. (3.27). Another interesting point to make based on the plots we made is that the plateau phase occurs at a time scale $t \gtrsim \sigma^{-1} = \langle \delta E\rangle^{-1}$, where $\langle \delta E\rangle$ is the average spacing between eigenvalues.

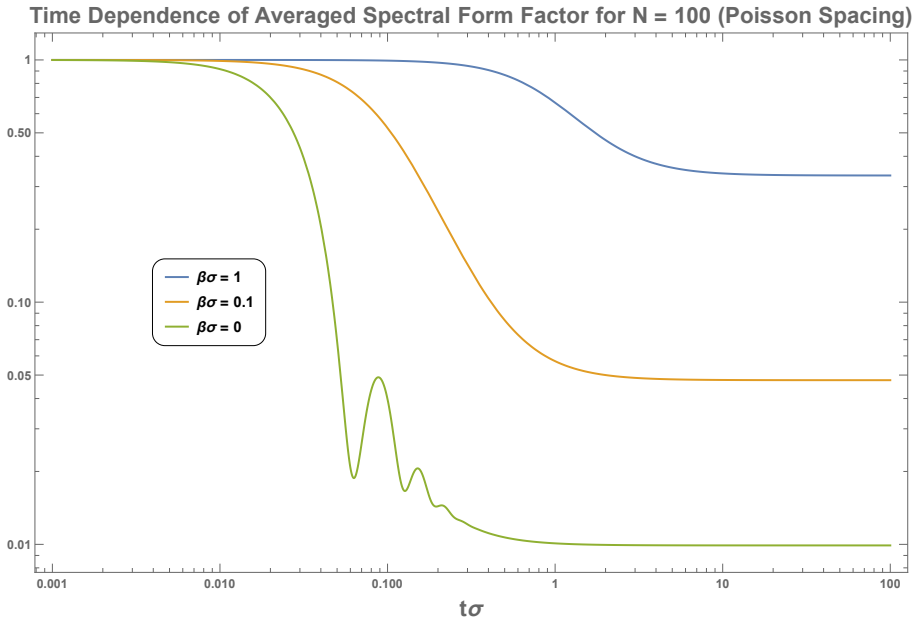

Figure 3.3: Above is a Log-Log plot of the averaged spectral form factor of a spectrum generated by the i.i.d model with Poisson NNS distribution given by Eq. (3.23). The value of N is fixed at $N = 100$ and the form factor is plotted for different temperatures ranging from $\beta\sigma = 0$ to $\beta\sigma = 1$.

At infinite temperature, we see oscillations, these are similar to the oscillations in the form factor discussed in [42] they arise at high temperatures due to the spectral edges of the spectral density[14].

It is possible to explicitly calculate the averaged spectral density in the i.i.d model with Poisson NNS statistics (details are given in Appendix B.2) it is given by the following expression:

$$\langle \rho(E) \rangle = \delta(E - E_0) + \sum_{m=1}^{N} \left[\frac{(E - E_0)^{m-1}}{\sigma^{m-1}(m-1)!} \right] \Theta(E - E_0) \frac{e^{-(E-E_0)/\sigma}}{\sigma}. \tag{3.28}$$

[14]One might wonder if these oscillations can be interpreted as "echoes." The answer to this is no because echoes should persist at lower temperatures as well.

We can rewrite the sum in terms of the incomplete gamma function as follows:

$$\begin{aligned}\langle\rho(E)\rangle &= \delta(E-E_0) + \frac{\Theta(E-E_0)}{\sigma}\frac{\Gamma\left(N, \frac{E-E_0}{\sigma}\right)}{\Gamma(N,0)} \\ \Gamma(N,x) &= \int_x^\infty t^{N-1}e^{-t}dt.\end{aligned} \tag{3.29}$$

By taking the derivatives of incomplete gamma function we can show that the function is monotonically decreasing and has an inflection point at $E - E_0 = (N-1)\sigma$. We expect the function to very slowly decrease up until one gets close to the inflection point. Then after the inflection point we expect the spectral density to be very small. In Figure 3.4 we plot the spectral density and verify this.

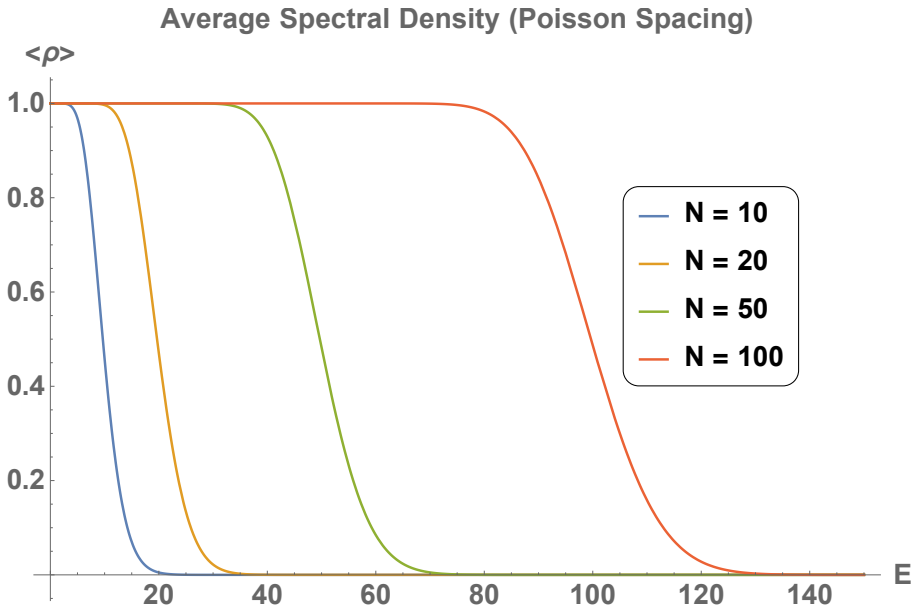

Figure 3.4: Above we plot the average spectral density of a random spectrum generated from the i.i.d. model using the Poisson NNS distribution defined in Eq. (3.23) (setting $\sigma = 1$ and $E_0 = 0$ and changing N). The averaged spectral density is given by Eq. (3.28). The width roughly scales with N.

Ignoring the delta function at $E = 0$, we can see the spectral density is approximately constant then quickly goes to zero near the inflection point. We can also see that as N increases the nearly constant phase is extended. The nearly constant phase can be regarded

as a natural consequence of the i.i.d spacing assumption in our model. We will generally expect that spectral densities generated by the i.i.d model will have an approximately constant portion far from the edges of the spectrum. We can also see that width of the density scales with N.

3.3.3 Wigner Surmise (Quantum Chaotic Systems)

In this section we will compute the spectral form factor in the i.i.d model when the NNS distribution is given by the Wigner surmise. The Wigner surmise is known to be a good approximation to the NNS distribution for classical Gaussian ensembles [62, 48, 93]. The Wigner surmise NNS distribution is defined below[15]:

$$\mathcal{P}_c(x = \delta E) = \Theta(x)\frac{2x^c}{\Gamma\left(\frac{1+c}{2}\right)}\frac{e^{-x^2/\sigma^2}}{\sigma^{c+1}}. \tag{3.30}$$

The value of c (sometimes called the Dyson index) depends on the type of Gaussian ensemble one wants to consider. In particular, the three main classical Gaussian ensembles are orthogonal ($c = 1$), unitary ($c = 2$), and symplectic ($c = 4$). In Figure 3.5 we plot the distributions for the three ensembles for $\sigma = 1$.

For the sake of simplicity we will mainly focus on the Gaussian unitary ensemble, $c = 2$[16]. In this case we will have the following NNS distribution:

$$\mathcal{P}_2(x = \delta E) = \Theta(x)\frac{4x^2}{\sigma^3\sqrt{\pi}}e^{-x^2/\sigma^2}. \tag{3.31}$$

The average spacing between adjacent eigenvalues is given by $\langle \delta E \rangle = \frac{2\sigma}{\sqrt{\pi}} \sim 1.1\sigma$.

The expressions for a, b, and b^* in this case are given by:

$$\begin{aligned}
a &= -\frac{2\beta\sigma}{\sqrt{\pi}} + e^{\beta^2\sigma^2}(1 + 2\beta^2\sigma^2)\left(1 - \mathrm{erf}(\beta\sigma)\right) \\
b &= -\frac{1}{2\sqrt{\pi}}\left[2\sigma(\beta + it) + \sqrt{\pi}e^{-\frac{-\sigma^2(t-i\beta)^2}{4}}\left(-2 + (t - i\beta)^2\sigma^2\right)\left(1 - \mathrm{erf}\left(\frac{1}{2}(\beta + it)\sigma\right)\right)\right] \\
b^* &= -\frac{1}{2\sqrt{\pi}}\left[2\sigma(\beta - it) + \sqrt{\pi}e^{-\frac{-\sigma^2(t+i\beta)^2}{4}}\left(-2 + (t + i\beta)^2\sigma^2\right)\left(1 - \mathrm{erf}\left(\frac{1}{2}(\beta - it)\sigma\right)\right)\right].
\end{aligned} \tag{3.32}$$

[15] The value of σ fixes the average spacing between eigenvalues and is usually chosen so that the spacing is unity. Just as in the Poisson spacing case we will not make assumptions on the value of σ and simply keep σ in our expressions.

[16] One can also easily do similar calculations for the other ensembles and get similar results.

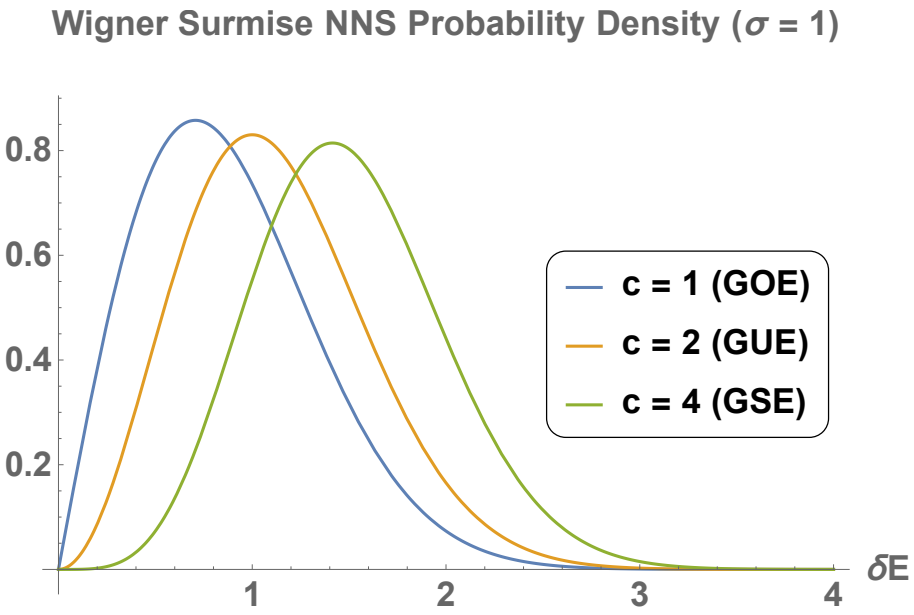

Figure 3.5: The Wigner surmise NNS distribution for three ensembles. The Gaussian orthogonal ensemble (GOE) occurs when $c = 1$. The Gaussian unitary ensemble (GUE) occurs when $c = 2$. The Gaussian symplectic ensemble (GSE) occurs when $c = 4$.

One can easily check that for $\beta > 0$ we have $|a| < 1$ and $|b| < 1$. This means that the thermodynamic approximation given by Eq. (3.15) will be valid for sufficiently large N at finite temperatures. Also, we can check that $\lim_{t\to\infty} b = 0$, which tells us that the asymptotic value of the form factor at infinite temperature is $(N+1)^{-1}$. We can plot the form factor to get a sense of the general features that appear for various choices of parameters.

In Figure 3.6, we compare the thermodynamic approximation given by Eq. (3.15) with the exact result given by Eq. (3.14). As expected, for sufficiently large N the thermodynamic approximation converges to the exact result, and one can further verify that for lower temperatures the convergence will occur more quickly at lower values of N.

In Figure 3.7, we plot the exact form factor for fixed N at different temperatures. We can see that the form factor initially decreases and eventually reaches a minimum value[17]. After reaching the minimum, in a time scale roughly given by $t \sim \langle \delta E \rangle^{-1}$, the form factor

[17] At high temperatures we see oscillations similar to what we saw for Poisson spacing, this is again due to the spectral edges being probed at high temperatures (not to be interpreted as "echoes").

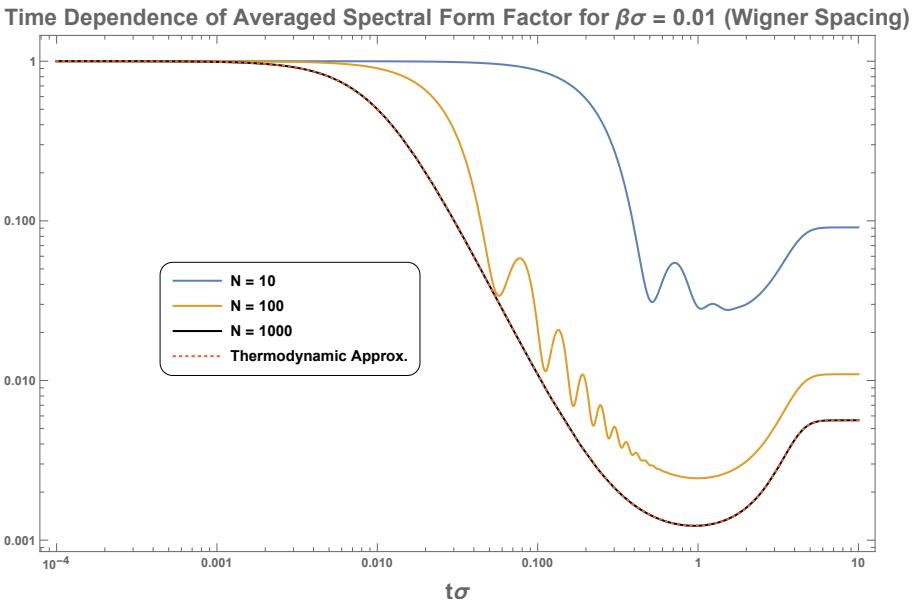

Figure 3.6: Above is a Log-Log plot of the averaged spectral form factor of a spectrum generated by the i.i.d model with Wigner surmise NNS distribution for the GUE given by Eq. (3.31). The temperature is fixed at $\beta\sigma = 0.01$ and we vary N.

increases along a "ramp" and finally plateaus toward an asymptotic value that is given by taking the $t \to \infty$ limit.

The ramp and plateau also appears in numerical calculations of the averaged form factor of the SYK model discussed in [42]. This occurs since the spectrum spacing statistics of the SYK model can be understood in terms of the spacing statistics of random matrices pulled from Gaussian ensembles. Although it is true that the form factors of the SYK and the classical Gaussian ensembles have many features in common, it is important to note that there are differences. One important distinction to make is the time scale over which the "ramp" begins to manifest in the form factor. In the case of the form factor generated by random matrices pulled from the GUE (and also our i.i.d. model see Appendix B.3) the beginning of the ramp occurs on time scales comparable to the Heisenberg time, which is $\mathcal{O}(\langle \delta E \rangle^{-1})$. This is in stark contrast to the SYK model where the ramp phase begins on time scales which are much shorter than the Heisenberg time[18].

[18] [13] estimates the ramp in the SYK form factor to start at times scales of the order $\mathcal{O}(N^{1/2}\ln(N))$. This is much shorter than the Heisenberg time for the SYK model which is of the order $\mathcal{O}(e^N)$ [14]. For more physical quantum chaotic theories, the time scale after which the universal ramp and plateau

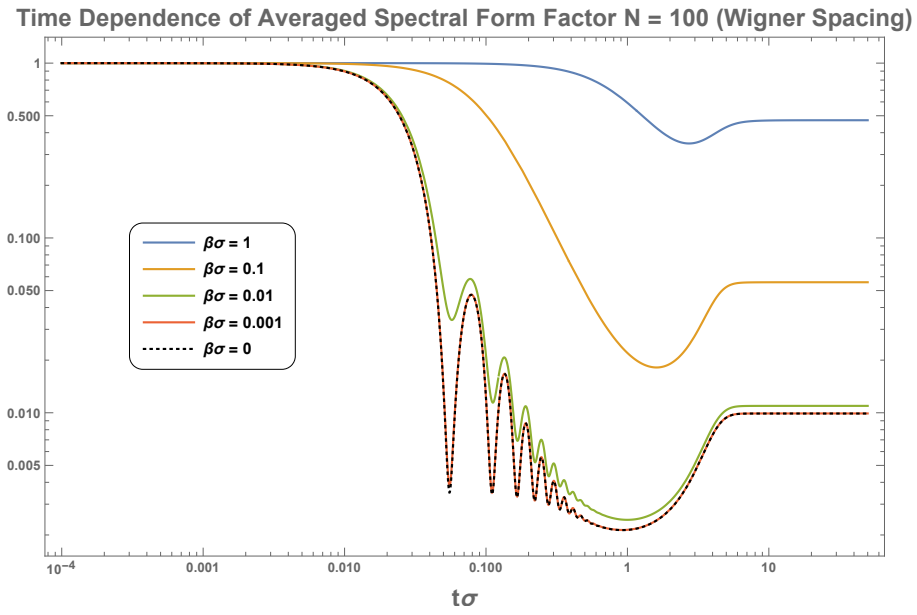

Figure 3.7: Above is a Log-Log plot of the averaged spectral form factor of a spectrum generated by the i.i.d model with Wigner surmise NNS distribution for the GUE given by Eq. (3.31). We fixed the value of $N = 100$ and plot the averaged form factor for different temperatures.

In Appendix B.3, we do a numerical study which compares the form factor generated by eigenvalues from a Hermitian random matrix to the form factor of a random spectrum generated by the i.i.d model with Wigner surmise NNS distribution. We show that if one focuses on the eigenvalues near the centre of the spectrum then our model is in reasonable agreement with actual numerical computations of the form factor associated with the truncated spectrum near the centre of the spectral density.

It is not possible to get a closed form expression for the spectral density when we have Wigner surmise spacings. However, we can numerically compute the averaged spectral density by generating a large number of eigenvalues from the i.i.d model for Wigner surmise spacing. As an example, in Figure 3.8, we generate a histogram from the eigenvalues generated by the i.i.d model for 10^4 samples with each sample having 100 eigenvalues (for simplicity we set $\sigma = 1$ and $E_0 = 0$). Unsurprisingly, we find that the density away from the edges is approximately constant and similar to the Poisson case. However, it

manifest , the so-called "Thouless time", is *not* universal (i.e. it changes depending on the model and the observable. We thank Julian Sonner for pointing this out).

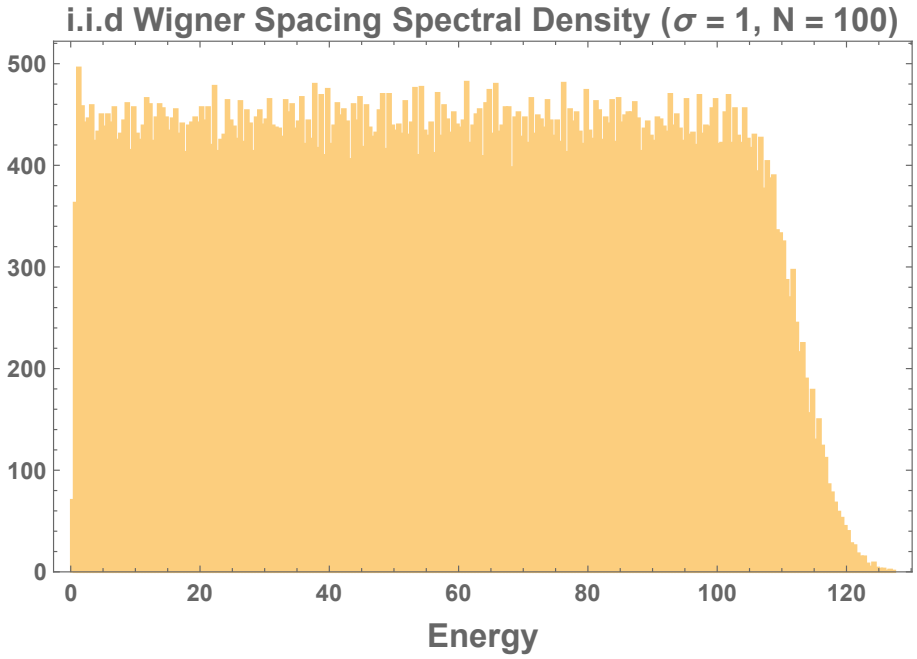

Figure 3.8: Above is a histogram of eigenvalues generated by the i.i.d model for 100 eigenvalues (excluding the ground state at $E = 0$) defined in Eq. (3.5). The NNS distribution is given by Eq. (3.31) with $\sigma = 1$. We expect the width of the spectral density to scale with N.

will differ from the Poisson density near the ground state where it will be zero due to the repulsion between the ground state and the rest of the excited states (Poisson case exhibits "attraction toward the ground state"). Another important point to make is that the averaged spectral density of the spectrum generated by the i.i.d model is not the semi-circle as it is for classical Guassian ensembles (e.g., see Figure B.1). This is not surprising since our model only captures correlations between nearest neighbors and not the longer range correlations that conspire to give the semi-circle. Nonetheless, the i.i.d model still captures the general features of the ramp and plateau in the averaged form factor.

In the next subsection, we will introduce a new NNS distribution which retains the interesting features of the Wigner surmise (i.e. repulsion in NNS statistics) but will be easier to analytically handle in our model when computing the averaged spectral density in the i.i.d model. We will also discuss generalizations of classical Gaussian ensembles and how the late time behaviour of the form factor of such ensembles differ from the usual ramp and plateau behaviour of the form factor of classical Gaussian ensembles.

3.3.4 Form Factor of Gamma NNS Distribution and β-Ensembles

In the previous subsection, we looked at the Wigner surmise as a canonical example of what the NNS distribution of eigenvalues of a chaotic system looks like. Although we are able to compute the form factor, many other quantities of interest such as the spectral density are difficult to compute in closed form. This is primarily due to the e^{-x^2} in the NNS density makes the integrals in Eq. (3.10) difficult to compute. To facilitate more explicit calculations - while still retaining the essential repulsion between eigenvalues - we will consider a slightly different NNS distribution. We define the gamma distribution for NNS:

$$\mathcal{P}_q(x = \delta E) = \Theta(x)\frac{x^q e^{-x/\sigma}}{\Gamma(1+q)\sigma^{1+q}}. \tag{3.33}$$

The value of q (plays the role of the Dyson index in the Wigner surmise) fixes the degree of repulsion between eigenvalues. For a fixed value of q, σ fixes the average spacing between nearest neighbor pairs to $\langle \delta E \rangle = (1+q)\sigma$.

At leading order, it is clear that such a distribution will contain the same repulsion behaviour near zero spacing as the Wigner surmise with c in Eq. (3.30) identified with q in Eq. (3.33). The major difference being the tail; the Wigner surmise has a Gaussian tail whereas the gamma distribution has an exponentially decaying tail. The advantage to using this is that it still contains the important repulsion of a chaotic system for any $q > 0$. Furthermore, due to the exponential tail of the gamma function the spectral density can be computed exactly.

We begin by computing the necessary integrals that define the averaged form factor in the i.i.d model:

$$\begin{aligned} a &= (1+2\beta\sigma)^{-(1+q)} \\ b &= (1+\sigma(\beta+it))^{-(1+q)} \\ b^* &= (1+\sigma(\beta-it))^{-(1+q)}\,. \end{aligned} \tag{3.34}$$

We can clearly see that $|a|, |b| < 1$ at finite temperature for $q \geq 0$, therefore in the large N regime we can use the thermodynamic expression of the form factor given in Eq. (3.15). We find:

$$g(t,\beta) \approx \frac{(1+\beta\sigma)^{q+1}-1}{(1+\beta\sigma)^{q+1}+1}\left[1 + \frac{1}{[1+\sigma(\beta+it)]^{q+1}-1} + \frac{1}{([1+\sigma(\beta-it)]^{q+1}-1}\right]. \tag{3.35}$$

The plateau at sufficiently large N and finite temperature regime has an approximate

height equal to:

$$\lim_{t\to\infty} g(t,\beta) \approx \frac{(1+\beta\sigma)^{q+1}-1}{(1+\beta\sigma)^{q+1}+1}. \tag{3.36}$$

We plot the averaged form factor in the i.i.d model using Eq. (3.14) for various choices of parameters.

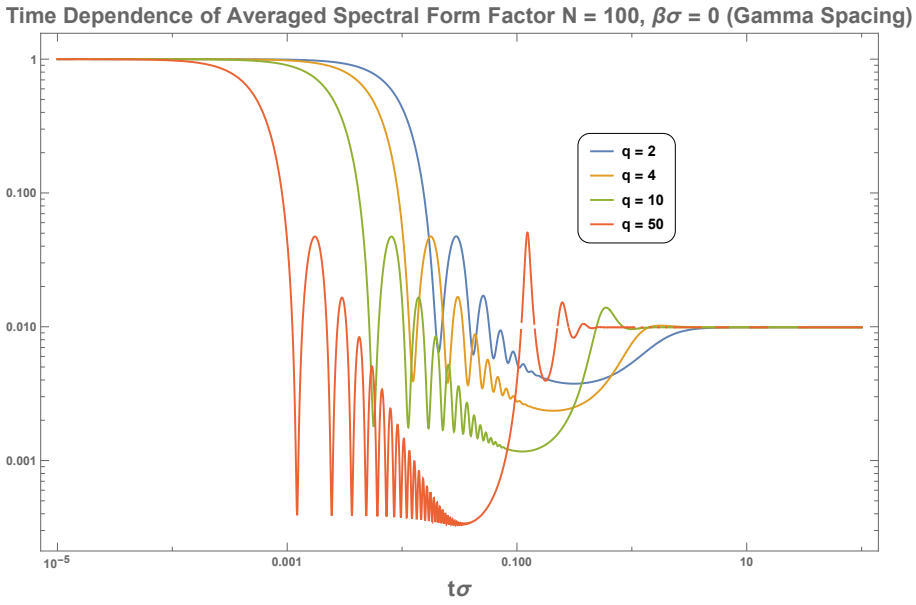

Figure 3.9: Above is a Log-Log plot of the averaged spectral form factor at, infinite temperature, for a spectrum generated by the i.i.d model with a NNS distribution given by the gamma distribution defined in Eq. (3.33). The value of N is fixed and the form factor is plotted for different values of q. The energy scale, σ, is related to the average energy spacing between nearest neighbor eigenvalues, $\langle \delta E \rangle$, through the following relation $\langle \delta E \rangle = (q+1)\sigma$.

In Figure 3.9, we plot the averaged form factor at infinite temperature with $N = 100$ and vary q. At lower values of $q > 1$, we still see that ramp and plateau (like the Wigner surmise), however as we increase the value of q we start to see oscillations after the initial dip before saturation to the plateau. In Figure 3.10, we verify that these late time oscillations, at large q persist at lower temperatures with the period roughly being the same as the temperature varies.

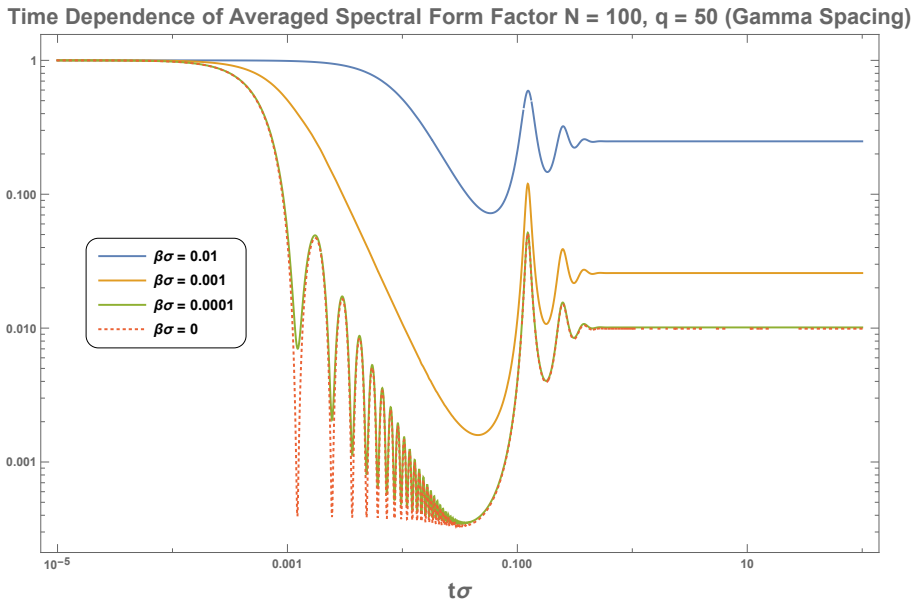

Figure 3.10: Above is a Log-Log plot of the averaged spectral form factor at, for a spectrum generated by the i.i.d model with a NNS distribution given by the gamma distribution defined in Eq. (3.33). In this plot $q = 50$ and $N = 100$ are fixed and the temperature is varied. The energy scale, σ, is related to the average energy spacing between nearest neighbor eigenvalues, $\langle \delta E \rangle$, through the following relation $\langle \delta E \rangle = (q+1)\sigma$.

The existence of these oscillations for larger values of q can be attributed to the NNS distribution localizing far from the origin and forming a substantial "gap" between the origin and the main distribution. One can check that the form factor of any system that has NNS density with a large gap will exhibit oscillations (although depending on the details of the NNS distribution the shape of the oscillations as well has how long they persist will vary). In particular, if one allows the Dyson index, c, in Eq. (3.30) to be sufficiently large one can also check that similar oscillations will arise for the Wigner surmise.

It is also useful to compare the averaged form factor with the form factor of a single sample in our model. In Figure 3.11, we can see that the regular late time oscillations are not self averaging. This is similar to the nature of the ramp and plateau behaviour studied in form factors of Gaussian ensembles [42]. The ramp and plateau manifest most clearly after averaging over many samples but is more difficult to ascertain when one analyzes only a single sample.

Due to the simple expression of the form factor in the large N and finite temperature

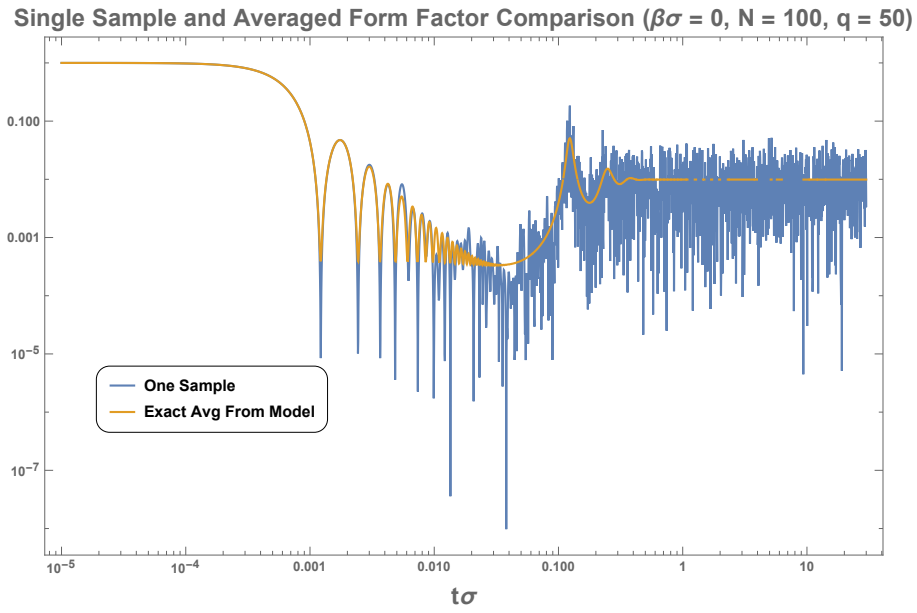

Figure 3.11: Above is a Log-Log plot that compares the spectral form factor of a single sample (blue curve), and the averaged form factor (yellow curve) from the i.i.d model with gamma distribution spacing defined in Eq. (3.33), with $q = 50$, $N = 100$, and $\beta\sigma = 0$.

regime it is possible to get a sense of where the oscillations occur by finding local extrema. By taking the first derivative of the expression in Eq. (3.35) and setting it to zero we find the following condition:

$$\begin{aligned} &\frac{z^q}{\left[z^{q+1}-1\right]^2} = \frac{(z^*)^q}{\left[(z^*)^{q+1}-1\right]^2} \\ &z = 1+\sigma(\beta+it) \\ &z^* = 1+\sigma(\beta-it). \end{aligned} \tag{3.37}$$

In general, the solution to this equation cannot be found exactly (in Appendix B.4 we discuss the special cases when $q = 1, 2, 4$ where exact solutions can be found). In the $q \gg 1$ regime it can be argued (see Appendix B.4 for the argument) that the period of the visible oscillations in the form factor will roughly be given by:

$$\tau \approx \frac{2\pi(1+\beta\sigma)}{q\sigma} \approx \frac{2\pi(1+\beta\sigma)}{\langle\delta E\rangle} \approx \begin{cases} \frac{2\pi}{\langle\delta E\rangle}, & \beta\sigma \ll 1 \\ \frac{2\pi\beta\sigma}{\langle\delta E\rangle}, & \beta\sigma \gg 1 \end{cases} . \tag{3.38}$$

Above, we used that the average spacing between adjacent energy levels in our model is $\langle \delta E \rangle = (q+1)\sigma \approx q\sigma$.

Now that we have discussed the general features of the form factor we consider the averaged spectral density - which is given by (see Appendix B.5 for details of the calculation):

$$\langle \rho(E) \rangle = \delta(E - E_0) + \frac{1}{\sigma} \sum_{m=1}^{N} \left[\frac{(E-E_0)^{mq+m-1}}{\Gamma\left[m(1+q)\right] \sigma^{m(1+q)-1}} \right] \Theta(E-E_0) e^{-(E-E_0)/\sigma}. \tag{3.39}$$

Ignoring the delta function at the ground state, we can see the left most edge of the spectral density near $E = E_0$ is dominated by the first term in the sum over m and vanishes at zero. To get an estimate for how wide the spectral density is, we analyze the $m = N$ term in the sum. This will give us a rough sense of what the tail of the spectral density looks like:

$$\langle \rho_{tail}(E) \rangle \approx \frac{e^{-(E-E_0)/\sigma}}{\sigma \Gamma(N(1+q))} \left(\frac{E-E_0}{\sigma} \right)^{N(1+q)-1}. \tag{3.40}$$

This function will give a bell shaped curve. We will be interested in the right most inflection point of the bell curve to give us an idea of where the edge of the spectral density is. This involves solving $\frac{d^2}{dE^2} \rho_{tail}(E) = 0$ which yields a simple quadratic equation. The larger root gives us an estimate for where the right edge of the spectral density is:

$$\frac{E_{edge} - E_0}{\sigma} = N(1+q) - 1 + \sqrt{N(1+q) - 1}. \tag{3.41}$$

So, for $N \gg 1$ and $q \geq 1$, the width of the spectral density roughly scales as $N(q+1)$. In Figure 3.12 we can verify these findings by a simple plot of the spectral density with $\sigma = 1$ and $N = 20$ for various values of q. We can see that for larger values of q the low energy part of the spectrum exhibits visible oscillations. This is due to the fact that there is little overlap between the lower m terms that make up the spectral density. A straightforward calculation of the local maximum of each term reveals that the distance between the visible local maxima is roughly $q+1$.

It is interesting to ask what type of random matrix ensembles give rise to NNS statistics with a more general Dyson index. One answer to this question can be found in the study of "β-ensembles" which are discussed in [46]. These ensembles have been shown to arise

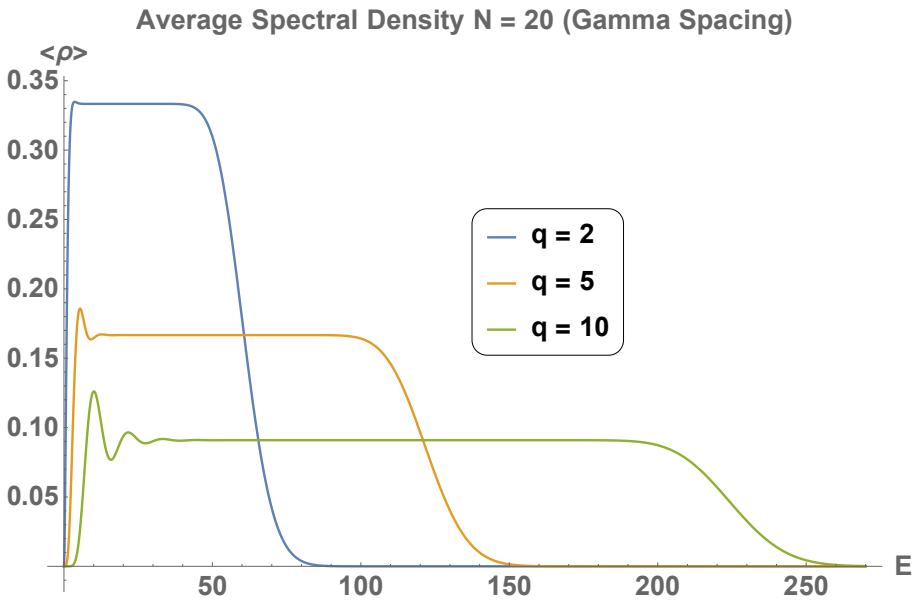

Figure 3.12: The above plot depicts the averaged spectral density in Eq. (3.39). We fix $N = 20$ and plot the density at various values of q (we set $\sigma = 1$ and $E_0 = 0$). The width the spectrum roughly scales as $N(q+1)$ for $N \gg 1$.

from $N \times N$ tri-diagonal random matrices of the form[19]:

$$H_\beta = \frac{1}{\sqrt{2}} \begin{bmatrix} N(0,2) & \chi_{(N-1)\beta} & 0 & 0 & \cdots & 0 \\ \chi_{(N-1)\beta} & N(0,2) & \chi_{(N-2)\beta} & 0 & \ddots & \vdots \\ 0 & \chi_{(N-2)\beta} & N(0,2) & \ddots & \ddots & 0 \\ 0 & 0 & \ddots & \ddots & \chi_{2\beta} & 0 \\ \vdots & \ddots & \ddots & \chi_{2\beta} & N(0,2) & \chi_\beta \\ 0 & \cdots & 0 & 0 & \chi_\beta & N(0,2) \end{bmatrix}, \tag{3.42}$$

where $N(0,2)$ denotes random real variables pulled from a normal distribution with variance of 2 and mean of 0. The χ_m denotes positive real random variables pulled from the Chi-distribution with m degrees of freedom[20]. It can be proved that the joint eigenvalue

[19]Note: β is not the temperature in this context. It is a parameter that plays the role of the Dyson index in the usual classical Gaussian ensembles.

[20]A random variable y following the Chi-distribution with m degrees of freedom has a probability density function given by $\chi_m(y) = \Theta(y)\frac{2}{\Gamma(m/2)} y^{m-1} e^{-y^2}$.

density (up to a normalization constant) of these matrices is given by:

$$P_\beta(\lambda) \sim \prod_{i<j} |\lambda_i - \lambda_j|^\beta \, e^{-\sum_i \lambda_i^2/2}. \tag{3.43}$$

The joint eigenvalue density for the classical Gaussian ensembles are reproduced when $\beta = 1, 2, 4$ - but more general values of β can also occur[21]. Since β controls the degree of repulsion between eigenvalues, it seems reasonable to identify it with the Dyson index, c, in the Wigner surmise for NNS distribution. This conjecture was explored numerically in [89], where it was found that a (generalized) gamma distribution provided reasonable approximation to the NNS distribution of β-ensembles. Based on the results we obtained using the i.i.d model in this section, we suggest that with sufficiently large values of β (here β is not inverse temperature it is the Dyson index which labels the β-ensemble) the form factor of β-ensembles will have late time oscillations in the ensemble averaged form factor.

In the next subsection, we briefly explore a class of simple oscillator systems that demonstrate sharp gaps in the NNS statistics. In these systems one can also see regular decaying oscillations in the late time behaviour similar to the ones we studied here.

3.3.5 Chaotic Perturbation of a Harmonic Oscillator

One concrete example of a class of systems that have large gaps in the NNS distribution are interacting oscillator systems whose Hamiltonian may be written in the form:

$$\mathcal{H} = \mathcal{H}_0 + \lambda \mathcal{H}_{chaos}, \tag{3.44}$$

where $\mathcal{H}_0$ is a Hamiltonian with a regularly spaced spectrum. $\mathcal{H}_{chaos}$ is a chaotic Hamiltonian in the sense that the NNS statistics of the eigenvalues of $\mathcal{H}_{chaos}$ obey a Wigner surmise type distribution. The parameter λ controls the relative strength of the two terms.

One familiar example of a system that has an evenly spaced spectrum is the one dimensional Harmonic oscillator vibrating at a frequency ω_0. The introduction of the a chaotic term in such a scenario would be analogous to adding an additional potential term in the Hamiltonian which generates chaotic dynamics. Concretely, we write:

$$\mathcal{H} = \omega_0 \mathcal{H}_0 + \epsilon \mathcal{H}_{chaos}, \tag{3.45}$$

[21] It was shown in [46] that the matrices in the classical Gaussian ensembles can be written in the tridiagonal form. For example, a matrix pulled from the GOE ensemble can be tridiagonalized and the matrix will belong to a "$\beta = 1$-ensemble."

where ω_0 is some characteristic energy scale of the unperturbed oscillator and ϵ is a characteristic energy scale for the chaotic Hamiltonian. In terms of matrices we let $\mathcal{H}_0$ be an $N \times N$ diagonal matrix with entries $(\mathcal{H}_0)_{ij} = N^{-1}(i-1)\delta_{ij}$ (we choose to normalize by N so that the width of the unperturbed spectrum does not change). We model $\mathcal{H}_{chaos}$ using a random matrix. Roughly speaking, the NNS distribution between adjacent eigenvalues will be delta functions when $\epsilon = 0$ once the chaotic term is turned on we will expect the delta functions to broaden and look similar to a kind of translated Wigner surmise. This results in a large gap in the NNS distribution which would lead to oscillations in the form factor. To get approximation for what the NNS distribution might look like, it is useful to compute the NNS distribution for 2×2 matrices. This is a straightforward exercise which is done explicitly in Appendix B.6, the final result is given by:

$$\mathcal{P}(s) = \frac{s}{\sqrt{\pi}\epsilon\omega_0}\left(e^{\frac{\omega_0 s}{2\epsilon^2}} - 1\right) e^{-\left(\frac{2s+\omega_0}{4\epsilon}\right)^2}. \tag{3.46}$$

Using the i.i.d model with the NNS distribution given by Eq. (3.46) we can compute the form factor. Figure 3.13 plots the form factor at infinite temperature for various choices of ϵ/ω_0.

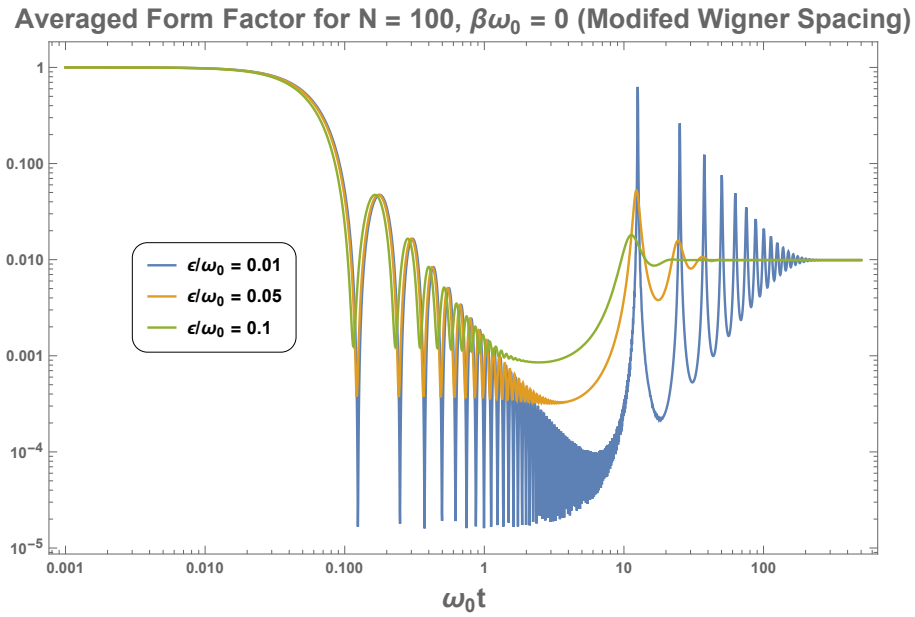

Figure 3.13: Above is a plot of the infinite temperature average form factor of a spectrum generated by our i.i.d model ($N = 100$) with the NNS distribution (modified Wigner surmise) given in Eq. (3.46) for various choices of the dimensionless ratio ϵ/ω_0.

We can see that oscillations appear for smaller values of ϵ/ω_0 and begin to go away as the chaotic term becomes larger. The decay of the oscillations occur due to the random chaotic term in the Hamiltonian. In this scenario the parameter ω_0/ϵ characterizes the sharpness and size of the gap in the NNS distribution. Using the results we found in the previous subsection for gamma NNS statistics, we expect the period of the oscillations in the form factor in the $\epsilon/\omega_0 \ll 1$ regime to be approximated by:

$$\tau \approx \frac{2\pi(1+\beta\omega_0)}{\langle \delta E \rangle} \approx \frac{4\pi(1+\beta\omega_0)}{\omega_0}, \tag{3.47}$$

where we used the fact that $\langle \delta E \rangle \approx \omega_0/2$ when $\epsilon/\omega_0 \ll 1$.

3.4 Systems with Self-Averaging Oscillations in the Form Factor (Echoes)

In the previous section, we studied features of the averaged form factor and spectral densities associated with different choices of NNS distributions using the i.i.d model. For the i.i.d. model of random spectra we generally found that the spectral form factor decays until a time scale roughly given by $t \sim \langle \delta E \rangle^{-1}$, where $\langle \delta E \rangle$ is the average nearest neighbor spacing between eigenvalues. At time scales $t \ll \langle \delta E \rangle^{-1}$ the spectral density can be approximated as smooth and gives rise to self averaging behaviour at early times. After this time scale, the discreteness of the system manifests and the form factor is no longer self averaging. The averaged late time behaviour over many samples depends on the details of the NNS distribution for the eigenvalues of the system. From the examples we studied, we had three classes of behaviour after the initial dip:

1. Continues to decrease and plateaus to a value (e.g., Poisson NNS where eigenvalues exhibit "attraction").

2. Increases for a duration of time along a "ramp" followed by a plateau (e.g., Wigner surmise NNS where eigenvalues exhibit "repulsion").

3. Increases and exhibits damped oscillations toward a plateau value (e.g., large q gamma NNS where the eigenvalues exhibit "enhanced" repulsion resulting in large/sharp gaps between adjacent eigenvalues).

Case 1 describes the NNS statistics of generic quantum integrable systems and has no "ramp" in the form factor [22]. Case 2 describes NNS statistics of quantum chaotic systems whose spectral form factors contain a "ramp." In both these cases, we can see that there are no regular oscillations. In Case 3, there are oscillations in the averaged spectral form factor. These oscillations, however, occur in the late time behaviour of the form factor when it is no longer self-averaging (e.g., Figure 3.11). Furthermore, the time scale over which these oscillations manifest are of the order of the Heisenberg time, $\langle \delta E \rangle^{-1}$. In the context of black holes one usually regards the energy spacing between black hole microstates to be of the order e^{-S}. This gives a Heisenberg time of the order e^{S}. So if we want to interpret the late time oscillations as echoes then we would have to wait a time scale of the order of the Heisenberg time which is extremely long for a macroscopic black hole and for practical purposes unobservable[23].

In this section, we shall revisit one of the key assumption of Sections 3.2 and 3.3, i.e. that the NNS distribution are independent identically distributed (i.i.d). As an example, the i.i.d assumption can be significantly violated if there are approximate degeneracies in the spectrum - causing many states to cluster around the same value while also being widely separated from other clusters of states. An example of this phenomenon is the hydrogen atom, where the splitting of degenerate states is controlled by the fine structure constant, α. We can see that the assumption of "independent-identically-distributed" is not valid anymore, as the energy spacing is different by a factor of α, depending on whether states belong to the same, or a different degenerate sub-sector. We shall see that this structure can also lead to self-averaging oscillations in the spectral form factor. What one needs is to have an averaged spectral density that contains regularly spaced "spikes" (or near-degenerate sub-sectors). The introduction of random interactions (regardless of how small) will generally lead to chaotic level splittings (a broadening of the "spikes") within each degenerate sub-sector. We will discuss one simple but explicit example in the following subsection which illustrates this.

[22] Systems with constant energy spacings, such as harmonic oscillator are exceptions. Such systems have form factors that oscillate forever and never saturate to a particular value.

[23] There might be a "caveat" to these findings. In particular, we only discussed the late time oscillations in the context of the i.i.d. model. If we decided to use the i.i.d. model (with Wigner surmise spacing) to describe the spectrum of the SYK model we would correctly predict the existence of a ramp and plateau at late times. However, we would fail in predicting the time scale when the ramp would start, i.e. the Thouless time. In the same manner, just because the i.i.d. model predicts late time oscillations to manifest on time scales of the order of the Heisenberg time, it does not rule out the possibility of having a theory where the form factor exhibits late time oscillations on much shorter time scales which could potentially be observable in experiments.

3.4.1 Randomly Coupled Identical Fermionic Oscillators

In this subsection, we will analyze a system of $N/2$ Fermionic oscillators (N is even) which are coupled by a random matrix pulled from the GUE [24].

The Hamiltonian describing $N/2$ uncoupled Fermionic oscillators, which we denote as $\mathcal{H}_{FHO}$, can be written as:

$$\mathcal{H}_{FHO} = \frac{1}{2}\sum_{k=1}^{N/2} \omega_k [b_k^\dagger, b_k], \tag{3.48}$$

where b_k and $b_k^\dagger$ are operators which satisfy the anti-commutation relations, $\{b_k, b_l^\dagger\} = \delta_{kl}$, $\{b_k, b_l\} = \{b_k^\dagger, b_l^\dagger\} = 0$, and ω_k is the frequency of oscillation of the k-th oscillator (set $\hbar = 1$). Before analyzing the effect of the GUE coupling we review the eigenstates of $\mathcal{H}_{FHO}$.

We denote the ground state of the FHO Hamiltonian as $|0\rangle$, it satisfies the following identity:

$$b_k |0\rangle = 0. \tag{3.49}$$

The operators b_k and $b_k^\dagger$ play the role of annihilation and creation operators respectively. We can check that the following identities are true:

$$\begin{aligned} \left[\mathcal{H}_{FHO}, b_k^\dagger\right] &= \omega_k b_k^\dagger \\ [\mathcal{H}_{FHO}, b_k] &= -\omega_k b_k. \end{aligned} \tag{3.50}$$

We can create any state in the Fock space by starting with the ground state and acting with the creation and annihilation operators. There are exactly $2^{N/2}$ distinct states in the Hilbert space since we can only act once on the ground state using $b_k^\dagger$ for a particular k. These states (by convention) can be written as:

$$|\vec{n}\rangle = |n_1, n_2, ..., n_{N/2}\rangle = \left(b_1^\dagger\right)^{n_1} \left(b_2^\dagger\right)^{n_2} \cdots \left(b_{N/2}^\dagger\right)^{n_{N/2}} |0\rangle\,, \tag{3.51}$$

where $n_1, .., n_{N/2} = 0$ or 1 (we define $\left(b_k^\dagger\right)^0 = \mathcal{I}$, the identity operator). When we act with

[24] Although we choose to work with fermionic oscillators, similar techniques can also be used to model a system of bosonic oscillators. We primarily choose fermionic degrees of freedom since they can be discussed in the context of the SYK model (a toy model describing the near horizon dynamics of extremal black holes) where the eigenstates of fermionic oscillator are the pure states studied in [81]. Furthermore, eigenstates can also be mapped to binary strings making this an interesting "qubit" model.

a creation operator we find that:

$$\begin{aligned} b_k^\dagger \left|n_1, n_2, ..n_k.., n_{N/2}\right\rangle &= b_k^\dagger \left(b_1^\dagger\right)^{n_1} \left(b_2^\dagger\right)^{n_2} \cdot\cdot \left(b_k^\dagger\right)^{n_k} \cdot\cdot \left(b_{N/2}^\dagger\right)^{n_{N/2}} |0\rangle \\ &= (-1)^{\sigma_k} \delta_{0,n_k} \left|n_1, n_2, .., n_k + 1, .., n_{N/2}\right\rangle , \end{aligned} \tag{3.52}$$

where $\sigma_k = \sum_{i=1}^{k-1} n_i$. Similarly acting with an annihilation operator gives:

$$\begin{aligned} b_k \left|n_1, n_2, ..n_k.., n_{N/2}\right\rangle &= b_k \left(b_1^\dagger\right)^{n_1} \left(b_2^\dagger\right)^{n_2} \cdot\cdot \left(b_k^\dagger\right)^{n_k} \cdot\cdot \left(b_{N/2}^\dagger\right)^{n_{N/2}} |0\rangle \\ &= (-1)^{\sigma_k} \delta_{1,n_k} \left|n_1, n_2, .., n_k - 1, .., n_{N/2}\right\rangle . \end{aligned} \tag{3.53}$$

We define the k-th number operator $\mathcal{N}_k$ as:

$$\begin{aligned} \mathcal{N}_k &= b_k^\dagger b_k \\ \mathcal{N}_k \left|\vec{n}\right\rangle &= n_k \left|\vec{n}\right\rangle . \end{aligned} \tag{3.54}$$

This means the Fock states are eigenstates of the number operator and since the Hamiltonian can also be written in terms of the number operator the Fock states diagonalize the Hamiltonian. In particular, we have:

$$\begin{aligned} \mathcal{H}_{FHO} &= \frac{1}{2} \sum_{k=1}^{N/2} \omega_k \left(2\mathcal{N}_k - 1\right) \\ \Rightarrow \mathcal{H}_{FHO} \left|\vec{n}\right\rangle &= \frac{1}{2} \sum_{k=1}^{N/2} \omega_k (2n_k - 1) \left|\vec{n}\right\rangle . \end{aligned} \tag{3.55}$$

To simplify our considerations we will set $\omega_k = \omega_0$ for all k - sometimes referred to as a mass term. In this case, we will have a regularly spaced spectrum which is easy to analyze. We define $p = 0, 1, 2, .., N/2$ as the number of "occupied" sites for a particular state (i.e. the number of 1s in the ket). Then the energy of such a state is given by:

$$E(p) = \omega_0 \left(p - \frac{N}{4}\right) . \tag{3.56}$$

The number of microstates with the energy $E(p)$ is given by:

$$\Omega(p) = \frac{(N/2)!}{p!(N/2 - p)!}. \tag{3.57}$$

Using these results we can find the canonical partition function for the system given by:

$$\mathcal{Z}(\beta) = \sum_{p=0}^{N/2} \Omega(p) e^{-\beta E(p)} = e^{\frac{N\beta\omega_0}{4}} \left[1 + e^{-\beta\omega_0}\right]^{N/2} = \left[2\cosh\left(\frac{\beta\omega_0}{2}\right)\right]^{N/2}. \tag{3.58}$$

The spectral form factor for this system will oscillate with a period given by:

$$\tau = \frac{2\pi}{\omega_0}. \tag{3.59}$$

Now that we have discussed the details of the FHO, we address what happens when we add a random chaotic coupling. In particular, we will consider:

$$\mathcal{H} = \mathcal{H}_{FHO} + \epsilon \mathcal{H}_{chaos}. \tag{3.60}$$

We know that the unperturbed energies are given by Eq. (3.56) and we know that these energies are degenerate. We will label each degenerate sector by p, which is equal to the number of occupied sites. We define the degenerate eigenstates in the p-th degenerate sector as $\{|\vec{n}_p\rangle\}_{p=1}^{\Omega(p)}$. Within the p-th degenerate sector we would go about computing the matrix elements:

$$\langle \vec{m}_p | \mathcal{H}_{chaos} | \vec{n}_p \rangle \,. \tag{3.61}$$

Diagonalizing a matrix with the matrix elements given above would tell us the information about how the degenerate energies within the p-th sector split. At leading order in degenerate perturbation theory, the splitting of the energy levels only depend on the details of the sub-block in the degenerate sector. This means that first order theory will contain no information about correlations between different degenerate energy sectors. In other words, at leading order we can treat our random matrix as block diagonal with each block having the same size as the particular degenerate sector. More specifically, we can write:

$$\mathcal{H} = \bigoplus_{p=0}^{N/2} \left[E(p)\mathcal{I}(p) + \epsilon \mathcal{H}_{chaos}(p)\right], \tag{3.62}$$

where $\mathcal{I}(p)$ is an identity matrix of dimension $\Omega(p) \times \Omega(p)$ and $\mathcal{H}_{chaos}(p)$ is a sub-block of the chaotic interaction Hamiltonian of dimension $\Omega(p) \times \Omega(p)$.

To simplify our considerations, we will assume that the $\mathcal{H}_{chaos}$ is given by a random matrix pulled from the GUE[25]. If $\mathcal{H}_{chaos}$ is a random matrix from the GUE, then we know

[25]The elements of the GUE are Hermitian matrices. The off-diagonal elements will be of the form $x+iy$ where x and y are random variables pulled from a Gaussian distribution with a mean of zero and variance of 1/2. The diagonal elements are real random variables pulled from a Gaussian with mean of zero and variance of 1. In this case it is well known that the width of the semi-circle spectral density goes as $4\sqrt{N}$ [93]. This width of the semi-circle can be scaled by multiplying the matrices in the ensemble by a factor c then the new width is $4c\sqrt{N}$.

the splitting of degenerate states within a sector will occur so that the NNS statistics are consistent with the GUE (i.e. you will have Wigner surmise spacing). Furthermore, we expect the spectral density to spread out from a delta function at the degenerate energies to "semi-circles" centered around the degenerate energies. The width of the spread for the p-th degenerate sector will roughly go as:

$$W(p) \approx 4\epsilon\sqrt{\Omega(p)}. \tag{3.63}$$

This allows us to define a rough criterion in which we expect perturbation theory to hold:

$$\frac{\max_p W(p)}{\omega_0} = \frac{4\epsilon\sqrt{\max_p \Omega(p)}}{\omega_0} \ll 1. \tag{3.64}$$

This essentially states we want to work in a regime where the spread has a width much smaller than the spacing between energy levels of the unperturbed oscillator. Figure 3.14 depicts numerically generated spectral density at $N = 22$ for different choices of the parameter ϵ/ω_0. One can check that in the specific case we plotted the condition given in Eq. (3.64) for being in the perturbative regime translates to $\epsilon/\omega_0 \ll 10^{-2}$. We can see that the average spectral densities on the top row of Figure 3.14 satisfy the condition and the spread within the degenerate sectors is much smaller than the spacing between different degenerate sectors. In contrast, the plots on the bottom row do not satisfy the perturbative condition and we can see that at $\epsilon/\omega_0 = 10^{-2}$, the spread within the degenerate sectors start to become comparable to the spacing between them. The spread will increase as we increase ϵ/ω_0 and there will be substantial overlap between sectors, eventually leading to a point where the overall density simply looks like that of the GUE at $\epsilon/\omega_0 = 10^{-1}$. In Appendix B.7, we do a numerical analysis of the exact width of the spread within the degenerate sectors and compare to what we expect from first order degenerate perturbation theory, finding reasonable agreement for $\epsilon/\omega_0 \leq 10^{-2}$.

Now that we have discussed the spectral density, we can turn our attention to the spectral form factor. Within the perturbative regime, there are two distinct time scales. One is given by the oscillator frequency ω_0^{-1} and the other scale is given by ϵ^{-1} which gives the strength of the chaotic perturbation (roughly related to the average spacing of eigenvalues within a degenerate sector). At time scales $t \ll \epsilon^{-1}$, the form factor will be dominated by the coarse grained spectrum which is a sharply spiked spectrum with regular spacing. Due to this we expect to see oscillations in the form factor with a period that is well described by the unperturbed form factor, $\tau = 2\pi\omega_0^{-1}$. We will also expect these oscillations to gradually decay due to the repulsion of adjacent eigenvalues within a degenerate sector. For time scales $t \gtrsim \epsilon^{-1}$, the form factor will become sensitive to fine structure of the degenerate sectors. In this regime, the form factor should contain a ramp

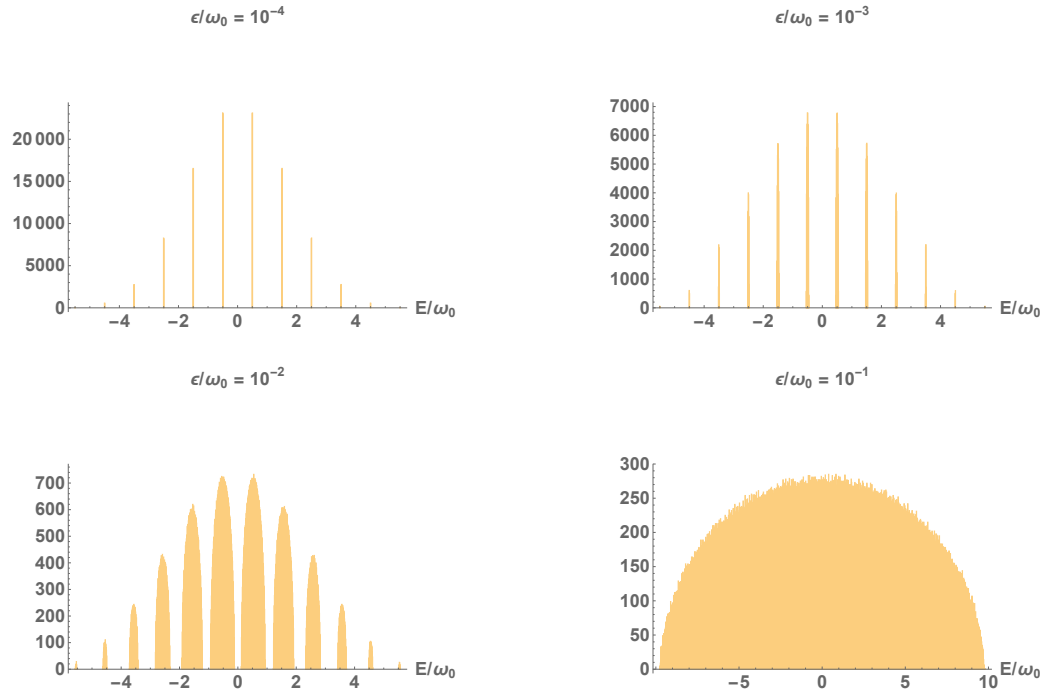

Figure 3.14: Above is depiction of the averaged spectral density (histogram of eigenvalues) of a system of 11 identical fermionic oscillators coupled together with random interactions represented by a matrix pulled from a GUE for various values of ϵ/ω_0. The top two plots labelled by $\epsilon/\omega_0 = 10^{-4}, 10^{-3}$ depict the spectral density at weak coupling. The bottom two plots labelled by $\epsilon/\omega_0 = 10^{-2}, 10^{-1}$ depict the spectral density at intermediate coupling ($\epsilon/\omega_0 = 10^{-2}$) and strong coupling ($\epsilon/\omega_0 = 10^{-1}$).

and a plateau consistent with the late time behaviour of a form factor in the GUE, as we have seen before.

In Figures 3.15 and 3.16, we numerically plot the form factor (averaged over 100 samples) for different values of ϵ/ω_0 at $\beta\omega_0 = 0$. The the perturbative regimes (weakly coupled) occurs when $\epsilon/\omega_0 = 10^{-4}, 10^{-3}$ and the non-perturbative regimes (strongly coupled) occur at $\epsilon/\omega_0 = 10^{-2}, 10^{-1}$. Figure 3.15 depicts the early time behaviour of the form factor and it shows that the form factor oscillates at early times with a frequency $2\pi\omega_0^{-1}$ (the red dots indicate the value of the form factor at regular time steps given by the period $\tau = 2\pi\omega_0^{-1}$). The oscillations have a decaying amplitude bounded by an envelope which

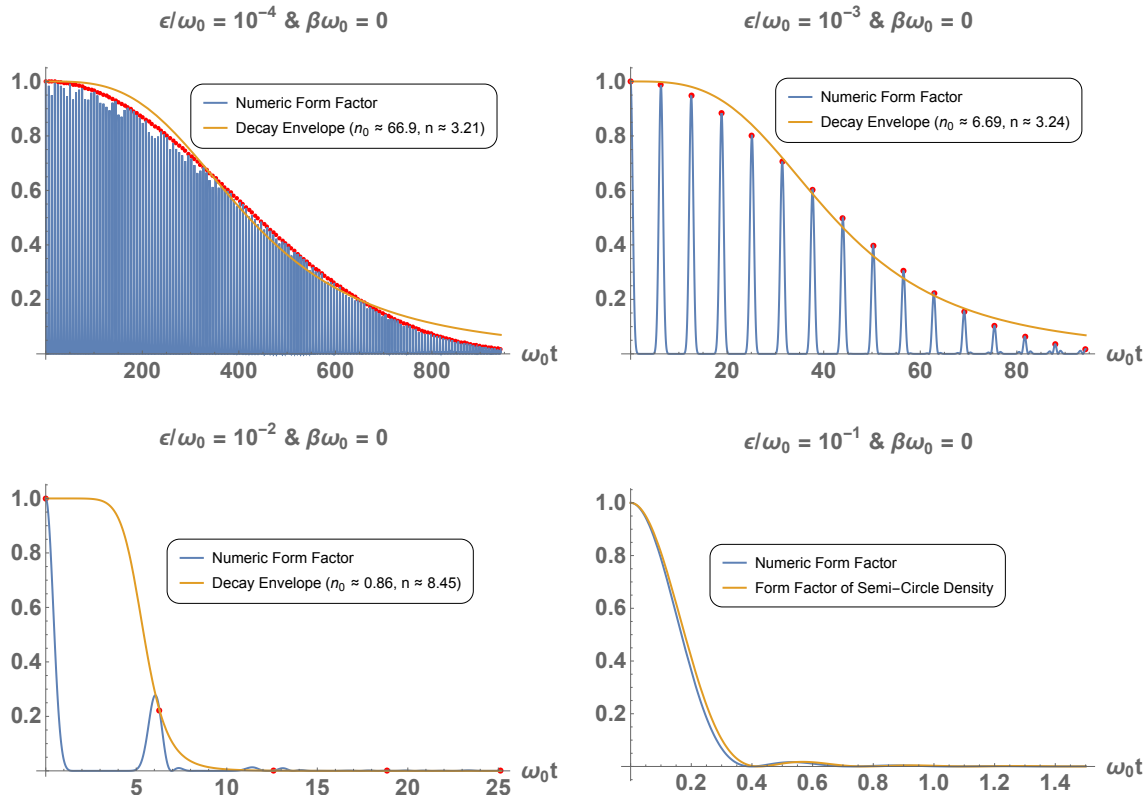

Figure 3.15: The plots in the figure above depicts the self averaging early time behaviour in the infinite temperature form factor computed numerically for a system of 11 fermionic oscillators coupled together by a $(2^{11} \times 2^{11})$ random GUE matrix for various values of ϵ/ω_0 ranging from 10^{-4} to 10^{-1}. The blue line depicts the numerical calculation of the form factor for a single sample (due to the self averaging behaviour at early times one can check the single sample will agree with the numerical average to high precision). The red dots indicate the value of the form factor at regularly spaced time intervals given by $\omega_0 t_k = 2\pi k$. The yellow line is a numeric fit of the red data points to a function given by Eq. (3.65) with fitting parameters n_0, n (shown in the legend of the plots). For the bottom right plot we compare the numeric early time behaviour to the behaviour predicted by Eq. (3.66), which is the form factor of a semi-circle spectral density.

can be numerically fit by:

$$A(t) = \frac{1}{1 + \left(\frac{\omega_0 t}{2\pi n_0}\right)^n}, \tag{3.65}$$

where n_0 and n are fit parameters. We can see from the legend in Figure 3.15 that the amplitude of the oscillations in the weakly coupled regime decays through a power law with a power $n \sim 3$, furthermore we can see that $n_0 \sim C\omega_0/\epsilon$ where C is a proportionality constant that will depend on N[26].

In the non-perturbative regime (the bottom two plots of Figure 3.15), we can see that the regular oscillations start to disappear and give way to the more familiar features present in the early time behaviour of the form factor for the GUE. The early time behaviour of the form factor in the case when $\epsilon/\omega_0 = 10^{-1}$ is well approximated by the form factor associated with a semi-circle density (SCD) given by:

$$\left|\frac{\mathcal{Z}(\beta+it)}{\mathcal{Z}(\beta)}\right|^2_{SCD} = \left|\frac{\int_{-1}^{1}\sqrt{1-x^2}e^{-ixE_0(t-i\beta)}dx}{\int_{-1}^{1}\sqrt{1-x^2}e^{-ixE_0(-i\beta)}dx}\right|^2 = \frac{\beta^2}{\beta^2+t^2}\frac{J_1\left[E_0(t-i\beta)\right]J_1\left[-E_0(t+i\beta)\right]}{\left[J_1(-i\beta E_0)\right]^2}, \tag{3.66}$$

where E_0 is the half the width of the semi-circle density (in our case we used $E_0/\omega_0 = \sqrt{2^{13}}/10 \approx 9.05$).

In Figure 3.16, we depict the averaged form factor on a Log-Log scale at longer time scales (averaged over 100 samples). The early time behaviour contains oscillations in the weakly coupled regime which we already described in our discussion of Figure 3.15. The averaged late time behaviour in all coupling regimes contains the ramp and plateau. This late time behaviour occurs due to the manner in which each degenerate sector of the uncoupled oscillator theory splits in the presence of the GUE matrix coupling.

[26] In this case it is well approximated by $C \approx \frac{1}{7\sqrt{\max_p \Omega(p)}} \approx 0.00665$. More generally, we expect $C \sim \frac{1}{\sqrt{\max_p \Omega_p}}$ with some numerical pre-factor.

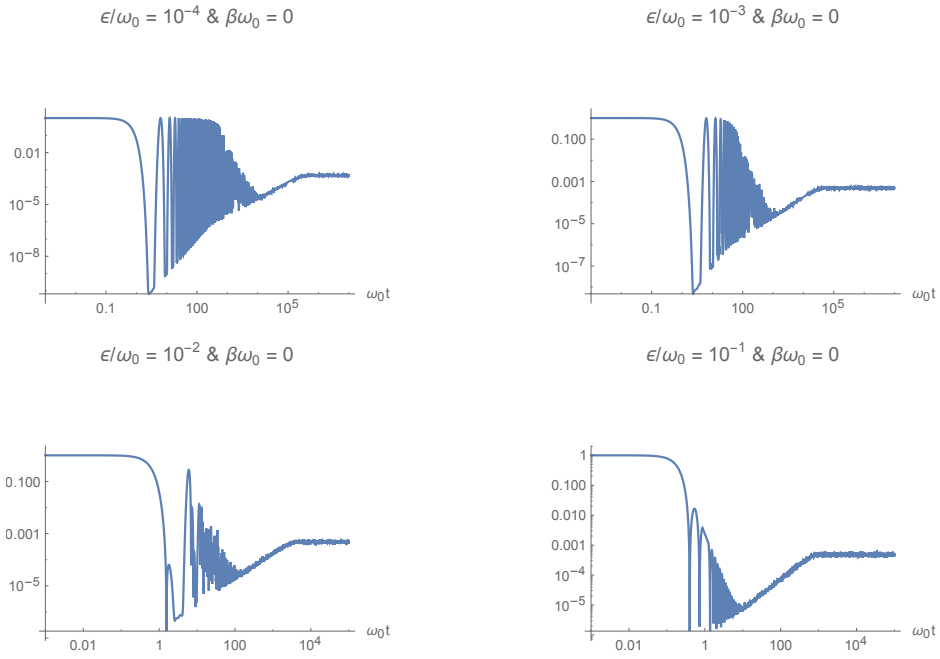

Figure 3.16: The plots above depict the numerically averaged form factor on a Log-Log scale (averaged over 100 samples) at infinite temperature for a system of 11 fermionic oscillators coupled together by a $(2^{11} \times 2^{11})$ random GUE matrix for various values of ϵ/ω_0 ranging from 10^{-4} to 10^{-1}.

3.4.2 Randomly Coupled Oscillators as a Toy Model for the Membrane

Let us now see how our system of chaotically coupled oscillators, can act as a quantum mechanical toy model to describe gravitational waves echoes (e.g., [3]).

To do this, we recall that gravitational wave echoes are thought to arise due to quantum gravity effects near the horizon which result in the partial reflection of perturbations. These reflections are usually modelled by cutting off the semi-classical black hole geometry close to the horizon and then placing semi-reflective boundary conditions at the cutoff. In the context of large AdS black holes, one can also place a cutoff near the horizon and echoes will arise due to the reflection of perturbations near the horizon and also at the conformal boundary [133]. In this chapter, we adopt the view that the cutoff with modified boundary conditions describe some kind of dynamical membrane deep in the bulk near the horizon.

This membrane has its own internal spectrum which should resemble the chaotic and discrete spectrum of a black hole.

If one begins with a perfectly reflective membrane, then perturbations to the geometry will not decay and the geometry will have normal modes (rather than quasi-normal modes). The dynamics of the perturbations on the spacetime may be roughly modelled by some kind of oscillator system similar to the one discussed in the previous section. The characteristic frequency of the oscillators in the previous subsection would be identified with the spacing between normal modes in the cutoff spacetime. For example, for a spherical Schwarzschild AdS black hole (with $r_H/L \gg 1$), if the cutoff is a proper radial length, l_{prop}, from the horizon, then we expect massless scalar perturbations to make a round trip (from the cutoff to the conformal boundary and back) in a time scale roughly given by [133]:

$$\tau \sim \beta \ln\left(\frac{L^2}{l_{prop}^2}\right) \sim \frac{L^2}{r_H} \ln\left(\frac{L^2}{l_{prop}^2}\right), \tag{3.67}$$

where r_H and L is the horizon and AdS radii, respectively. We identify $\omega_0 = 2\pi\tau^{-1}$ with the characteristic oscillator frequencies[27]. This will give rise to a periodic form factor with oscillations that have a period equal to τ. To introduce dissipation into the system, we can further add chaotic interactions between the oscillators. In the weak coupling regime, these interactions are responsible for the decay of the regular oscillations at early times in the form factor and also will be responsible for the ramp and plateau at late times making late time thermalization similar to SYK theory.

To interpret the energy scale ϵ in Eq. (3.60), we turn off the oscillator term by sending the cutoff to the horizon (i.e. $l_{prop} = 0$ in Eq. (3.67)) so that $\omega_0 = 0$, and we are left with the chaotic term. This gives rise to the usual semi-circle spectral density and gives a standard SYK/JT gravity type model for a black hole - where no oscillations are present at early times. In this case, the energy scale, ϵ, controls the average spacing between adjacent energy levels which is of the order $\delta E \sim \epsilon e^{-S/2}$ where S is the entropy of the black hole[28]. At the same time, if we consider the first law of black hole thermodynamics it suggests that the average spacing between adjacent levels is of the order $\delta E_{\text{min}} = \delta S_{\text{min}}/\beta$. We will be agnostic about what δS_{min} should be. We know the smallest possible value of δS_{min} is of the order e^{-S} but there might also be other choices (for example, $\delta S_{\text{min}} \sim 1$ might also be sensible when discussing entropy changes by emission of a single Hawking quanta).

[27]Notice that the frequencies have a linear temperature dependence, this could arise as a thermally induced mass from a renormalization procedure in QFT at finite temperature [12, 82].

[28]We obtain $\epsilon e^{-S/2}$ by recalling that the width of the semi-circle scales with the size of the matrix $\epsilon\sqrt{2^{N/2}}$. Then we take the width of the semi-circle and divide by the total number of states which is $2^{N/2}$, to get an average spacing $\delta E \sim \epsilon 2^{-N/4}$. Finally we identify $S \sim \ln\left(2^{N/2}\right)$ to obtain $\delta E \sim \epsilon e^{-S/2}$.

Identifying the δE expression from the random matrix model to the $\delta E_{\min}$ from the first law gives $\epsilon \sim \beta^{-1}\delta S_{\min} e^{S/2}$. When we do this and consider the dimensionless ratio between ϵ and ω_0 we have:

$$\frac{\epsilon}{\omega_0} \sim e^{S/2} \ln\left(\frac{L^2}{l_{prop}^2}\right) \delta S_{\min}. \tag{3.68}$$

If $\delta S_{\min} \sim e^{-S}$ (the smallest possible change in entropy) and $l_{prop} \sim \ell_p$, where ℓ_p is the Planck length, then our oscillator system is in the weakly coupled regime and will exhibit echoes that manifest after a scrambling time scale. Such echoes would be observable within a reasonable window of time for astrophysical black holes, making this model interesting in the discussion of gravitational wave echoes.

3.5 Discussion and Conclusion

The AdS/CFT correspondence formulates quantum gravitational systems in AdS in terms of CFT systems on the boundary. In such a scenario, the statement that a black hole is a quantum chaotic system is understood in terms of the high energy eignestates of the CFT. In the context of spacing statistics of the CFT spectrum, one could imagine diagonalizing the Hamiltonian $\mathcal{H}$ to find a complete orthogonal basis of eigenstates $|n\rangle$ and eigenvalues E_n. Any state can then be written in terms of the eigenstates of the Hamiltonian including the black hole. As one goes to "very high" energies, one should expect the spectrum of the CFT to exhibit chaotic spacing statistics (i.e. eigenvalue repulsion). If one assumes that the a black hole is a thermal ensemble of such microstates, then how the black hole relaxes after being perturbed should be described by thermal correlation functions. The question of how quantum aspects of a black hole manifest in the ringdown and whether they are potentially observable could be addressed using this picture.

In this chapter, we explored the concept of echoes due the black hole microstructure from the perspective of the thermalization behaviour of quantum chaotic systems. The form factor served as a convenient proxy to study this behaviour for systems with varying spectral statistics. We employed a simple model for a random spectrum that involved summing a set of independent-identically-distributed (i.i.d) random variables which represent the spacing between adjacent eigenvalues in the spectrum. By defining a random spectrum in this manner, we were able to specify the resulting spectrum's Nearest Neighbor Spacing (NNS) statistics. Despite the simplicity of the i.i.d model, we demonstrated that it could reproduce various important late time features seen in the spectral form factor of strongly coupled chaotic systems. Most notably, by using Wigner surmise NNS statistics we were able to obtain the ramp and plateau behaviour. We also used the i.i.d model to study

more general NNS distributions where the "Dyson index" is allowed to be any real positive number, rather than the canonical values of $1, 2$, and 4 (corresponding to the GOE, GUE, and GSE ensembles respectively).

We briefly discussed how more general choices of the Dyson index could correspond to more general random matrix ensembles called "β-ensembles," which are constructed from certain types of tri-diagonal matrices. We also argued that for a large Dyson index, the averaged form factor of a β-ensemble would have damped oscillations at late times before approaching a plateau. The origin of these oscillations are the large regularly spaced "gaps" in NNS distribution which are expected to arise when the Dyson index becomes large. We further showed that such gaps could be realized in systems with an evenly spaced spectrum - like a harmonic oscillator with an additional chaotic potential. Although such oscillations might be thought of as "echoes" in the black hole context, such echoes would manifest on extremely long time scales of the order e^S, disqualifying them as being observable in the context of astrophysical black hole microstructure. Although, the late time oscillations found in Section 3.3.4 may not be interesting in the astrophysical context, they may be connected to the discussion of form factors in more exotic theories of gravity. In particular, in the work [39], the form factor of Narain's family of free boson CFTs (which is dual to "U(1) gravity" in AdS_3) has been shown to have a form factor that contains oscillations at late time similar to the ones we found in Section 3.3.4. Our results suggest that such oscillations occur due to enhanced "repulsion" between eigenvalues in the spectrum. It would be interesting to investigate if the late time oscillations showing up in the form factor of Narain ensemble CFTs can also be traced back to enhanced repulsion statistics in the spectrum.

Studies using the i.i.d. model in Sections 3.2 and 3.3 suggested that the quantum aspects of the thermalization behaviour of black holes usually manifest at very late times which are unobservable in the astrophysical context. A common aspect of the spectra generated by the i.i.d. model was that there was a single large cluster of microstates with very little coarse-grained structure. To get non-trivial behaviour on observable time scales, we thus proposed that there must be additional structure in the coarse grained density of states. In particular, for echoes to manifest, we showed that the coarse-grained density had to have large clusters of states widely separated from other clusters. In Section 3.4, we considered a many body system of identical fermionic oscillators coupled by an interaction term modelled by a random matrix in the GUE. In the weakly coupled regime, we used degenerate perturbation theory to argue that degenerate sectors of $\mathcal{H}_{FHO}$ would split in a way consistent to the random matrix statistics of the GUE. This naturally led to regularly spaced decaying oscillations at early times followed by a ramp and plateau in the averaged form factor. We then discussed the possibility of using our model of coupled oscillators as

a toy model that describe near horizon modifications that give rise to gravitational wave echoes.

Although we were able to show that one can construct quantum chaotic systems with echoes, there are still a number of issues that need to be addressed before we can view them as reasonable models for describing black holes with microstructure near the horizon. Aside from the condition that a black hole has a quantum chaotic energy spectrum, it must also satisfy additional constraints which are usually discussed in the context of out-of-time-order correlators (OTOCs) [94, 67, 41]. In particular, quantum chaotic systems describing black holes are expected to also saturate the Lyapunov bound discussed in [94]. We did not demonstrate that the coupled oscillator systems introduced in Section 3.4 satisfy this constraint. A good place to start exploring the issue of OTOCs (and also other types of correlators) is with the following concrete oscillator model[29]:

$$\mathcal{H} = -i\omega_0 \sum_{k=1}^{N/2} \chi^{2k-1}\chi^{2k} + \epsilon \sum_{1\leq\alpha<\beta<\mu<\nu\leq N} j_{\alpha\beta\mu\nu}\chi^{\alpha}\chi^{\beta}\chi^{\mu}\chi^{\nu}, \tag{3.69}$$

where χ's are Majorana fermions: $\{\chi^{\alpha}, \chi^{\beta}\} = \delta^{\alpha\beta}$, and $j_{\alpha\beta\mu\nu}$ is a completely anti-symmetric coupling tensor where each component is an independent random Gaussian variable with a mean of zero. The quadratic term in Eq. (3.69) describes $N/2$ free identical fermionic oscillators expressed in the Majorana basis[30] and the quartic interaction is the standard SYK model Hamiltonian. As before, the quantity ϵ/ω_0, would control the strength of the interactions between the oscillators. One would then have a family of theories labeled by ϵ/ω_0. In the limit when $\epsilon/\omega_0 \to \infty$ we should recover the SYK model with no echoes which saturates the Lyapunov bound (i.e. the Lyapunov exponent $\lambda_L = \frac{2\pi}{\beta}$). In the opposite limit, when $\epsilon/\omega_0 \to 0$, we would have free fermionic oscillators (non-decaying periodic behaviour in form factor) and the Lyapunov exponent will be zero. In the intermediate regime, we should have regular decaying oscillations; similar to the ones discussed in Section 3.4.1. We expect the Lyapunov exponent in intermediate regimes to interpolate between the values of 0 and $2\pi/\beta$ (perhaps even in a discontinuous manner). The central question is what the Lyapunov exponent is when echoes manifest in the form factor. If we are able to show that in the regime where echoes exist the Lyapunov bound is nearly saturated[31] then

[29] It is interesting to point out that a coupled oscillator system is similar to the kinds of models studied in [56], although the quadratic term is random in those models and of a more general form.

[30] The transformation between the creation and annihilation operators defined in Eq. (3.48) and the Majorana fermions χ is $b_k = \left(\chi^{2k-1} - i\chi^{2k}\right)/\sqrt{2}$ and $b_k^{\dagger} = \left(\chi^{2k-1} + i\chi^{2k}\right)/\sqrt{2}$.

[31] The reason we say the Lyapunov bound is nearly saturated is due to results of a work that computes the Lyapunov exponent in a fuzzball geometry by analyzing geodesic motion in the vicinity of the fuzzball

it might be plausible that the quantum chaotic system described by a Hamiltonian given in Eq. (3.69) describes a black hole with microstructure near the horizon which exhibits echoes when perturbed. If we find that echoes only exist in coupled oscillator models when the Lyapunov exponent is nearly zero then the modified black hole interpretation is not plausible, we will likely have to consider more complicated models where we can tune the value of the Lyapunov exponent. We leave this exploration to future work.

An important point to make in the discussion of modifications to the near horizon description of black holes and their imprints on the ringdown is that they may not manifest as dramatically as described by the models discussed in Section 3.4. In particular, the model of identical oscillators coupled by a random interaction can give sharp echoes like the ones shown in Figure 3.15 at weak coupling. These models have evenly spaced clusters of states. If the clusters were not evenly spaced one might get less dramatic echoes or no discernible echoes at all. Presumably, a completely random placement of these clusters would completely "wash out" a clear echo signal in the form factor. It would be interesting to explore where on the spectrum between evenly spaced clusters and randomly spaced clusters echoes persist. This might give a sense of how "resilient" the "echo" phenomenon may be to deviations from the ideal evenly-spaced clusters scenario.

Although we expect the high energy sector of a holographic CFT to exhibit chaos, the exact structure of the spectrum is unknown. The results in this chapter suggest a wide variety of deviations can occur at early times before the universal ergodic behaviour manifests (i.e. ramp and plateau). The origin of possible deviations at intermediate and early times may be additional coarse-grained structure in the spectrum of states that give rise to clustering effects on energy separations $\gg \beta^{-1}e^{-S}$. In our randomly coupled oscillator models, degenerate states were responsible for this clustering. This is interesting because degeneracies arise due to "symmetries" in a system. The symmetries thus act as "seeds" for additional structure at intermediate energy spacings. If there are symmetries in a holographic CFT that have the same effect, then this may also give rise to additional structure in the spectrum which would imprint itself in the thermalization behaviour of a black hole and potentially be detected as echoes (or other deviations from GR predictions) that could be searched for in future gravitational wave experiments. The i.i.d. model might serve as a useful phenomenological tool to model the wave-forms for unitary black hole ringdowns.

To conclude our discussion, it is worth clarifying a few points. In this chapter, we explored the possibility of echoes from black hole microstructure in the context of unitary

[24]. The work suggests that fuzzballs tend to have a slightly smaller Lyapunov exponent when compared to their black hole counter parts. This may also be true more generally for highly compact objects that resemble black holes far away but deviate near the horizon.

quantum chaotic systems. Our primary conclusion is that echoes may appear, either due to enhanced repulsion between individual microstates, or the occurrence of regular spacing between clusters of microstates. Appearance of echoes in the unitary quantum description on time scales comparable to the scrambling time suggests the existence of Planck-scale microstructure near the horizon. The reason we asserted this was because the echo time scale found in the classical models with a cutoff depends on how close the cutoff is placed from the horizon. In particular, cutoffs placed a proper-radial Planck length from the horizon (i.e. $r_{\text{cutoff}} \sim r_h + \ell_p^2/\beta$) give echoes around a scrambling time scale $\beta \ln(S)$,[32][133]. The randomly coupled oscillator example in Section 3.4 served as a simple toy model to illustrate how self-averaging echoes can arise due to non-trivial clustering of microstates. The oscillations found in Section 3.3.4, however, are of a different type. They are not self-averaging and arose from enhanced repulsion statistics between individual adjacent microstates. Furthermore, in the context of the i.i.d. model, these non-self averaging oscillations occur on time scales of the order of the Heisenberg time $\mathcal{O}(e^S)$, which is typically much longer than the scrambling time[33]. The physical interpretation of non-self averaging echoes that occur on the Heisenberg time scale is more subtle and might require a more careful understanding in terms various saddles (or even off-shell effects) that occur in the Euclidean path integral. While the time scale of e^S is what one may expect from quantum tunneling from structure behind the horizon, this is more likely an upper limit, given that black hole evaporation happens on polynomial times. We hope to explore these ideas in more detail in future work.

[32] Note that the $S \sim L/\ell_p \sim N$ for large AdS black holes.

[33] Assuming the average spacing between adjacent microstates was of the order e^{-S}.

Part II

Aspects of Evaporating Black Holes, Islands, and Entanglement Wedge Nesting

Chapter 4

Extracting Hawking Radiation Near the Horizon of AdS Black Holes

We study how the evaporation rate of spherically symmetric black holes is affected through the extraction of radiation close to the horizon. We adopt a model of extraction that involves a perfectly absorptive screen placed close to the horizon and show that the evaporation rate can be changed depending on how close to the horizon the screen is placed. We apply our results to show that the scrambling time defined by the Hayden-Preskill decoding criterion, which is derived in Pennington's work (arXiv:1905.08255) through entanglement wedge reconstruction is modified. The modifications appear as logarithmic corrections to Pennington's time scale which depend on where the absorptive screen is placed. By fixing the proper distance between the horizon and screen we show that for small AdS black holes the leading order term in the scrambling time is consistent with Pennington's scrambling time. However, for large AdS black holes the leading order Log contains the Bekenstein-Hawking entropy of a cell of characteristic length equal to the AdS radius rather than the entropy of the full horizon. Furthermore, using the correspondence between the radial null energy condition (NEC) and the holographic c-theorem, we argue that the screen cannot be arbitrarily close to the horizon. This leads to a holographic argument that black hole mining using a screen cannot significantly alter the lifetime of a black hole.

4.1 Introduction

The AdS/CFT correspondence is a conjecture that relates gravitational systems in asymptotically AdS spacetimes to conformal field theories in one fewer spatial dimension [96,

125, 153]. This provides an ideal setting to resolve the black hole information paradox [70, 99, 122, 140]. In particular, it suggests that information thrown into a black hole is not lost. The reason for this is that the AdS black hole undergoing evaporation is dual to unitary time evolution of a thermal state on the CFT side of the duality, which does not allow for information loss. The information thrown into a black hole is thus argued to be scrambled by some kind of unitary dynamics and then remitted via Hawking radiation [73, 134, 86]. The question of how long one needs to wait for information thrown into a black hole to emerge in the subsequent Hawking radiation was first addressed in [73]. It stated that information thrown into a black hole after the Page time would re-emerge within a scrambling time scale which is given by:

$$t_{scr} \sim \beta \ln(S), \tag{4.1}$$

where β is the inverse Hawking temperature and S is the number of degrees of freedom in the black hole which take part in scrambling.

Usually in the context of AdS/CFT one considers black holes well beyond the Hawking-Page transition. These black holes, often referred to as large AdS black holes, are dual to large N gauge theories [157, 97]. They have a horizon radius, r_s, that satisfies $r_s \gg L$ where L is the AdS radius. A peculiar property of large AdS black holes is that they are thermally stable. This is due to the confining potential which comes from the asymptotics of AdS spacetimes. In such a case any Hawking radiation that the black hole emits reaches the conformal boundary and bounces back, being reabsorbed into the black hole. Eventually the black holes reaches stable equilibrium with the surrounding Hawking radiation and will not evaporate [71, 76]. This makes large AdS black holes ill-suited to discuss the information paradox. To remedy this issue, it has been suggested to start with a large AdS black hole and then couple the bulk fields to an auxiliary field (called the evaporon) which carries energy away from the AdS black hole into an auxiliary system thereby allowing the black hole to evaporate [127, 128].

In such constructions, it is the joint system of the reservoir and black hole which satisfy unitarity. Such constructions have been of recent interest in explorations of the information paradox. For example, [117, 7] rely on such setups to show how information from the black hole gets released in the Hawking radiation (see [8] for a recent overview of the literature). They use entanglement wedge reconstruction to show how information inside a black hole after the Page time scale is encoded in the subsequent Hawking radiation. In particular, Pennington showed that a small amount of information thrown into a black hole (after the Page time) will re-emerge in Hawking radiation after a time scale given by:

$$t_{emerge} = \frac{\beta}{2\pi} \ln \left(\frac{2\pi C}{\beta \left| \frac{dr_s}{dt} \right|} \right), \tag{4.2}$$

where C can be thought of as the radial distance away from the horizon that one expects the Rindler description to hold, dr_s/dt is the average rate of change of the horizon radius during evaporation, and β is the inverse Hawking temperature. Moreover, as we shall review in Section 4.3, t_{emerge} is the scrambling time scale discussed in [73]. A key assumption that was made in the calculation was that radiation was being extracted close to the horizon by some type of "super-observer" in a non-local manner. Since the radiation was extracted sufficiently close to the horizon it was assumed that greybody factors can be ignored and the 2D Stefan-Boltzmann law was used for the evaporation rate:

$$\frac{dM}{dt} = \frac{c_{evap}\pi}{12\beta^2}, \tag{4.3}$$

where c_{evap} represents the number of modes being extracted near the horizon. Using this evaporation rate in conjunction with the first law of black hole thermodynamics ($dM = TdS$) gave an information emergence time of the form[1]:

$$t_{emerge} \sim \frac{\beta}{2\pi} \ln\left(\frac{S - S_{ext}}{c_{evap}}\right). \tag{4.4}$$

A similar result is also derived for 2D black holes in Jackiw-Teitelboim (JT) gravity studied in [7]. Which is given by:

$$t_{emerge} \sim \frac{\beta}{2\pi} \ln\left(\frac{S - S_{ext}}{c}\right), \tag{4.5}$$

where c is the central charge (a measure of the degrees of freedom of a CFT) of a CFT that describes bulk matter in the 2D gravity theory. In light of the two results in Eqs. (4.4 - 4.5) for the emergence time, it is tempting to make a rough identification of $c \sim c_{evap}$. The central charge, c, in Eq. (4.5) seems to be a fixed parameter which does not appear to have any kind of dependence on quantities that characterize the black hole such as temperature.

However, it is clear that in Pennington's setup c_{evap} depends on details of where and how radiation is extracted near the horizon. For example, c_{evap} should depend on how close one is extracting radiation near the horizon. The closer we are, the larger c_{evap} can get. Furthermore, c_{evap} will depend on the means by which one extracts radiation from the horizon; if we choose to place a surface at a radial distance δr from the horizon with perfectly absorbing boundary conditions then c_{evap} would be larger than if we chose some kind of semi-reflective boundary conditions. All these details will have some effect on the value of c_{evap} and therefore on the evaporation rate.

[1] We will review some of the details of the calculation in Section 4.3

In light of these observations, we explore how the evaporation rate of a black hole depends on how close we extract radiation from the horizon. In this chapter, we will model the "super-observer" using an absorptive screen placed close to the horizon. Roughly speaking, we assume that the screen can be understood from the prospective of the holographic renormalization group in AdS/CFT [51, 43]. At infinity we have a full UV complete (local) theory. The degrees of freedom on the screen and their dynamics are going to be viewed as a lower energy coarse grained version of the UV theory. We expect that the lower energy theory will become increasingly non-local as we push the screen closer to the horizon[2].

To simplify considerations, we assume that the screen will absorb any radiation that reaches it [3]. In Section 4.2.1, we review how to calculate the average evaporation rate of a black hole and discuss how greybody factors affect this rate. By doing this we are able to clearly identify Pennington's c_{evap} in terms of an infinite sum over angular momentum modes. We discuss how in two dimensions c_{evap} in Eq. (4.4) can be reasonably identified with c in Eq. (4.5) with no further dependence on parameters that characterize the black hole. However, in higher dimensions we find that such a naive identification is not valid. We introduce the notion of a generalized greybody factor which quantifies the fraction of radiation that gets to a point at a radial distance δr away from the horizon. At this distance away we introduce a perfectly absorbing screen which will absorb any radiation that hits it. We then write down an expression for the evaporation rate in terms of the generalized greybody factor. After doing this we restrict ourselves to massless scalar perturbations and write down a model for the generalized greybody factor which treats the effective potential as a "hard wall." In Section 4.2.2, we apply the hard wall model to AdS Schwarzschild black holes and find the evaporation rate. In Section 4.2.3, we discuss why the hard wall model for the generalized greybody factor is not sufficient for near extremal AdS Reissner–Nordstrom (RN) black holes. We motivate a correction that "softens" the wall and accounts for radiation being able to tunnel into the classically forbidden region. We then provide an estimate using this modified model for the evaporation rate of near extremal AdS RN black holes. In Section 4.3, we review Pennington's calculation of t_{emerge} and then use the modified evaporation rates that we calculated in Sec. 4.2 and find t_{emerge}. In particular, for AdS black holes with $r_s/L \ll 1$ we find results that agree with Pennington's calculation up to some logarithmic correction which depends on how far we

[2]We will evaluate this interpretation of the screen in more detail in Section 4.4.2 when we discuss the null energy condition for the screen and connections to the holographic c-theorem.

[3]By doing this we are not actually defining the effective theory living on the screen that is consistent with some UV completed theory on the boundary. If we did make the effective theory on the screen consistent with a UV completed theory, we should not expect a perfectly absorptive screen. However, we still believe that a perfectly absorptive screen near the horizon is a reasonable approximation. In Section 4.4.1, we propose a more rigorous way of defining how the screen should absorb radiation.

choose to extract radiation. However, in the case of $r_s/L \gg 1$ we find a slightly different result; the argument that goes into the Log is not the entropy of the entire horizon, but rather the entropy of a cell of size L controlled by the AdS radius (in addition to the usual logarithmic correction which depends on the extraction radius). In Section 4.3.4, we discuss the subtleties involved in choosing the β dependence of the subleading Log correction for near extremal black holes. By fixing the proper distance between the screen and horizon we find that t_{emerge} is consistent with the scrambling time for near extremal black holes (up to a sub-leading Log correction that has no further dependence on the temperature of the black hole). We speculate that fixing the proper radial distance of the screen from the horizon to corresponds to fixing the energy scale of the effective holographic theory on the screen. In Section 4.4.1 we formulate a more rigorous framework to calculate how the screen will absorb Hawking radiation. This is done by viewing the screen as an interface which patches the interior black hole spacetime to an exterior "reservoir" spacetime. By doing this we reduce the problem of finding how the screen absorbs the radiation to a calculation of finding the transmission amplitude of scalar perturbations through an effective potential. We argue that by using this approach one should recover the results in reasonable agreement with the toy models discussed in this chapter. In Section 4.4.2 we briefly review the holographic c-function and the role that the null energy condition (NEC) plays in its formulation. We then consider the radial NEC for the matter that makes up the screen and show that it satisfies the radial NEC a finite distance from the horizon as long as the AdS radius of the spacetime enclosed by the screen is smaller than the AdS radius of the exterior spacetime. This provides a heuristic way to quantify the effective coarse-grained degrees of freedom as the screen is moved toward the horizon. In Section 4.4.3 we discuss how extracting Hawking radiation near the horizon of an AdS black hole can be tied in with discussions of black hole mining. We show that the radial NEC places non-trivial constraints on how close the screen is allowed to be to the horizon. The constraints show that small AdS black holes cannot be mined by placing a screen very close to the horizon. However, mining for very large AdS black holes is possible since the screen can be placed very close to the horizon without violations of the radial NEC. We compute how long it takes for a very large AdS black hole to transition to a small AdS black hole through screen mining. We estimate that to leading order a the transition time (in units of the AdS radius) is given by the Bekenstein-Hawking entropy of an AdS radius sized cell.

We then conclude this work by summarizing the major results of this chapter as well as some outstanding questions and issues which can be explored further.

4.2 Changing Evaporation Rates via Near Horizon Extraction

4.2.1 Modelling Hawking Radiation Extraction Through Generalized Greybody Factors

It is well known that close to the horizon, a black hole will emit radiation as a black body. However, by the time this radiation reaches an observer very far away from the black hole the spectrum of the radiation is modified. This is because the black hole generates a non-trivial potential that perturbations travelling through the background will experience, resulting in partial reflection and transmission of perturbations. These effects are contained in greybody factors and they have a non-trivial effect on the evaporation rate of a black hole. We will review the basics of how greybody factors affect the the evaporation rate. We will then introduce the notion of a generalized greybody factor which will depend on how far one is extracting radiation from the horizon.

We begin with the well known result which describes the occupation number distribution of Hawking quanta emitted by a black hole (not accounting for greybody factors):

$$\langle n(\omega)\rangle_{\pm} = \frac{1}{e^{\beta\omega}\pm 1}. \tag{4.6}$$

The plus is for fermionic Hawking quanta and the minus is for bosonic Hawking quanta. For the sake of simplicity we will restrict ourselves to bosonic quanta in this chapter. The total evaporation rate (ignoring greybody factors) of the black hole is given by:

$$\frac{dM}{dt} = \frac{1}{2\pi}\sum_{\ell} N_\ell \int_0^\infty N_b\omega \,\langle n(\omega)\rangle_- \, d\omega = \frac{1}{2\pi}\sum_{\ell} N_\ell \int_0^\infty \frac{N_b\omega}{e^{\beta\omega}-1} d\omega = \frac{N_b\pi}{12\beta^2}\sum_{\ell} N_\ell, \tag{4.7}$$

where N_b is the number of different bosonic species and N_ℓ is the degeneracy of the ℓ-th hyper-spherical harmonic[4]. Note that we recover the 2D Stefan-Boltzmann law used by Pennington with the identification, $c_{evap} = N_b \sum_\ell N_\ell$. This is only finite in 2D where the sum over ℓ disappears and we are left with $c_{evap} = N_b$ which does not depend on the parameters that characterize the black hole (or even the exact position of the screen) this is similar to the behaviour of c in Eq. (4.5) which we discussed in Section 4.1.

[4]To understand why N_ℓ is present recall that the solution to the massless scalar wave equation in a spherically symmetric background can be decomposed as a product $\Psi(t,r,\vec{\phi}) = e^{-i\omega t} r^{(1-d)/2}\psi(r)\Phi_\ell(\vec{\phi})$ where Φ_ℓ are hyper-spherical harmonics for a given ℓ angular momentum mode there are N_ℓ degenerate eigenfunctions. In particular, we identify Pennington's $c_{evap} = N_b \sum_\ell N_\ell$.

In higher dimensions the sum persists and will be divergent resulting in an infinite evaporation rate. The effective potential near the horizon is essential for understanding how the divergence is regulated in higher dimensions. Generally speaking, if we extract Hawking radiation a finite radial distance δr from the horizon we should expect some fraction of the total radiation emitted by the black hole to to reach $r = r_s + \delta r$. This is due to the fact that the effective potential is only zero at the horizon and strictly increases (at least in some neighborhood of the horizon). The larger ℓ is the more quickly it increases, this causes the higher angular momentum modes to reflect back into the black hole, effectively placing a cutoff over the sum of angular momentum modes which result in a finite evaporation rate.

We define the generalized greybody factor, $\gamma_\ell(\omega, \delta r)$, for each ℓ. It quantifies the fraction of radiation that gets to some surface a finite distance δr from the horizon[5]. If the absorptive surface is sitting at $r = r_s + \delta r$ then, the generalized greybody factor represents the fraction of energy absorbed by the screen from the ℓ-th mode. Then the total rate at which the black hole losses mass is given by:

$$\frac{dM}{dt} = \frac{1}{2\pi} \sum_\ell \int_0^\infty \frac{N_\ell N_b \gamma_\ell(\omega, \delta r)\omega}{e^{\beta\omega} - 1} d\omega. \tag{4.8}$$

The generalized greybody factor will be essential in regulating the infinite sum over ℓ. In general, we can compute $\gamma_\ell(\omega, \delta r)$ by considering the wave equation on the black hole background. However, doing this analytically is difficult. To circumvent this issue we will introduce models for the generalized greybody factor which will capture the essential physics of the situation near the horizon.

For the sake of concreteness we will consider the massless scalar wave equation for a spherically symmetric black hole background in $d+1$-dimensions [6]. We are interested in the radial part of the solution which can be shown to obey the Regge-Wheeler equation:

$$\frac{d^2\psi}{dr_*^2} + (\omega^2 - V_\ell)\psi = 0, \tag{4.9}$$

where r_* is the tortoise coordinate defined by the relation $dr_* = \frac{dr}{f(r)}$, and V_ℓ is the effective potential given by:

$$V_\ell(r) = f(r)\left[\frac{d-1}{2r}\frac{df}{dr} + \frac{(d-1)(d-3)}{4r^2} f(r) + \frac{\ell(\ell+d-2)}{r^2}\right]. \tag{4.10}$$

[5] In particular $\lim_{\delta r \to \infty} \gamma_\ell(\omega, \delta r)$ will reproduce the greybody factors that are usually discussed in the context of an observer sitting at asymptotic infinity.

[6] These black hole spacetimes will generally have a metric of the following form $ds^2 = -f(r)dt^2 + dr^2/f(r) + r^2 d\Omega_{d-1}^2$.

If we choose to extract radiation close to the horizon (i.e. $r - r_s \ll r_s$) we can approximate V_ℓ to linear order as:

$$V_\ell(r) \simeq \frac{4\pi}{\beta}\left[\frac{(d-1)2\pi}{\beta r_s} + \frac{\ell(\ell+d-2)}{r_s^2}\right](r-r_s) + ..., \tag{4.11}$$

where β is the inverse Hawking temperature. We place a perfectly absorbing surface at $r - r_s = \delta r$ where $\delta r/r_s \ll 1$. Now consider the quantity:

$$\omega^2 - V_\ell(r) \simeq \omega^2 - \frac{4\pi}{\beta}\left[\frac{(d-1)2\pi}{\beta r_s} + \frac{\ell(\ell+d-2)}{r_s^2}\right](r-r_s) + ... \tag{4.12}$$

As long as $\omega^2 \gg V_\ell$ we should be able to ignore the effects of V_ℓ; the radiation will experience little to no hindrance to get to the absorbing screen we place near the horizon (i.e. $\gamma_\ell(\omega, \delta r) \sim 1$). However, once $\omega^2 \leq V_\ell$ we should expect most of the radiation to be reflected back into the black hole and reabsorbed (i.e. $\gamma_\ell(\omega, \delta r) \sim 0$). We depict the scenario in Figure. 4.1. We model this sort of "hard wall" potential by introducing the following generalized greybody factor:

$$\gamma_\ell(\omega, \delta r) = \Theta\left[\omega^2 - V_\ell(r_s + \delta r)\right], \tag{4.13}$$

where Θ is the Heaviside step function. Using this model the evaporation rate using Eq. (4.8) is given by:

$$\frac{dM}{dt} = \frac{N_b}{2\pi}\sum_{\ell=0}^{\infty}\int_{\omega_{min,\ell}}^{\infty}\frac{N_\ell\omega}{e^{\beta\omega}-1}d\omega = \frac{N_b}{2\pi\beta^2}\sum_{\ell=0}^{\infty}\left(N_\ell\int_{x_{min,\ell}}^{\infty}\frac{x}{e^x-1}dx\right), \tag{4.14}$$

where $\omega_{min,\ell}$ satisfies:

$$\omega_{min,\ell}^2 - V_\ell(r_s + \delta r) = 0. \tag{4.15}$$

In the next section, we use this model to find the evaporation rate of AdS Schwarzschild black holes. We will also use a similar model with some adjustments to calculate the evaporation rate of near extremal AdS RN black holes.

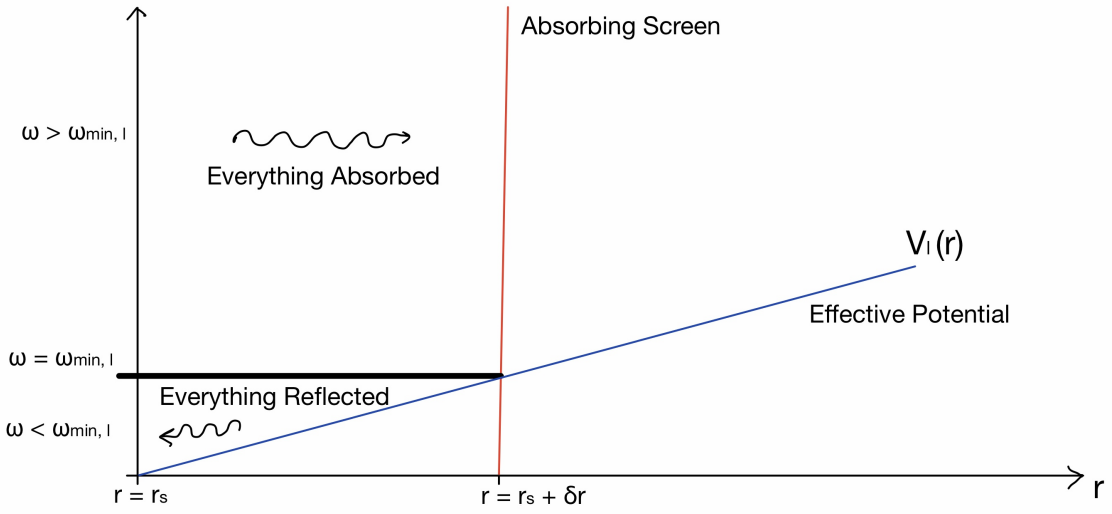

Figure 4.1: Above is a depiction of how perturbations behave near the horizon with a generalized greybody factor given in Eq. (4.13). Near the horizon the Potential $V_\ell(r)$ is linear and is depicted by the solid blue line. The slope of the blue line increases with ℓ. The absorptive boundary is depicted by the vertical red line at $r = r_s + \delta r$. The thick black line is a lower bound for the frequency of radiation that gets absorbed. Everything below the thick line has frequency $\omega < \omega_{min,\ell} = \sqrt{V_\ell(r_s + \delta r)}$ and cannot get to the absorbing surface, it bounces off the potential and gets reabsorbed. Everything above the thick line has frequency $\omega > \omega_{min,\ell}$ and is able to reach the absorptive surface and gets completely absorbed.

4.2.2 AdS Schwarzschild Black Holes

In this section we will estimate the evaporation rate of a $d+1$ - dimensional AdS Schwarzschild black hole[7]. We start by doing the integral in Eq. (4.14) and obtain the following result:

$$\frac{dM}{dt} = \frac{N_b}{2\pi\beta^2}\sum_{\ell=0}^{\infty} N_\ell \left[Li_2\left(e^{-x_{min,\ell}}\right) - x_{min,\ell}\ln\left(1-e^{-x_{min,\ell}}\right)\right], \tag{4.16}$$

[7]The AdS Schwarzschild black hole has the following line element $ds^2 = -f(r)dt^2 + \frac{dr^2}{f(r)} + r^2 d\Omega^2_{d-1}$, where $f(r) = 1 + \frac{r^2}{L^2} - \left(\frac{r_s}{r}\right)^{d-2}\left(1 + \frac{r_s^2}{L^2}\right)$. The Hawking temperature of these black holes are given by $T_H = \frac{dr_s^2 + (d-2)L^2}{4\pi r_s L^2}$

where the $x_{min,\ell}$ is given by:

$$x_{min,\ell} = \beta\omega_{min,\ell} = \sqrt{4\pi\left(2\pi(d-1) + \frac{\beta\ell(\ell+d-2)}{r_s}\right)\frac{\delta r}{r_s}}, \tag{4.17}$$

and $Li_m(x)$ is the m-th order polylog function in x. We estimate the value of the series as follows. We note that $x_{min,\ell}$ increases with ℓ. So for sufficiently large ℓ we have the following leading order approximation for the evaporation rate:

$$Li_2\left(e^{-x_{min,\ell}}\right) - x_{min,\ell}\ln\left(1-e^{-x_{min,\ell}}\right) \simeq (1+x_{min,\ell})e^{-x_{min,\ell}} + \mathcal{O}\left(e^{-2x_{min,\ell}}\right). \tag{4.18}$$

We expect the approximation used above is accurate for very large values of ℓ. In Figure 4.2 we plot the exact function and the approximation. If we use the approximated function

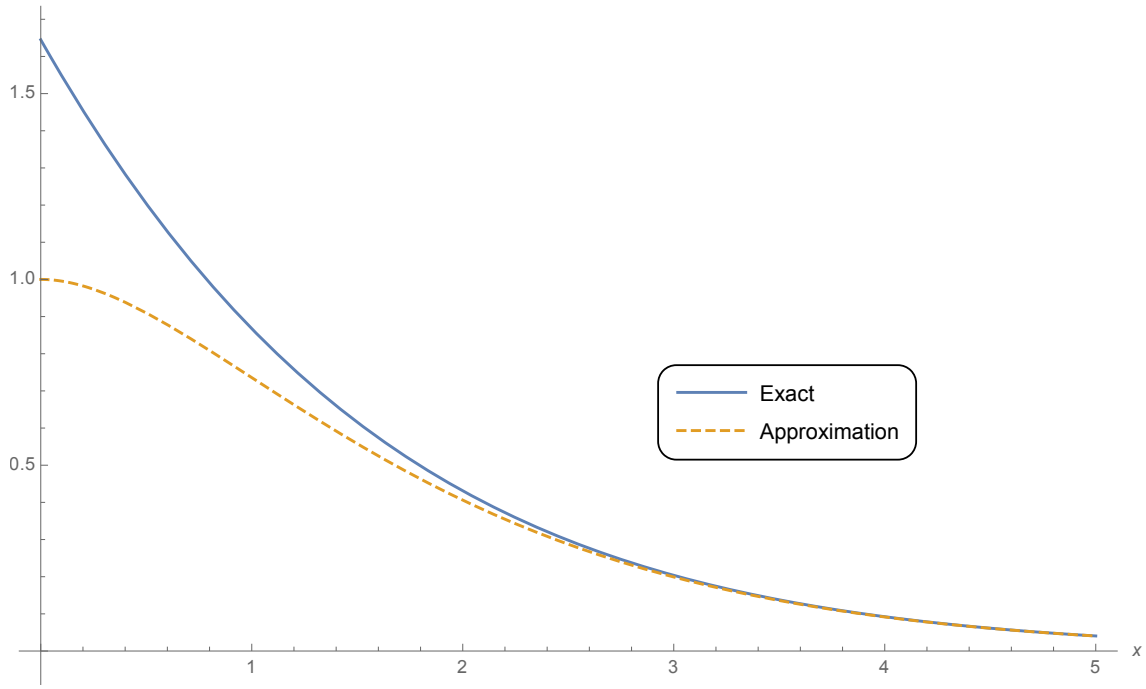

Figure 4.2: The solid blue line labeled "Exact" is the left hand side of Eq. (4.18) and the dotted yellow line labeled "Approximation" is the right hand side of Eq. (4.18).

for any $\ell \geq 1$ we expect to get a reasonable estimate for the series (accurate within an

order of magnitude). We approximate the degeneracy of angular momentum modes as $N_\ell \sim \ell^{d-2}$ so we have:

$$\frac{dM}{dt} \approx \frac{N_b}{2\pi\beta^2}\left[\frac{\pi^2}{6} + \sum_{\ell=1}^{\infty}\left[\ell^{d-2}\left(1+x_{min,\ell}\right)e^{-x_{min,\ell}}\right]\right], \tag{4.19}$$

where the $\pi^2/6$ term comes from the $\ell = 0$ mode in the limit where $\delta r/r_s \to 0$. To do the sum over modes with $\ell \geq 1$ in closed form we need to make an additional approximation that simplifies the functional form of $x_{min,\ell}$:

$$\begin{aligned} x_{min,\ell} &\approx \alpha\ell \\ \alpha &= \sqrt{\frac{4\pi\beta\delta r}{r_s^2}} \ll 1. \end{aligned} \tag{4.20}$$

This approximation comes from the leading order expansion of $x_{min,\ell}$ for large ℓ. We can then do the sum in closed form and get:

$$\begin{aligned} \frac{dM}{dt} &\approx \frac{N_b}{2\pi\beta^2}\left[\frac{\pi^2}{6} + \sum_{\ell=1}^{\infty}\ell^{d-2}\left(1+\alpha\ell\right)e^{-\alpha\ell}\right] \\ &= \frac{N_b}{2\pi\beta^2}\left[\frac{\pi^2}{6} + \alpha Li_{1-d}\left(e^{-\alpha}\right) + Li_{2-d}\left(e^{-\alpha}\right)\right]. \end{aligned} \tag{4.21}$$

If $\delta r/r_s$ is sufficiently small (i.e. the screen is sufficiently close to the horizon) we can do a series expansion in α near zero. The leading order contribution to the estimate for the evaporation rate is given by:

$$\frac{dM}{dt} \approx \frac{N_b}{2\pi\beta^2}\left[d(d-2)!\left(\frac{r_s^2}{4\pi\beta\delta r}\right)^{\frac{d-1}{2}} + \mathcal{O}(1)\right]. \tag{4.22}$$

In Appendix C.1 we do a detailed comparison of our leading order estimate for the evaporation rate given in Eq. (4.22) with numerical calculations. We find that our estimate for the series agrees with numerical results up to a pre-factor of order 1 (see Tables C.1 - C.3). Notice that the $\ell = 0$ mode is a order one correction to the leading order term which is much larger if $\delta r/r_s$ is sufficiently small (i.e. the screen is placed sufficiently close). To avoid clutter in our leading order expression we will define a dimension dependent coefficient $\mathcal{A}_d$ and write the evaporation rate as:

$$\frac{dM}{dt} \approx \frac{\mathcal{A}_d N_b}{\beta^2}\left(\frac{r_s^2}{\beta\delta r}\right)^{\frac{d-1}{2}}$$
$$\mathcal{A}_d = \frac{d(d-2)!\,(4\pi)^{\frac{1-d}{2}}}{2\pi}. \tag{4.23}$$

4.2.3 Near Extremal AdS RN Black Holes

Now lets consider $d+1$ - dimensional near extremal AdS RN black holes[8]. We analyze how the evaporation rate depends on where we extract radiation near the horizon. In this case we should expand V_ℓ to second order. This is because the first order expansion of V_ℓ is proportional the temperature which will go to zero in the extremal limit. Sufficiently close to the extremal regime the second order term will dictate the leading order behaviour of the potential close to the horizon.

$$\begin{aligned}
V_\ell(r) &\simeq V_1(r-r_s) + \frac{V_2}{2}(r-r_s)^2 + ... \\
V_1 &= \frac{4\pi}{\beta}\left[\frac{(d-1)2\pi}{\beta r_s} + \frac{\ell(\ell+d-2)}{r_s^2}\right] \\
V_2 &= f''(r_s)\frac{\ell(\ell+d-2)}{r_s^2} \\
&+ \frac{4\pi}{\beta}\left[2\frac{d}{dr}\left(\frac{d-1}{2r}\frac{df}{dr} + \frac{(d-1)(d-3)f(r)}{4r^2} + \frac{\ell(\ell+d-2)}{r^2}\right) + f''(r)\frac{d-1}{2r}\right]\Bigg|_{r=r_s}.
\end{aligned} \tag{4.24}$$

The expansion above will be valid if $r - r_s \ll r_s$. Sufficiently close to the extremal regime we will have the leading order contribution equal to:

$$V_\ell(r) = \frac{f''_{ext}(r_s)}{2}\frac{\ell(\ell+d-2)}{r_s^2}(r-r_s)^2. \tag{4.25}$$

As before, we can consider placing a perfectly absorbing surface a radial distance δr from the horizon. If we decide to use the Heaviside step model in Eq. (4.13) then we will need

[8]The $d+1$ - dimensional AdS RN black hole has a line element of the form $ds^2 = -f(r)dt^2 + \frac{dr^2}{f(r)} + r^2 d\Omega_{d-1}^2$, where $f(r) = \left(1 - \frac{r_s^{d-2}}{r^{d-2}}\right)\left(1 - \frac{Q^2}{r^{d-2}r_s^{d-2}}\right) + \frac{r^2}{L^2}\left(1 - \frac{r_s^d}{r^d}\right)$, where r_s is the radius of the horizon and Q is the charge of the black hole. The black hole is extremal when the charge and horizon radius satisfy the following relation, $Q^2 = r_s^{2(d-2)}\left(1 + \frac{d}{d-2}\frac{r_s^2}{L^2}\right)$, this occurs when $T_H = \frac{f'(r_s)}{4\pi} = 0$.

to do the integral in Eq. (4.14) with the lower bound:

$$x_{min,\ell} = \beta\omega_{\min,\ell} = \frac{\beta\delta r}{r_s}\sqrt{\frac{f''_{ext}(r_s)\ell(\ell+d-2)}{2}}. \tag{4.26}$$

Unlike the non-extremal case we discussed previously the lower bound is much larger than unity sufficiently close to the extremal regime. This means that we are well into the exponentially decaying tail of the integrand. Recall that the Heaviside step function model was used to simulate the effective potential as a "hard" wall. In reality we know that the waves can actually enter the classically forbidden region. The amplitude of the solution will decay through some power law in the classically forbidden region. By the time a wave with $\omega < \omega_{min,\ell}$ reaches the absorptive surface its amplitude would be power law suppressed as depicted in Fig 4.3. The Heaviside model completely disregards these effects. This would

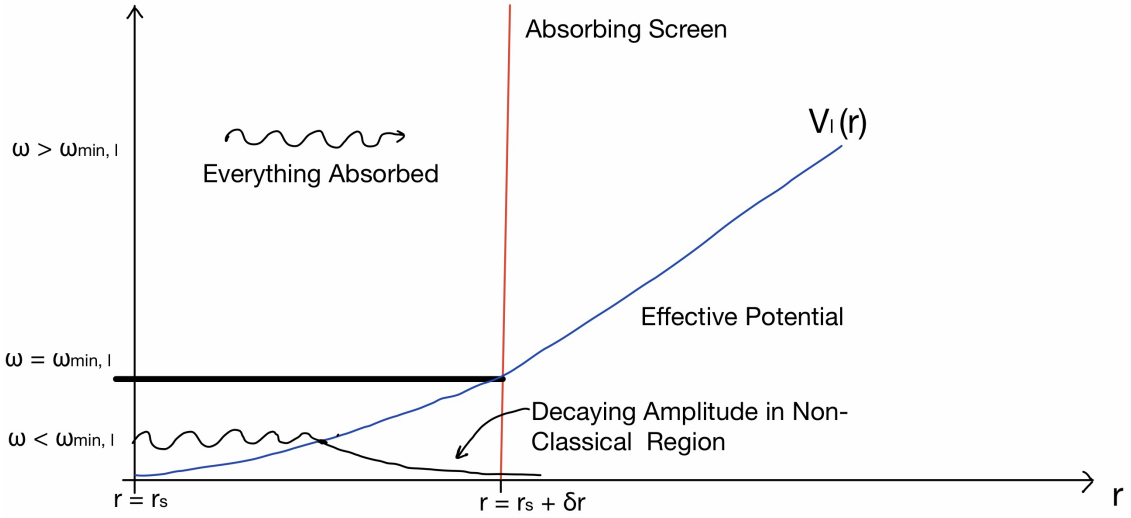

Figure 4.3: Above is a depiction of how perturbations behave near the horizon with a generalized greybody factor given in Eq. (4.28). For $\omega_{min,\ell}$ the model is unchanged and everything is absorbed. However, for $\omega < \omega_{min,\ell}$ we account for the wave-like behaviour of the solution which allows for the solution to tunnel into the classically forbidden region. The amplitude the the solution would decay as some power law after the classical turning point. We estimate the amount of energy that tunnels to the absorptive surface by taking the ratio between the amplitude of the solution at the turning point and the amplitude at the absorptive surface. Doing this gives a power law suppression of the generalized greybody factor for $\omega < \omega_{min,\ell}$ in Eq. (4.28).

be okay if the contribution of modes with $\omega \geq \omega_{min,\ell}$ was not exponentially suppressed, but since it is suppressed in the near extremal regime we need to consider the effects of $\omega < \omega_{min,\ell}$. Therefore, for a near extremal black hole we need a generalized greybody factor of the form:

$$\gamma_\ell(\omega, \delta r) = \Theta(\omega - \omega_{min,\ell}) + \left(\frac{\omega}{\omega_{min,\ell}}\right)^{q(\ell)} \Theta\left(\omega_{min,\ell} - \omega\right), \tag{4.27}$$

where $q(\ell)$ is some function of ℓ which will be determined by analyzing the dynamics of the perturbations near the horizon and gives us the power law decay we need. The details of how to obtain a reasonable model for $q(\ell)$ for scalar wave perturbations is detailed in Appendix C.2. The result for $\ell \geq 1$ is:

$$\begin{aligned} \gamma_\ell(\omega, \delta r) &= \Theta(\omega - \omega_{min,\ell}) + \left(\frac{\omega}{\omega_{min,\ell}}\right)^{2\nu_\ell+1} \Theta\left(\omega_{min,\ell} - \omega\right) \\ \nu_\ell &= \sqrt{\frac{1}{4} + \alpha_\ell^2} \\ \alpha_\ell^2 &= \frac{2\ell(\ell + d - 2)}{r_s^2 f''_{ext}(r_s)}, \end{aligned} \tag{4.28}$$

where $f''_{ext}(r_s)$ is the second derivative of $f(r)$ evaluated at the horizon radius r_s, in the limit where the Hawking temperature goes to zero. Using this, the expression for the contribution to the evaporation rate for $\ell \geq 1$ is given by[9]:

$$\begin{aligned} \frac{dM}{dt} &= \frac{N_b}{2\pi} \sum_{\ell=1}^{\infty} \left[\int_0^{\omega_{min,\ell}} \frac{N_\ell \omega}{e^{\beta\omega} - 1} \left(\frac{\omega}{\omega_{min,\ell}}\right)^{2\nu_\ell+1} d\omega + \int_{\omega_{\min,\ell}}^{\infty} \frac{N_\ell \omega}{e^{\beta\omega} - 1} d\omega \right] \\ &= \frac{N_b}{2\pi} \sum_{\ell=1}^{\infty} \omega_{min,\ell}^2 N_\ell \left[\int_0^1 \frac{\epsilon^{2(\nu_\ell+1)}}{e^{\beta\omega_{min,\ell}\epsilon} - 1} d\epsilon + \int_1^{\infty} \frac{\epsilon}{e^{\beta\omega_{min,\ell}\epsilon} - 1} d\epsilon \right]. \end{aligned} \tag{4.29}$$

With some work detailed in Appendix C.3 we can do the integrals in closed form and write the total evaporation rate as the following series over ℓ:

[9] We are not including the $\ell = 0$ mode in this section, in Appendix C.6 we treat the $\ell = 0$ mode. We show that for very large AdS black holes sufficiently close to the extremal regime the $\ell = 0$ contribution is sub-leading compared to the contribution of modes with $\ell \geq 1$. For very small AdS black holes and asymptotically flat black holes the $\ell = 0$ mode has a leading order effect on the evaporation rate when $d \leq 8$ in the near extremal regime, we discuss this point and also discuss its consequences on the information re-emergence time. Overall we find that including the $\ell = 0$ results in minor changes in the expressions for information re-emergence time which are consistent with the usual scrambling time scales for nearly extremal AdS RN black holes.

$$
\begin{aligned}
\frac{dM}{dt} &= \frac{N_b}{2\pi\beta^2}\sum_{\ell=1}^{\infty}\left[S_{tun,\ell}+S_{ntun,\ell}\right] \\
S_{tun,\ell} &= N_\ell\left[\frac{\Gamma\left(3+\sqrt{1+4\alpha_\ell^2}\right)Li_{3+\sqrt{1+4\alpha_\ell^2}}\left(1\right)}{x_{min,\ell}^{1+\sqrt{1+4\alpha_\ell^2}}}\right] \\
S_{ntun,\ell} &= N_\ell\left[Li_2\left(e^{-x_{min,\ell}}\right)-x_{min,\ell}\ln\left(1-e^{-x_{min,\ell}}\right)\right] \\
x_{min,\ell} &= \beta\omega_{min,\ell} = \frac{\beta\delta r\, f''_{ext}(r_s)\alpha_\ell}{2} = \frac{\beta\delta r}{r_s}\sqrt{\frac{f''_{ext}(r_s)\ell(\ell+d-2)}{2}}.
\end{aligned}
\tag{4.30}
$$

The terms $S_{tun,\ell}$ in Eq. (4.30) represents the contribution of to the evaporation rate of modes that tunnel through the effective potential. The terms $S_{ntun,\ell}$ in Eq. (4.30) represent the contribution to the evaporation rate of modes that do not need to tunnel through the barrier to reach the screen. When we are sufficiently close to the extremal regime we can show that $S_{tun,\ell} \gg S_{ntun,\ell}$ (this point is discussed in Appendix C.4). This means that sufficiently close to the extremal regime we can ignore $S_{ntun,\ell}$ and write:

$$
\frac{dM}{dt} \approx \frac{N_b}{2\pi\beta^2}\sum_{\ell=1}^{\infty}S_{tun,\ell} = \frac{N_b}{2\pi\beta^2}\sum_{\ell=1}^{\infty}\ell^{d-2}\left[\frac{\Gamma\left(3+\sqrt{1+4\alpha_\ell^2}\right)Li_{3+\sqrt{1+4\alpha_\ell^2}}\left(1\right)}{x_{min,\ell}^{1+\sqrt{1+4\alpha_\ell^2}}}\right], \tag{4.31}
$$

where we used $N_\ell \sim \ell^{d-2}$. We cannot evaluate the series in closed form so we resort to additional approximations.

We begin by considering the case of very large AdS black holes where $r_s/L \gg 1$. In this case we have:

$$
\alpha_{\ell+1}-\alpha_\ell = \frac{\sqrt{2\ell(\ell+d-2)}-\sqrt{2(\ell+1)(\ell+d-1)}}{\sqrt{d(d-1)}}\frac{L}{r_s} \sim \left(\frac{r_s}{L}\right)^{-1} \ll 1. \tag{4.32}
$$

The spacing between consecutive α_ℓ becomes smaller as the AdS black holes we are considering become larger relative to the AdS radius. In this case, we estimate the sum using

an integral as follows:

$$\begin{aligned}\frac{dM}{dt} &\approx \frac{N_b}{2\pi\beta^2}\int_1^\infty \ell^{d-2}\left[\frac{\Gamma\left(3+\sqrt{1+4\alpha_\ell^2}\right)Li_{3+\sqrt{1+4\alpha_\ell^2}}(1)}{x_{min,\ell}^{1+\sqrt{1+4\alpha_\ell^2}}}\right]d\ell \\ &= \frac{N_b}{2\pi\beta^2}\int_{\alpha_1}^\infty\left(\frac{d-2}{2}\left[-1+\sqrt{1+\frac{2r_s^2 f''_{ext}(r_s)\alpha_\ell^2}{(d-2)^2}}\right]\right)^{d-2} \\ &\times\left[\frac{\Gamma\left(3+\sqrt{1+4\alpha_\ell^2}\right)Li_{3+\sqrt{1+4\alpha_\ell^2}}(1)}{\left(\frac{\beta\delta r f''_{ext}(r_s)\alpha_\ell}{2}\right)^{1+\sqrt{1+4\alpha_\ell^2}}}\right]\left(\frac{\alpha_\ell r_s^2 f''_{ext}(r_s)}{(d-2)\sqrt{1+\frac{2r_s^2 J''_{ext}(r_s)\alpha_\ell^2}{(d-2)^2}}}\right)d\alpha_\ell,\end{aligned} \tag{4.33}$$

where in the last line we simply changed the variables of integration from ℓ to α_ℓ using the definition of α_ℓ in Eq. (4.28). The lower bound of integration is α_1, equal to:

$$\alpha_1 = \sqrt{\frac{d-1}{(d-2)^2+d(d-1)\frac{r_s^2}{L^2}}} \approx \sqrt{\frac{L^2}{dr_s^2}} \ll 1. \tag{4.34}$$

For very large AdS black holes ($d \geq 4$) we use the following approximation for the integrand: (The steps to arrive at this approximation are described in Appendix C.5 we also make plots to show that the the approximation will become more accurate as r_s/L becomes larger.):

$$\begin{aligned}\left.\frac{dM}{dt}\right|_{d\geq 4} &\approx \frac{N_b}{2\pi\beta^2}\int_0^\infty \frac{\pi^4}{15}\left(\frac{r_s^2 f''_{ext}(r_s)}{2}\right)^{\frac{d-1}{2}}\left(\frac{\beta\delta r f''_{ext}(r_s)}{2}\right)^{-2-2\alpha_\ell^2}\alpha_\ell^{d-4}d\alpha_\ell \\ &= \frac{N_b}{2\pi\beta^2}\frac{\pi^4}{15}\left(\frac{r_s^2 f''_{ext}(r_s)}{4}\right)^{\frac{d-1}{2}}\left[\ln\left(\frac{\beta\delta r f''_{ext}(r_s)}{2}\right)\right]^{\frac{3-d}{2}}\left(\frac{2}{\beta\delta r f''_{ext}(r_s)}\right)^2\Gamma\left(\frac{d-3}{2}\right) \\ &\approx \frac{N_b}{2\pi\beta^2}\frac{\pi^4}{15}\left(\frac{2d(d-1)r_s^2}{4L^2}\right)^{\frac{d-1}{2}}\left[\ln\left(\frac{d(d-1)\beta\delta r}{L^2}\right)\right]^{\frac{3-d}{2}}\left(\frac{L^2}{d(d-1)\beta\delta r}\right)^2\Gamma\left(\frac{d-3}{2}\right).\end{aligned} \tag{4.35}$$

Note that the expression above is ill defined for $d = 3$. This is because we approximated the lower bound of the integral using 0. If we instead use α_1 for the lower bound we will

get a well defined result for $d = 3$ given by:

$$\begin{aligned}\left.\frac{dM}{dt}\right|_{d=3} &\approx \frac{N_b}{2\pi\beta^2}\frac{\pi^4}{15}\left(\frac{r_s^2 f''_{ext}(r_s)}{2}\right)\int_{\alpha_1}^{\infty}\left(\frac{\beta\delta r f''_{ext}(r_s)}{2}\right)^{-2-2\alpha_\ell^2}\alpha_\ell^{-1}d\alpha_\ell \\ &= \frac{N_b}{2\pi\beta^2}\frac{\pi^4}{15}\left(\frac{r_s^2 f''_{ext}(r_s)}{2}\right)\left[-\frac{Ei\left[-2\alpha_1^2\ln\left(\frac{\beta\delta r f''_{ext}(r_s)}{2}\right)\right]}{2\left(\frac{\beta\delta r f''_{ext}(r_s)}{2}\right)^2}\right],\end{aligned} \tag{4.36}$$

where $Ei(x)$ is the exponential integral function. The leading order contribution for $\alpha_1 \ll 1$ expansion gives the following evaporation rate:

$$\left.\frac{dM}{dt}\right|_{d=3} \approx \frac{N_b}{2\pi\beta^2}\frac{\pi^4}{15}\left(\frac{r_s^2 f''_{ext}(r_s)}{2}\right)\left[\frac{-\gamma-\ln\left[2\alpha_1^2\ln\left(\frac{\beta\delta r f''_{ext}(r_s)}{2}\right)\right]}{2\left(\frac{\beta\delta r f''_{ext}(r_s)}{2}\right)^2}\right], \tag{4.37}$$

where $\gamma \approx 0.577$ is the Euler–Mascheroni constant. Note that for this expansion to make sense $\alpha_1^2\ln\left(\beta\delta r f''_{ext}(r_s)\right) \ll 1$, this will be true if r_s/L is sufficiently large (i.e. for very large AdS black holes):

$$\left.\frac{dM}{dt}\right|_{d=3} \approx -\frac{N_b}{2\pi\beta^2}\frac{\pi^4}{15}\frac{6r_s^2}{L^2}\left[\frac{\ln\left[\frac{2L^2}{3r_s^2}\ln\left(\frac{6\beta\delta r}{L^2}\right)\right]+\gamma}{2\left(\frac{6\beta\delta r}{L^2}\right)^2}\right]. \tag{4.38}$$

We compare the estimated evaporation rate to a numerical calculation of the full evaporation rate in Table 4.1. We find that the approximated result differs from the numerical result by a order one pre-factor, one can also check that the approximations will get better as r_s/L becomes larger (we can see this graphically by comparing Figures (C.1 - C.2)).

For very small AdS black holes (or asymptotically flat black holes) in the near extremal regime we will not need to sum all the modes to infinity. We can get a rough estimate by

d	3	4	6	8	10
Numerical	3.48×10^{-8}	2.87×10^{-7}	1.03×10^{-3}	4.02×10^{1}	6.25×10^{6}
Approximation	3.40×10^{-8}	2.91×10^{-7}	7.80×10^{-4}	2.38×10^{1}	2.79×10^{6}
$\mathcal{C}_{ext} = \frac{Numerical}{Approximation}$	1.02	0.99	1.32	1.69	2.24

Table 4.1: We fix $\frac{\beta\delta r}{r_s^2} = 100$ and $r_s/L = 100$. For different d we numerically calculate the series defined in Eq. (4.30) and compare to the approximated evaporation rate we found in Eq. (4.35) and Eq. (4.38) for $d \geq 4$ and $d = 3$ respectively. We can see that in higher dimensions the approximation is not as good as it is in lower dimension but the results differ by an order one factor given by $\mathcal{C}_{ext}$. Furthermore, if one does similar calculations for larger values of r_s/L we will find better agreement between the numerical result and approximated result.

simply computing the first term in the limit where $r_s/L \to 0$ we have[10]:

$$\frac{dM}{dt} \approx \frac{N_b}{2\pi\beta^2}\left[\frac{\Gamma\left(3+\sqrt{1+4\alpha_1^2}\right) Li_{3+\sqrt{1+4\alpha_1^2}}(1)}{x_{min,1}^{1+\sqrt{1+4\alpha_1^2}}}\right]$$
$$= \frac{N_b}{2\pi\beta^2}\left[\frac{\Gamma\left(\frac{2(2d-3)}{d-2}\right) Li_{\frac{2(2d-3)}{(d-2)}}(1)}{\left((d-1)(d-2)^2\left(\frac{\beta\delta r}{r_s^2}\right)^2\right)^{\frac{d-1}{d-2}}}\right] = \frac{N_b}{2\pi\beta^2}\left[\frac{\Gamma\left(\frac{2(2d-3)}{d-2}\right) Li_{\frac{2(2d-3)}{(d-2)}}(1)}{((d-1)(d-2)^2)^{\frac{d-1}{d-2}}}\right]\left(\frac{r_s^2}{\beta\delta r}\right)^{\frac{2(d-1)}{d-2}}. \tag{4.39}$$

In Table 4.2 we numerically verify that our estimation is valid when sufficiently close to the extremal regime.

Now that we have derived estimates for the evaporation rate it is useful to keep in mind that all the calculations we did in this subsection made the assumption that $\beta\omega_{min,\ell} \gg 1$.

[10]One can check that the ratio between the first and and second term in the series in the near extremal regime for very small AdS black holes will go as, $S_{tun,1}/S_{tun,2} \sim \left(\frac{\beta\delta r}{r_s^2}\right)^{\frac{2}{d-2}} \gg 1$. So the closer we are to the extremal regime smaller the sub-leading terms are compared to the first term. Furthermore, in higher dimensions we need to be closer to the extremal regime to similar errors as we might have in lower dimensions. We verify these statements with the results given in Table 4.2.

$\beta\delta r/r_s^2$	10^2	10^4	10^8	10^{16}	10^{32}
$\mathcal{C}_{d=3}$	1.00	1.00	1.00	1.00	1.00
$\mathcal{C}_{d=4}$	1.01	1.00	1.00	1.00	1.00
$\mathcal{C}_{d=5}$	1.07	1.00	1.00	1.00	1.00
$\mathcal{C}_{d=6}$	1.33	1.03	1.00	1.00	1.00
$\mathcal{C}_{d=7}$	2.32	1.16	1.00	1.00	1.00
$\mathcal{C}_{d=8}$	6.40	1.70	1.03	1.00	1.00
$\mathcal{C}_{d=9}$	26.6	3.82	1.15	1.00	1.00
$\mathcal{C}_{d=10}$	153	13.0	1.64	1.01	1.00

Table 4.2: We are setting $r_s/L = 0$ (asymptotically flat black holes or very small AdS black holes). We are computing $\mathcal{C}_d$ which is the ratio between the numerical calculation of Eq. (4.30) divided by the approximated result given by Eq. (4.39) for spacetime dimension $d+1$. We can see that for larger values of β the estimate for the evaporation rate using only $\ell = 1$ mode becomes more precise. This is because of the for larger β the $\ell = 1$ mode is dominant compared to all the $\ell > 1$ modes.

this implies that $\frac{\delta r}{r_s} \gg \left(\beta^2 f''_{ext}(r_s)\right)^{-1/2}$. We define the parameter Λ as follows:

$$\frac{\delta r}{r_s} = \frac{\Lambda}{\beta\sqrt{f''_{ext}(r_s)}} = \begin{cases} \frac{\Lambda L}{\beta\sqrt{2d(d-1)}}, & \text{for very large AdS BH in planar limit } (r_s/L \to \infty) \\ \frac{\Lambda r_s}{\beta\sqrt{2(d-2)^2}}, & \text{for very small AdS (or asymptotically flat) BH,} \end{cases} \tag{4.40}$$

where we require, $1 \ll \Lambda \ll \beta\sqrt{f''_{ext}(r_s)}$. In terms of Λ we express the evaporation rates of very large AdS black holes for $d \geq 4$ as:

$$\begin{aligned} \left.\frac{dM}{dt}\right|_{d\geq 4} &\approx \mathcal{A}^{large}_{d\geq 4}\left[\ln\left(\sqrt{\frac{d(d-1)}{2}}\frac{r_s}{L}\Lambda\right)\right]^{\frac{3-d}{2}} \frac{N_b}{\beta^2\Lambda^2}\left(\frac{r_s}{L}\right)^{d-3} \\ \mathcal{A}^{large}_{d\geq 4} &= \frac{\pi^3}{30}\left(\frac{d(d-1)}{2}\right)^{\frac{d-3}{2}}\Gamma\left(\frac{d-3}{2}\right). \end{aligned} \tag{4.41}$$

For very large AdS black holes for $d = 3$ we have:

$$\left.\frac{dM}{dt}\right|_{d=3} \approx \frac{\pi^3}{30}\frac{N_b}{\beta^2\Lambda^2}\left[\ln\left(\frac{3r_s^2}{2L^2}\right) - \ln\left(\ln\left(\frac{\sqrt{3}r_s\Lambda}{L}\right)\right) - \gamma\right] \sim \frac{\pi^3}{30}\frac{N_b}{\beta^2\Lambda^2}\ln\left(\frac{3r_s^2}{2L^2}\right). \tag{4.42}$$

For very small AdS black holes (or asymptotically flat ones) we have:

$$\frac{dM}{dt} \approx \frac{\mathcal{A}_d^{small} N_b}{\beta^2 \Lambda^{\frac{2(d-1)}{d-2}}}$$
$$\mathcal{A}_d^{small} = \frac{\left(\sqrt{2}(d-2)\right)^{\frac{2(d-1)}{d-2}}}{2\pi} \left[\frac{\Gamma\left(\frac{2(2d-3)}{d-2}\right) Li_{\frac{2(2d-3)}{(d-2)}}(1)}{((d-1)(d-2)^2)^{\frac{d-1}{d-2}}} \right]. \tag{4.43}$$

We will come back to the physical relevance of Λ when discussing the ambiguities of "fixing" the screen a certain distance from the horizon in Section 4.3.4.

4.3 Hayden-Preskill Decoding Criterion from Entanglement Wedge Reconstruction

4.3.1 Review of Pennington's Calculation

As we discussed in the introduction, it was shown in [73] that after the Page time a small amount of information thrown into a black hole could be reconstructed from subsequent Hawking radiation after the scrambling time scale. The works [117, 7] are able to reproduce this result in a holographic setting. The setup is to have the usual black hole in AdS which is dual to some CFT on the boundary. This is then supplemented by some type of absorbing boundary condition at the boundary which allows the radiation emitted by the black hole to be absorbed and stored. The radiation in the reservoir purifies the the black hole CFT state. There are two entanglement wedges in this scenario, one corresponds to the entanglement wedge of the black hole and the other is the entanglement wedge of the reservoir where radiation is absorbed. As the black hole evaporates these entanglement wedges have time dependence and it can be shown that information that is initially sitting in the entanglement wedge of the black hole a scrambling time in the past (assuming we are considering a time after the Page time) will end up in the entanglement wedge of the reservoir. This is equivalent to saying that information thrown into a black hole, after a Page time has elapsed, will re-emerge in the subsequent radiation after a scrambling time as is claimed in the Hayden-Preskill decoding protocol [73].

In this section, we review some of the details of how this scrambling time scale appears in Pennington's calculations [117]. It comes from trying to find the location of a classical "maximin" surface in the spacetime of a spherically symmetric evaporating black hole

(which happens to be a good approximation for where the quantum extremal surface is after a Page time has elapsed[11]). The determination of the location of the surface eventually comes down to the following calculation. The first step is to start with a static spherically symmetric black hole metric of the form:

$$ds^2 = -f(r)dt^2 + \frac{dr^2}{f(r)} + r^2 d\Omega_{d-1}^2. \tag{4.44}$$

Then one defines ingoing Eddington-Finkelstein coordinates $v = t + r_*$ where $dr = f(r)dr_*$. With some simple manipulations one arrives at the following metric:

$$ds^2 = -f(r)dv^2 + 2dvdr + r^2 d\Omega_{d-1}^2. \tag{4.45}$$

Upon doing this one approximates the metric of an evaporating black hole by introducing time dependence into f by allowing the Schwarzschild radius r_s to become time dependent (i.e. $r_s = r_s(v)$). One then considers radial null geodesics on this evaporating black hole spacetime. The radial coordinate r_{lc} describing the trajectory of these null geodesics satisfy:

$$\frac{dr_{lc}}{dv} = \frac{f(r_{lc})}{2} \simeq \frac{2\pi}{\beta}(r_{lc} - r_s). \tag{4.46}$$

The right most expression comes from expanding $f(r_{lc})$ to first order and $\beta = T_H^{-1} = 4\pi/f'(r_s)$. Define a coordinate $r'_{lc} = r_{lc} - r_s$ then we will find:

$$\frac{dr'_{lc}}{dv} = \frac{2\pi}{\beta} r'_{lc} - \frac{dr_s}{dv}. \tag{4.47}$$

Under the assumption that $dr_s/dv < 0$ and approximately constant the equation can be integrated to find:

$$r_{lc} = r_s + Ce^{2\pi v/\beta} + \frac{\beta}{2\pi}\frac{dr_s}{dv}, \tag{4.48}$$

where C is an integration constant. It is clear that when $C = 0$, then r_{lc} is constant (up to corrections caused by dr_s/dv not being constant.) this defines the horizon of the

[11] It should be noted that we are actually interested in the quantum extremal surface which is found by applying the maximin prescription to a functional given by $\frac{A(\chi)}{4G_N} + S_{bulk}(\chi)$. The calculation we are reviewing here finds the classical maximin surface, which is found by applying the maximin prescription to the area term ignoring the S_{bulk} term. In [117], Pennington argues that the classical maximin surface will only deviate slightly (even when one accounts for greybody factors) when the S_{bulk} term is included and the quantum extremal surface will stabilize close to the classical maximin surface which lies on the lightcone. Throughout this chapter we are going to assume that these arguments are still valid for our construction.

evaporating black hole which is given by:

$$r_{hor} = r_s \left(1 + \frac{\beta}{2\pi r_s}\frac{dr_s}{dv}\right) < r_s. \tag{4.49}$$

Lets compute dr_{hor}/dv:

$$\frac{dr_{hor}}{dv} = \frac{dr_s}{dv} + \frac{d\beta/dv}{2\pi}\frac{dr_s}{dv} = \frac{dr_s}{dv} + \mathcal{O}((dr_s/dv)^2) \sim \frac{dr_s}{dv}. \tag{4.50}$$

With this we can compute dr_{lc}/dv:

$$\frac{dr_{lc}}{dv} \simeq \frac{2\pi C}{\beta} e^{2\pi v/\beta}\left(1 - \frac{v}{\beta}\frac{d\beta}{dv}\right) + \frac{dr_s}{dv} + \mathcal{O}((dr_s/dv)^2). \tag{4.51}$$

Assuming that $\left|\frac{v}{\beta}\frac{d\beta}{dv}\right| \ll 1$ we can solve for when $dr_{lc}/dv = 0$ this occurs when[12]:

$$v = v_0 = -\frac{\beta}{2\pi}\ln\left(\frac{2\pi C}{\beta\left|\frac{dr_s}{dv}\right|}\right). \tag{4.52}$$

To determine $|dr_s/dv|$, Pennington makes the assumption that Hawking quanta emitted by the black hole is assumed to be extracted sufficiently close to the horizon so that one can use the 2D Stefan-Boltzman law:

$$\frac{dM}{dv} = \frac{c_{evap}\pi}{12\beta^2}, \tag{4.53}$$

where $c_{evap} = N_b + N_f/2$ where N_b and N_f are the number of bosonic and fermionic modes respectively. Using the first law of black hole thermodynamics the rate of energy loss can be related to dr_s/dv the final result is:

$$\left|\frac{dr_s}{dv}\right| = \frac{4\beta\ell_p^{d-1}}{\Omega_{d-1}(d-1)r_s^{d-2}}\left|\frac{dM}{dv}\right| = \frac{c_{evap}\pi\ell_p^{d-1}}{3\beta(d-1)r_s^{d-2}\Omega_{d-1}}. \tag{4.54}$$

This results in:

$$v_0 \simeq -\frac{\beta}{2\pi}\ln\left(\frac{Cr_s^{d-2}\Omega_{d-1}}{c_{evap}G_N}\right) \sim \begin{cases} -\frac{\beta}{2\pi}\ln\left(\frac{r_s^{d-1}}{c_{evap}\ell_p^{d-1}}\right), & \text{for non-extremal BH} \\ -\frac{\beta}{2\pi}\ln\left(\frac{r_s}{c_{evap}\beta}\frac{r_s^{d-1}}{\ell_p^{d-1}}\right), & \text{for near extremal BH.} \end{cases} \tag{4.55}$$

[12]The length scale of C was chosen by analyzing how far the expansion $f(r)$ near the horizon is valid to first order. In particular, it is not hard to see that $C \sim \frac{1}{\beta f''(r_s)}$. For small AdS black holes $f''(r_s) \sim r_s^{-2}$ (as noted by Pennington) and for large AdS black holes $f''(r_s) \sim L^{-2}$ (not discussed by Pennington), where r_s and L are the horizon and AdS radius respectively.

So after the Page time, information thrown into the black hole reemerges after waiting for the time scale $|v_0| = t_{emerge}$ in Eq. (4.2). Note that in the near extremal case the expression written down above is valid for small near extremal AdS black holes. For large near extremal AdS black holes $C \sim L^2/\beta$ so there will be some awkward L dependence inside the Log. As we will see in the following sections, by properly understanding c_{evap} for large AdS black holes, the length scale in the Log will come out to be L instead of r_s.

4.3.2 Information Emergence Time for AdS Schwarzschild Black Hole

Using our newly derived evaporation rate in Eq. (4.23) along with the first law of black hole thermodynamics and the area law for entropy of a black hole we will get:

$$\begin{aligned}\left|\frac{dr_s}{dt}\right| &= \frac{4\beta\ell_p^{d-1}}{(d-1)\Omega_{d-1}r_s^{d-2}}\left|\frac{dM}{dt}\right| = \frac{4\mathcal{A}_d}{(d-1)\Omega_{d-1}}\frac{N_b\ell_p^{d-1}}{\beta r_s^{d-2}}\left(\frac{r_s^2}{\delta r\beta}\right)^{\frac{d-1}{2}} \\ &\sim \frac{N_b\ell_p^{d-1}}{\beta r_s^{d-2}}\left(\frac{r_s^2}{\delta r\beta}\right)^{\frac{d-1}{2}}.\end{aligned} \tag{4.56}$$

To avoid clutter in our expressions we drop Ω_{d-1} and other dimensionless factors. Plugging this into Eq. (4.2) we find for non-extremal black holes:

$$t_{emerge} \sim \frac{\beta}{2\pi}\ln\left(\frac{(\delta r\beta)^{\frac{d-1}{2}}}{N_b\ell_p^{d-1}}\right). \tag{4.57}$$

For very large AdS Schwarzschild black holes ($r_s \gg L$) and the inverse temperature goes as $\beta \sim L^2/r_s$. Plugging this into Eq. (4.57) we find that Pennington's scrambling time scale results in:

$$t_{emerge} \sim \frac{\beta}{2\pi}\left[\ln\left(\frac{L^{d-1}}{N_b\ell_p^{d-1}}\right) - \frac{d-1}{2}\ln\left(\frac{r_s}{\delta r}\right)\right], \tag{4.58}$$

where we assume that $L/\ell_p \gg r_s/\delta r$. The interesting thing to note here is that the leading order term is not the the Log of the entropy of the horizon of the black hole. It is actually the entropy of a small cell on the horizon which has the size of the AdS radius L. We can do a similar calculation for very small AdS black holes ($r_s \ll L$) in this case $\beta \sim r_s$ and we will obtain a more familiar result that Pennington got up to a Log correction that depends on where we place our absorptive screen:

$$t_{emerge} \sim \frac{\beta}{2\pi}\left[\ln\left(\frac{r_s^{d-1}}{N_b\ell_p^{d-1}}\right) - \frac{d-1}{2}\ln\left(\frac{r_s}{\delta r}\right)\right]. \tag{4.59}$$

As we can see from Eq. (4.58), by understanding the explicit dependence of c_{evap} on β we find that t_{emerge} contains the Bekenstein-Hawking entropy of a cell on the horizon of characteristic length L inside the Log. This reasonable and consistent with the scrambling time discussed in [134] for large AdS black holes dual to large N gauge theories[13].

4.3.3 Information Emergence Time for Near Extremal AdS RN Black Hole

Now lets consider what happens for near extremal AdS RN black holes. We can compute $|dr_s/dt|$ using the first law up to some dimensionless pre-factors we have:

$$\left|\frac{dr_s}{dt}\right| \sim \frac{\beta \ell_p^{d-1}}{r_s^{d-2}} \left|\frac{dM}{dt}\right| . \tag{4.60}$$

We can compute $|dr_s/dt|$ using the evaporation rates in Eqs. (4.41)-(4.43). We then plug these into Eq. (4.2) and obtain the following results.

Case 1, small AdS black hole: $r_s \ll L$

In this case we have:

$$t_{emerge} \sim \frac{\beta}{2\pi} \ln\left(\frac{r_s^2}{\beta^2 \left|\frac{dr_s}{dt}\right|}\right) \sim \frac{\beta}{2\pi}\left[\ln\left(\frac{r_s}{\beta}\frac{r_s^{d-1}}{N_b \ell_p^{d-1}}\right) + \frac{2(d-1)}{(d-2)}\ln(\Lambda)\right], \tag{4.61}$$

where $1 \ll \Lambda \ll \beta/r_s$.

Case 2, large AdS black hole: $r_s \gg L$

In this case we have:

$$\frac{2\pi t_{emerge}}{\beta} \sim \ln\left(\frac{L^2}{\beta^2 \left|\frac{dr_s}{dt}\right|}\right) \sim \begin{cases} \ln\left(\frac{r_s}{\beta}\frac{L^2}{N_b \ell_p^2}\right) + \ln\left(\frac{\Lambda^2}{\ln(3r_s^2/L^2)}\right), & d = 3 \\ \ln\left(\frac{r_s}{\beta}\frac{L^{d-1}}{N_b \ell_p^{d-1}}\right) + \ln\left(\Lambda^2\left[\ln\left(\sqrt{\frac{d(d-1)r_s^2\Lambda^2}{2L^2}}\right)\right]^{\frac{d-3}{2}}\right), & d \geq 4, \end{cases} \tag{4.62}$$

where $1 \ll \Lambda \ll \beta/L$.

[13] Recall that the ratio $(L/\ell_p)^{d-1} \sim N^2$ [126].

If we make the assumption that Λ has no additional β dependence then we see the for small AdS black hole the first term matches what Pennington had. For large AdS black holes we again see that L instead of r_s appears in the leading order Log term. In the next section we will discuss an ambiguity that Λ presents us with for near extremal black holes which is related to where we place our absorptive screen.

4.3.4 Information Emergence Time as Scrambling Time

In the previous sections we found that the time scale after which information re-emerges for AdS Schwarzschild black holes is given as:

$$t_{emerge} \sim \begin{cases} \frac{\beta}{2\pi}\left[\ln\left(\frac{r_s^{d-1}}{N_b \ell_p^{d-1}}\right) - \frac{d-1}{2}\ln\left(\frac{r_s}{\delta r}\right)\right], & r_s \ll L \\ \frac{\beta}{2\pi}\left[\ln\left(\frac{L^{d-1}}{N_b \ell_p^{d-1}}\right) - \frac{d-1}{2}\ln\left(\frac{r_s}{\delta r}\right)\right], & r_s \gg L. \end{cases} \tag{4.63}$$

For near extremal AdS RN black holes ($d \geq 4$) we have:

$$t_{emerge} \sim \begin{cases} \frac{\beta}{2\pi}\left[\ln\left(\frac{r_s}{\beta}\frac{r_s^{d-1}}{N_b \ell_p^{d-1}}\right) + \frac{d-1}{d-2}\ln\left(\Lambda^2\right) + ...\right], & r_s \ll L \\ \frac{\beta}{2\pi}\left[\ln\left(\frac{r_s}{\beta}\frac{L^{d-1}}{N_b \ell_p^{d-1}}\right) + \ln\left(\Lambda^2\right) + ...\right], & r_s \gg L, \end{cases} \tag{4.64}$$

where the "..." stand for double Log terms which we did not explicitly write. In the case of AdS Schwarzschild black holes we should assume the following hierarchy of scales that $\ell_p \ll \delta r \ll r_s$. By doing this it is clear that the dependence on δr for the re-emergence time is sub-leading to the first term in the limit where $\ell_p \to 0$. We can reasonably identify t_{emerge} with the scrambling time scales discussed in [73, 134].

The case of a near extremal AdS RN black holes is more subtle. For near extremal AdS RN black holes we have an additional length scale that we did not have for the AdS Schwarzschild case. This length scale is β and it causes problems when we try to decide on where the screen should be placed. To understand the issue, recall that we introduced Λ through the following definition which relates it to δr:

$$\Lambda = \frac{\delta r}{r_s}\beta\sqrt{f''_{ext}(r_s)}, \tag{4.65}$$

where we required that $1 \ll \Lambda \ll \beta\sqrt{f''_{ext}(r_s)}$. The issue is that there are a number of choices we can make for the β-dependence of Λ. In Pennington's paper it is suggested that we extract radiation at a fixed distance from the horizon. There are at least two natural ways to do this.

The first way is to set the radial coordinate distance from the horizon, δr, to some constant that does not depend explicitly on β. Then it is clear that $\Lambda \sim \beta/r_s$. In this case we would have results that look like:

$$t_{emerge} \sim \begin{cases} \frac{\beta}{2\pi}\left[\ln\left(\left(\frac{\beta}{r_s}\right)^{\frac{d}{d-2}}\frac{r_s^{d-1}}{N_b\ell_p^{d-1}}\right)+\frac{d-1}{d-2}\ln\left(\frac{\delta r^2}{r_s^2}\right)\right], & r_s \ll L \\ \frac{\beta}{2\pi}\left[\ln\left(\frac{\beta}{r_s}\frac{L^{d-1}}{N_b\ell_p^{d-1}}\right)+\ln\left(\frac{\delta r^2}{L^2}\right)\right], & r_s \gg L. \end{cases} \tag{4.66}$$

These results are at odds with what Pennington has for near extremal AdS black holes and also with the literature [91, 29] which discusses the scrambling time for near extremal black holes. In particular, the main difference is how β appears in the Log. One should expect β to appear in the denominator rather than the numerator. This suggests that fixing an absorptive screen at a constant coordinate distance will yield a re-emergence time that is much longer than the scrambling time, $\frac{\beta}{2\pi}\ln(S-S_{ext})$.

Now consider the second way, which is to fix the proper radial distance from the screen to the horizon. Then we can show $\delta r \sim l_{prop}^2/\beta$, where l_{prop} is the proper radial distance between the screen and horizon [14]. By doing this, we see that Λ will have no additional dependence on β and we can write:

$$t_{emerge} \sim \begin{cases} \frac{\beta}{2\pi}\left[\ln\left(\frac{r_s}{\beta}\frac{r_s^{d-1}}{N_b\ell_p^{d-1}}\right)+\frac{2(d-1)}{d-2}\ln\left(\frac{l_{prop}^2}{r_s^2}\right)\right], & r_s \ll L \\ \frac{\beta}{2\pi}\left[\ln\left(\frac{r_s}{\beta}\frac{L^{d-1}}{N_b\ell_p^{d-1}}\right)+\ln\left(\frac{l_{prop}^2}{L^2}\right)\right], & r_s \gg L, \end{cases} \tag{4.67}$$

then we can be reasonably identify the information re-emergence time with the scrambling time for near extremal black holes. So the question is what we should be fixing, the coordinate distance or proper distance, or perhaps something else? We believe the answer lies in the idea of fixing the energy scale of our effective theory on the screen. We know in the AdS/CFT correspondence the radial direction in the bulk corresponds to the energy scale of the CFT on the boundary. So by fixing the energy scale we should unambiguously fix how δr scales with β. However, it is not clear exactly how the energy scale of the boundary theory depends on the radial distance. If it depends on the proper radial distance then we should fix the proper length between the horizon and screen. In discussions of the holographic renormalization group one usually considers metrics written in the form [43]:

$$ds^2 = dz^2 + e^{2z/L}\gamma_{ij}(z,x^i)dx^i dx^j, \tag{4.68}$$

[14] To see this consider the proper radial length from the horizon to a point δr from the horizon this is given by the an integral $l_{prop} = \int_{r_s}^{r_s+\delta r}\frac{dr}{\sqrt{f(r)}}$, for $\delta r \ll \min\{r_s, L\}$ we can expand to first order and do the integral to find $\delta r \sim \frac{l_{prop}^2}{\beta}$

where z is the radial direction in the bulk and x^i are coordinates on the boundary and γ_{ij} is the induced metric on a constant z slice. The fixing of energy scales can be interpreted as the fixing of z. The way the metric is written suggests that z is the proper radial length in the bulk. Therefore, it seems that fixing the proper length between the screen and horizon seems like a reasonable way to fix the energy scale, although this may not be valid for metrics that significantly differ from (4.68).

To summarize our discussion, we found that there are many ways to fix the β dependence of Λ (which is related to where the screen is placed). Depending on how δr depends on β we can get t_{emerge} that may or may not resemble the scrambling time for near extremal AdS black holes. In particular, we find that by fixing the proper radial distance between the horizon and absorptive screen we get an information emergence time that is consistent with the scrambling time for near extremal AdS black holes. We suggested that fixing the proper radial distance between the screen and horizon can be interpreted as fixing the energy scale of the theory on the screen. We also find an additional sub-leading Log term which contains information on exactly where the screen absorbs radiation (which should not explicitly depend on β). It is interesting to note that for large AdS black holes it is not the entropy of the entire horizon that goes into the Log but instead the entropy of a cell on the horizon of characteristic length L. This is reasonable if we recall that large AdS black holes are dual to large N gauge theories with $N^2 \sim L^{d-1}/\ell_p^{d-1}$[126].

4.4 Discussion of the Physics of the Screen

4.4.1 Absorptive Screen as a Thin Shell of Matter

As we have demonstrated, the effect of extracting Hawking radiation near the horizon of a black hole generally has non-trivial consequences for the evaporation rate. In this work we adopted a model which extracted radiation close to the horizon using a perfectly absorbing screen that would absorb any Hawking radiation that gets to it. The rate at which energy was being absorbed by the screen for each angular momentum mode is captured through the generalized greybody factor. We did not rigorously compute this factor but instead proposed models that would capture the essential behaviour of the generalized greybody factor near the horizon. Here we will discuss a way to calculate the generalized greybody factor by treating the screen as an interface which patches an interior and exterior solution to the Einstein equations.

In this picture, the screen is not really literally absorbing radiation, it is acting as an interface between the interior spacetime containing the black hole and an exterior "reser-

voir" spacetime which collects and stores the radiation emitted by the interior black hole. Assuming that the interior and exterior spacetimes are spherically symmetric, the scalar perturbations that propagate in this spacetime would satisfy the following radial wave equation:

$$\frac{d^2\psi}{dr_*^2} + \left(\omega^2 - V_{screen,\ell}\right)\psi = 0, \tag{4.69}$$

where $V_{screen,\ell}$ is the effective potential defined in a piece-wise manner in terms of the interior and exterior spacetimes:

$$V_{screen,\ell} = \begin{cases} V_{int,\ell}(r), & r_s \leq r \leq r_s + \delta r \\ V_{ext,\ell}(r), & r > r_s + \delta r. \end{cases} \tag{4.70}$$

The basic idea behind this is that we want to keep the spacetime unchanged until we arrive at the absorptive screen. The process of the screen "absorbing" radiation at $r + \delta r$ can be thought of a gluing an asymptotically flat region, just behind the screen and letting the wave "escape to infinity"[15] as depicted in Figure 4.4. To find the fraction of radiation "absorbed" by the screen (i.e. the generalized greybody factor) we would solve the wave equation in each region. In the interior region where $r \in (r_s, r_s + \delta r)$ the general solution will be some linear combination of two independent solutions:

$$\psi_{I,\ell}(r_*) = c_{1,\ell} f_\ell(r_*) + c_{2,\ell} g_\ell(r_*). \tag{4.71}$$

By analyzing the solution near the horizon we will find that they take on the form of plane waves and normalize the outgoing wave to unity (i.e. we start with outgoing Hawking radiation) this will fix some type of relation between $c_{1,\ell}$ and $c_{2,\ell}$. In the exterior region where the potential goes to zero far from the screen the solution should be purely outgoing plane wave (i.e. absorptive screen boundary condition):

$$\psi_{II,\ell}(r_*) = T_\ell e^{i\omega r_*}. \tag{4.72}$$

We have 2 unknowns left now, namely T and one of the coefficients of the solution of the interior region which will represent how much of the wave is reflected back. We can fix these by requiring the solution and its first derivative at $r = r_s + \delta r$ be continuous. This

[15] The region behind the interface that we are gluing does not necessarily have to be an asymptotically flat space it could be more general. We choose an asymptotically flat space since the wave escaping to infinity would be the analogue of a purely absorptive boundary condition for the screen. One is also free to glue another asymptotically AdS space behind the screen. We will discuss this perspective in Section 4.4.2.

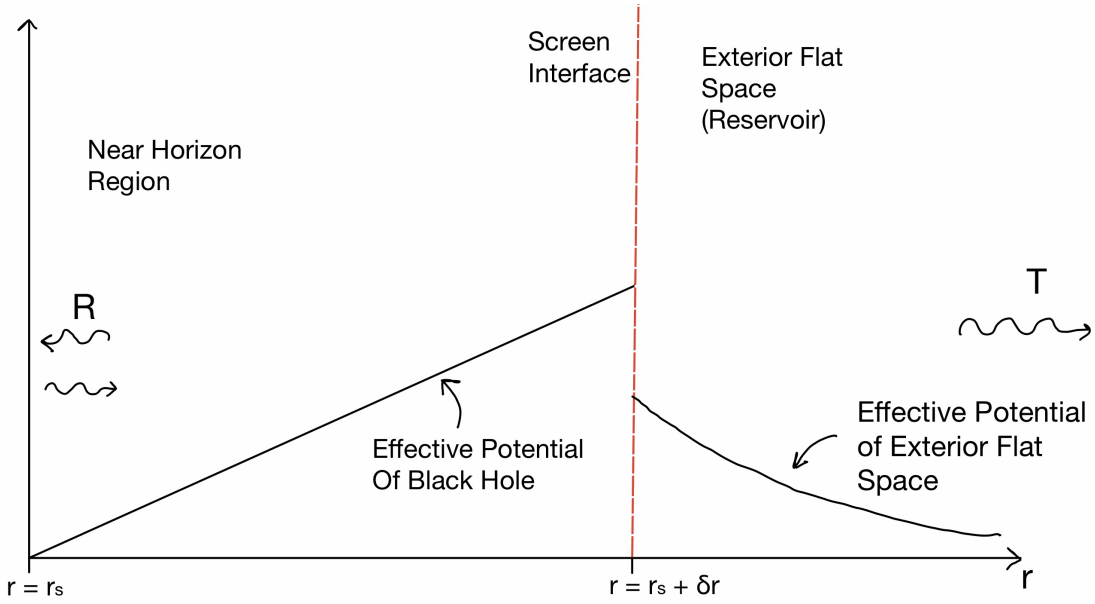

Figure 4.4: Above is a depiction of the potential that we are considering to emulate an absorptive screen placed at $r = r_s + \delta r$ depicted by the dotted red line. We keep the effective potential the same as the black hole up until we get to the screen interface. We then transition to a potential for a flat space which will act as a reservoir for the extracted Hawking radiation. Close to the horizon the solution takes on the form of in-going and out-going plane waves. We normalize the outgoing wave near the horizon to unity and the amplitude of the in-going plane wave is R. The absorptive screen boundary condition is enforced by only allowing outgoing plane waves in the flat region with amplitude T. We patch the solutions and uniquely determine T and R by requiring continuity of the solution and its derivative at the screen interface. Then the generalized greybody factor is defined by $|T|^2$.

will fix T_ℓ uniquely. The generalized greybody factor is then defined by the the amplitude square of the transmission coefficient:

$$\gamma_\ell(\omega, \delta r) = |T_\ell(\omega, \delta r)|^2. \tag{4.73}$$

The procedure we outlined above would be a more rigorous way to find the generalized greybody factor. As one can imagine doing this analytically for any choice of δr would be difficult, however the procedure we just outlined can be implemented numerically to find the exact behaviour of the generalized greybody factors. We expect that the generalized greybody factors to mimic the behaviour of the idealized models we analyzed in this chapter

at least in the limit where $\delta r \ll \min\{r_s, L\}$. It would be interesting to see how this method of extracting radiation at a finite distance from the horizon compares to other models that have been proposed to extract radiation from AdS black holes. For example, one could move the screen further from the horizon and ask how the generalized greybody factor at infinity (which is really just a greybody factor now) compares to greybody factors of models that use the evaporon [128, 127] to absorb energy from the black hole.

4.4.2 Null Energy Condition for the Screen and the Holographic c-Theorem

Recall that in Section 4.1 of this work we wanted to view the absorptive screen near the horizon as a coarse-grained version of the conformal boundary (with absorbing boundary conditions). The goal of this discussion is to elaborate on this idea in the context of the holographic c-theorem and the role that the null energy condition plays in its formulation.

The idea of the radial direction in the bulk being a measure of the energy scale of the dual boundary theory is formalized by discussing holographic c-theorems [51, 103, 104]. When discussing c-theorems one usually considers two d-dimensional CFTs, one has a central charge c_{UV} and the other has a central charge c_{IR} where $c_{IR} < c_{UV}$. These two CFTs are assumed to be connected by an RG flow which starts from a UV fixed point and flows towards an IR fixed point. One can define a monotonic c-function which measures the effective degrees of freedom of the of the coarse-grained theory along the RG flow between the fixed points. If the two CFTs are holographic, one can make use of the AdS/CFT duality to construct a holographic c-function in terms of quantities defined in a $d+1$-dimensional gravity theory with matter. A central aspect of the construction relies on matter in the bulk satisfying the null energy condition (NEC). In particular, if one chooses appropriate coordinates so that the "radial" direction identifies the energy scales along the RG flow, then one needs the radial NEC to be satisfied in order to construct a monotonic c-function. Due to this fact, we will mainly focus on analyzing the radial NEC for the matter on the screen. Doing this we will provide a heuristic picture of how the effective degrees of freedom on the screen change as the screen is moved radially in the bulk.

To make things concrete, we will assume the interior spacetime, enclosed by the screen interface, is that of a $d+1$-dimensional AdS Schwarzschild black hole with a line element

of the form:

$$\begin{aligned} ds_- &= g^-_{\mu\nu} dx^\mu dx^\nu = -f_-(r) dt^2 + \frac{dr^2}{f_-(r)} + r^2 d\Omega^2_{d-1}, \\ f_-(r) &= 1 + \frac{r^2}{L_-^2} - \left(\frac{r_H}{r}\right)^{d-2} \left(1 + \frac{r_H^2}{L_-^2}\right), \end{aligned} \tag{4.74}$$

where r_H is the radial coordinate of the horizon, L_- is the AdS radius for the solution. The "$-$" subscripts and superscripts mean we are dealing with quantities within the region enclosed by the screen. The exterior spacetime will be a pure AdS space with an AdS radius L_+ ("+" superscripts and subscripts denote quantities in the exterior). The line element will be given by:

$$\begin{aligned} ds_+ &= g^+_{\mu\nu} dx^\mu dx^\nu = -\Delta(r_0) f_+(r) dt^2 + \frac{dr^2}{f_+(r)} + r^2 d\Omega^2_{d-1}, \\ f_+(r) &= 1 + \frac{r^2}{L_+^2}, \end{aligned} \tag{4.75}$$

where r_0 is the radial coordinate where the screen is placed. The lapse function $\Delta(r_0) = f_-(r_0)/f_+(r_0)$ ensures that the induced metric on either side of the screen is the same. Using the formalism described in Appendix C.7 it can be shown that the stress energy tensor of the screen is given by Eq. (C.54) and it resembles the stress energy tensor of a perfect fluid in d-dimensions with an energy density, ρ, and pressure, p given by the following expressions:

$$\begin{aligned} \rho &= \frac{(d-1)\left(f_-(r_0)^{1/2} - f_+(r_0)^{1/2}\right)}{8\pi r_0}, \\ p &= \frac{1}{16\pi r_0}\left[2(d-2)\left(f_+(r_0)^{1/2} - f_-(r_0)^{1/2}\right) + r_0\left(\frac{f_+'(r_0)}{f_+(r_0)^{1/2}} - \frac{f_-'(r_0)}{f_-(r_0)^{1/2}}\right)\right]. \end{aligned} \tag{4.76}$$

To summarize, we see that the patching of an interior black hole solution to an exterior AdS solution requires the screen to have a stress energy tensor of a d-dimensional perfect fluid with energy density and pressure given in Eq. (4.76). In Appendix C.8 we found the radial NEC translates to the screen having a positive energy density, $\rho \geq 0$. It turns out that the expression for the energy density of the screen can be positive only if $L_+ \geq L_-$. Furthermore, the closest the screen can get to the horizon before the radial NEC is violated is given by:

$$r_c = r_H \left(\frac{1 + \frac{L_-^2}{r_H^2}}{1 - \frac{L_-^2}{L_+^2}}\right)^{1/d}. \tag{4.77}$$

For any screen position $r_0 > r_c$ the screen will have a positive energy density and the radial NEC is satisfied. Now consider holding r_H and L_- fixed and define $\mathcal{R} = L_+/L_-$. We will allow $\mathcal{R}$ to vary by changing the value of L_+. When $\mathcal{R} = 1$ we know $r_c \to \infty$ so the screen has to be sitting at the conformal boundary in order to satisfy the radial NEC. If we increase $\mathcal{R}$ the screen is allowed to move deeper into the bulk. Now recall the standard dictionary in AdS/CFT which states that the AdS radius in Planck units is related to the effective number of degrees of freedom of the dual CFT [126]:

$$\left(\frac{L}{\ell_p}\right)^{d-1} \sim c_{eff}. \tag{4.78}$$

Under the assumption that the screen is holographic we have a way to view the ratio $\mathcal{R}$ in terms of c_{eff}:

$$\mathcal{R}^{d-1} \sim \frac{c^+_{eff}}{c^-_{eff}} \geq 1, \tag{4.79}$$

where we defined $L_\pm^{d-1}/\ell_p^{d-1} \sim c^\pm_{eff}$. We view $\mathcal{R}$ as the ratio between the number of effective degrees of freedom of the screen and boundary theory. When the number of effective degrees of freedom of the screen equals the number effective degrees of freedom the boundary theory the screen must coincide with the boundary. If we coarse-grain the boundary theory (screen) the number of degrees of freedom on the screen are reduced and this corresponds to moving the screen deeper into the bulk. From this, we can heuristically see how satisfying the radial NEC for the screen gives rise to a monotonic decrease in the effective number of degrees of freedom on the screen as it is moved closer to the horizon of the black hole.

4.4.3 The Null Energy Condition and Black Hole Mining

The idea of changing the evaporation rate of a black hole by extracting radiation near the horizon has also been discussed in the context of black hole mining [150, 88, 52]. In particular, Brown suggests that energy conditions (most notably the null energy condition) impose constraints on how quickly one can extract radiation from the horizon [28]. In the previous subsection, we found that satisfying the radial NEC at a finite distance from the horizon places a constraint on how close the screen is allowed to be to the horizon. The closest radial coordinate is given by r_c in Eq. (4.77). Then $\delta r_{min} = r_c - r_H$ is given by:

$$\delta r_{min} = \left[\left(1 + \frac{L_-^2}{r_H^2}\right)^{1/d} - 1\right] r_H \simeq \begin{cases} \left(\frac{L_-}{r_H}\right)^{2/d} r_H, & r_H \ll L_- \\ \frac{1}{d}\left(\frac{L_-}{r_H}\right)^2 r_H, & r_H \gg L_-, \end{cases} \tag{4.80}$$

where the expression above is taken in the limit that $L_+ \to \infty$ so the exterior spacetime is asymptotically flat. An interesting observation is that δr_{min} monotonically increases as the black hole evaporates. Due to this, we can see that for small AdS black holes the screen cannot be placed very close to the horizon, so we are not really mining very small AdS black holes with the screen[16]. However, for very large AdS back holes the screen can be placed very close to the horizon. In this case it is interesting to ask how long it takes for a very large AdS black hole to transition to a small AdS black hole via screen mining. We estimate this time by setting $\delta r = \delta r_{min}$ in Eq. (4.23) to get the following evaporation rate for very large AdS black holes:

$$\frac{dM}{dt} \sim \frac{N_b}{L_-^2}\left(\frac{r_H}{L_-}\right)^{\frac{4d+3}{2}}, \tag{4.81}$$

We use the relation between the mass and horizon radius of very large AdS black holes, given by $M \sim r_H^d/(L_-^2 \ell_p^{d-1})$, to replace the derivative of mass with derivative of the horizon radius. We integrate the equation to estimate the duration of time elapsed for the large AdS black hole with an initial radius of $r_H = r_s \gg L_-$ to evaporate to a black hole of radius L_-. We find:

$$\Delta t \sim \left(\frac{L_-}{\ell_p}\right)^{d-1}\left[1-\left(\frac{L_-}{r_s}\right)^{d+\frac{3}{2}}\right]\frac{L_-}{N_b} \approx \left(\frac{L_-}{\ell_p}\right)^{d-1}\frac{L_-}{N_b}. \tag{4.82}$$

At leading order we find that the time it takes (in units of AdS radius) for a very large AdS black hole to transition to the small AdS black hole regime via screen mining is proportional the Bekenstein-Hawking entropy of an AdS cell. After the black hole enters the small regime the evaporation rate will mimic that of a black hole evaporating in asymptotically flat space (i.e. evaporation rate will go as $dM/dt \sim N_b \beta^{-2}$). It is difficult to directly compare our result for the evaporation rate of large AdS black holes with the results of Brown [28] which are concerned with asymptotically flat black holes. However, we can see that once the black hole enters the small regime the bounds derived by Brown are not violated because the screen is far from the horizon (i.e. radial NEC only allows near horizon screen mining of very large AdS black holes).

It is interesting to mention that the time scale in Eq. (4.82) we found using near horizon screen mining is agrees with the evaporation time scale found in an earlier work by Page

[16]The reader may be concerned with the evaporation rate we derived in Eq. (4.23) for the small AdS black hole regime. The equation was derived assuming the screen is placed close to the horizon, but respecting the radial NEC does not allow this. This should not be a particularly big issue since, up to an order one pre-factor, the evaporation rate should go as $dM/dt \sim \beta^{-2}$ [102]. Which is consistent with Pennington's results [117] as well as ours.

[116]. Page's work considers large AdS black hole evaporation assuming absorptive boundary conditions at infinity. Having absorptive boundary conditions at infinity is analogous to placing our absorptive screen at infinity. The fact that the lifetimes in either case (i.e. near or far screen mining) are comparable to each other suggests that the lifetime of very large AdS black holes does not significantly change when mined by a screen obeying the radial NEC.

So far, we have restricted ourselves to discussing the NEC for null vectors with only a radial component. This was primarily because of the connection between the radial NEC and discussions of the holographic c-theorem. One may ask what kind of constraints the the NEC gives if the null vectors are tangent to the screen (i.e. no radial component). In Appendix C.8 we show that the screen violates the tangential NEC at any finite distance from the horizon. The violations of the tangential NEC become milder the further the screen is placed from the horizon and is actually saturated in the limit where the screen is sent to infinity. This is unsurprising as a screen composed of ordinary matter will not sit at a fixed distance from the horizon, but rather would fall into the black hole. In order for it not to fall in the matter composing the screen must violate energy conditions. However, it is worth noting that the calculations we did, did not account for Hawking radiation being emitted from the black hole. It is well known that Hawking radiation violates energy conditions, which is why the area of the horizon decreases [50, 92]. An interesting idea worth considering is whether the screen can be prevented from falling into the black hole by the pressure generated by the Hawking radiation emitted by the black hole. Naively, the pressure due to Hawking radiation will become larger the closer the screen gets to the horizon this may counteract the gravitational pull on the screen generated by the horizon.

4.5 Conclusion and Future Prospects

In this work, we investigated how the evaporation rate of AdS black holes change when radiation is absorbed near the horizon using an absorptive screen, which is motivated by the entanglement wedge reconstruction framework described by Pennington [117]. We used idealized toy models, motivated by physical arguments, which would capture the essential physics of radiation propagating towards the absorptive screen. We showed that by fixing the screen at a proper radial distance from the horizon, the re-emergence time for the information thrown into an AdS black hole is given by the expressions in Eq. (4.63) and Eq. (4.67). For small AdS black holes (or asymptotically flat black holes) the expressions, at leading order, contain the Log of the entropy of the whole horizon. This is consistent with Pennington's calculations [117]. In contrast, however, for large AdS black holes, we

find that the re-emergence time depends on the log of the entropy of an AdS cell on the horizon (rather than that of the entire horizon). Such a modification is reasonable and consistent with the scrambling time discussed in the work [134].

In Sections 4.4.1 and 4.4.2, we attempted to provide a more physical description of what governs wave propagation and internal physics of our putative screen. The interior spacetime enclosed by the screen contains the black hole, while an exterior asymptotically flat or AdS spacetime can represent the auxiliary system that could store radiation. The "absorption" of radiation by the screen would then be equivalent to radiation passing through the screen interface and escaping to infinity. The calculation of how radiation would be "absorbed" can be translated to a well-defined computation of greybody factors. We used Israel junction conditions to compute the stress associated with the screen. The requirement of the matter on the screen having a positive energy density (which comes from the radial NEC used to formulate a monotonic c-function in a holographic RG description) sets a minimum distance for the screen from the black hole horizon if it is the dual description of a coarse-grained unitary boundary CFT.

The calculations done in this chapter have been done from a gravitational perspective. In order to explore the ideas discussed in Sections 4.4.1 and 4.4.2 more rigorously it will be necessary to translate the gravitational picture we proposed to a coupled quantum system description. The $T\bar{T}$ formalism described in [101] will likely be an important ingredient and a good starting point for defining the screen theory. We would then couple the screen theory defined by the $T\bar{T}$ deformation to a holographic CFT describing an AdS bulk with a brick wall. We leave such a formulation to future work.

Chapter 5

Entanglement Wedge Nesting with an End-Of-The-World Brane

This chapter will go over some results and findings of an on-going work (in collaboration with Dominik Neuenfeld) which explores the issue of entanglement wedge nesting in 3D asymptotically AdS spacetimes which involve an end-of-the-world brane. Although more work is still needed to properly interpret the results and also determine their limitations[1]. The methods discussed provide a useful and concrete starting point toward a much more broad research program which seeks to explore the issues of how of how one should view gravity theories living on end-of-the-world branes and the role that non-locality might play in such setups. Ultimately we hope that such investigations may shed more light into the nature of non-local effects/maps that appear to be involved in the discussion of the island formula for Hawking radiation entropy.

5.1 Motivation

A great deal of progress has been made in the past five years in understanding how to obtain the Page curve of an evaporating black hole. This has been made possible by studying black hole systems coupled to non-gravitational baths[7, 8, 38, 37]. A particularly useful formalism to study such systems is double holography[38, 37, 107, 90]. A central ingredient in such formalisms is the presence of an end-of-the-world brane[149, 53]. Essentially, one can reproduce the recently discovered island formula for the entropy of Hawking radiation

[1] At the time of writing this chapter.

in the bath using double holography[38, 37, 107]. In double holography there are three descriptions of a gravitational system. We describe them below:

- "The boundary perspective": this involves a holographic boundary CFT or $BCFT_d$ coupled to a $d-1$ dimensional quantum mechanical system sometimes called a defect living on the boundary.
- "The bulk perspective": this is the holographic gravity dual system in $d+1$ dimensions, it involves an asymptotically AdS spacetime cutoff by an end-of-the-world brane.
- "The brane perspective": this is an intermediate d-dimensional description. In this description, the quantum defect is replaced by the gravitating region on the end-of-the-world brane. Essentially we have a non-gravitating CFT coupled to a gravitating one living on the brane.

The boundary and bulk descriptions are equivalent in much the same way as the CFT is equivalent to a bulk in standard AdS/CFT. However the brane perspective is not. It is only a low energy effective description of the higher dimensional bulk theory (see Figure 5.1).

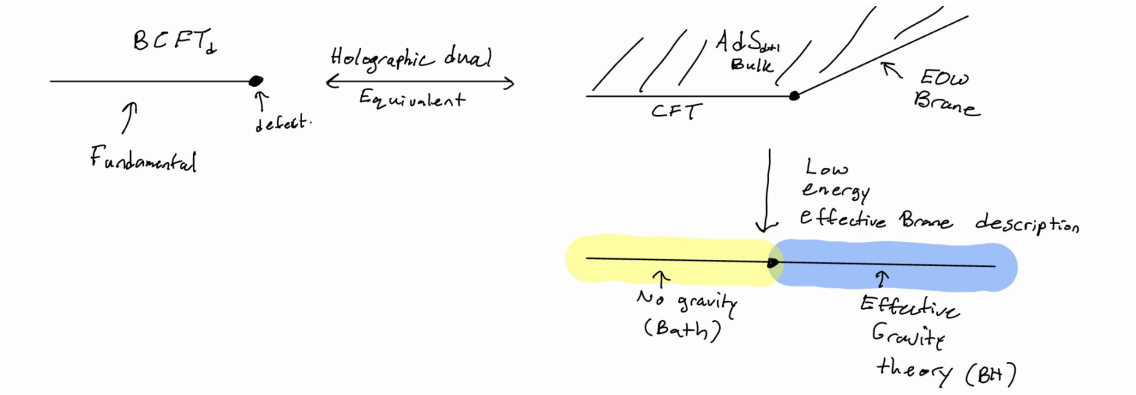

Figure 5.1: We depict the three descriptions that are used in doubly holographic setups. The top two pictures are descibing the equivalent systems which are the $BCFT_d$ and AdS_{d+1} cut off by an end-of-the-world brane. The brane perspective is on the bottom right, the defect is replaced by a gravitating region on the end-of-the-world brane whose gravitational physics is a low energy effective theory of the more complete UV theory in the bulk.

In such setups if we want to compute entanglement entropy of some subregion on the boundary in the brane perspective then we can use a standard Ryu-Takayanagi (RT) prescription in the bulk[149, 126, 37]. In general there are two phases the disconnected phase where the RT surface does not connect a brane and boundary region and the connected/island phase where the RT surface connects a boundary sub region to a brane sub region. We depict the two cases in Figure 5.2.

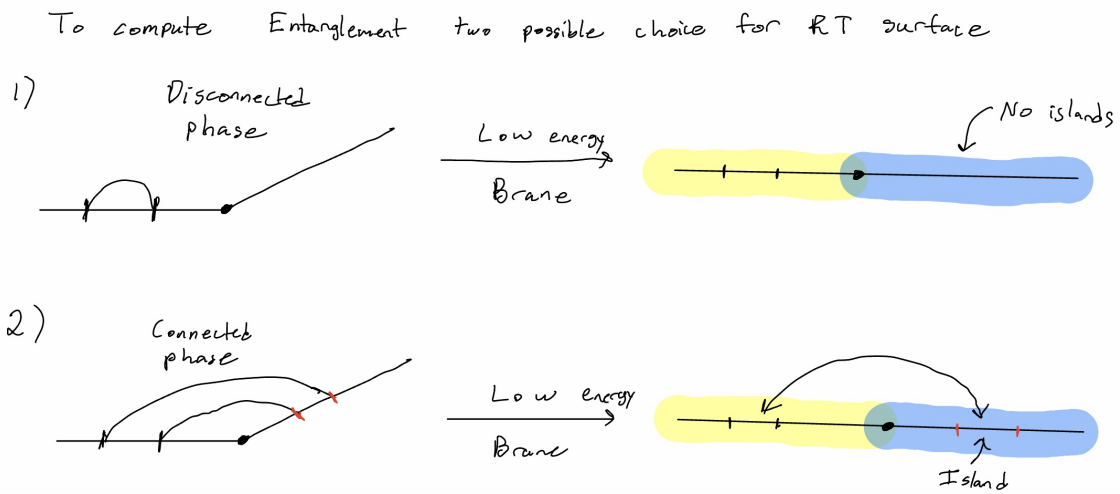

Figure 5.2: Depicted above are the two possible choices of RT surfaces which are allowed. The disconnected phase looks standard and does not connect to the brane. The connected phase connects a region on the brane to the boundary region. In the low energy brane description the connected phase corresponds to the appearance of an island in the gravitating system.

In this chapter we will take the perspective that in such a setup we can associate an "entanglement entropy" to gravitating subregions on the brane and that the entanglement entropy of these subregions can be computed holographically with an RT prescription. We will also state that having access to information in the subregion on the brane will allow one to reconstruct the bulk within the entanglement wedge of the subregion on the brane (similar to the standard AdS/CFT story). With this we can consider fixing two subregions. One on the boundary and another on the brane. We suppose that the connected phase is dominant and then require that the entanglement wedge for the brane subregion is completely contained inside the entanglement wedge associated to the connected RT surface which is really a wedge that is associated to both brane and boundary regions.

The goal of this chapter is to explore when this might fail in 3D AdS spacetimes involving end-of-the-world branes.

5.2 Conditions for Entanglement Wedge Nesting AdS_3 Poincare Patch

In the following subsections we will be consider entanglement wedge nesting in three dimensional AdS spacetimes in the presence of an end-of-the-world brane. In the analysis we will be fixing a spacelike subregion on the boundary denoted A and another spacelike subregion on the brane denoted B. The types of extremal surfaces we will be considering in this setup are:

- $\chi_{dis.}(A)$, is defined as the extremal surface which is anchored to the entangling surface ∂A on the boundary and does not connect to the brane.
- $\chi_{dis.}(B)$, is defined as the extremal surface which is anchored to the entangling surface ∂B on the brane and does not connect to the boundary.
- $\chi_{con.}(A \cup B)$, is defined as the extremal surface which is anchored to both the entangling surfaces ∂A on the boundary and ∂B on the brane, and connects the boundary to the brane.

5.2.1 AdS_3 Poincare Patch

In this subsection we will be discussing the Poincare patch of AdS_3 cut off by an end-of-the-world brane and we will precisely define the subregions A and B.

We start by writing down the metric:

$$ds^2 = \frac{L^2\left(dz^2 - dt^2 + dx^2\right)}{z^2}, \tag{5.1}$$

where L is the AdS radius, $z \in \mathbb{R}^+$ is the radial bulk coordinate and $z = 0$ is the conformal boundary which is parameterized by $t, x \in \mathbb{R}$. The end of the world brane is a co-dimension 1 surface in the bulk whose coordinate description is given by:

$$\begin{aligned} &z = z(x) = \cot\theta_0 x \\ &x > 0, \end{aligned} \tag{5.2}$$

where $\theta_0 \in (0, \pi/2)$ is a free parameter that controls the tension of the brane. In these coordinates we consider the following boundary and brane subregions:

- $A = \{(t, x, z)|t = t_a, x \in [-a_2, -a_1], z = 0\}$, which is an interval on the conformal boundary of size $a_2 - a_1$ at a constant time slice, where $a_2 > a_1 > 0$.
- $B = \{(t, x, z)|t = t_b, x \in [b_1 \sin\theta_0, b_2 \sin\theta_0], z \in [b_1 \cos\theta_0, b_2 \cos\theta_0]\}$, which is an interval on the brane of size $b_2 - b_1$ at a constant time slice, where $b_2 > b_1 > 0$.

5.2.2 Discussion of Candidate RT Surfaces in AdS_3

Now that we have defined the subregions A and B we will now consider the different extremal surfaces which are anchored to the subregions. Since the bulk is three dimensional co-dimension 2 extremal surfaces are curves. We will parameterize these curves in terms of the Poincare coordinate x and extremize the following functional:

$$L \int dx \frac{\sqrt{1 + \dot{z}^2 - \dot{t}^2}}{z(x)}, \tag{5.3}$$

where $\dot{z} = \frac{dz}{dx}$ and $\dot{t} = \frac{dt}{dx}$. The general solutions to the equations of motion associated with the functional in Eq. (5.3) are given by (see Appendix D.1.1 for details of the derivation of the general solution):

$$\begin{aligned} t(x) &= kx + c_1 \\ z(x) &= \sqrt{\frac{L^2}{H_x^2(1-k^2)} - (1-k^2)(x+c_2)^2}. \end{aligned} \tag{5.4}$$

The general solution above will have four undetermined constants namely, k, H_x, c_1, c_2. We can uniquely fix these by specifying the starting and ending points for the curves which will lie on the endpoints of the intervals we are interested in. With the general solution we can find easily fix the undetermined constants to obtain the specific RT curves corresponding to $\chi_{dis.}(A)$, $\chi_{dis.}(B)$, and $\chi_{con.}(A \cup B)$.

For $\chi_{dis.}(A)$ we will obtain:

$$\begin{aligned} &t(x) = t_a \\ &z(x) = \sqrt{-(a_1 + x)(a_2 + x)} \\ &x \in [-a_2, -a_1]. \end{aligned} \tag{5.5}$$

This is simply a semi-circle of radius $\frac{a_2-a_1}{2}$ centred at $\left(x=-\frac{a_1+a_2}{2}, z=0\right)$ on the constant $t=t_a$ plane.

For $\chi_{dis.}(B)$ we will obtain:

$$\begin{aligned} &t(x) = t_b \\ &z(x) = \sqrt{-x^2 + \frac{b_1+b_2}{\sin\theta_0}x - b_1 b_2} \\ &x \in [b_1\sin\theta_0, b_2\sin\theta_0]. \end{aligned} \tag{5.6}$$

This curve is a section of the semi-circle whose radius is given by $R_b = \frac{\sqrt{b_1^2+b_2^2+2b_1b_2\cos(2\theta_0)}}{2\sin\theta_0}$ centred at $\left(x=\frac{b_1+b_2}{2\sin\theta_0}, z=0\right)$ on the constant $t=t_b$ plane.

For $\chi_{con.}(A\cup B)$ the extremal surface is the the union of two separate extremal line segments which connect the boundary and brane. One segment connects the following two points $(t=t_a, x=-a_2, z=0)$ and $(t=t_b, x=b_2\sin\theta_0, z=b_2\cos\theta_0)$ we will denote this line segment, χ_2 and it will have a trajectory through the bulk given by the following parametric equations:

$$\begin{aligned} &t_2(x) = t_a + k_2\,(x+a_2) \\ &z_2(x) = \sqrt{\frac{(x+a_2)\,(b_2^2\cos^2\theta_0 - (1-k_2^2)(x-b_2\sin\theta_0)(a_2+b_2\sin\theta_0))}{a_2+b_2\sin\theta_0}} \\ &x \in [-a_2, b_2\sin\theta_0] \\ &k_2 = \frac{t_b-t_a}{a_2+b_2\sin\theta_0}. \end{aligned} \tag{5.7}$$

The other segment connects the points $(t=t_a, x=-a_1, z=0)$ and $(t=t_b, x=b_1\sin\theta_0, z=b_1\cos\theta_0)$ we will denote this line segment, χ_a, and it will have a trajectory through the bulk given by the following parametric equations:

$$\begin{aligned} &t_1(x) = t_a + k_1\,(x+a_1) \\ &z_1(x) = \sqrt{\frac{(x+a_1)\,(b_1^2\cos^2\theta_0 - (1-k_1^2)(x-b_1\sin\theta_0)(a_1+b_1\sin\theta_0))}{a_1+b_1\sin\theta_0}} \\ &x \in [-a_1, b_1\sin\theta_0] \\ &k_1 = \frac{t_b-t_a}{a_1+b_1\sin\theta_0}. \end{aligned} \tag{5.8}$$

This completes our explicit characterization of $\chi_{con.}(A \cup B) = \chi_1 \cup \chi_2$. In general, χ_1 and χ_2 are conic sections in the $z - x$ plane. In the special case where $t_a = t_b$ (i.e. when $k_1 = k_2 = 0$) the line segments χ_1 and χ_2 will be half circles in $z - x$ plane. In the more general case when $t_a \neq t_b$ the line segments will have $|k_1| \geq |k_2| > 0$ and the line segments will be one of three conic section (ellipse, parabola, hyperbola) in the $z - x$ plane. The issue of what specific conic section the line segments χ_1 and χ_2 correspond to depends on the value of k_1 and k_2 respectively. We summarize the classification in the table below:

$\lvert k\rvert$	$z(x)$
0	circle
$0 < \lvert k\rvert < 1$	ellipse
1	parabola
$\lvert k\rvert > 1$	hyperbola

Usually in AdS/CFT (i.e. when no end-of-the-world brane is present) we are usually only interested in RT curves that have $|k| < 1$ (i.e. circles and ellipses). This is because when there is no brane, all the extremal surfaces have to end on the $z = 0$ boundary. The parabola and hyperbola may start on one boundary point but they will never come back and end on the boundary which is why they are not usually discussed in standard AdS/CFT. However, in the presence of the brane we can now attach one endpoint of the extremal surface to the brane which generally has some $z > 0$ this allows for the novel configurations where the RT curve has $|k| \geq 1$. An interesting point to make here is that if we allow for configurations that have $|k| > 1$ then one might suggest it is possible for the RT curve to become timelike in the bulk if $|k|$ is sufficiently larger than 1. In Appendix D.1.2 we explicitly demonstrate that in order to connect the boundary to the brane, with a single smooth line segment, the value of $|k|$ must be bounded above. It turns out that the bound we find is equivalent to requiring that the endpoints the boundary and brane must be spacelike separated. This places a non-trivial constraint on the quantity $|t_b - t_a|$ (for a given choice of endpoints for χ_1 whose spatial coordinates are fixed):

$$|t_b - t_a| < \sqrt{a_1^2 + b_1^2 + 2a_1 b_1 \sin\theta_0}. \tag{5.9}$$

In Fig. 5.3 we give an example of the boundary and brane subregions along with the associated extremal surfaces in the $z - x$ plane. The shaded grey region is the portion of AdS which is cut-off by the end of the world brane and is not physically relevant in our discussion. The blue curve, $\chi_{dis}(A)$ and the yellow curve, $\chi_{dis}(B)$ are half circles. The union of the red line segments form the connected surface, $\chi_{con.}(A \cup B)$. In this particular case the two line red line segments correspond to ellipses in the $z - x$ plane.

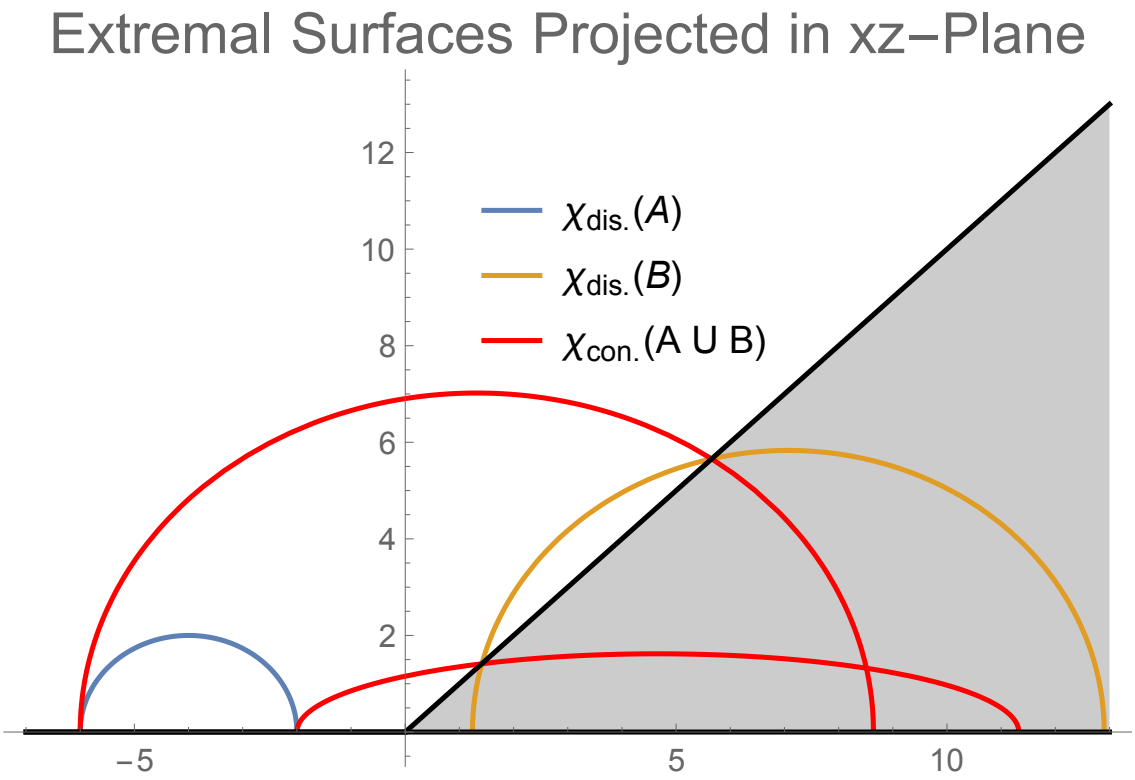

Figure 5.3: In this particular plot $\theta_0 = \pi/4$ and the shaded region is cut-off by the end of the world brane which intersects with the conformal boundary at the origin. The intervals on the boundary and brane are defined by fixing $a = \tilde{a} = 2$, $b = 6$, and $\tilde{b} = 8$. We also set $|t_b - t_a| = 0.97(2+\sqrt{2}) \approx 3.3$. The blue curve is $\chi_{dis.}(A)$ and is anchored to the boundary and lies on the constant time slice $t = t_a$. The yellow curve is $\chi_{dis.}(B)$ and is anchored to the brane and lies on the constant time slice $t = t_b$. Both the blue and yellow curves are half-circles. The union of two red line segments which connect the brane and boundary subregions is $\chi_{con.}(A \cup B)$. Unlike the blue and yellow curves the red curves do not remain on a constant time slice they interpolates between times t_b and t_a. For our our particular choice of parameters we have $|k_a| = 0.97$ and $|k_b| = 0.97\left[\frac{2-\sqrt{2}}{2}\right] \approx 0.28$ which implies that both red line segments are ellipses in the $x - z$ plane.

5.2.3 Discussion of Entanglement Wedges (AdS_3)

Now we will characterize the entanglement wedges associated with the boundary subregions A, B, and $A \cup B$.

Lets start with A on the boundary, we define Σ_A as a partial Cauchy surface with a boundary, $\partial\Sigma_A = A \cup \chi_{dis}(A)$. Using Σ_A we define the entanglement wedge of A, denoted $\mathcal{W}_E(A)$, as the domain of dependence of Σ_A. A convenient prescription which can be used to explicitly construct the entanglement wedge of the boundary interval A is by considering the a family of null geodesics beginning on $\chi_{dis.}(A)$ which are also orthogonal to $\chi_{dis.}(A)$ and evolve towards the boundary. The set of these null geodesics enclose a co-dimension 0 region which is exactly $\mathcal{W}_E(A)$ as shown in Figure 5.4. As we discuss in Appendix D.1.4 the entanglement wedge and causal wedge for a constant time interval on the boundary are the same in particular we have the following explicit expression for the null surface that encloses the points inside $\mathcal{W}_E(A)$ (see Appendix D.1.4 for details of where this comes from):

$$|t - t_a| = \frac{a_2 - a_1}{2} - \sqrt{z^2 + \left(x + \frac{a_2 + a_1}{2}\right)}. \tag{5.10}$$

We say that $(t, x, z) \in \mathcal{W}_E(A)$ if the points satisfy the inequality:

$$\frac{a_2 - a_1}{2} - |t - t_a| > \sqrt{z^2 + \left(x + \frac{a_2 + a_1}{2}\right)}. \tag{5.11}$$

In an analogous manner we can define the entanglement wedge associated with the region B on the brane. We define Σ_B as the partial Cauchy slice whose boundary is given by $\partial\Sigma_B = B \cup \chi_{dis.}(B)$. Then the entanglement wedge of B, denoted $\mathcal{W}_E(B)$, is simply the domain of dependence of the Σ_B. Furthermore a more explicit construction of the of the wedge can be made by considering the a family of null geodesics beginning on $\chi_{dis.}(B)$ which are also orthogonal to $\chi_{dis.}(B)$ and evolve towards the boundary. The set of these null geodesics enclose a co-dimension 0 region which is exactly $\mathcal{W}_E(B)$ as shown in Figure 5.5. Based on the discussion in Appendix D.1.4 we can obtain the following inequality which characterizes the set of points in $\mathcal{W}_E(B)$:

$$R_b - |t - t_b| > \sqrt{\left(x - \frac{b_1 + b_2}{2\sin\theta_0}\right) + z^2}, \tag{5.12}$$

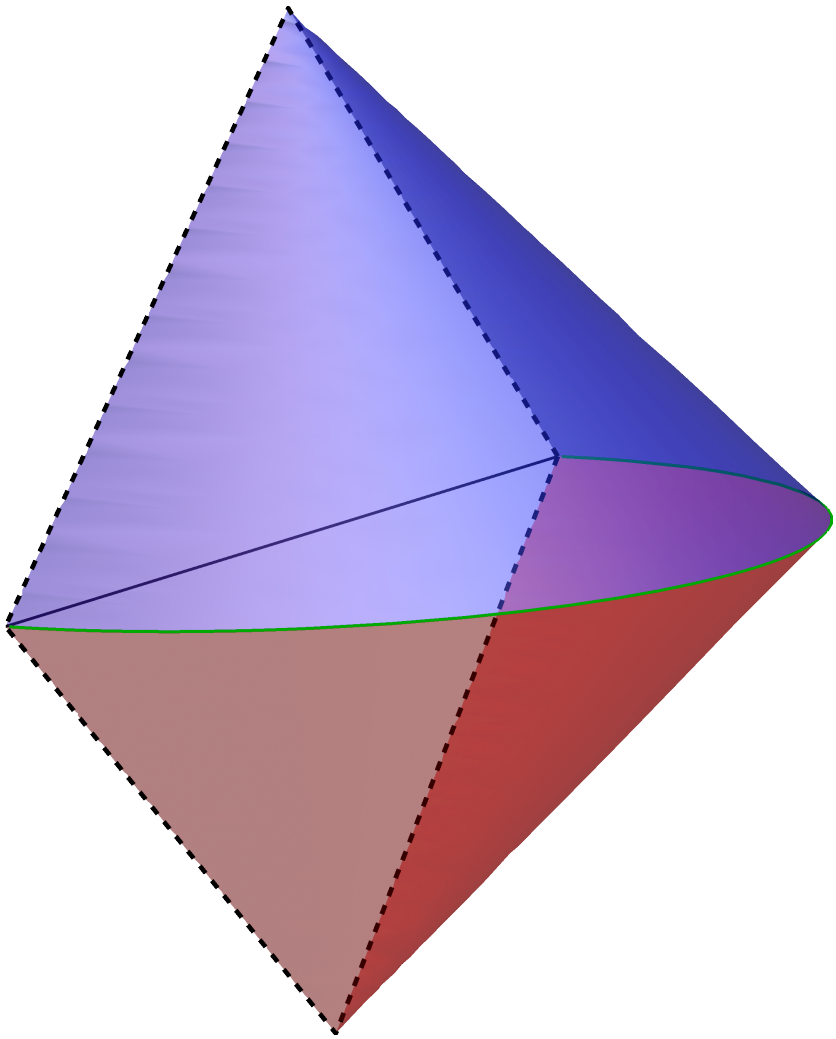

Figure 5.4: Depicted in the figure above is an example of what $\mathcal{W}_E(A)$ might look like. The intersection of the past and future cones is the RT surface $\chi_{dis.}(A)$ shown in green. The dotted "diamond" is the causal diamond on the boundary associated with the interval A which horizontally splits the diamond to the future and past of the interval.

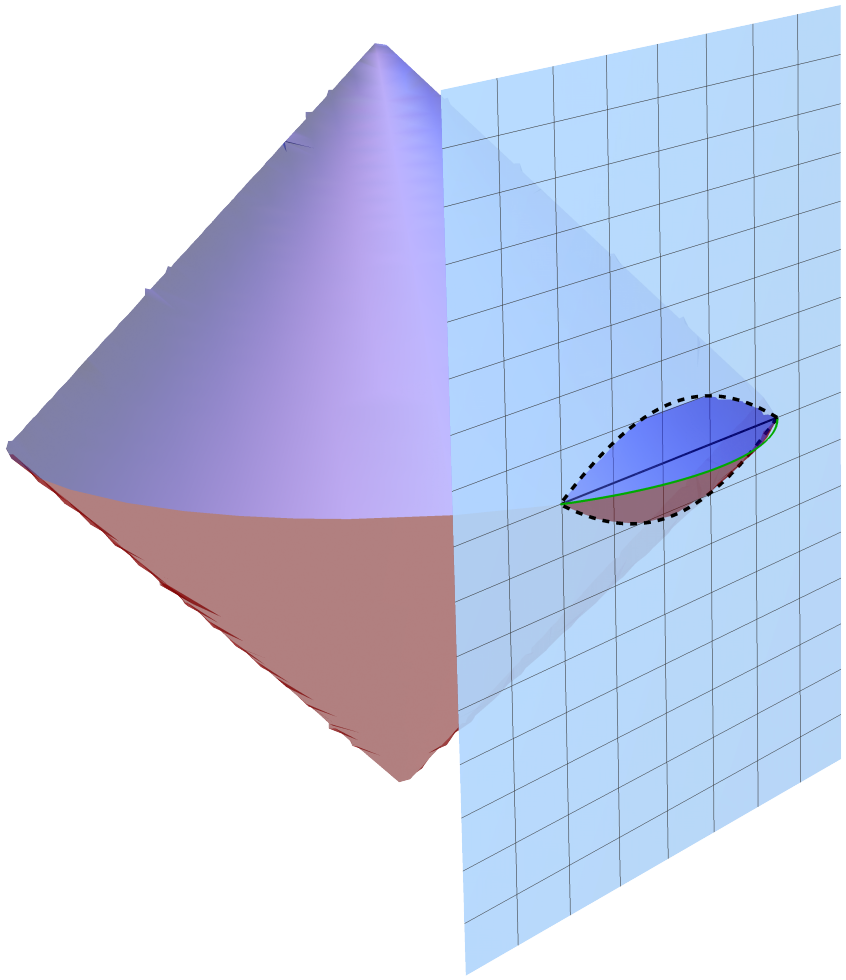

Figure 5.5: Depicted in the figure above is an example of $\mathcal{W}_E(B)$. There are actually two entanglement wedges in the figure. The very large wedge is what we called $\mathcal{W}_E(\mathrm{Vir}(B))$ in Appendix D.1.4. The actual entanglement wedge $\mathcal{W}_E(B)$ is the small piece that is cut out of the larger wedge by the slanted plane which is the end-of-the-world brane. We can see that the intersection of $\mathcal{W}_E(B)$ with the end-of-the-world brane is not the naive causal diamond associated with the interval B on the brane.

where we make the implicit restriction on (t, x, z) to be in Phys(AdS_3) which simply denotes the bulk region that physically exists and not cut off by the brane.

Now we turn to the construction of the entanglement wedge associated with $A \cup B$, denoted, $\mathcal{W}_E(A \cup B)$. Lets start by noting there are actually two possible "phases" for $\mathcal{W}_E(A \cup B)$ which we call the "disconnected phase" or the "connected phase". In the disconnected phase we have $\mathcal{W}_E(A \cup B) = \mathcal{W}_E(A) \cup \mathcal{W}_E(B)$, this is simply the union of the separate entanglement wedges of A and B which we already discussed. In the connected phase we define $\Sigma_{A\cup B}$ as the partial Cauchy slice with a boundary given by $\partial\Sigma_{A\cup B} = \chi_{con.}(A \cup B) \cup A \cup B$. Then using this partial Cauchy slice we define the connected phase entanglement wedge as the domain of dependence of $\Sigma_{A\cup B}$.

The condition that we are going to explore is when $\mathcal{W}_E(B) \subset \mathcal{W}_E(A \cup B)$. It is clear that in the disconnected phase the $\mathcal{W}_E(B) \subset \mathcal{W}_E(A \cup B)$ is always satisfied because $\mathcal{W}_E(A \cup B) = \mathcal{W}_E(A) \cup \mathcal{W}_E(B)$ in the disconnected phase. Therefore, we will be interested in the issue of if $\mathcal{W}_E(B) \subset \mathcal{W}_E(A \cup B)$ when we are in the connected phase (we will come back to the issue of when a connected phase might actually exist near the end of the chapter).

5.2.4 A Sufficient Condition for EWN (AdS_3)

In this subsection we will derive constraints on the parameters defining the boundary and brane subregions such that $\mathcal{W}_E(B) \subset \mathcal{W}_E(A \cup B)$ in the connected phase.

Lets begin with the special case where $t_a = t_b = t_0$. In this case $\chi_{dis.}(A)$, $\chi_{dis.}(B)$, and $\chi_{con.}(A \cup B)$ all lie on the same time slice. In this case, it is clear that since $\Sigma_B \subset \Sigma_{A\cup B}$ the domain of dependence of Σ_B will be contained in the domain of dependence of $\Sigma_{A\cup B}$ which is equivalent to saying that $\mathcal{W}_E(B) \subset \mathcal{W}_E(A \cup B)$[2]. Now lets take the more general case where $t_a \neq t_b$. In this case, the strategy will be to ensure that all null geodesics originating from either χ_1 or χ_2 are unable to reach $\mathcal{W}_E(B)$ (i.e. no causal signals originating from $\chi_{con.}(A \cup B)$ can influence events in $\mathcal{W}_E(B)$). As long as such a condition holds we are guaranteed that $W_E(B) \subset W_E(A \cup B)$. A simple way to ensure this is to take the causal future and past of Σ_B, which we denote as $J^+(\Sigma_B)$ and $J^-(\Sigma_B)$ respectively, and require that $\chi_1, \chi_2 \notin J^+(\Sigma_B) \cup J^-(\Sigma_B) \cup \Sigma_B$. This will ensure that no light rays from χ_1 or χ_2

[2]To see this suppose we take any $p \in \mathcal{W}_E(B)$ then any causal curve going through the point p must also go through Σ_B. But since $\Sigma_B \subset \Sigma_{A\cup B}$ (not too sure if it is important that the partial Cauchy slices be simply connected) then it also means that that all causal curves going through p also go through $\Sigma_{A\cup B} \Rightarrow p \in \mathcal{W}_E(A \cup B) \Rightarrow \mathcal{W}_E(B) \subset \mathcal{W}_E(A \cup B)$.) We can also see this more explicitly by studying lightcones/null geodesics.

will be able to reach points in $\mathcal{W}_E(B)$ and guarantee that $W_E(B) \subset W_E(A \cup B)$. In order to enforce such a condition we need to get an understanding of $J^+(\Sigma_B) \cup J^-(\Sigma_B) \cup \Sigma_B$. This is actually not as simple as it sounds due the the presence of the brane. We might naively suggest that the condition to use is simply given by requiring that:

$$|t_\chi - t_b| + R_b \leq \sqrt{\left(x_\chi - \frac{b_1 + b_2}{2\sin\theta_0}\right)^2 + z_\chi^2}, \tag{5.13}$$

where (t_χ, x_χ, z_χ) are points on either χ_1 or χ_2. The motivation behind this condition is that the set of spacelike separated points from $\mathcal{W}_E(\text{Vir}(B))$ must also be spacelike separated from $\mathcal{W}_E(B)$ due to the fact that $\mathcal{W}_E(B) \subseteq \mathcal{W}_E(\text{Vir}(B))$. Although this would serve as a sufficient condition to entanglement wedge nesting it would generally not be equivalent to saying that the points on $\chi_{con.}(A \cup B)$ are spacelike separated from $\mathcal{W}_E(B)$. In fact as we will discuss near the end of this chapter the condition that $\chi_{con.}(A \cup B)$ is spacelike separated from $\mathcal{W}_E(B)$ will excude a smaller region than our naive condition. Even so, it is still interesting to study the naive sufficient condition which we wrote in Eq. (5.13). In Appendix D.1.5 we study the naive sufficient condition given in Eq. (5.13) to obtain the following constraint:

$$|t_b - t_a| \leq a_1 + \frac{b_1 + b_2 - \sqrt{b_1^2 + b_2^2 + 2b_2 b_1 \cos(2\theta_0)}}{2\sin\theta_0}. \tag{5.14}$$

5.2.5 Discussion of Constraints for Poincare AdS_3

To summarize the previous section we found two distinct constraints. The first was the constraint we obtained had nothing to do with entanglement wedge nesting. It was obtained by asking if it was possible to have a single continuous line segment connecting brane and boundary points for arbitrary values of k. As we showed in Appendix D.1.2 there had to be an upper bound on k which allowed us to show that in the Poincare setup the following inequality had to be satisfied even before any considerations of EWN:

$$|t_b - t_a| < \sqrt{a_1^2 + b_1^2 + 2a_1 b_1 \sin\theta_0}. \tag{5.15}$$

To better understand this condition it is useful to define the 2D brane-boundary system. This is simply the 2D system described by the following expression:

$$z(x) = \Theta(x)\cot\theta_0 x, \tag{5.16}$$

which is simply the system that lives on the conformal boundary for $x < 0$ and the end-of-the-world brane for $x > 0$. In Appendix D.1.6 we study the propagation of null geodesics which originate on the boundary system ($x < 0$) and propagate to the brane ($x > 0$). We found that an observer restricted to the 2D brane boundary system would define causal relationships between a point on the boundary at $(t = t_a, x = -a_1, z = 0)$ and a point on the brane at $(t = t_b, x = b_1 \sin\theta_0, z = b_1 \cos\theta_0)$ as follows:

- The points are lightlike separated if $|t_b - t_a| = a_1 + b_1$.
- The points are timelike separated if $|t_b - t_a| > a_1 + b_1$.
- The points are spacelike separated if $|t_b - t_a| < a_1 + b_1$.

On the other hand, in Appendix D.1.6, we also studied a notion of "bulk-induced." In particular we studied the projection of a bulk lightcone whose apex sits in the boundary and then computed the intersection of the cone with the 2D brane-boundary system what we found in was that the right-hand side of Eq. (5.15) defined a new kind of induced causal structure on the boundary summarized below:

- They are bulk lightlike separated if $|t_b - t_a| = \sqrt{a_1^2 + b_1^2 + 2a_1 b_1 \sin\theta_0}$.
- They are bulk timelike separated if $|t_b - t_a| > \sqrt{a_1^2 + b_1^2 + 2a_1 b_1 \sin\theta_0}$.
- They are bulk spacelike separated if $|t_b - t_a| < \sqrt{a_1^2 + b_1^2 + 2a_1 b_1 \sin\theta_0}$.

We also proved that $a_1 + b_1 \geq \sqrt{a_1^2 + b_1^2 + 2a_1 b_1 \sin\theta_0}$. This is interesting in the context of what an observer living solely inside the brane-boundary system. In particular certain local and causal processes in the bulk perspecive will appear to occur at "superluminal" speeds (this was also discussed in a recent paper [112]) in a non-local manner according to the observer that defines causality solely within the brane-boundary system (who is oblivious to the existence of the bulk). This mismatch between causal notions in the brane-boundary system will become less pronounced as the brane is deflected less away from the boundary and will completely disappear once the brane actually coincides with the boundary (i.e. in the limit when $\theta_0 \to \pi/2$).

Now that we have discussed this interesting notion of the emergence of non-locality in the brane boundary system and the interpretation of the expression on the right-hand side of 5.15. It is interesting to ask how the sufficient condition for EWN fits into this picture.

In particular, is the constraint stronger or weaker than what we have discussed thus far? With some work we can see that we have the following hierarchy between constraints:

$$a_1 + b_1 \geq \sqrt{a_1^2 + b_1^2 + 2a_1 b_1 \sin\theta_0} \geq a_1 + \frac{b_1 + b_2 - \sqrt{b_1^2 + b_2^2 + 2b_2 b_1 \cos(2\theta_0)}}{2\sin\theta_0}. \tag{5.17}$$

This suggests that that requiring that the brane and boundary intervals are bulk spacelike separated may not be enough to guarantee EWN in the connected phase. However, this statement must be taken with a grain of salt. As we already eluded to in the previous subsections the constraint we derived for EWN is sufficient but possibly not necessary. This is because, the sufficient condition we wrote required that points on the connected RT curves be spacelike separated from $\mathcal{W}_E(\mathrm{Vir}(B))$. This is too strong because we can prove that the set of spacelike separated points from $\mathcal{W}_E(\mathrm{Vir}(B))$ are not the same as the set of spacelike separated points from $\mathcal{W}_E(B)$. The issue lies at the endpoints of the interval on the brane and the fact that $\chi_{dis.}(B)$ does not end at right angles on the brane in general. If we try to construct the causal development of Σ_B the presciption of simply shooting null geodesics orthogonally outwards from the $\chi_{dis.}(B)$ will leave a portion of bulk "unfilled." We can remedy this by including bulk lightcones at the endpoints of the intervals and then the causal development must be defined in the following piecewise manner.

We split up the bulk into three distinct regions defined below:

- The "Left Region" denoted $\mathcal{R}_L$: This is the set of points in the physical bulk region which are to the left of the line:

$$z(x) = -\frac{b_1 \sin(2\theta_0)x}{b_2 + b_1\cos(2\theta_0)} + \frac{b_1(b_1+b_2)\cos\theta_0}{b_2 + b_1\cos(2\theta_0)}. \tag{5.18}$$

- The "Right Region" denoted $\mathcal{R}_R$: This is the set of points in the physical bulk which lie to the right of the line:

$$z(x) = -\frac{b_2 \sin(2\theta_0)x}{b_1 + b_2\cos(2\theta_0)} + \frac{b_2(b_1+b_2)\cos\theta_0}{b_1 + b_2\cos(2\theta_0)}. \tag{5.19}$$

- The "Middle Region" denoted $\mathcal{R}_M$: This is the set of points in the physical bulk which lie in between the lines in Eqs. (5.18 - 5.19).

Using these defined regions we have the following piece-wise condition for spacelike separated points from $\mathcal{W}_E(B)$ when $\theta_0 \in (0, \pi/2)$ for the three regions we described above:

$$\begin{aligned} &[|t - t_b| + R_b]^2 < \left[x - \frac{b_1 + b_2}{2\sin\theta_0}\right]^2 + z^2 \\ &(x, z) \in \mathcal{R}_M \end{aligned} \tag{5.20}$$

$$|t - t_b|^2 < [x - b_1 \sin\theta_0]^2 + [z - b_1 \cos\theta_0]^2 \quad (x,z) \in \mathcal{R}_L \tag{5.21}$$

$$|t - t_b|^2 < [x - b_2 \sin\theta_0]^2 + [z - b_2 \cos\theta_0]^2 \quad (x,z) \in \mathcal{R}_R. \tag{5.22}$$

In the limit where $\theta_0 \to \pi/2$ we only have $\mathcal{R}_M$. In the case where $\theta_0 \to 0$ the extremal surface $\chi_{dis.}(B)$ no longer extends outside the brane (so we will not be interested in this case when discussing entanglement wedge nesting).

We can see that in $\mathcal{R}_M$ the statement that we have spacelike separated points from $\mathcal{W}_E(B)$ is equivalent to to the condition of having spacelike separated points from $\mathcal{W}_E(\mathrm{Vir}(B))$. Furthermore if we extended the condition in $\mathcal{R}_M$ past the permitted region we would cut out a larger portion of the bulk than what is necessary. This therefore suggests the naive condition we wrote in Eq. (5.14) is likely not necessary it may be weakened and maybe it would even be weakened enough that the necessary condition for EWN might coincide with a notion of bulk causality.

5.3 Conditions for Entanglement Wedge Nesting for Planar BTZ BH

In the following subsections we will be working towards finding sufficient conditions for entanglement wedge nesting. The setup will involve a two-sided Planar BTZ black hole which we will discuss in the following.

5.3.1 Two Sided BTZ Black Hole

In this section we will discuss entanglement wedge nesting for a two sided planar BTZ black hole with one side having an end-of-the-world brane. The line element for the two sided BTZ black hole can be written in Kruskal-Szekeres coordinates as follows:

$$ds^2 = \frac{1}{\cos^2 y}\left[L^2\left(-d\tau^2 + dy^2\right) + \frac{r_+^2}{L^2}\cos^2\tau dx^2\right], \tag{5.23}$$

where $\tau, y \in [-\pi/2, \pi/2]$, $x \in \mathbb{R}$, L is the AdS radius, and r_+ is the horizon "radius" in Schwarzschild coordinates (which we will discuss shortly). There are two conformal boundaries, the right conformal boundary will be at $y = \pi/2$ and the left conformal

boundary will be at $y = -\pi/2$. The event horizon of a two-sided black hole in these coordinates are described by the the lines $\tau = \pm y$. The event horizon splits the spacetime into 4 distinct regions which we describe below:

- The "Right Exterior" this is the set of points in the spacetime that satisfy:

$$\text{Ext}_R = \{(\tau, y, x) : |\tau| < y, y \in (0, \pi/2]\}. \tag{5.24}$$

  As the name suggests these are points in the right exterior of the spacetime which lie outside the event horizon (Blue shaded region in Figure 5.6).

- The "Left Exterior" this is the set of points in the spacetime that satisfy:

$$\text{Ext}_L = \{(\tau, y, x) : |\tau| < -y, y \in [-\pi/2, 0)\}. \tag{5.25}$$

  As the name suggests these are points in the left exterior of the spacetime which lie outside the event horizon (Orange shaded region in Figure 5.6).

- The "Future Interior" this is the set of points in the spacetime that satisfy:

$$\text{Int}_{Fut.} = \{(\tau, y, x) : |y| < \tau, \tau \in (0, \pi/2]\}. \tag{5.26}$$

  As the name suggests these are points in the interior of the black hole. Future directed causal curves starting in either the left or right exterior will eventually end up in the future interior (Green shaded region in Figure 5.6).

- The "Past Interior" this is the set of points in the spacetime that satisfy:

$$\text{Int}_{Past.} = \{(\tau, y, x) : |y| < -\tau, \tau \in [-\pi/2, 0)\}. \tag{5.27}$$

  As the name suggests these are points in the interior of the black hole. Past directed causal curves starting in either the left or right exterior will eventually end up in the past interior (Red shaded region in Figure 5.6).

Now that we have discussed the basics of the two sided BTZ black hole spacetime in Kruskal coordinates we will discuss the Schwarzschild coordinate description of the exterior regions, $\text{Ext}_{L,R}$. To do this, we define the following coordinate transformations from Kruskal coordinates (τ, y, x) to Schwarzschild coordinates $(t, r, \bar{x})$:

$$\begin{aligned} r &= r_+ \frac{\cos\tau}{\cos y} \\ t &= \frac{L^2}{2r_+} \ln\left[-\frac{\tan\left(\frac{\tau+y}{2}\right)}{\tan\left(\frac{\tau-y}{2}\right)}\right] = \frac{L^2}{2r_+} \ln\left[\frac{\sin y + \sin\tau}{\sin y - \sin\tau}\right] \\ \bar{x} &= x. \end{aligned} \tag{5.28}$$

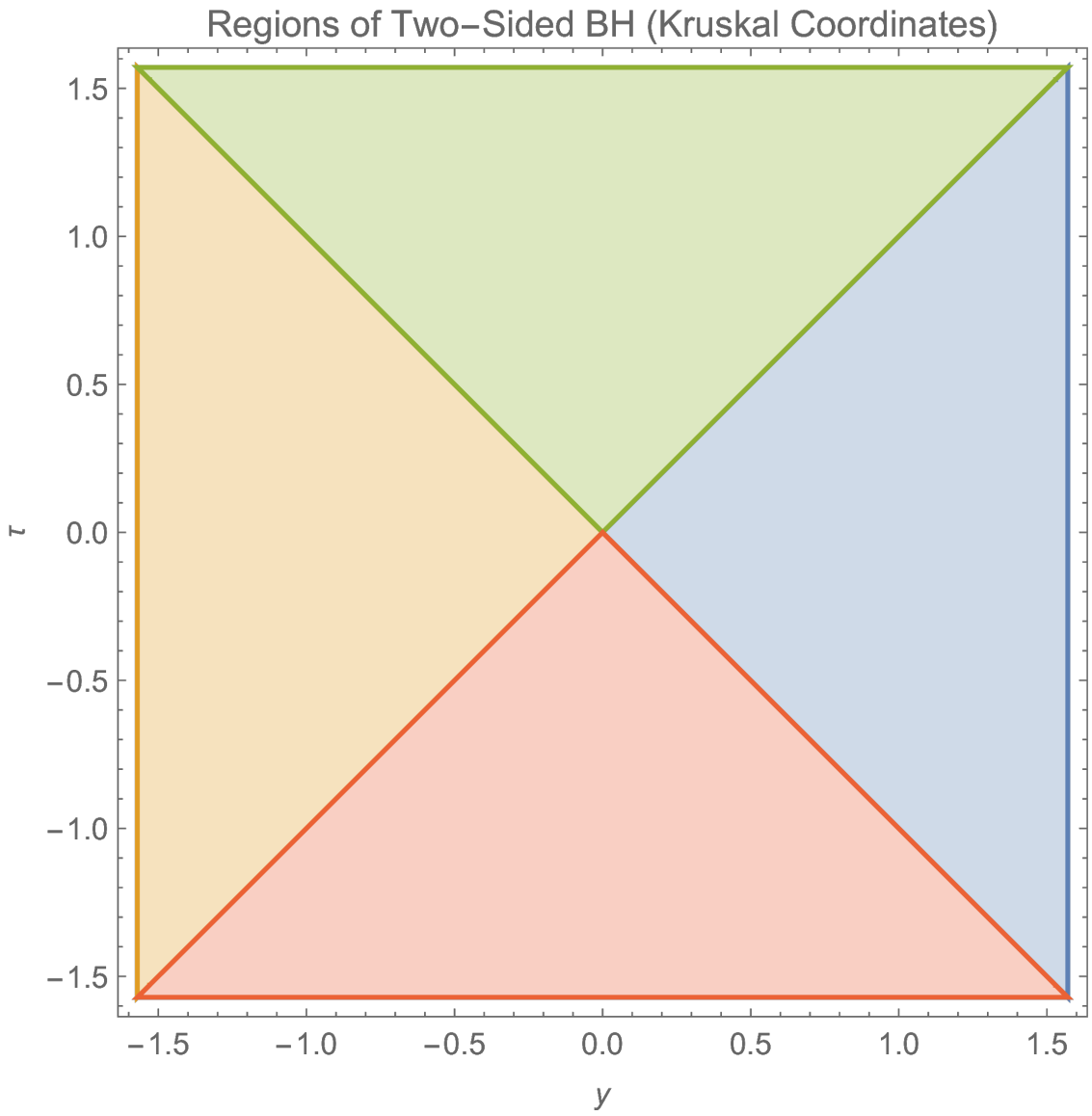

Figure 5.6: Depicted above is a Two-Sided Planar BTZ black hole spacetime in Kruskal coordinates (with the x coordinate suppressed but one can imagine it coming out/into the page). The horizon of the black hole are diagonal lines which split up the square into 4 quadrants which we described in the main text.

Applying these coordinate transformations to the exterior regions $\text{Ext}_{R,L}$ the line element given in Eq. (5.23) takes the form of the familar (planar) BTZ metric line element in Schwarzschild coordinates:

$$\begin{aligned} ds^2 &= -f(r)dt^2 + \frac{dr^2}{f(r)} + \frac{r^2}{L^2}dx^2 \\ f(r) &= \frac{r^2 - r_+^2}{L^2}. \end{aligned} \tag{5.29}$$

Where, $t \in \mathbb{R}$, $r > r_+$, and $x \in \mathbb{R}$. In these coordinates the metric becomes singular at the horizon $r = r_+$ and should really only be used when discussing either the left or right exteriors of the two sided black hole [3]. In fact, to be more precise we should actually have two copies of the the metric given in Eq. (5.29) one for the left exterior which Schwarzschild coordinates (t_L, r_L, x_L) and one for the right exterior (t_R, r_R, x_R). A simple analysis of the coordinate transformation defined in Eq. (5.28) shows that if we fix $|y|$ and τ then $r_R = r_L$ but $t_R = -t_L$. In particular, constant time slices in Schwarzschild coordinates are tilted planes in Kruskal coordinates which all go through the bifurcate horizon at $y = 0, \tau = 0$.

A particularly useful redefinition of the radial coordinate is $r = \frac{L^2}{z}$ so that the exterior exists for $z \in (0, z_+)$. Using this new radial coordinate gives the following expression for the planar BTZ black hole line element:

$$\begin{aligned} ds^2 &= \frac{L^2}{z^2}\left[-\tilde{f}(z)dt^2 + \frac{dz^2}{\tilde{f}(z)} + dx^2\right] \\ \tilde{f}(z) &= 1 - \frac{z^2}{z_+^2}. \end{aligned} \tag{5.30}$$

Now that we have reviewed some basic facts of the two sided BTZ black hole in both Kruskal and Schwarzschild coordinates we will introduce an end-of-the-world brane in our setup. The end-of-the-world brane will be a time-like co-dimension 1 surface. Which satisfies the following equations of motion involving the extrinsic curvature and induced metric:

$$K_{ab} - h_{ab} + T_0 h_{ab} = 0. \tag{5.31}$$

[3] One may wonder why bother working in Schwarzschild coordinates when one can simply use the Kruskal description. The reason for this that it is often easier to look for extremal surfaces in one coordinate system as opposed to another. In particular, finding the RT surface anchored to the boundary or brane (i.e. the thermal RT surface) will be much easier in Schwarzschild coordinates. In contrast, finding a RT surface which goes through the horizon and connects the boundary of the left exterior to the brane in the right exterior will be more straightforward in Kruskal coordinates.

One can check that a hypersurface $y = y_{Br}$ = constant, satisfies the equation of motion above with:

$$T_0 = \sin y_{Br}. \tag{5.32}$$

We will primarily be interested in the case where the end-of-the-world brane is in the right exterior (i.e. $y_{Br} \in (0, \pi/2]$). With the help of the coordinate transformations in Eq. (5.28), we can also express the end-of-the-world brane $y = y_{Br}$ in the right exterior in Schwarzschild coordinates as follows:

$$r(t) = r_+ \sqrt{\frac{1 - \sin^2 y_{Br} \tanh^2\left(\frac{r_+ t}{L^2}\right)}{\cos^2 y_{Br}}}. \tag{5.33}$$

We can see that in Schwarzschild coordinates the brane comes out from the past horizon at $t = -\infty$ and falls into the future horizon at $t = \infty$ with some non-trivial profile in r in the right exterior region. Now that we have described the setup of the two-sided BTZ black hole with an end-of-the-world brane we can talk about the subregions on the brane and boundary we want to consider.

For the sake of mathematical simplicity we will restrict ourselves to a very limited configuration of boundary and brane intervals. In particular, we will consider constant Schwarzschild time slice intervals of equal length on both the boundary and brane centred at $x = 0$. We will only allow for a relative shift in time for the boundary and brane intervals. We will denote the the constant time interval on the left boundary at Schwarzschild time $t = t_{bdry}$ as A_{bdry}. The constant time interval on the brane in the right exterior at Schwarzschild time $t = t_{Br}$ will be denoted by A_{Br}. In the next subsection we will discuss the candidate RT surfaces that will be anchored to such boundary and brane subregions (intervals).

5.3.2 Discussion of RT Surfaces for Two-Sided Planar BTZ BH

In this subsection we will be dealing with two kinds of RT surfaces in the two sided BTZ black hole spacetime with an end-of-the-world brane:

- "Thermal RT Surfaces": These are RT surfaces that are anchored to the endpoints of constant Schwarzschild time intervals on the brane or boundary centred around $x = 0$ of length $2a$. Such RT surfaces never cross the horizon and remain in either the left exterior anchored to a boundary interval or the right exterior anchored to a brane interval. We will denote the thermal surface in left exterior anchored to the boundary as $\chi_{\text{ther.}}(A_{bdry})$. We will denote the thermal surface in the right exterior anchored to the brane as $\chi_{\text{ther.}}(A_{Br})$.

- "Connected RT Surface": This is an RT surface that connects the boundary and brane interval and goes through the horizon to connect the left and right exteriors. We will denote this RT surface as, $\chi_{\text{con.}}(A_{bdry} \cup A_{Br})$ since these connected surfaces are associated with both A_{bdry} and A_{Br}.

Thermal RT Surface Anchored to Boundary or Brane:
Lets begin by finding the thermal RT surface using Schwarzschild coordinates (with a slight redefinition of the radial coordinate r to $z = \frac{L^2}{r}$ so the conformal boundary is at $z = 0$). This will be obtained by extremizing the following functional:

$$\begin{aligned} &\mathcal{A}[t, \dot{t}, z, \dot{z}; x] \int dx \frac{L}{z} \sqrt{-\tilde{f}(z)\dot{t}^2 + \frac{\dot{z}^2}{\tilde{f}(z)} + 1} \\ &z_+ = \frac{L^2}{r_+} \\ &\tilde{f}(z) = 1 - \frac{z^2}{z_+^2}. \end{aligned} \tag{5.34}$$

With some work, detailed in Appendix D.2.1, we can obtain the following expression for a thermal RT surface anchored to a constant time slice ($t_L = t_{bdry}$) interval in Ext_L on the conformal boundary (i.e. $\chi_{\text{ther.}}(A_{bdry})$):

$$\begin{aligned} &t(x) = t_{bdry} \\ &z(x) = z_+ \sqrt{1 - \frac{\cosh^2\left(\frac{x}{z_+}\right)}{\cosh^2\left(\frac{a}{z_+}\right)}}. \end{aligned} \tag{5.35}$$

Using the expression above for the thermal RT surface anchored to a boundary interval we can also easily deduce the expression for the thermal RT surface that which is anchored to a constant time slice interval on the brane at time $t = t_{Br}$ in the right exterior (i.e. $\chi_{\text{ther.}}(A_{Br})$). To do this we define the "virtual interval" associated to the interval on the brane denoted $\text{Vir}(A_{Br})$ which is defined to be an interval which is obtained by continuing the RT surface anchored to the brane past the brane into the non-physical region. In particular, we can define this interval as follows:

$$\begin{aligned} &\text{Vir}(A_{Br}) = \{(t, x, z) | t = t_{Br}, x \in [-a', a'], z = 0\}. \\ &a' = z_+ \text{arccosh}\left[\frac{\cosh\left(\frac{a}{z_+}\right)}{\sqrt{1 - \left(\frac{z_{Br}}{z_+}\right)^2}}\right] \geq a. \end{aligned} \tag{5.36}$$

Associated with this boundary interval we can write the following thermal RT surface $\chi_{ther.}(\text{Vir}(A_{Br}))$:

$$\begin{aligned} t(x) &= t_{Br} \\ z(x) &= z_+ \sqrt{1 - \frac{\cosh^2\left(\frac{x}{z_+}\right)}{\cosh^2\left(\frac{a'}{z_+}\right)}}. \end{aligned} \tag{5.37}$$

It it straightforward to see that $\chi_{ther.}(A_{Br}) = \chi_{ther.}(\text{Vir}(A_{Br})) \cap \text{Phys}(BTZ)$, where $\text{Phys}(BTZ)$ is the part of the Planar BTZ spacetime not cut off by the brane. In other words we have the following expression for $\chi_{ther.}(A_{Br})$:

$$\begin{aligned} z(x) &= z_+ \sqrt{1 - \frac{\cosh^2\left(\frac{x}{z_+}\right)}{\cosh^2\left(\frac{a}{z_+}\right)}\left(1 - \frac{z_{Br}^2}{z_+^2}\right)}. \\ t(x) &= t_{Br} \\ x &\in [-a, a]. \end{aligned} \tag{5.38}$$

We can see from the expression above that at $x = \pm a$ we have $z = z_{Br}$ which is what we want.

Now that we have discussed the thermal RT surface in exterior Schwarzschild coordinates we can use our results to rewrite the same thermal RT surface in Kruskal coordinates. To do this we need to invert the transformation in Eq. (5.28). With a little bit of algebra and a careful distinction between the left and right exteriors we have the following transformation from Schwarzschild coordinates to Kruskal coordinates:

$$\begin{aligned} \tan(v) &= \pm e^{-\frac{t}{z_+}} \sqrt{\frac{z_+ - z}{z_+ + z}} \\ \tan(u) &= \mp e^{\frac{t}{z_+}} \sqrt{\frac{z_+ - z}{z_+ + z}} \\ u &= \frac{\tau + y}{2} \\ v &= \frac{\tau - y}{2}, \end{aligned} \tag{5.39}$$

where the different choice of signs give us the right and left exteriors. In particular, the left exterior is given when $-u, v > 0$ and the right exterior is given when $-v, u > 0$. With

some work detailed in Appendix D.2.1 we can express $\chi_{\text{ther.}}(A_{bdry})$ as follows:

$$\begin{aligned}\sin(\tau(x)) &= -\frac{\cosh\left(\frac{x}{z_+}\right)\sinh\left(\frac{t_{bdry}}{z_+}\right)}{\sqrt{\cosh^2\left(\frac{a}{z_+}\right)+\cosh^2\left(\frac{x}{z_+}\right)\sinh^2\left(\frac{t_{bdry}}{z_+}\right)}}\\ \sin(y(x)) &= -\frac{\cosh\left(\frac{t_{bdry}}{z_+}\right)\cosh\left(\frac{x}{z_+}\right)}{\sqrt{\cosh^2\left(\frac{a}{z_+}\right)+\cosh^2\left(\frac{x}{z_+}\right)\sinh^2\left(\frac{t_{bdry}}{z_+}\right)}}.\end{aligned} \tag{5.40}$$

In a similar manner $\chi_{\text{ther.}}(A_{Br})$ is given by (see Appendix D.2.1 for details of derivation):

$$\begin{aligned}\sin(\tau(x)) = \sin[v(x)+u(x)] &= \frac{\sqrt{1-\frac{z_{Br}^2}{z_+^2}}\cosh\left(\frac{x}{z_+}\right)\sinh\left(\frac{t_{Br}}{z_+}\right)}{\sqrt{\cosh^2\left(\frac{a}{z_+}\right)+\left(1-\frac{z_{Br}^2}{z_+^2}\right)\cosh^2\left(\frac{x}{z_+}\right)\sinh^2\left(\frac{t_{Br}}{z_+}\right)}}\\ \sin(y(x)) = \sin[u(x)-v(x)] &= \frac{\sqrt{1-\frac{z_{Br}^2}{z_+^2}}\cosh\left(\frac{x}{z_+}\right)\cosh\left(\frac{t_{Br}}{z_+}\right)}{\sqrt{\cosh^2\left(\frac{a}{z_+}\right)+\left(1-\frac{z_{Br}^2}{z_+^2}\right)\cosh^2\left(\frac{x}{z_+}\right)\sinh^2\left(\frac{t_{Br}}{z_+}\right)}}.\end{aligned} \tag{5.41}$$

Connected RT Surface Connecting Brane and Boundary:

To find the connected RT surface we will resort to using Kruskal coordinates. In Kruskal coordinates we need to extremize the following functional:

$$\mathcal{A}[\tau,\dot{\tau},x,\dot{x};y] = \int dy \frac{\sqrt{L^2\left(-\dot{\tau}^2+1\right)+\frac{r_+^2}{L^2}\cos^2\tau\dot{x}^2}}{\cos y}. \tag{5.42}$$

For reasons discussed in Appendix D.2.2 we will be interested in connected RT curves in which $\dot{x}=0$ and we will be left with the task of extremizing a much simpler functional given by:

$$\mathcal{A}[\tau,\dot{\tau},x,\dot{x};y] = \int dy \frac{\sqrt{L^2\left(-\dot{\tau}^2+1\right)}}{\cos y}. \tag{5.43}$$

With the work detailed in Appendix D.2.2. We arrive at the following general expression for the RT curve(s) that goes through the horizon and connects the brane and boundary

intervals:

$$\begin{aligned} x(y) &= \pm a \\ \tau(y) &= \tau_{bdry} + \arcsin\left(\frac{c_\tau}{\sqrt{1+c_\tau^2}}\sin y\right) + \arcsin\left(\frac{c_\tau}{\sqrt{1+c_\tau^2}}\right). \end{aligned} \tag{5.44}$$

We define $\tau_{Br} = \tau(y_{Br})$. We can see that for a given a fixed value of τ_{bdry} (in the left exterior) the constant parameter $c_\tau \in \mathbb{R}$ will determine what τ_{Br} (in the right exterior) will be and vice-versa. We can see that in the special case where $c_\tau = 0$ the connected surface has a trivial horizontal profile in Kruskal time coordinates. For all values of c_τ the connected RT curve will have a spacelike tangent vector and in the limits where $c_\tau \to \pm\infty$ the RT curves become null.

When we do our analysis of entanglement wedge nesting we will find it useful to work in Schwarzschild coordinates since the expressions for entanglement wedge of the thermal RT surfaces can be expressed in terms regions enclosed by lightcones. For this reason it is useful to write down the expressions for the connected RT curves in the exterior Schwarzschild coordinates. To do this start with the expression in Eq. (5.44) and make use of the coordinate transformation that takes Exterior regions in Kruskal coordinates to Schwarzschild coordinates given by Eq. (5.28). With the work detailed in Appendix D.2.2 we obtain the following expression/description for the connected surface in the right exterior (where the brane is located) in Schwarzschild coordinates:

$$\begin{aligned} x(t) &= \pm a \\ \left(\frac{z(t)}{z_+}\right)^2 &= 1 - \frac{1-\frac{z_{Br}^2}{z_+^2}}{\left[\cosh\left(\frac{|\Delta t|}{z_+}\right) + \left|\frac{B}{A}\right|\sinh\left(\frac{|\Delta t|}{z_+}\right)\right]^2} \\ \Delta t &= t - t_{Br} \\ A &= \cos\tau_* \sinh\left(\frac{t_{Br}}{z_+}\right) - c_t \cosh\left(\frac{t_{Br}}{z_+}\right) \\ B &= \cos\tau_* \cosh\left(\frac{t_{Br}}{z_+}\right) - c_t \sinh\left(\frac{t_{Br}}{z_+}\right) \\ \tau_* &= \tau_{Br} - \arcsin(c_t \sin y_{Br}) \\ c_t &= \frac{c_\tau}{\sqrt{1+c_\tau^2}}. \end{aligned} \tag{5.45}$$

It should be noted that the appearance of the absolute value signs in the expressions is a "book-keeping" tool which circumvents the issue of worrying about the specific signs

we need to use for Δt for a given c_t (see Appendix D.2.2 for a complete treatment and explanation for the appearance of the absolute values).

5.3.3 Discussion of Entanglement Wedges (Planar BTZ BH)

Now that we have discussed both the thermal and connected RT surfaces we will discuss the entanglement wedges associated to the regions A_{bdry}, A_{Br}, and $A_{bdry} \cup A_{Br}$.

Starting with A_{bdry}, we define $\Sigma_{A_{bdry}}$ as a partial Cauchy surface with a boundary, $\partial\Sigma_{A_{bdry}} = A_{bdry} \cup \chi_{\text{ther.}}(A_{bdry})$. Using $\Sigma_{A_{bdry}}$ we define the entanglement wedge of A_{bdry}, denoted $\mathcal{W}_E(A_{bdry})$, as the domain of dependence of $\Sigma_{A_{bdry}}$. A convenient prescription which can be used to explicitly construct the entanglement wedge of the boundary interval A is by considering the a family of null geodesics beginning on $\chi_{ther.}(A_{bdry})$ which are also orthogonal to $\chi_{ther.}(A_{bdry})$ and evolve towards the boundary. The set of these null geodesics enclose a co-dimension 0 region which is exactly $\mathcal{W}_E(A_{bdry})$ as shown in Figure 5.7.

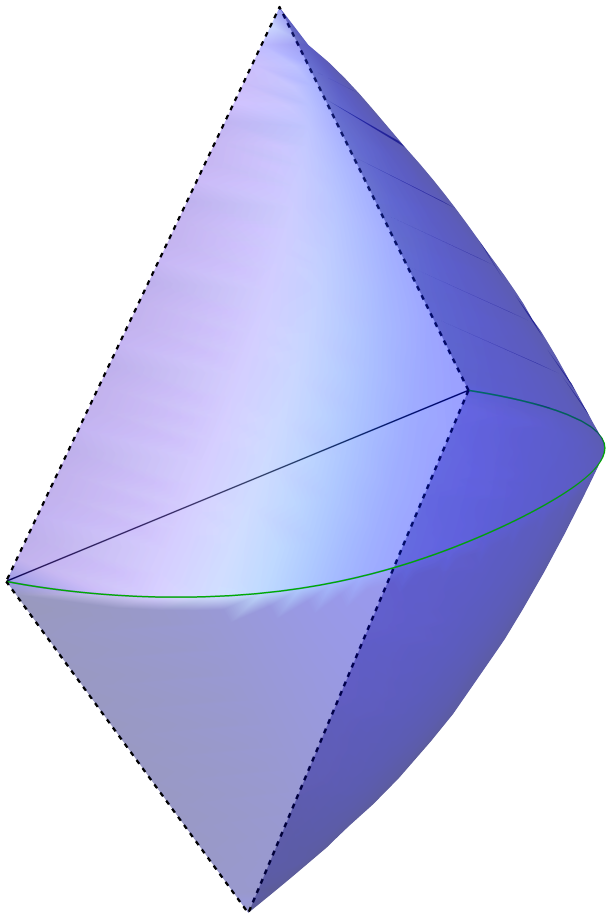

Figure 5.7: Depicted in the figure above is an example of what $\mathcal{W}_E(A_{bdry})$ might look like. The intersection of the past and future cones is the RT surface $\chi_{ther.}(A_{bdry})$ shown in green. The dotted "diamond" is the causal diamond on the boundary associated with the interval A_{bdry} which horizontally splits the diamond to the future and past of the interval. We can see the "flattening" effect on the entanglement wedge deeper in the bulk due to the horizon of the Planar BTZ black hole.

As we discuss in Appendix D.2.4 the entanglement wedge and causal wedge for a constant time interval on the boundary are the same. We have the following explicit expression for the null surface that encloses the points inside $\mathcal{W}_E(A)$ (see Appendix D.2.4 for details

of where this comes from):

$$a - |t - t_{bdry}| = z_+ \text{arctanh}\left[\sqrt{1 - \frac{1 - \frac{z^2}{z_+^2}}{\cosh^2\left(\frac{x}{z_+}\right)}}\right]. \tag{5.46}$$

We say that $(t, x, z) \in \mathcal{W}_E(A_{bdry})$ if the points satisfy the inequality:

$$a - |t - t_{bdry}| > z_+ \text{arctanh}\left[\sqrt{1 - \frac{1 - \frac{z^2}{z_+^2}}{\cosh^2\left(\frac{x}{z_+}\right)}}\right]. \tag{5.47}$$

In an analogous manner we can define the entanglement wedge associated with the region A_{Br} on the brane. We define $\Sigma_{A_{Br}}$ as the partial Cauchy slice whose boundary is given by $\partial\Sigma_{A_{Br}} = A_{Br} \cup \chi_{ther.}(A_{Br})$. Then the entanglement wedge of A_{Br}, denoted $\mathcal{W}_E(A_{Br})$, is simply the domain of dependence of the $\Sigma_{A_{Br}}$. Furthermore a more explicit construction of the of the wedge can be made by considering the a family of null geodesics beginning on $\chi_{ther.}(A_{Br})$ which are also orthogonal to $\chi_{dis.}(B)$ and evolve towards the boundary. The set of these null geodesics enclose a co-dimension 0 region which is exactly $\mathcal{W}_E(A_{Br})$ as shown in Figure 5.8.

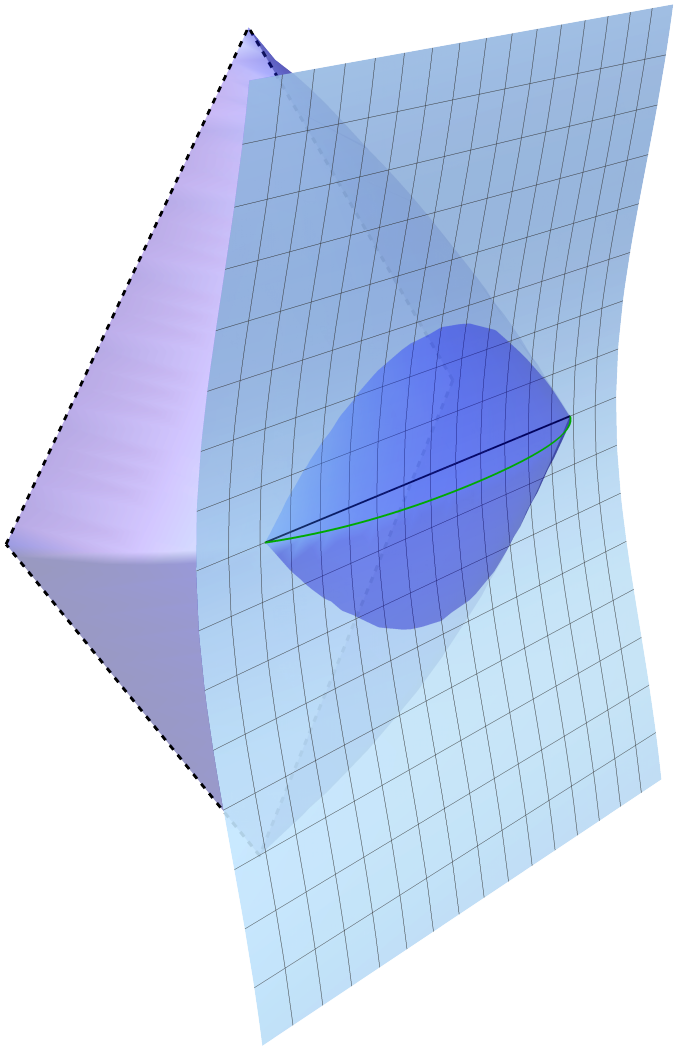

Figure 5.8: Depicted in the figure above is an example of $\mathcal{W}_E(A_{Br})$. There are actually two entanglement wedges in the figure. The very large wedge which extends behind the brane is what we called $\mathcal{W}_E(\mathrm{Vir}(A_{Br}))$ in Appendix D.2.4. The actual entanglement wedge $\mathcal{W}_E(A_{Br})$ is the small piece that is cut out of the larger wedge by the wrapped plane which is the end-of-the-world brane.

Based on the discussion in Appendix D.2.4 we can obtain the following inequality which characterizes the set of points in $\mathcal{W}_E(A_{Br})$:

$$\begin{aligned} a' - |t - t_{Br}| &> z_+ \text{arctanh}\left[\sqrt{1 - \frac{1 - \frac{z^2}{z_+^2}}{\cosh^2\left(\frac{x}{z_+}\right)}}\right] \\ a' &= z_+ \text{arccosh}\left[\frac{\cosh\left(\frac{a}{z_+}\right)}{\sqrt{1 - \frac{z_{Br}^2}{z_+^2}}}\right]. \end{aligned} \tag{5.48}$$

where we make the implicit restriction on (t, x, z) to be in Phys(BTZ) which simply denotes the bulk region that physically exists and not cut off by the brane.

Finally we turn to the construction of the entanglement wedge associated with $A_{bdry} \cup A_{Br}$, denoted, $\mathcal{W}_E(A_{bdry} \cup A_{Br})$. As in the Poincare case we note there are actually two possible "phases" for $\mathcal{W}_E(A_{bdry} \cup A_{Br})$ which we call the "disconnected phase" or the "connected phase". In the disconnected phase we have $\mathcal{W}_E(A_{bdry} \cup A_{Br}) = \mathcal{W}_E(A_{bdry}) \cup \mathcal{W}_E(A_{Br})$, this is simply the union of the separate entanglement wedges of A_{bdry} and A_{Br} which we already discussed. In the connected phase we define $\Sigma_{A_{bdry} \cup A_{Br}}$ as the partial Cauchy slice with a boundary given by $\partial\Sigma_{A_{bdry} \cup A_{Br}} = \chi_{con.}(A_{bdry} \cup A_{Br}) \cup A_{bdry} \cup A_{Br}$. Then using this partial Cauchy slice we define the connected phase entanglement wedge as the domain of dependence of $\Sigma_{A_{Br} \cup A_{bdry}}$.

5.3.4 Sufficient Condition for Entanglement Wedge Nesting (Planar BTZ BH)

In this subsection we will derive constraints on the parameters defining the separation of boundary and brane subregions in Kruskal time such that $\mathcal{W}_E(A_{Br}) \subset \mathcal{W}_E(A_{Br} \cup A_{bdry})$ in the connected phase.

Just as we did in the Poincare AdS_3 analysis in Section 5.2.4 we can argue that a sufficient condition for EWN is given by requiring that all null geodesics originating from $\chi_{con}(A_{bdry} \cup A_{Br})$ are unable to reach $\mathcal{W}_E(A_{Br})$ (i.e. no causal signals originating from $\chi_{con.}(A_{bdry} \cup A_{Br})$ can influence events in $\mathcal{W}_E(A_{Br})$). Once again we will consider the naive (and likely over constraining) condition that the the points on the connected surface be spacelike separated from $\mathcal{W}_E(\text{Vir}(A_{Br}))$. Such a condition is relatively straightforward to explore and manipulate mathematically. In particular, the points $(t, z, x) \in Phys(BTZ)$

are spacelike (or possibly null) separated from points in $\mathcal{W}_E(\text{Vir}(A_{Br}))$ if the following inequality is satisfied:

$$a' + |t - t_{Br}| \leq z_+ \text{arctanh}\left[\sqrt{1 - \frac{1 - \frac{z^2}{z_+^2}}{\cosh^2\left(\frac{x}{z_+}\right)}}\right]. \tag{5.49}$$

Points that satisfy such an inequality cannot influence events inside $\mathcal{W}_E(\text{Vir}(A_{Br}))$ and, by extension, cannot influence events inside $\mathcal{W}_E(A_{Br})$ either. This will guarantee that $\mathcal{W}_E(A_{Br}) \subseteq \mathcal{W}_E(A_{bdry} \cup A_{Br})$. So let $(t_\chi, z_\chi, x_\chi = \pm a)$ be points on the connected surface which are described by the expression we wrote in Eq. (5.45) then EWN is satisfied if:

$$a' + |t_\chi - t_{Br}| \leq z_+ \text{arctanh}\left[\sqrt{1 - \frac{1 - \frac{z_\chi^2}{z_+^2}}{\cosh^2\left(\frac{a}{z_+}\right)}}\right]. \tag{5.50}$$

In Appendix D.2.5 we study the sufficient condition given in Eq. (5.50) to obtain the following inequality:

$$\left|\frac{B}{A}\right| \geq \Xi(a, z_{Br}) = \sqrt{1 - \frac{1 - \frac{z_{Br}^2}{z_+^2}}{\cosh^2\left(\frac{a}{z_+}\right)}}. \tag{5.51}$$

So as long as the expression above is satisfied we expect to have EWN. It is actually possible to go even further and derive a specific constraint on the parameter c_t which characterizes the connected surface. If we fix the parameters y_{Br}, τ_{Br}, and a and allow c_t to vary (i.e. we fix the location and size of the brane interval and move the boundary interval up and down in time) then we can visualize the constraint with the help of the listed facts about B/A discussed in Appendix D.2.2. The visualization is depicted in Figure 5.9.

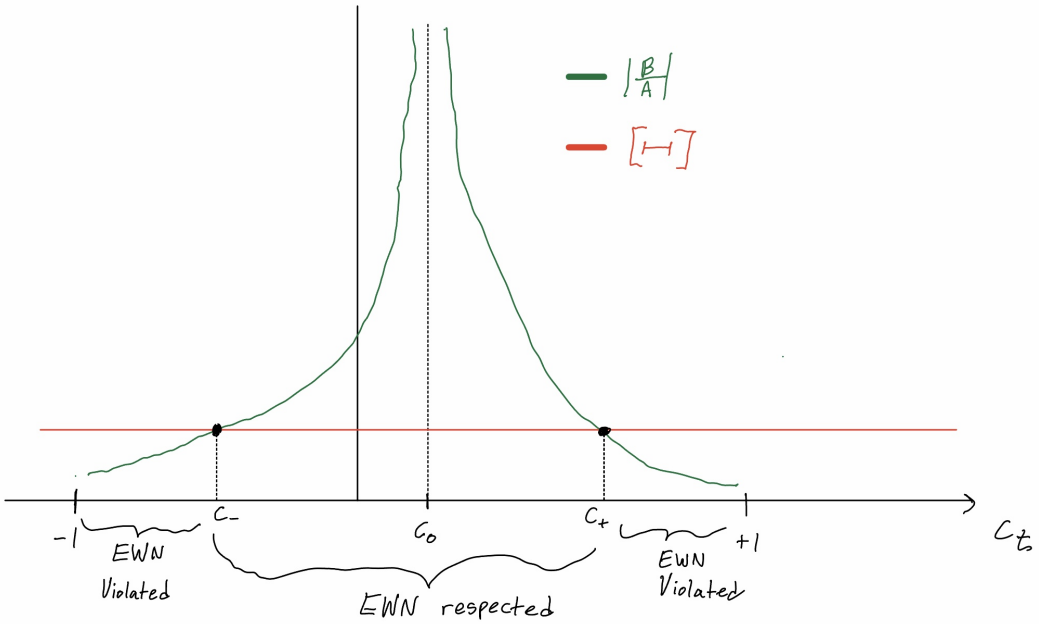

Figure 5.9: Depicted in the figure above is a visualization/sketch of the inequality given in Eq. (5.51). The green line is $|B/A|$ (it has a singularity at $c_t = c_0 = \frac{\sin \tau_{Br}}{\sin y_{Br}}$) and the red line is Ξ. Entanglement wedge nesting is respected when the green line is above the red line. This naturally gives an interval of values for c_t in which entanglement wedge nesting is satisfied. The lower and upper bounds of the interval are labeled c_- for the lower bound and c_+ for the upper bound whose expressions are generally given by Eq. (5.52). The smallest interval comes from the limit when $a \to \infty$ (i.e. size of the brane interval diverges), in that case $c_\pm$ is given by Eq. (5.53).

As we can see the right-hand side of the inequality in Eq. (5.51) is a constant horizontal line. The left hand side of the inequality as a function of c_t has a vertical asymptote at $c_t = c_0$ and is non-zero and well defined everywhere else in the regime $c_t \in (-1, 1)$. The inequality tells us keep the values of c_t where $|B/A|$ lies above the horizontal line. We can see that the range of values of c_t will lie in the interval $c_t \in [c_-, c_+]$ where $-1 < c_- < c_0 < c_+ < 1$. The specific values of $c_\pm$ can be obtained by solving the equations discussed in

Appendix D.2.5:

$$
\begin{aligned}
c_- &= -\left[1+\frac{\left[\cos(2\tau_{Br})-\cos(2y_{Br})\right]\left[\Xi^2\cos^2\tau_{Br}-\cos^2 y_{Br}\right]}{2\cos^2\tau_{Br}\left(\sin y_{Br}-\Xi\sin\tau_{Br}\right)^2}\right]^{-\frac{1}{2}} \\
c_+ &= \left[1+\frac{\left[\cos(2\tau_{Br})-\cos(2y_{Br})\right]\left[\Xi^2\cos^2\tau_{Br}-\cos^2 y_{Br}\right]}{2\cos^2\tau_{Br}\left(\sin y_{Br}+\Xi\sin\tau_{Br}\right)^2}\right]^{-\frac{1}{2}}.
\end{aligned}
\tag{5.52}
$$

The tightest interval occurs when we take the limit of the expressions above as $\Xi \to 1$ to give:

$$
\begin{aligned}
c_- &= -\frac{1}{\sqrt{1+\left(\frac{\sin\tau_{Br}+\sin y_{Br}}{\cos\tau_{Br}}\right)^2}} \\
c_+ &= \frac{1}{\sqrt{1+\left(\frac{\sin\tau_{Br}-\sin y_{Br}}{\cos\tau_{Br}}\right)^2}}.
\end{aligned}
\tag{5.53}
$$

5.3.5 Discussion of Constraints for Planar BTZ Black Hole Results

Now that we have derived a sufficient condition for having a respect for EWN in the connected phase we can continue and describe a nice geometric interpretation of what the tightest constraints given in Eq. (5.53) mean. The answer is quite simple. First lets recall that a-priori we just required that $|c_t| < 1$ so the connected RT surfaces are spacelike. The consequences of this is the following. Suppose we have a connected curve which starts on the left boundary at some Kruskal time $|\tau_{bdry}| < \pi/2$. For $c_t = 0$ the connected surface in Kruskal coordinates has a trivial horizontal profile and will end on the brane in the right exterior at the same time Kruskal time as it started with in the boundary. However for more general values of c_t less than unity one can imagine that there are certain values of c_t where the surface would go through the past or future "singularity" (into a new "universe") before it hits the brane. It turns out the the condition that EWN hold for intervals on the brane in the right exterior exactly excludes the configurations that would allow the connected surface to go through the singularity. In particular, if we fix the location of a constant time interval in the right exterior on the brane (i.e. fix τ_{Br} and y_{Br}) then the condition that EWN holds translates to:

$$
-\frac{1}{\sqrt{1+\left(\frac{\sin\tau_{Br}+\sin y_{Br}}{\cos\tau_{Br}}\right)^2}} \leq c_t \leq \frac{1}{\sqrt{1+\left(\frac{\sin\tau_{Br}-\sin y_{Br}}{\cos\tau_{Br}}\right)^2}}.
\tag{5.54}
$$

In Figure 5.10 we plot the connected surface in Kruskal coordinates in the $\tau - y$ plane for $c = c_+$, $c = c_-$, and $c = c_0$ and see that the condition prevents the connected surface from going past the future and past singularities.

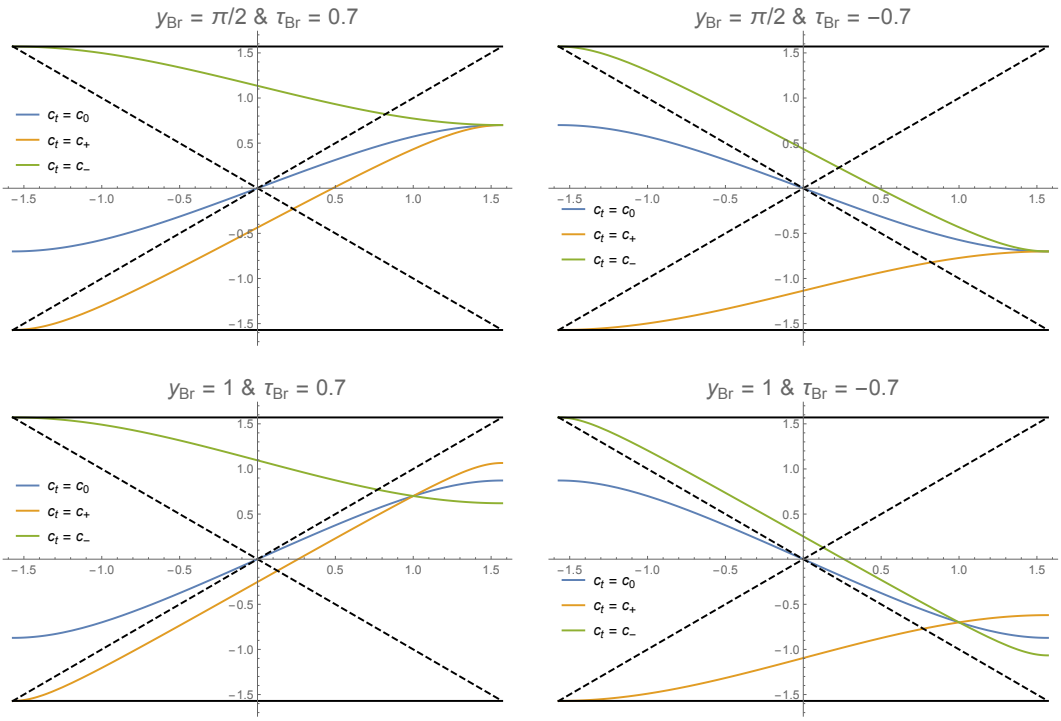

Figure 5.10: Above we fix τ_{Br} and y_{Br} for can consider trajectories of the connected surfaces which correspond to $c_\pm$ given in Eq. (5.53) as well as c_0 which we can see goes through the bifurcate horizon.

5.4 Future Efforts

We have studied/derived the constraints imposed by naive sufficient conditions which ensure EWN in 3D AdS spacetimes that are cutoff by an end-of-the-world brane we will conclude this chapter by discussing some open issues (at the time of writing this chapter). Perhaps the biggest issue is that we did not address is when the connected phase actually exists if there is no connected phase no violations can occur. Therefore, in the future we will be interested in trying to understand if the regimes where we have EWN violations are actually valid connected phases. The other open issue concerns the conditions them-

selves. The conditions we obtained are sufficient conditions and it is not entirely clear that they are necessary conditions for entanglement wedge nesting. We already suggested that the constraint we got in the Poincare AdS_3 analysis is likely too strong and more careful analysis is needed to understand the necessary condition. The intuition we currently have for future efforts in formulating a set of necessary conditions is to conjecture that if entanglement wedge nesting is violated in the connected phase then the violations should start in arbitrarily small bulk neighborhoods of the endpoints of the brane interval where the connected and disconnected RT surfaces meet. If such a conjecture is true then we can likely find a necessary condition for entanglement wedge violation by simply analyzing the trajectory of null geodesics in the vicinity of the entangling surface on the brane (this may also prove to be a useful approach in higher dimensions as well).

Part III

Concluding Remarks

Chapter 6

Thesis Conclusion

6.1 Review of Major Results

Now that we have gone through the main works of this thesis it is useful to give a brief summary.

In Chapter 2, we studied the relation between the scrambling and echo time scale for AdS black holes that are spherically symmetric. We showed that the integral in the echo time got most of its contribution near the horizon and it was this piece of the echo time scale which could be identified with the scrambling time scale. We also suggested that if one wanted to understand if echoes exist for a particular holographic CFT state (which resembled a black hole with horizon modifications) we should expect OTOCs at early times to exhibit exponential decay as they would for a standard black hole but after the scrambling time scale one might see echoes in the OTOC signalling the existence of some modifications near the horizon. We concluded the chapter by speculating on possible future avenues of exploration in Section 2.7.

In Chapter 3, we analyzed the idea of echoes from the perspective of black hole microstate statistics. We adopted the perspective that the unitary description of a black hole is given by a thermal ensemble of $e^{S_{BH}}$ microstates. The way by which the black hole thermalizes after being perturbed is then determined by correlators in the thermal ensemble of microstates. We adopted the spectral form factor as a convenient proxy for a two point function calculation and studied how the time dependence of the form factor depended on the spectral statistics of the microstates. We adopted the i.i.d. model which assumed the nearest neighbor spacing between adjacent eigenvalues obeyed the same distribution. With

this model, we could compute closed form expressions for the form factor. We reproduced standard behaviour of the form factor with a ramp and plateau for nearest neighbor spacing statistics that are given by the Wigner surmise. We then considered a generalization of the Wigner surmise statistics and considered a more general Dyson index which would show up in β ensembles. We showed that for β ensembles the form factor could exhibit late time "echoes." In particular, we suggested that the echoes that occur in β ensembles with a large Dyson index could be attributed to enhanced repulsion between eigenvalues which is not present in classical Gaussian ensembles. We also showed that it was possible to obtain early time echoes if one had regularly spaced clusters of microstates. We concluded the chapter by speculating on possible future avenues of exploration in Section 3.5.

In Chapter 4, we studied how the evaporation rate of black holes was affected by the extraction of radiation close to the horizon by an absorptive screen. We modelled the screen as a perfectly absorptive surface and defined the generalized greybody factor to understand what fraction of Hawking radiation would be able to reach the screen. Unsurprisingly, we found that the closer we place the screen to the black hole the faster its evaporation rate will be. We applied our results for Pennington information recovery time and found that for small AdS black holes the results are the same as what Pennington had in his paper. However, for large AdS black holes we had an information recovery time that was the scrambling time associated with a AdS sized cell on the horizon which is reasonable. We then proceeded to discuss the physics of the screen by viewing it as an interface that glued an interior spacetime containing the black hole with an exterior spacetime which acted as a bath to store the radiation. Using junction conditions we determined the stress energy tensor of the interface and showed that it satisfied a radial NEC but violated the angular NEC. We concluded the chapter by speculating on possible future avenues of exploration in Section 4.5.

In Chapter 5, we studied entanglement wedge nesting in 3D AdS spacetimes with an end-of-the-world branes. We considered a setup in Poincare AdS_3 where we defined a constant time interval on the boundary and another constant time interval on the brane. We then computed the different candidate RT curves that would be anchored to the subregions on the brane and boundary. Under the assumption that the connected phase existed for a particular choice of placement of the brane and boundary intervals we wanted to know when the entanglement wedge associated with the brane interval would be completely nested inside the connected wedge which formed a "tube" connecting the brane and boundary subregions. We found a sufficient constraint for EWN in the connected phase by requiring that the connected RT curves be spacelike separated from the entanglement wedge associated with the brane. We found that if we were to assume the sufficient condition as necessary then requiring the interval on the brane and boundary to be spacelike

separated in the bulk would not be enough to ensure entanglement wedge nesting. We also did a similar computation for entanglement wedge nesting for a two-sided Planar BTZ black hole. We found that in the limit where the brane and boundary intervals became infinitely large our sufficient condition for EWN had a nice geometric interpretation that the connected surface should stay within the allowed bounds of the Kruskal diagram. We concluded the chapter by speculating on future avenues of exploration in Section 5.4.

References

[1] Jahed Abedi and Niayesh Afshordi. Echoes from the Abyss: A highly spinning black hole remnant for the binary neutron star merger GW170817. 2018.

[2] Jahed Abedi and Niayesh Afshordi. Echoes from the Abyss: A Status Update. 1 2020.

[3] Jahed Abedi, Niayesh Afshordi, Naritaka Oshita, and Qingwen Wang. Quantum Black Holes in the Sky. *Universe*, 6(3):43, 2020.

[4] Jahed Abedi, Hannah Dykaar, and Niayesh Afshordi. Echoes from the Abyss: Tentative evidence for Planck-scale structure at black hole horizons. *Phys. Rev.*, D96(8):082004, 2017.

[5] Jahed Abedi, Hannah Dykaar, and Niayesh Afshordi. Comment on: "Low significance of evidence for black hole echoes in gravitational wave data". 2018.

[6] A. A. Abul-Magd and A. Y. Abul-Magd. Size effect of diagonal random matrices, 2011.

[7] Ahmed Almheiri, Netta Engelhardt, Donald Marolf, and Henry Maxfield. The entropy of bulk quantum fields and the entanglement wedge of an evaporating black hole. *JHEP*, 12:063, 2019.

[8] Ahmed Almheiri, Thomas Hartman, Juan Maldacena, Edgar Shaghoulian, and Amirhossein Tajdini. The entropy of Hawking radiation. 6 2020.

[9] Ahmed Almheiri and Byungwoo Kang. Conformal Symmetry Breaking and Thermodynamics of Near-Extremal Black Holes. *JHEP*, 10:052, 2016.

[10] Ahmed Almheiri, Donald Marolf, Joseph Polchinski, and James Sully. Black Holes: Complementarity or Firewalls? *JHEP*, 02:062, 2013.

[11] Ahmed Almheiri, Alexandros Mousatov, and Milind Shyani. Escaping the Interiors of Pure Boundary-State Black Holes. 3 2018.

[12] T. Altherr. Introduction to thermal field theory. *Int. J. Mod. Phys. A*, 8:5605–5628, 1993.

[13] Alexander Altland, Dmitry Bagrets, Pranjal Nayak, Julian Sonner, and Manuel Vielma. From operator statistics to wormholes. *Phys. Rev. Res.*, 3(3):033259, 2021.

[14] Alexander Altland and Julian Sonner. Late time physics of holographic quantum chaos. *SciPost Phys.*, 11:034, 2021.

[15] Martin Ammon and Johanna Erdmenger. *Gauge/gravity duality: Foundations and applications*. Cambridge University Press, Cambridge, 4 2015.

[16] Y. Y. Atas, E. Bogomolny, O. Giraud, and G. Roux. Distribution of the ratio of consecutive level spacings in random matrix ensembles. *Physical Review Letters*, 110(8), Feb 2013.

[17] J. L. F. Barbon and E. Rabinovici. Very long time scales and black hole thermal equilibrium. *JHEP*, 11:047, 2003.

[18] James M. Bardeen, B. Carter, and S. W. Hawking. The Four laws of black hole mechanics. *Commun. Math. Phys.*, 31:161–170, 1973.

[19] K. Becker, M. Becker, and J. H. Schwarz. *String theory and M-theory: A modern introduction*. Cambridge University Press, 2006.

[20] Jacob D. Bekenstein. Black holes and entropy. *Phys. Rev. D*, 7:2333–2346, 1973.

[21] Iosif Bena, Emil J. Martinec, Samir D. Mathur, and Nicholas P. Warner. Snowmass White Paper: Micro- and Macro-Structure of Black Holes. 3 2022.

[22] M. Berry and M. Tabor. Level clustering in the regular spectrum. *Proceedings of the Royal Society of London. A. Mathematical and Physical Sciences*, 356:375 – 394, 1977.

[23] Emanuele Berti, Vitor Cardoso, and Andrei O. Starinets. Quasinormal modes of black holes and black branes. *Class. Quant. Grav.*, 26:163001, 2009.

[24] Massimo Bianchi, Alfredo Grillo, and Jose Francisco Morales. Chaos at the rim of black hole and fuzzball shadows. *JHEP*, 05:078, 2020.

[25] Andreas Blommaert, Luca V. Iliesiu, and Jorrit Kruthoff. Gravity factorized. *JHEP*, 09:080, 2022.

[26] Andreas Blommaert, Thomas G. Mertens, and Henri Verschelde. Eigenbranes in Jackiw-Teitelboim gravity. *JHEP*, 02:168, 2021.

[27] O. Bohigas, M. J. Giannoni, and C. Schmit. Characterization of chaotic quantum spectra and universality of level fluctuation laws. *Phys. Rev. Lett.*, 52:1–4, 1984.

[28] Adam R. Brown. Tensile Strength and the Mining of Black Holes. *Phys. Rev. Lett.*, 111(21):211301, 2013.

[29] Adam R. Brown, Hrant Gharibyan, Alexandre Streicher, Leonard Susskind, Larus Thorlacius, and Ying Zhao. Falling Toward Charged Black Holes. *Phys. Rev.*, D98(12):126016, 2018.

[30] Luca Buoninfante and Anupam Mazumdar. Nonlocal star as a blackhole mimicker. *Phys. Rev.*, D100(2):024031, 2019.

[31] Vitor Cardoso, Edgardo Franzin, and Paolo Pani. Is the gravitational-wave ringdown a probe of the event horizon? *Phys. Rev. Lett.*, 116(17):171101, 2016. [Erratum: Phys. Rev. Lett.117,no.8,089902(2016)].

[32] Vitor Cardoso, Seth Hopper, Caio F. B. Macedo, Carlos Palenzuela, and Paolo Pani. Gravitational-wave signatures of exotic compact objects and of quantum corrections at the horizon scale. *Phys. Rev.*, D94(8):084031, 2016.

[33] Vitor Cardoso and Paolo Pani. Tests for the existence of black holes through gravitational wave echoes. *Nat. Astron.*, 1(9):586–591, 2017.

[34] Vitor Cardoso and Paolo Pani. The observational evidence for horizons: from echoes to precision gravitational-wave physics. 2017.

[35] Vitor Cardoso and Paolo Pani. Testing the nature of dark compact objects: a status report. 2019.

[36] Sean M. Carroll. *Spacetime and Geometry*. Cambridge University Press, 7 2019.

[37] Hong Zhe Chen, Robert C. Myers, Dominik Neuenfeld, Ignacio A. Reyes, and Joshua Sandor. Quantum Extremal Islands Made Easy, Part I: Entanglement on the Brane. *JHEP*, 10:166, 2020.

[38] Hong Zhe Chen, Robert C. Myers, Dominik Neuenfeld, Ignacio A. Reyes, and Joshua Sandor. Quantum Extremal Islands Made Easy, Part II: Black Holes on the Brane. *JHEP*, 12:025, 2020.

[39] Scott Collier and Alexander Maloney. Wormholes and Spectral Statistics in the Narain Ensemble. 6 2021.

[40] Randy S. Conklin, Bob Holdom, and Jing Ren. Gravitational wave echoes through new windows. *Phys. Rev.*, D98(4):044021, 2018.

[41] Jordan Cotler, Nicholas Hunter-Jones, Junyu Liu, and Beni Yoshida. Chaos, Complexity, and Random Matrices. *JHEP*, 11:048, 2017.

[42] Jordan S. Cotler, Guy Gur-Ari, Masanori Hanada, Joseph Polchinski, Phil Saad, Stephen H. Shenker, Douglas Stanford, Alexandre Streicher, and Masaki Tezuka. Black Holes and Random Matrices. *JHEP*, 05:118, 2017. [Erratum: JHEP 09, 002 (2018)].

[43] Jan de Boer. The Holographic renormalization group. *Fortsch. Phys.*, 49:339–358, 2001.

[44] Ramit Dey and Niayesh Afshordi. Echoes in the Kerr/CFT correspondence. *Phys. Rev. D*, 102(12):126006, 2020.

[45] Ramit Dey, Sumanta Chakraborty, and Niayesh Afshordi. Echoes from braneworld black holes. *Phys. Rev. D*, 101(10):104014, 2020.

[46] Ioana Dumitriu and Alan Edelman. Matrix models for beta ensembles. *Journal of Mathematical Physics*, 43(11):5830–5847, Nov 2002.

[47] Gia Dvali, Daniel Flassig, Cesar Gomez, Alexander Pritzel, and Nico Wintergerst. Scrambling in the Black Hole Portrait. *Phys. Rev.*, D88(12):124041, 2013.

[48] Laszlo Erdos and Horng-Tzer Yau. Universality of local spectral statistics of random matrices, 2012.

[49] Bertrand Eynard, Taro Kimura, and Sylvain Ribault. Random matrices. 10 2015.

[50] L.H. Ford and Thomas A. Roman. Averaged energy conditions and evaporating black holes. *Phys. Rev. D*, 53:1988–2000, 1996.

[51] D.Z. Freedman, S.S. Gubser, K. Pilch, and N.P. Warner. Renormalization group flows from holography supersymmetry and a c theorem. *Adv. Theor. Math. Phys.*, 3:363–417, 1999.

[52] Valeri P. Frolov and D. Fursaev. Mining energy from a black hole by strings. *Phys. Rev. D*, 63:124010, 2001.

[53] Mitsutoshi Fujita, Tadashi Takayanagi, and Erik Tonni. Aspects of AdS/BCFT. *JHEP*, 11:043, 2011.

[54] Adwait Gaikwad and Ritam Sinha. Spectral Form Factor in Non-Gaussian Random Matrix Theories. *Phys. Rev. D*, 100(2):026017, 2019.

[55] Antonio M. García-García and Jacobus J. M. Verbaarschot. Spectral and thermodynamic properties of the Sachdev-Ye-Kitaev model. *Phys. Rev. D*, 94(12):126010, 2016.

[56] Antonio M. García-García, Bruno Loureiro, Aurelio Romero-Bermúdez, and Masaki Tezuka. Chaotic-Integrable Transition in the Sachdev-Ye-Kitaev Model. *Phys. Rev. Lett.*, 120(24):241603, 2018.

[57] G. W. Gibbons and S. W. Hawking. Action Integrals and Partition Functions in Quantum Gravity. *Phys. Rev. D*, 15:2752–2756, 1977.

[58] Steven B. Giddings. Nonviolent unitarization: basic postulates to soft quantum structure of black holes. *JHEP*, 12:047, 2017.

[59] Steven B. Giddings. Black holes in the quantum universe. 2019.

[60] Steven B. Giddings. A "black hole theorem," and its implications. 10 2021.

[61] Michel Goossens, Frank Mittelbach, and Alexander Samarin. *The LaTeX Companion*. Addison-Wesley, Reading, Massachusetts, 1994.

[62] Thomas Guhr, Axel Muller-Groeling, and Hans A. Weidenmuller. Random matrix theories in quantum physics: Common concepts. *Phys. Rept.*, 299:189–425, 1998.

[63] Monica Guica and Simon F. Ross. Behind the geon horizon. *Class. Quant. Grav.*, 32(5):055014, 2015.

[64] Bin Guo, Shaun Hampton, and Samir D. Mathur. Can we observe fuzzballs or firewalls? *JHEP*, 07:162, 2018.

[65] Daniel Harlow. Jerusalem Lectures on Black Holes and Quantum Information. *Rev. Mod. Phys.*, 88:015002, 2016.

[66] Daniel Harlow and Hirosi Ooguri. Symmetries in quantum field theory and quantum gravity. 2018.

[67] Koji Hashimoto, Keiju Murata, and Ryosuke Yoshii. Out-of-time-order correlators in quantum mechanics. *JHEP*, 10:138, 2017.

[68] S. W. Hawking. Particle Creation by Black Holes. *Commun. Math. Phys.*, 43:199–220, 1975. [Erratum: Commun.Math.Phys. 46, 206 (1976)].

[69] S. W. Hawking. Breakdown of Predictability in Gravitational Collapse. *Phys. Rev. D*, 14:2460–2473, 1976.

[70] S. W. Hawking. Breakdown of predictability in gravitational collapse. *Phys. Rev. D*, 14:2460–2473, Nov 1976.

[71] S. W. Hawking and Don N. Page. Thermodynamics of black holes in anti-de sitter space. *Comm. Math. Phys.*, 87(4):577–588, 1982.

[72] Patrick Hayden and Geoff Penington. Black hole microstates vs. the additivity conjectures. 12 2020.

[73] Patrick Hayden and John Preskill. Black holes as mirrors: Quantum information in random subsystems. *JHEP*, 09:120, 2007.

[74] Samuli Hemming and Larus Thorlacius. Thermodynamics of Large AdS Black Holes. *JHEP*, 11:086, 2007.

[75] Gary T. Horowitz and Veronika E. Hubeny. Quasinormal modes of AdS black holes and the approach to thermal equilibrium. *Phys. Rev.*, D62:024027, 2000.

[76] Veronika E. Hubeny, Donald Marolf, and Mukund Rangamani. Hawking radiation from AdS black holes. *Class. Quant. Grav.*, 27:095018, 2010.

[77] W. Israel. Singular hypersurfaces and thin shells in general relativity. *Il Nuovo Cimento B (1965-1970)*, 44(1):1–14, 1966.

[78] Viktor Jahnke. Recent developments in the holographic description of quantum chaos. *Adv. High Energy Phys.*, 2019:9632708, 2019.

[79] Donald Knuth. *The TEXbook*. Addison-Wesley, Reading, Massachusetts, 1986.

[80] Zohar Komargodski and Adam Schwimmer. On Renormalization Group Flows in Four Dimensions. *JHEP*, 12:099, 2011.

[81] Ioanna Kourkoulou and Juan Maldacena. Pure states in the SYK model and nearly-AdS_2 gravity. 7 2017.

[82] Mikko Laine and Aleksi Vuorinen. *Basics of Thermal Field Theory*, volume 925. Springer, 2016.

[83] Leslie Lamport. *LATEX — A Document Preparation System*. Addison-Wesley, Reading, Massachusetts, second edition, 1994.

[84] Nima Lashkari, Jennifer Lin, Hirosi Ooguri, Bogdan Stoica, and Mark Van Raamsdonk. Gravitational positive energy theorems from information inequalities. *PTEP*, 2016(12):12C109, 2016.

[85] Nima Lashkari, Charles Rabideau, Philippe Sabella-Garnier, and Mark Van Raamsdonk. Inviolable energy conditions from entanglement inequalities. *JHEP*, 06:067, 2015.

[86] Nima Lashkari, Douglas Stanford, Matthew Hastings, Tobias Osborne, and Patrick Hayden. Towards the Fast Scrambling Conjecture. *JHEP*, 04:022, 2013.

[87] Nima Lashkari and Mark Van Raamsdonk. Canonical Energy is Quantum Fisher Information. *JHEP*, 04:153, 2016.

[88] Albion E. Lawrence and Emil J. Martinec. Black hole evaporation along macroscopic strings. *Phys. Rev. D*, 50:2680–2691, 1994.

[89] G. Le Caër, C. Male, and R. Delannay. Nearest-neighbour spacing distributions of the beta-hermite ensemble of random matrices. *Physica A: Statistical Mechanics and its Applications*, 383(2):190–208, Sep 2007.

[90] Ji Hoon Lee, Dominik Neuenfeld, and Ashish Shukla. Bounds on gravitational brane couplings and tomography in AdS_3 black hole microstates. *JHEP*, 10:139, 2022.

[91] Stefan Leichenauer. Disrupting Entanglement of Black Holes. *Phys. Rev.*, D90(4):046009, 2014.

[92] Martin Lesourd. A remark on the energy conditions for hawking's area theorem. *General Relativity and Gravitation*, 50(6):61, 2018.

[93] Giacomo Livan, Marcel Novaes, and Pierpaolo Vivo. Introduction to random matrices - theory and practice, 2017. cite arxiv:1712.07903.

[94] Juan Maldacena, Stephen H. Shenker, and Douglas Stanford. A bound on chaos. *JHEP*, 08:106, 2016.

[95] Juan Maldacena and Douglas Stanford. Remarks on the Sachdev-Ye-Kitaev model. *Phys. Rev.*, D94(10):106002, 2016.

[96] Juan Martin Maldacena. The Large N limit of superconformal field theories and supergravity. *Int. J. Theor. Phys.*, 38:1113–1133, 1999. [Adv. Theor. Math. Phys.2,231(1998)].

[97] Juan Martin Maldacena. Eternal black holes in anti-de Sitter. *JHEP*, 04:021, 2003.

[98] Zachary Mark, Aaron Zimmerman, Song Ming Du, and Yanbei Chen. A recipe for echoes from exotic compact objects. *Phys. Rev.*, D96(8):084002, 2017.

[99] Samir D. Mathur. The Information paradox: A Pedagogical introduction. *Class. Quant. Grav.*, 26:224001, 2009.

[100] Samir D. Mathur. What happens at the horizon? *Int. J. Mod. Phys.*, D22:1341016, 2013.

[101] Lauren McGough, Márk Mezei, and Herman Verlinde. Moving the CFT into the bulk with $T\overline{T}$. *JHEP*, 04:010, 2018.

[102] Ravi Mistry, Sudhaker Upadhyay, Ahmed Farag Ali, and Mir Faizal. Hawking radiation power equations for black holes. *Nucl. Phys. B*, 923:378–393, 2017.

[103] Robert C. Myers and Aninda Sinha. Seeing a c-theorem with holography. *Phys. Rev. D*, 82:046006, 2010.

[104] Robert C. Myers and Aninda Sinha. Holographic c-theorems in arbitrary dimensions. *JHEP*, 01:125, 2011.

[105] Yu Nakayama. Does anomalous violation of null energy condition invalidate holographic c-theorem? *Phys. Lett. B*, 720:265–269, 2013.

[106] Pranjal Nayak, Ashish Shukla, Ronak M. Soni, Sandip P. Trivedi, and V. Vishal. On the Dynamics of Near-Extremal Black Holes. *JHEP*, 09:048, 2018.

[107] Dominik Neuenfeld. Double Holography as a Model for Black Hole Complementarity. 5 2021.

[108] Dominik Neuenfeld, Krishan Saraswat, and Mark Van Raamsdonk. Positive gravitational subsystem energies from CFT cone relative entropies. *JHEP*, 06:050, 2018.

[109] Michael A. Nielsen and Isaac L. Chuang. *Quantum Computation and Quantum Information*. Cambridge University Press, 2000.

[110] Takahiro Nishinaka and Seiji Terashima. A note on Sachdev–Ye–Kitaev like model without random coupling. *Nucl. Phys.*, B926:321–334, 2018.

[111] Tatsuma Nishioka, Shinsei Ryu, and Tadashi Takayanagi. Holographic Entanglement Entropy: An Overview. *J. Phys.*, A42:504008, 2009.

[112] Hidetoshi Omiya and Zixia Wei. Causal structures and nonlocality in double holography. *JHEP*, 07:128, 2022.

[113] Naritaka Oshita and Niayesh Afshordi. Probing microstructure of black hole spacetimes with gravitational wave echoes. *Phys. Rev.*, D99(4):044002, 2019.

[114] Naritaka Oshita, Qingwen Wang, and Niayesh Afshordi. On Reflectivity of Quantum Black Hole Horizons. 2019.

[115] Don N. Page. Information in black hole radiation. *Phys. Rev. Lett.*, 71:3743–3746, 1993.

[116] Don N. Page. Finite upper bound for the Hawking decay time of an arbitrarily large black hole in anti–de Sitter spacetime. *Phys. Rev. D*, 97(2):024004, 2018.

[117] Geoffrey Penington. Entanglement Wedge Reconstruction and the Information Paradox. 2019.

[118] Michael E. Peskin and Daniel V. Schroeder. *An Introduction to quantum field theory*. Addison-Wesley, Reading, USA, 1995.

[119] Eric Poisson. *Hypersurfaces*, page 59–117. Cambridge University Press, 2004.

[120] Eric Poisson. *A Relativist's Toolkit: The Mathematics of Black-Hole Mechanics*. Cambridge University Press, 12 2009.

[121] Joseph Polchinski. Introduction to Gauge/Gravity Duality. In *Theoretical Advanced Study Institute in Elementary Particle Physics: String theory and its Applications: From meV to the Planck Scale*, 10 2010.

[122] Joseph Polchinski. The Black Hole Information Problem. In *Proceedings, Theoretical Advanced Study Institute in Elementary Particle Physics: New Frontiers in Fields and Strings (TASI 2015): Boulder, CO, USA, June 1-26, 2015*, pages 353–397, 2017.

[123] Joseph Polchinski and Vladimir Rosenhaus. The Spectrum in the Sachdev-Ye-Kitaev Model. *JHEP*, 04:001, 2016.

[124] Mostafizur Rahman and Arpan Bhattacharyya. Ringdown of charged compact objects using membrane paradigm. *Phys. Rev. D*, 104(4):044045, 2021.

[125] Alfonso V. Ramallo. Introduction to the AdS/CFT correspondence. *Springer Proc. Phys.*, 161:411–474, 2015.

[126] Mukund Rangamani and Tadashi Takayanagi. Holographic Entanglement Entropy. *Lect. Notes Phys.*, 931:pp.1–246, 2017.

[127] Jorge V. Rocha. Evaporation of large black holes in AdS: Coupling to the evaporon. *JHEP*, 08:075, 2008.

[128] Jorge V. Rocha. Evaporation of large black holes in AdS: Greybody factor and decay rate. *JHEP*, 08:027, 2009.

[129] Shinsei Ryu and Tadashi Takayanagi. Holographic derivation of entanglement entropy from AdS/CFT. *Phys. Rev. Lett.*, 96:181602, 2006.

[130] Phil Saad, Stephen H. Shenker, and Douglas Stanford. A semiclassical ramp in SYK and in gravity. 6 2018.

[131] Phil Saad, Stephen H. Shenker, and Douglas Stanford. JT gravity as a matrix integral. 3 2019.

[132] Krishan Saraswat and Niayesh Afshordi. Extracting Hawking Radiation Near the Horizon of AdS Black Holes. 2020.

[133] Krishan Saraswat and Niayesh Afshordi. Quantum Nature of Black Holes: Fast Scrambling versus Echoes. *JHEP*, 04:136, 2020.

[134] Yasuhiro Sekino and Leonard Susskind. Fast Scramblers. *JHEP*, 10:065, 2008.

[135] Stephen H. Shenker and Douglas Stanford. Black holes and the butterfly effect. *JHEP*, 03:067, 2014.

[136] Stephen H. Shenker and Douglas Stanford. Multiple Shocks. *JHEP*, 12:046, 2014.

[137] Peter W. Shor. Scrambling Time and Causal Structure of the Photon Sphere of a Schwarzschild Black Hole. 2018.

[138] Sergey N. Solodukhin. Can black hole relax unitarily? In *1st Balkan Workshop on Mathematical, Theoretical and Phenomenological Challenges Beyond the Standard Model: Perspectives of Balkans Collaboration*, 6 2004.

[139] Douglas Stanford and Edward Witten. JT Gravity and the Ensembles of Random Matrix Theory. 7 2019.

[140] Ovidiu Cristinel Stoica. Revisiting the black hole entropy and the information paradox. *Adv. High Energy Phys.*, 2018:4130417, 2018.

[141] L. Susskind and J. Lindesay. *An Introduction to Black Holes, Information, and the String Theory Revolution: The Holographic Universe*. World Scientific, 2005.

[142] Leonard Susskind. The World as a hologram. *J. Math. Phys.*, 36:6377–6396, 1995.

[143] Leonard Susskind, Larus Thorlacius, and John Uglum. The Stretched horizon and black hole complementarity. *Phys. Rev.*, D48:3743–3761, 1993.

[144] Leonard Susskind and Edward Witten. The Holographic bound in anti-de Sitter space. 1998.

[145] Gábor Sárosi. AdS_2 holography and the SYK model. *PoS*, Modave2017:001, 2018.

[146] Gerard 't Hooft. Dimensional reduction in quantum gravity. *Conf. Proc. C*, 930308:284–296, 1993.

[147] Gerard 't Hooft. The Scattering matrix approach for the quantum black hole: An Overview. *Int. J. Mod. Phys. A*, 11:4623–4688, 1996.

[148] Gerard 't Hooft. The Holographic principle: Opening lecture. *Subnucl. Ser.*, 37:72–100, 2001.

[149] Tadashi Takayanagi. Holographic Dual of BCFT. *Phys. Rev. Lett.*, 107:101602, 2011.

[150] W. G. Unruh and R. M. Wald. How to mine energy from a black hole. *General Relativity and Gravitation*, 15(3):195–199, March 1983.

[151] W.G. Unruh and Robert M. Wald. Acceleration Radiation and Generalized Second Law of Thermodynamics. *Phys. Rev. D*, 25:942–958, 1982.

[152] Mark Van Raamsdonk. Evaporating Firewalls. *JHEP*, 11:038, 2014.

[153] Mark Van Raamsdonk. Lectures on Gravity and Entanglement. In *Proceedings, Theoretical Advanced Study Institute in Elementary Particle Physics: New Frontiers in Fields and Strings (TASI 2015): Boulder, CO, USA, June 1-26, 2015*, pages 297–351, 2017.

[154] Robert M. Wald. *General Relativity*. Chicago Univ. Pr., Chicago, USA, 1984.

[155] Qingwen Wang and Niayesh Afshordi. Black hole echology: The observer's manual. *Phys. Rev.*, D97(12):124044, 2018.

[156] Julian Westerweck, Alex Nielsen, Ofek Fischer-Birnholtz, Miriam Cabero, Collin Capano, Thomas Dent, Badri Krishnan, Grant Meadors, and Alexander H. Nitz. Low significance of evidence for black hole echoes in gravitational wave data. *Phys. Rev.*, D97(12):124037, 2018.

[157] Edward Witten. Anti-de Sitter space, thermal phase transition, and confinement in gauge theories. *Adv. Theor. Math. Phys.*, 2:505–532, 1998. [,89(1998)].

[158] Beni Yoshida and Alexei Kitaev. Efficient decoding for the Hayden-Preskill protocol. 2017.

APPENDICES

Appendix A

Chapter 2 Appendix Materials

A.1 Derivation of Effective Potential for Scalar Perturbations

In this appendix, we derive the effective potential and wave equation for a minimally coupled massless scalar field propagating a spacetime with a metric of the following form:

$$ds^2 = g_{\mu\nu}dx^\mu dx^\nu = -f(r)dt^2 + \frac{dr^2}{f(r)} + r^2 g^\Omega_{IJ} d\phi^I d\phi^J, \tag{A.1}$$

where g^Ω_{IJ} is the metric on a $d-1$ unit sphere and ϕ^I are angular coordinates on the $d-1$ unit sphere. Notice that we made no assumptions of the functional form $f(r)$ so our results will work for any metric of the form given above. The equation of motion for the scalar field is a wave equation given by:

$$\Box\Psi = \frac{1}{\sqrt{-g}}\partial_\mu\left(\sqrt{-g}g^{\mu\nu}\partial_\nu\Psi\right) = 0. \tag{A.2}$$

Upon expansion of the sums we can write the wave equation in the form:

$$\Box\Psi = -\frac{1}{f(r)}\partial_t^2\Psi + \frac{1}{r^{d-1}}\partial_r\left(r^{d-1}f(r)\partial_r\Psi\right) + \frac{1}{r^2\sqrt{g^\Omega}}\partial_I\left(\sqrt{g^\Omega}\left(g^\Omega\right)^{IJ}\partial_J\Psi\right) = 0. \tag{A.3}$$

We make the anzatz $\Psi = \frac{R(t,r)}{r^\Delta}\Phi_l(\phi^I)$, where $\Delta = \frac{d-1}{2}$ and $\Phi_l(\phi^I)$ are hyper-spherical harmonics on the unit $d-1$ sphere which obeys the eigenvalue equation:

$$\frac{1}{\sqrt{g^{\Omega}}}\partial_I\left(\sqrt{g^{\Omega}}\left(g^{\Omega}\right)^{IJ}\partial_J\Phi_l\right) = l(2-d-l)\Phi_l. \tag{A.4}$$

Using the anzatz outlined above along with the eigenvalue expression for the hyperspherical harmonics the wave equation can be written as:

$$-\partial_t^2 R + \partial_{r_*}^2 R - f(r)\left[\frac{\Delta}{r}\frac{\partial f}{\partial r} + \frac{\Delta(d-2-\Delta)}{r^2}f(r) + \frac{l(l+d-2)}{r^2}\right]R = 0. \tag{A.5}$$

Where we introduced a simple change of variables in the radial coordinate $dr_* = \frac{dr}{f(r)}$. The resulting equation is a simple radial wave equation with an effective potential given by:

$$\begin{aligned} &-\partial_t^2 R + \partial_{r_*}^2 R - V_{\text{eff}}(r)R = 0 \\ &V_{\text{eff}}(r) = f(r)\left[\frac{d-1}{2r}\frac{\partial f}{\partial r} + \frac{(d-1)(d-3)}{4r^2}f(r) + \frac{l(l+d-2)}{r^2}\right]. \end{aligned} \tag{A.6}$$

This gives the form of the effective potential. The angular momentum barrier occurs at a local maxima of the effective potential outside the horizon radius. In general it is not as clear that such a local maxima will exist until one specifies $f(r)$. In the large l limit we can approximate the effective potential by:

$$V_{\text{eff}}(r) \approx \frac{l^2}{r^2}f(r). \tag{A.7}$$

This is only valid in a finite neighborhood of the horizon but it is much easiler to analyze and find local maxima and minima of the potential in this regime. To conclude, we can plug in the Anzatz $R(t,r) = e^{-i\omega t}\mathcal{R}(r_*)$ to write down the radial equation as:

$$\frac{d^2\mathcal{R}}{dr_*^2} + \left(\omega^2 - V_{\text{eff}}(r)\right)\mathcal{R} = 0. \tag{A.8}$$

The equation above makes it clear why the turning points of the effective potential depend on the frequency, ω, of the scalar perturbation.

A.2 Near Extremal AdS RN Black Holes

In this section we will go over the AdS RN black hole solution and its extremal regime. The AdS RN black hole has the metric given by Eq. (4.68) with:

$$f(r) = 1 - \frac{2M}{r^{d-2}} + \frac{Q^2}{r^{2(d-2)}} + \frac{r^2}{L^2}. \tag{A.9}$$

The horizon occurs at $r = r_+$ where $f(r_+) = 0$. Using this we can rewrite f in terms of the horizon radius r_H and the charge Q:

$$f(r) = \left(1 - \frac{r_+^{d-2}}{r^{d-2}}\right)\left(1 - \frac{Q^2}{r^{d-2}r_+^{d-2}}\right) + \frac{r^2}{L^2}\left(1 - \frac{r_+^d}{r^d}\right). \tag{A.10}$$

Using this we can compute the temperature of the black hole:

$$T = \frac{f'(r_+)}{4\pi} = \frac{d-2}{4\pi r_+}\left(1 - \frac{Q^2}{r_+^{2(d-2)}} + \frac{d}{d-2}\frac{r_+^2}{L^2}\right). \tag{A.11}$$

We set the temperature equal to zero to compute the relation between Q and r_{ext} when the black hole is extremal. We find that:

$$Q^2 = r_{ext}^{2(d-2)}\left(1 + \frac{d}{d-2}\frac{r_{ext}^2}{L^2}\right). \tag{A.12}$$

We can plug this back into the expression for f and write:

$$f(r) = \left(1 - \frac{r_+^{d-2}}{r^{d-2}}\right)\left[1 - \left(1 + \frac{d}{d-2}\frac{r_{ext}^2}{L^2}\right)\frac{r_{ext}^{2(d-2)}}{r^{d-2}r_+^{d-2}}\right] + \frac{r^2}{L^2}\left(1 - \frac{r_+^d}{r^d}\right). \tag{A.13}$$

We get $f_{ext}(r)$ by setting $r_+ = r_{ext}$. Using this we will find that:

$$f''_{ext}(r_+ = r_{ext}) = \frac{2(d-2)^2}{r_+^2} + \frac{2d(d-1)}{L^2}. \tag{A.14}$$

Now we can analyze what happens when $r_+ \gg L$ and $r_+ \ll L$:

$$f''_{ext}(r_+) = \begin{cases} \frac{2(d-2)^2}{r_+^2} + \ldots & r_+ \ll L \\ \frac{2d(d-1)}{L^2} + \ldots & r_+ \gg L. \end{cases} \tag{A.15}$$

We can use these results to compute the leading order contribution to the echo time for AdS RN black holes in the near extremal regime.

A.3 Calculating t_* with $\delta R = \pi \ell_p^2/\beta$

To calculate t_* with the choice $\delta R = \pi \ell_p^2/\beta$ it will be useful to manipulate Eq. (2.59) as follows. Using the first law of black hole thermodynamics at constant charge we know $\delta S = \beta \delta E$. Where δE is the energy of the perturbation. Using the fact that the entropy of a black hole is proportional to its area ($A \sim R_H^{d-1}$) we can rewrite everything in terms of δR, R_H, and R_{ext}:

$$t_* \sim \frac{\beta}{2\pi} \ln\left[\frac{R_H}{(d-1)\delta R}\left(1 - \frac{R_{ext}^{d-1}}{R_H^{d-1}}\right)\right] = \begin{cases} \frac{\beta}{2\pi}\left[\ln\left(\frac{R_H}{\delta R}\right) + \mathcal{O}\left(\ln\left(1 - \frac{R_{ext}^{d-1}}{R_H^{d-1}}\right)\right)\right] & R_{ext} \ll R_H \\ \frac{\beta}{2\pi}\left[\ln\left(\frac{R_H - R_{ext}}{\delta R}\right) + \mathcal{O}\left(1 - \frac{R_{ext}}{R_H}\right)\right] & R_{ext} \approx R_H, \end{cases} \tag{A.16}$$

where R_H is the radius of the black hole, δR is the change in the radius of the black hole, and R_{ext} is the radius of an extremal black hole with the same charge as the black hole we are considering. Now we set $\delta R = \pi \ell_p^2/\beta$ and then substitute this into the leading order terms in the two cases in Eq. (A.16) we will find:

$$t_* \sim \begin{cases} \frac{\beta}{2\pi} \ln\left(\frac{\beta R_H}{\ell_p^2}\right) & R_{ext} \ll R_H \\ \frac{\beta}{2\pi} \ln\left(\frac{\beta(R_H - R_{ext})}{\ell_p^2}\right) & R_{ext} \approx R_H. \end{cases} \tag{A.17}$$

From this, we can clearly see that far from the extremal limit, we reproduce the echo time scale. The second case which corresponds to a near extremal black hole requires a bit more work.

First we start with:

$$t_*^{ext} \simeq \frac{\beta}{2\pi} \ln\left(\frac{\beta(R_H - R_{ext})}{\ell_p^2}\right). \tag{A.18}$$

Using Eqs. (A.11-A.12) we can express the temperature in terms of R_H and R_{ext}:

$$T = \beta^{-1} = \frac{d-2}{4\pi R_H}\left[\left(1 - \frac{R_{ext}^{2(d-2)}}{R_H^{2(d-2)}}\right) + \frac{d}{d-2}\frac{R_H^2}{L^2}\left(1 - \frac{R_{ext}^{2(d-1)}}{R_H^{2(d-1)}}\right)\right]. \tag{A.19}$$

Using this this we can do a series expansion for t_* in the near extremal limit to get:

$$t_* \simeq \frac{\beta}{2\pi} \ln\left(\frac{2\pi R_H^2}{\ell_p^2\left[(d-2)^2+\frac{R_H^2}{L^2}d(d-1)\right]}\right) + \mathcal{O}\left(1-\frac{R_{ext}}{R_H}\right). \tag{A.20}$$

Using the result above we will find:

$$t_*^{ext} \sim \begin{cases} \frac{\beta}{2\pi}\ln\left(\frac{R_H^2}{\ell_p^2}\right) & R_H \ll L \\ \frac{\beta}{2\pi}\ln\left(\frac{L^2}{\ell_p^2}\right) & R_H \gg L. \end{cases} \tag{A.21}$$

Therefore, t_* with the choice $\delta R = \pi \ell_p^2 T_H$, reproduces the echo time scale correctly to leading order for both large and small black holes in extremal and non-extremal regimes Eqs. (2.52 - 2.53).

A.4 Entropy Shift corresponding to a Proper Planck Shift of the Horizon

In this appendix we study how the entropy of an AdS RN black hole changes when its horizon is shifted by a proper Planck length. We define the the physical shift in the horizon radius of a spherical black hole through the following integral expression:

$$\delta R_{phys} = \int_{R_H}^{R_H+\delta R} \frac{dr}{\sqrt{f(r)}}. \tag{A.22}$$

This is simply the proper length between the horizons of the unperturbed black at R_H hole and the perturbed black hole at $R_H + \delta R$. Therefore, δR is the coordinate change in the radius of the horizon which goes into the formula for calculating the entropy of a black hole.

The the semi-classical description of spacetime as a smooth manifold is an effective description only valid on proper length scales larger than a Planck length. Due to this fact we impose the constraint, $\delta R_{phys} \gtrsim \ell_p$. Essentially, this means that the smallest possible perturbation to a black hole (which a classical observer can resolve) must shift the horizon by a proper Planck length[1].

[1]One may object to the way we define the shift in the horizon of a black hole on the grounds that the perturbed black hole and the unperturbed black hole are not equivalent spacetime manifolds. The integral

Now we analyze how a proper Planck shift changes the entropy content of a black hole. Using Eq. (2.61) and $\delta R = \pi \ell_p^2 T_H$ we can obtain the following change in the entropy of the black hole:

$$\delta S = \pi C_d (d-1) R_H T_H \left(\frac{R_H}{\ell_p}\right)^{d-3}. \tag{A.23}$$

Based on the arguments we made, the above expression represents the smallest perturbation to a black hole which results in a shift in the horizon which is classically measurable. We see that the entropy shift corresponding to a proper Planck length shift of the horizon depends on the temperature of the black hole being perturbed. In particular, there is a critical temperature below which when the change in entropy of the black hole is less than one. Setting $\delta S \geq 1$ gives us the following constraint on the temperature of the black hole:

$$T_H \geq \frac{1}{C_d (d-1) \pi R_H} \left(\frac{\ell_p}{R_H}\right)^{d-3} \tag{A.24}$$

Now we substitute the expression for the temperature of an AdS RN black hole, given in terms of R_{ext} and R_H which is given by combining Eqs. (A.11 - A.12). We will get:

$$\frac{d-2}{4\pi R_H}\left[1 - \frac{R_{ext}^{2(d-2)}}{R_H^{2(d-2)}} + \frac{d}{d-2}\frac{R_H^2}{L^2}\left(1 - \frac{R_{ext}^{2(d-1)}}{R_H^{2(d-1)}}\right)\right] \geq \frac{1}{C_d (d-1)\pi R_H}\left(\frac{\ell_p}{R_H}\right)^{d-3}. \tag{A.25}$$

Rearranging the terms in the inequality above gives:

$$\left[1 - \frac{R_{ext}^{2(d-2)}}{R_H^{2(d-2)}} + \frac{d}{d-2}\frac{R_H^2}{L^2}\left(1 - \frac{R_{ext}^{2(d-1)}}{R_H^{2(d-1)}}\right)\right] \geq \frac{4}{C_d (d-1)(d-2)}\left(\frac{\ell_p}{R_H}\right)^{d-3}. \tag{A.26}$$

Where R_H is the horizon radius, R_{ext} is the radius if the extremal RN black hole with the same charge, and L is the AdS radius.

For an uncharged AdS Schwarzschild black hole one can set $R_{ext} = 0$. In this case, it is easy to see that the constraint is satisfied whenever $R_H \gg \ell_p$. This means that for

we defined is not a good measure of how much the horizon changed because it does not account for the fact that the perturbed black hole represents a new manifold. To address this concern we show, in Appendix A.5, that a more reasonable definition that measures the change in the horizon radius essentially gives back the same result we would get using the naive integral defined in Eq. (A.22)

any Schwarzschild AdS black hole ($R_H \gg \ell_p$) a proper Planck shift in the horizon always changes the entropy by an amount larger than one. However, once we consider black holes sufficiently close to the extremal regime it is clear that the inequality will be violated. To understand exactly how close we need get to the extremal regime before violating the inequality. We do a series expansion of the left hand side of Eq. (A.26) near $R \simeq R_{ext}$ and find to leading order that:

$$1 - \frac{R_{ext}}{R_H} \gtrsim \frac{2}{C(d-1)(d-2)\left[d-2+\frac{d(d-1)}{d-2}\frac{R_H^2}{L^2}\right]}\left(\frac{\ell_p}{R_H}\right)^{d-3}. \tag{A.27}$$

Based on the result above, it is clear that if $d \geq 4$ we can get "reasonably" close to an extremal black hole (i.e. arbitrarily close in limit $\ell_p/R_H \to 0$) before a proper Planck length shift changes the entropy by an amount less than 1.

In the case when $d = 3$ we can show that Eq. (A.26) exactly takes the form of a quadratic:

$$-3x_H^2 y^2 - y + \left(1 + 3x_H^2 - \frac{2}{\pi}\right) \geq 0, \tag{A.28}$$

where $y = R_{ext}^2/R_H^2$ and $x_H = R_H/L$. Taking a derivative of the left hand side of the inequality with respect to y reveals that in the interval $y \in [0,1]$ the function is strictly decreasing. Furthermore, we know that the y-intercept of the quadratic function is positive. This means that it will become negative after it achieves its positive root. The location of the root will tell us how close we can get to the extremal regime before $\delta S < 1$. Therefore, the problem simplifies to finding the positive root of the quadratic on the left hand side of the inequality. Using the quadratic formula it is easy to see that the positive zero is at:

$$y = y_0 = \frac{-1 + \sqrt{1 + 12x_H^2\left(1 + 3x_H^2 - \frac{2}{\pi}\right)}}{6x_H^2}. \tag{A.29}$$

Using the previous arguments it is clear that the the inequality given by Eq. (A.28) is satisfied as long as $y \in [0, y_0]$. This gives us the result in Eq. (A.30).

$$\frac{R_{ext}^2}{R^2} \leq \frac{-1 + \sqrt{1 + \frac{12R_H^2}{L^2}\left(1 + \frac{3R_H^2}{L^2} - \frac{2}{\pi}\right)}}{\frac{6R_H^2}{L^2}}. \tag{A.30}$$

In Fig. A.1 we plot the the square root of the right hand side of the inequality as a function of R_H/L to get an idea of how close we can get to the extremal regime for small

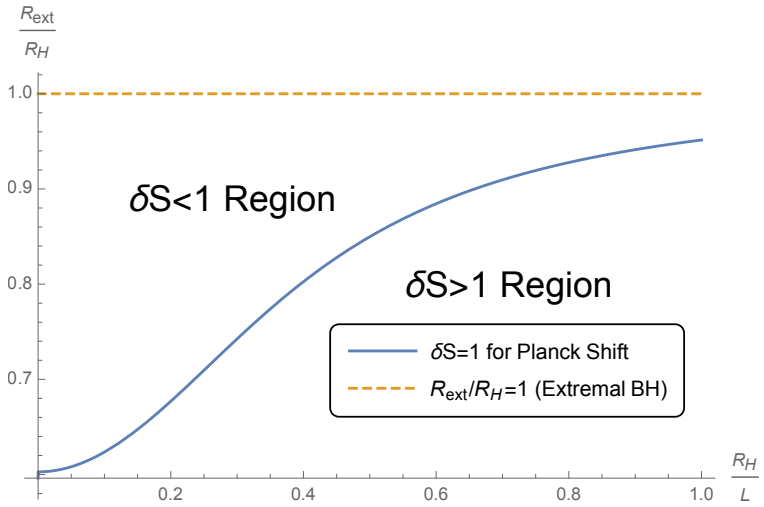

Figure A.1: Above is a plot of R_{ext}/R_H as a function of R_H/L for $d = 3$ (plot of the square root of the right hand side of Eq. (A.30)). The solid line represents the closest one can get to the extremal regime (i.e. $R_{ext}/R_H = 1$ represented by the dashed line) before a proper Planck length shift of the horizon results in $\delta S < 1$.

AdS black holes in 4D. Any black hole below the solid line whose horizon is shifted by a proper Planck length will result in $\delta S > 1$. Black holes above the solid line whose horizon is shifted by a proper Planck length will have $\delta S < 1$. Analyzing Fig. A.1, we see that for asymptotically flat black holes in 4D, one cannot get very close to the extremal regime (i.e. $R_{ext}/R_H \lesssim 0.6$) before a proper Planck length shift results in $\delta S < 1$. However, we see that as R_H/L becomes larger, one can get asymptotically closer to the extremal regime. For example, we see that once $R_H/L = 1$ one can get as close as $R_{ext}/R_H \approx 0.95$. Based on these results we can conclude that that for very large AdS black holes in 4D (i.e. $R_H/L \gg 1$) we can get very close to the extremal regime before $\delta S < 1$.

A.5 A Semi-Classical Notion of Black Hole Distinguishability

In this appendix we will consider a family of spherically symmetric black hole metrics, labelled by their horizon radius, which can be written in the form:

$$ds^2 = -f_{R_H}(r)dt^2 + \frac{dr^2}{f_{R_H}(r)} + r^2 d\Omega_{d-1}^2. \tag{A.31}$$

Where the subscript R_H is the radial coordinate of the horizon. Now consider two black holes; one with a horizon at R_H and another at $R_H + \delta R$, with $\delta R \ll R_H$. In the semi-classical regime, spacetime is described by a smooth manifold. This is an effective description which is assumed to break down on length scales smaller than a Planck length. Since there is a limit on the distances we can resolve within a spacetime it also seems reasonable to suggest that there is a limit on how well we can semi-classically distinguish two nearby black hole solutions. We propose that the following constraint should be enforced for black holes described by Eq. (A.31):

$$\delta R_{phys} = \int_{R_H}^{\infty} \frac{dr}{\sqrt{f_{R_H}(r)}} - \int_{R_H+\delta R}^{\infty} \frac{dr}{\sqrt{f_{R_H+\delta R}(r)}} \gtrsim \ell_p. \tag{A.32}$$

The constraint above describes the difference between the proper radial lengths between infinity and the horizon of two black holes. In general, the two integrals on their own will diverge. However, the difference of the integrals will converge to a finite expression. We interpret this difference as the "proper" change in the horizon radius and posit that in the semi-classical regime, the proper change in the radius must be larger than a Planck length. This places a constraint on the smallest possible δR (and thereby the smallest semi-classical perturbation to a black hole). Before trying to obtain a result on the smallest δR we will write the difference in a suggestive manner:

$$\delta R_{phys} = \int_{R_H}^{R_H+\delta R} \frac{dr}{\sqrt{f_{R_H}(r)}} + \int_{R_H+\delta R}^{\infty} \left(\frac{1}{\sqrt{f_{R_H}(r)}} - \frac{1}{\sqrt{f_{R_H+\delta R}(r)}} \right). \tag{A.33}$$

Notice that the first integral is exactly the integral given in Eq. (A.22). We analyze the first integral in Eq. (A.33) by expanding f_{R_H} at $r = R_H$ to second order:

$$\begin{aligned} \int_{R_H}^{R_H+\delta R} \frac{dr}{\sqrt{f_{R_H}(r)}} &\approx \int_{R_H}^{R_H+\delta R} \frac{dr}{\sqrt{c_1(r-R_H) + c_2(r-R_H)^2}} \\ &= \frac{2}{\sqrt{c_2}} \ln \left[\sqrt{1 + \frac{c_2}{c_1}\delta R} + \sqrt{\frac{c_2}{c_1}\delta R} \right] \end{aligned} \tag{A.34}$$

Where $c_n = \frac{1}{n!}\frac{d^n f_{R_H}(R_H)}{dr^n}$, in particular $c_1 = 4\pi T_H$. We do an expansion in δR to find (for an AdS RN BH):

$$\int_{R_H}^{R_H+\delta R} \frac{dr}{\sqrt{f_{R_H}(r)}} \approx \sqrt{\frac{\delta R}{\pi T_H}} \left[1 - \frac{c_2 \delta R}{24\pi T_H} + ...\right]$$
$$c_2 = \frac{1}{R_H^2}\left[(d-2)^2 + \frac{d(d-1)R_H^2}{L^2} - (2d-5)2\pi R_H T_H\right] \tag{A.35}$$

Now we analyze the second integral in Eq. (A.33). To approximate the value of this integral we will again take the the example of an AdS RN black hole. We begin by expanding $f_{R_H+\delta R}(r)$ as a series in δR to second order:

$$f_{R_H+\delta R}(r) = f_{R_H}(r) + 4\pi R_H T_H \left(\frac{R_H}{r}\right)^{d-2} \frac{\delta R}{R_H}$$
$$- (d-2)^2 \left[1 + \frac{d-1}{(d-2)^2}\left(\frac{dR_H^2}{L^2} - 2\pi R_H T_H\right)\right] \left(\frac{R_H}{r}\right)^{d-2} \left(\frac{\delta R}{R_H}\right)^2 + ... \tag{A.36}$$

We can plug this expansion into the integrand of the second integral and expand the integrand order by order in δR. At each order in δR we will need to evaluate integrals of the form given below:

$$I_n = \int_{R_H+\delta R}^{\infty} \frac{dr}{\left(f_{R_H}(r)\right)^{1/2+n} r^{d-2}}. \tag{A.37}$$

These integrals clearly converge for any $n \in \mathbb{N}$ due to the fact that $f_{R_H}(r) \sim r^2/L^2$ at infinity. Since the largest contribution to the integrals will come from the lower limit of the integration, we should get a good approximation to the value of the integral by expanding $f_{R_H}(r)$ near $r = R_H$ to second order. Then we find the anti-derivative and evaluate at the lower and upper limits of integration. We then expand the result in δR and we will find the following result:

$$\int_{R_H+\delta R}^{\infty}\left(\frac{1}{\sqrt{f_{R_H}(r)}}-\frac{1}{\sqrt{f_{R_H+\delta R}(r)}}\right)dr\approx-\frac{5}{8}\sqrt{\frac{\delta R}{\pi T_H}}+\frac{\Gamma\left(d-\frac{3}{2}\right)}{2\Gamma(d-2)}\frac{\delta R}{\sqrt{R_H T_H}}$$
$$.-\frac{1}{64R_H^2}\left[\frac{5d(d-1)R_H^2}{L^2}+5(d-2)^2-2(7d-9)\pi R_H T_H\right]\left(\frac{\delta R}{\pi T_H}\right)^{3/2}+..$$
$$=\sqrt{\frac{\delta R}{\pi T_H}}\left[-\frac{5}{8}+\frac{\Gamma\left(d-\frac{3}{2}\right)}{2\Gamma(d-2)}\left(\frac{\pi\delta R}{R_H}\right)^{1/2}\right]$$
$$\sqrt{\frac{\delta R}{\pi T_H}}\left[-\frac{1}{64}\left(\frac{5d(d-1)R_H^2}{L^2}+5(d-2)^2-2(7d-9)\pi R_H T_H\right)\left(\frac{\delta R}{\pi T_H R_H^2}\right)\right]+\mathcal{O}(\delta R^2) \tag{A.38}$$

Once we factor out an overall factor of $\sqrt{\delta R/(\pi T_H)}$ we can see how the series organizes itself into two parts. One part will involve terms that are multiplied by powers of $\delta R/R_H$, such terms come from the upper limit of the integral at infinity. The other part of the series involves powers of $\delta R/(T_H R_H^2)$ which come from the lower limit of the integral at $R_H+\delta R$. Once we combine the series expansions given in Eq. (A.35) and Eq. (A.38) we will find the following terms in the expansion for δR_{phys}:

$$\delta R_{phys}\approx\sqrt{\frac{\delta R}{\pi T_H}}\left[\frac{3}{8}+\frac{\Gamma\left(d-\frac{3}{2}\right)}{2\Gamma(d-2)}\left(\frac{\pi\delta R}{R_H}\right)^{1/2}\right]$$
$$+\sqrt{\frac{\delta R}{\pi T_H}}\left[-\frac{1}{64R_H^2}\left(\frac{5d(d-1)R_H^2}{L^2}+5(d-2)^2-2(7d-9)\pi R_H T_H\right)\frac{\delta R}{\pi T_H R_H^2}\right]+... \tag{A.39}$$

We see that by ignoring the sub-leading terms we will have:

$$\delta R_{phys}\approx\frac{3}{8}\sqrt{\frac{\delta R}{\pi T_H}}\sim\ell_p\Rightarrow\delta R\sim T_H\ell_p^2. \tag{A.40}$$

It can be checked that if $\delta R_{phys}\sim T_H\ell_p^2$, then the sub-leading terms will be negligible as long as $\ell_p\ll min\{R_H,L\}$.

Therefore, the leading order behaviour of δR_{phys} is captured, up to an overall constant, by the first integral in Eq. (A.33). This is why we can safely use the the definition given in Eq. (A.22) to quantify the horizon shift.

Appendix B

Chapter 3 Appendix Materials

B.1 Deriving the Spectral Form Factor of the i.i.d Model

In this section we derive Eq. (3.14). We begin with the expression for the partition function for a spectrum given by Eq. (3.5). It is given by (in this derivation we will treat β as a general complex parameter):

$$\begin{aligned}\mathcal{Z}(\beta) &= \sum_{n=0}^{N} e^{-\beta\left(E_0+\sum_{k=1}^{n}\delta E_k\right)} = e^{-\beta E_0}\left(1+\sum_{n=1}^{N}\prod_{k=1}^{n} e^{-\beta\delta E_k}\right) \\ &= e^{-\beta E_0}\left[1+e^{-\beta\delta E_1}+\left(e^{-\beta\delta E_1}e^{-\beta\delta E_2}\right)+\cdots+\left(e^{-\beta\delta E_1}e^{-\beta\delta E_2}\cdots e^{-\beta\delta E_N}\right)\right].\end{aligned} \tag{B.1}$$

Now we define the following recursive indexed quantity:

$$\begin{aligned}Z_m(\beta) &= e^{-\beta\delta E_m}\left(1+Z_{m+1}(\beta)\right) \\ Z_{N+1}(\beta) &= 0 \Rightarrow Z_N(\beta) = e^{-\beta\delta E_N},\end{aligned} \tag{B.2}$$

where $m = 1, 2, ..., N-1, N$. Using these indexed quantities, we may express the partition function and its complex conjugate as follows:

$$\begin{aligned}\mathcal{Z}(\beta) &= e^{-\beta E_0}\left(1+Z_1(\beta)\right) \\ \mathcal{Z}(\beta^*) &= e^{-\beta^* E_0}\left(1+Z_1(\beta^*)\right),\end{aligned} \tag{B.3}$$

where β^* is the complex conjugate of β. We can then write:

$$\begin{aligned}\langle\mathcal{Z}(\beta)\mathcal{Z}(\beta^*)\rangle &= e^{-E_0(\beta+\beta^*)}\left\langle 1+Z_1(\beta)+Z_1(\beta^*)+Z_1(\beta)Z(\beta^*)\right\rangle \\ &= e^{-E_0(\beta+\beta^*)}\left[1+\langle Z_1(\beta)\rangle+\langle Z_1(\beta^*)\rangle+\langle Z_1(\beta)Z_1(\beta^*)\rangle\right].\end{aligned} \tag{B.4}$$

To compute $\langle Z_1(\beta)\rangle$, we will find a general formula for $\langle Z_m(\beta)\rangle$. We use the recursion relation given by Eq. (B.2) to find the following result for $\langle Z_N(\beta)\rangle$:

$$\begin{aligned}\langle Z_N(\beta)\rangle &= \langle e^{-\beta\delta E_N}\rangle = \int_{-\infty}^{\infty} dE_1\cdots dE_N P(E_1,..,E_N)e^{-\beta\delta E_N}\\ &= \int_{-\infty}^{\infty} d\delta E_1\cdots d\delta E_N \prod_{k=1}^{N}\mathcal{P}(\delta E_k)e^{-\beta\delta E_N} = b\\ b &= \int_{-\infty}^{\infty} dx\mathcal{P}(x)e^{-\beta x}.\end{aligned} \tag{B.5}$$

For $\langle Z_{N-1}(\beta)\rangle$, we have:

$$\begin{aligned}&\langle Z_{N-1}(\beta)\rangle = \langle e^{-\beta\delta E_{N-1}}\left(1+Z_N(\beta)\right)\rangle = \langle e^{-\beta\delta E_{N-1}} + e^{-\beta\delta E_{N-1}}e^{-\beta\delta E_N}\rangle\\ &= \langle e^{-\beta\delta E_{N-1}}\rangle + \langle e^{-\beta\delta E_{N-1}}e^{-\beta\delta E_N}\rangle = b+b^2.\end{aligned} \tag{B.6}$$

Continuing inductively we can show that:

$$\langle Z_{N-k}(\beta)\rangle = \langle e^{-\beta\delta E_{N-k}} + \sum_{\ell=1}^{k}\prod_{j=0}^{\ell} e^{-\beta\delta E_{N-k+j}}\rangle = b\sum_{p=0}^{k} b^p = \frac{b\left(1-b^{k+1}\right)}{1-b}. \tag{B.7}$$

Using these results we can conclude that:

$$\begin{aligned}\langle Z_m(\beta)\rangle &= \frac{b(1-b^{N-m+1})}{1-b}\\ \langle Z_m(\beta^*)\rangle &= \frac{b^*(1-(b^*)^{N-m+1})}{1-b^*},\end{aligned} \tag{B.8}$$

where b^* is the complex conjugate of b. We can immediately conclude that:

$$\begin{aligned}\langle \mathcal{Z}(\beta)\rangle &= e^{-\beta E_0}\left[1+\frac{b(1-b^N)}{1-b}\right]\\ \langle \mathcal{Z}(\beta^*)\rangle &= e^{-\beta^* E_0}\left[1+\frac{b^*(1-(b^*)^N)}{1-b^*}\right].\end{aligned} \tag{B.9}$$

In a similar manner, we consider the quantity $B_m = \langle Z_m(\beta)Z_m(\beta^*)\rangle$:

$$\begin{aligned}&B_m = \langle Z_m(\beta)Z_m(\beta^*)\rangle = \langle e^{-\delta E_m(\beta+\beta^*)}\left(1+Z_{m+1}(\beta)\right)\left(1+Z_{m+1}(\beta^*)\right)\rangle\\ &= \langle e^{-\delta E_m(\beta+\beta^*)}\rangle + \langle e^{-\delta E_m(\beta+\beta^*)}Z_{m+1}(\beta)\rangle + \langle e^{-\delta E_m(\beta+\beta^*)}Z_{m+1}(\beta^*)\rangle\\ &+ \langle e^{-\delta E_m(\beta+\beta^*)}Z_{m+1}(\beta)Z_{m+1}(\beta^*)\rangle\,.\end{aligned} \tag{B.10}$$

Using the fact that $Z_{N+1}(\beta) = 0$, we obtain the following result for B_N:

$$B_N = \langle e^{-\delta E_N(\beta+\beta^*)} \rangle = \int_{-\infty}^{\infty} dx \mathcal{P}(x) e^{-x(\beta+\beta^*)} = a. \tag{B.11}$$

Using the fact that Z_{m+1} is only a function of $\{\delta E_i\}_{i=N}^{m+1}$, we have the following recursion relation:

$$\begin{aligned} B_m &= a\left(1 + \langle Z_{m+1}(\beta)\rangle + \langle Z_{m+1}(\beta^*)\rangle + B_{m+1}\right) \\ &= a\left(1 + \frac{b(1-b^{N-m})}{1-b} + \frac{b^*(1-(b^*)^{N-m})}{1-b^*} + B_{m+1}\right) \\ a &= \langle e^{-\delta E_m(\beta+\beta^*)} \rangle = \int_{-\infty}^{\infty} dx \mathcal{P}(x) e^{-x(\beta+\beta^*)} \\ B_{N+1} &= 0 \Rightarrow B_N = a. \end{aligned} \tag{B.12}$$

Using the inductive relation above it is straightforward to show that:

$$\begin{aligned} B_{N-k} &= a\left[a^k + \sum_{p=0}^{k-1} a^p f_{N-k+p}\right] \\ f_m &= 1 + \frac{b(1-b^{N-m})}{1-b} + \frac{b^*(1-(b^*)^{N-m})}{1-b^*}. \end{aligned} \tag{B.13}$$

One can then explicitly evaluate the geometric sums involved and arrive at the following expression for B_m:

$$\begin{aligned} B_m = \frac{a-a^{N-m+2}}{1-a} + \frac{ab}{1-b}\left[\frac{a(1-a^{N-m}-b^{N-m+1}) - b(1-b^{N-m}-a^{N-m+1})}{(1-a)(a-b)}\right] \\ + \frac{ab^*}{1-b^*}\left[\frac{a(1-a^{N-m}-(b^*)^{N-m+1}) - b^*(1-(b^*)^{N-m}-a^{N-m+1})}{(1-a)(a-b^*)}\right]. \end{aligned} \tag{B.14}$$

We can check that this expression satisfies the recursion relation given in Eq. (B.12). By setting $m = 1$ we can obtain B_1:

$$B_1 = \frac{a}{1-a}\left[1 - a^N + \frac{b\left(a-b+a^N(b-1)+b^N(1-a)\right)}{(1-b)(a-b)} + \frac{b^*\left(a-b^*+a^N(b^*-1)+(b^*)^N(1-a)\right)}{(1-b^*)(a-b^*)}\right]. \tag{B.15}$$

Now that we have calculated all the necessary averages we can plug them into the Eq. (B.4) to find the following result:

$$\begin{aligned}
&\langle \mathcal{Z}(\beta)\mathcal{Z}(\beta^*)\rangle = e^{-(\beta+\beta^*)E_0}\left(1+\frac{b(1-b^N)}{1-b}+\frac{b^*(1-(b^*)^N)}{1-b^*}+B_1\right)\\
&= e^{-(\beta+\beta^*)E_0}\left(\frac{1-a^{N+1}}{1-a}+\frac{b}{1-b}\left[\frac{a-b+a^{N+1}(b-1)+b^{N+1}(1-a)}{(1-a)(a-b)}\right]\right)\\
&+ e^{-(\beta+\beta^*)E_0}\frac{b^*}{1-b^*}\left[\frac{a-b^*+a^{N+1}(b^*-1)+(b^*)^{N+1}(1-a)}{(1-a)(a-b^*)}\right]\\
&a = \langle e^{-(\beta+\beta^*)\delta E}\rangle = \int_{-\infty}^{\infty}\mathcal{P}(x)e^{-(\beta+\beta^*)x}dx\\
&b = \langle e^{-\beta\delta E}\rangle = \int_{-\infty}^{\infty}\mathcal{P}(x)e^{-\beta x}dx\\
&b^* = \langle e^{-\beta^*\delta E}\rangle = \int_{-\infty}^{\infty}\mathcal{P}(x)e^{-\beta^* x}dx.
\end{aligned} \tag{B.16}$$

Making the replacements $\beta \to \beta + it$ and $\beta^* \to \beta - it$ gives us the expression for spectral form factor given in Eq. (3.14).

B.2 Average Spectral Density For Poisson Spacing

In this section we go over the details of the computing the integrals involved in computing expression for the average spectral density for a Poisson spacing distribution. To begin we can write the JPDF for the energy levels given as:

$$\begin{aligned}
P(E_1,..,E_N) &= \prod_{k=1}^{N}\left[\Theta(E_k-E_{k-1})\frac{e^{-(E_k-E_{k-1})/\sigma}}{\sigma}\right]\\
&= \frac{e^{-(E_N-E_0)/\sigma}}{\sigma^N}\prod_{k=1}^{N}\Theta(E_k-E_{k-1}).
\end{aligned} \tag{B.17}$$

Using this we can write the average spectral density as:

$$\begin{aligned}
\langle\rho(E)\rangle &= \delta(E-E_0)+\int_{-\infty}^{\infty}dE_1\cdots dE_N P(E_1,..,E_N)\sum_{m=1}^{N}\delta(E-E_m)\\
&= \delta(E-E_0)+\sum_{m=1}^{N}\int_{-\infty}^{\infty}dE_1\cdots dE_N\frac{e^{-(E_N-E_0)/\sigma}}{\sigma^N}\delta(E-E_m)\prod_{k=1}^{N}\Theta(E_k-E_{k-1}).
\end{aligned} \tag{B.18}$$

With some work we can derive the following identities:

$$\begin{aligned}
&\int_{-\infty}^{\infty} dE_1 \cdots dE_{m-3} \prod_{k=1}^{m-2} \Theta(E_k - E_{k-1}) = \Theta(E_{m-2} - E_0) \frac{(E_{m-2} - E_0)^{m-3}}{(m-3)!} \\
&\int_{-\infty}^{\infty} dE_{m+2} \cdots dE_N e^{-(E_N - E_0)/\sigma} \prod_{k=m+2}^{N} \Theta(E_k - E_{k-1}) = \sigma^{N-m-1} e^{-(E_{m+1} - E_0)/\sigma}.
\end{aligned} \tag{B.19}$$

Using these integral identities we can show that:

$$\begin{aligned}
&\int_{-\infty}^{\infty} dE_1 \cdots dE_N \frac{e^{-(E_N - E_0)/\sigma}}{\sigma^N} \delta(E - E_m) \prod_{k=1}^{N} \Theta(E_k - E_{k-1}) \\
&= \Theta(E - E_0) \frac{(E - E_0)^{m-1}}{\sigma^m (m-1)!} e^{-(E - E_0)/\sigma}.
\end{aligned} \tag{B.20}$$

We therefore conclude that the average spectral density is given by:

$$\langle \rho(E) \rangle = \delta(E - E_0) + \sum_{m=1}^{N} \left[\frac{(E - E_0)^{m-1}}{\sigma^m (m-1)!} \right] \Theta(E - E_0) e^{-(E - E_0)/\sigma}. \tag{B.21}$$

This gives the averaged spectral density given in Eq. (3.28). By integrating $\langle \rho(E) \rangle$ over E we correctly get $N + 1$ which is the total number of states.

B.3 Form Factor of GUE vs i.i.d Model with Wigner Spacing

In this section we will do a brief numerical study of how well the Wigner Surmise distribution given by Eq. (3.31) fits the NNS distribution of eigenvalues of a 100×100 random Hermitian matrix (i.e. matrices in GUE). We will numerically compute the averaged form factor of the Gaussian unitary ensemble and compare to the form factor expression given by Eq. (3.14) with a, b, b^* given by Eq. (3.32). By doing this, we will get a sense of how well our naive model can capture certain aspects of the true form factor associated with matrices in GUE.

The numerical calculation is done by defining 10^5, 100×100 random Hermitian matrices. The diagonal entries M_{ii} are real and are pulled from the following Gaussian distribution:

$$P(M_{ii}) = \frac{1}{\sqrt{2\pi}} e^{-\frac{1}{2} M_{ii}^2}. \tag{B.22}$$

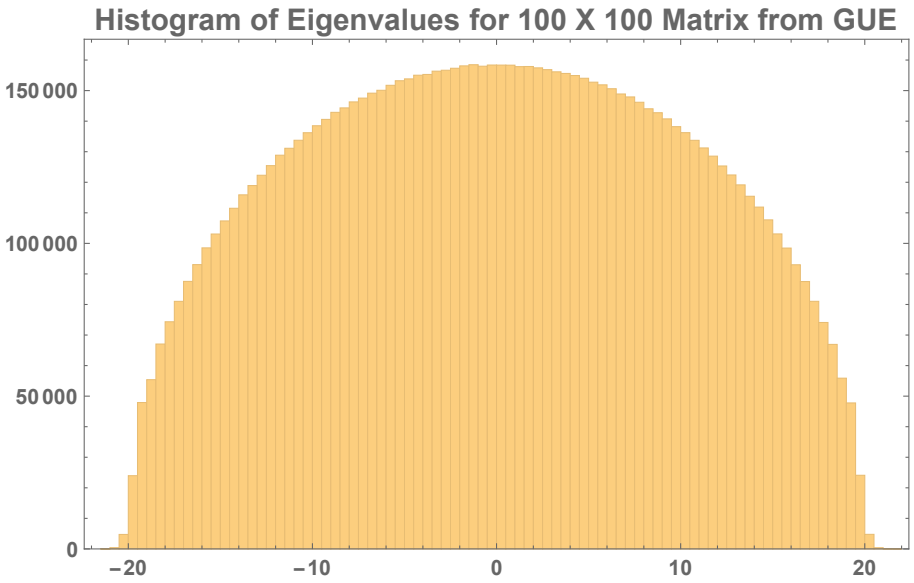

Figure B.1: Histogram for eigenvalues of a 100×100 random matrix pulled from the GUE. The histogram is generated from the eigenvalues of 10^5 random samples.

The off diagonal entries are complex entries of the form $x + iy$ and the real and imaginary parts of the entries are pulled from the following Gaussian distribution:

$$\begin{aligned} P(x) &= \frac{1}{\sqrt{\pi}} e^{-x^2} \\ P(y) &= \frac{1}{\sqrt{\pi}} e^{-y^2}. \end{aligned} \tag{B.23}$$

We can diagonalize all 10^5 matrices to get 10^7 eigenvalues and we will obtain the histogram (i.e. averaged spectral density) for the eigenvalues depicted in Figure B.1. From our sample of eigenvalues we can determine the NNS statistics. An interesting quantity to analyze is the sample averaged spacing of nearest neighbors, and how this changes between which nearest neighbor pairs we choose. We order the eigenvalues so that $E_1 \leq E_2 \leq \cdots \leq E_{100}$, then we define the average spacing between the i-th pair as:

$$\Delta_i = \frac{1}{10^5} \sum_{n=1}^{10^5} \left(E_{i+1}^{(n)} - E_i^{(n)} \right), \tag{B.24}$$

where $i = 1, 2, 3, .., 99$. This represents the average (over 10^5 samples) of the spacing between nearest neighbor pairs throughout the spectrum. We can do a discrete plot of

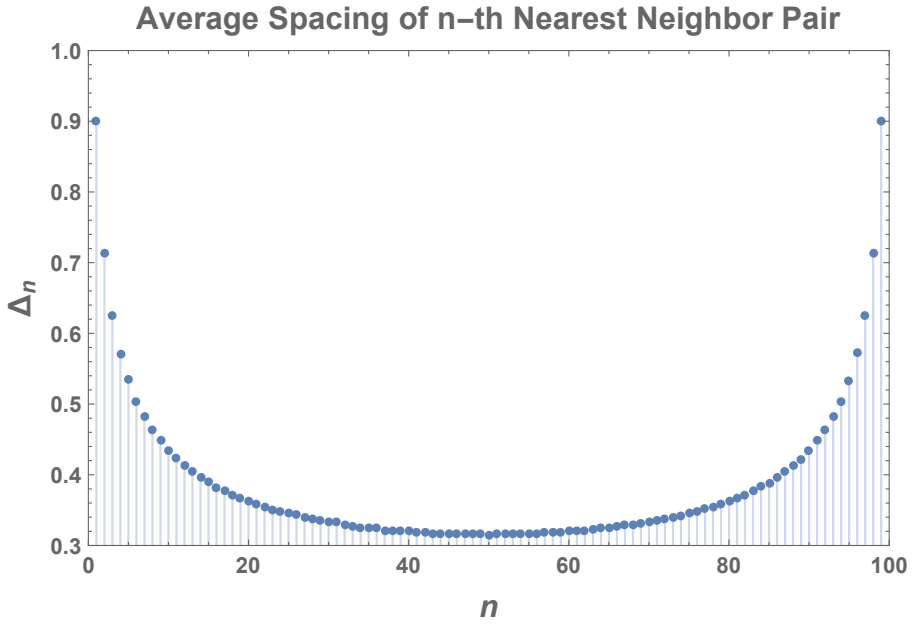

Figure B.2: We plot the average (over 10^5 samples) spacing, Δ_n, between the n-th nearest neighbor pairs of eigenvalues in the GUE (100×100 matrices). We can see that near the edge of the GUE spectrum, the average spacing between nearest neighbor pairs changes quickly. Near the centre of the spectral density of the GUE the average spacing changes slowly.

this as a function of i to obtain Figure B.2. We can see that for eigenvalue pairs located near the center, the average spacing between nearest neighbor pairs is roughly constant but as we approach the edges the spacing changes more quickly between one pair and the next. The range of values which the sample averaged spacings can take roughly lie in the interval $\Delta_i \in [0.32, 0.90]$. Based on this, we can see that the spacing statistics of Gaussian ensembles is not i.i.d (except approximately, near the centre of the spectrum where the average spacing changes slowly). Therefore, we expect the model introduced in Section 3.2.1 to give an accurate description of the spectrum of Gaussian ensembles near the centre of the spectrum and far from the edges[1]. Although, we do not expect our model to describe the edges of Gaussian ensembles to a high degree of accuracy it is still interesting to explore how the form factor of our model spectrum compares to the form factor of an actual Gaussian ensemble as we include eigenvalues near the edge of the

[1]More generally we expect our models with the i.i.d assumption to describe the statistics of eigenvalues located near local the extrema of the spectral density of a random matrix theory.

spectrum.

To do this we define the following numerically calculated quantity:

$$\frac{\langle \mathcal{Z}_{[a,b]}(\beta+it)\mathcal{Z}_{[a,b]}(\beta-it)\rangle}{\langle \mathcal{Z}_{[a,b]}(0)^2\rangle} = \frac{\sum_{l=1}^{S}\sum_{n,m=a}^{b} e^{-(\beta+it)E_n^{(l)}} e^{-(\beta-it)E_m^{(l)}}}{\sum_{l=1}^{S}\sum_{n,m=a}^{b} e^{-\beta E_n^{(l)}} e^{-\beta E_m^{(l)}}}. \tag{B.25}$$

This is computing the form factor in the GUE which contains the a-th through b-th eigenvalues anneal averaged over S samples. This is essentially describing a "microcanonical" anneal averaged form factor which focuses on eigenvalues within a window $[a, b]$. We want to compare this numerical result to our model which involves the i.i.d assumption on the NNS distribution.

We must specify the following two parameters c and σ for the NNS distribution given in Eq. (3.31). Since we are working with the GUE we should set $c = 2$ which leaves us one free parameter σ. Recall that σ controls the average spacing between eigenvalues in our model. In particular, for our model the with $c = 2$ the relation between the average spacing, Δ, and the parameter σ is simply:

$$\sigma = \frac{\sqrt{\pi}}{2}\Delta. \tag{B.26}$$

We will fix σ by analyzing the Δ_i's in the numerical simulation of the GUE. As we already showed in Figure B.2 the average spacing between eigenvalue pairs is roughly constant near the centre of the spectrum. Motivated by this observation we define following quantity which involves data of the eigenvalues $E_a, E_{a+1}, ..., E_{b-1}, E_b$:

$$\bar{\Delta}_{[a,b]} = \frac{1}{b-a}\sum_{i=a}^{b-1}\Delta_i. \tag{B.27}$$

In the above equation, a and b label the index of the a-th and b-th eigenvalues (which are ordered $E_a \leq E_b$ if $a < b$). The quantity $\Delta_{[a,b]}$ defines the sample averaged spacing, averaged over pairs within an interval that contains $E_a, E_{a+1}, ..., E_{b-1}, E_b$ eigenvalues. We define the averaged σ over the range of the eigenvalues as, $\bar{\sigma}_{[a,b]} = \frac{\sqrt{\pi}}{2}\Delta_{[a,b]}$. Then for a particular set of eigenvalues in the GUE with indices in the closed interval $[a, b]$ we identify the $\sigma = \bar{\sigma}_{[a,b]}$. This gives the following NNS distribution for our model spectrum:

$$\mathcal{P}_{[a,b]}(x) = \Theta(x)\frac{4x^2}{\sqrt{\pi}\sigma_{[a,b]}^3} e^{-x^2/\sigma_{[a,b]}^2}. \tag{B.28}$$

We use this NNS distribution along with $N = b - a$ and plug all this into Eq. (3.14) and plot it along-side the "microcanonical" GUE form factor defined by Eq. (B.25). At infinite temperature we get the plots given in Figure B.3.

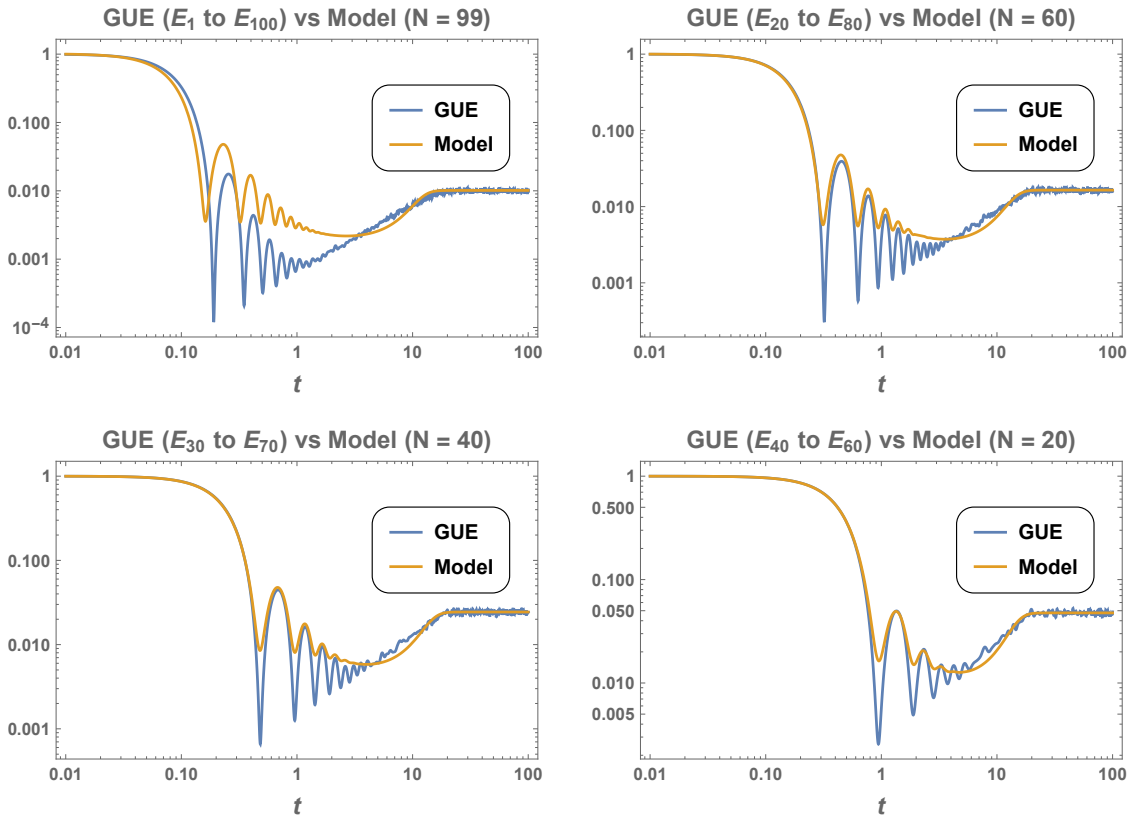

Figure B.3: Plot depicts a comparison of the infinite temperature form factor of the GUE computed numerically using Eq. (B.25) and our i.i.d model with NNS distribution given by Eq. (B.28). The top left plot depicts the a comparison with all eigenvalues in the GUE spectrum. Top right plot depicts a comparison with GUE form factor for roughly 60% of the eigenvalues within the centre of the spectrum. Bottom left depicts a comparison with GUE form factor for roughly 40% of the eigenvalues within the centre of the spectrum. Bottom right depicts a comparison with GUE form factor for roughly 20% of the eigenvalues within the centre of the spectrum. We see that as the window focuses on the centre eigenvalues the deviations between the form factor for the i.i.d model and GUE become smaller at all time scales.

The top left plot in Figure B.3 depicts the numerically averaged form factor of the

GUE (blue line) for the entire spectrum (i.e. it includes E_1 to E_{100}). We compare with our i.i.d model form factor (the yellow line) with $N = 99$ and NNS given by Eq. (B.28) with $\sigma_{[1,100]} \approx 0.345$. We can see that the plateau of the model matches the plateau of the model but at earlier times it deviates away from the GUE.

The top right plot depicts the GUE form factor with the edges of the spectrum cut off - only retaining the eigenvalues E_{20} to E_{80}. We compare with the i.i.d model form factor with parameters $N = 60$ and $\sigma_{[20,80]} \approx 0.292$. We see that the plateaus still match but now the early time behaviour is matching more closely than before.

The bottom left plot depicts the GUE form factor with the edges of the spectrum cut off even further than, only retaining the eigenvalues E_{30} to E_{70}. We compare with the i.i.d model form factor with parameters $N = 40$ and $\sigma_{[30,70]} \approx 0.285$.

Finally, the bottom right plot depicts the GUE, retaining the eigenvalues E_{40} to E_{60}. We compare with the i.i.d model form factor with parameters $N = 20$ and $\sigma_{[40,60]} \approx 0.281$.

Together the four plots in Figure B.3 plots of the form factor illustrates our claim that our model captures the behaviour spectrum of Gaussian ensembles near the centre of the semi-circle far from the edge. We can see that as we shrink our window of eigenvalues closer to the centre of the spectrum the form factor of the truncated GUE (blue lines) matches more closely with the form factor of our model (yellow line).

B.4 Local Extrema of Form Factor for Gamma Distribution NNS

In this section, we will analyze Eq. (3.37) which is given by:

$$\begin{aligned} &\frac{z^q}{\left[z^{q+1}-1\right]^2} = \frac{(z^*)^q}{\left[(z^*)^{q+1}-1\right]^2} \\ &z = 1 + \sigma(\beta + it) \\ &z^* = 1 + \sigma(\beta - it). \end{aligned} \tag{B.29}$$

By inspection, it is clear that $t = 0$ is a valid solution and corresponds to an extremal point. Furthermore, in the limit that $t \to \infty$, the equation is also satisfied, this represents the saturation of the form factor to a constant value (the plateau phase). Aside from these trivial solutions we should expect at least one other solution in the case when $q > 0$. This is because for $q > 0$ there is repulsion and therefore a ramp after the initial dip downward.

This will give a local minimum in the form factor. Furthermore for very large values of $q \gg 1$ we also expect oscillations to exist which will give further extremal points in the form factor.

To understand where these non-trivial extremal points occur it is useful to write the complex variable z in the polar coordinate representation:

$$\begin{aligned} z &= Ae^{i\theta} \\ A &= (1+\beta\sigma)\sqrt{1+\left(\frac{t\sigma}{1+\beta\sigma}\right)^2} \\ \theta &= \arctan\left(\frac{t\sigma}{1+\beta\sigma}\right). \end{aligned} \tag{B.30}$$

In this representation, Eq. (3.37) can be written in the following form:

$$-A^{2(q+1)}\sin\left[(q+2)\theta\right] + 2A^{q+1}\sin(\theta) + \sin(q\theta) = 0. \tag{B.31}$$

This is difficult to solve in general so we will consider the special cases when $q = 1, 2, 4$ where we can solve the equation exactly. We will also make some estimates in the $q \gg 1$ regime.

$q = 1$ **Case:**
In this case one will find five distinct solutions. One solution is the trivial solution when $t = 0$, the other four are non-trivial but only one is real and positive for $\beta\sigma > 0$, it is given by:

$$t\sigma = \sqrt{\beta\sigma + (1+\beta\sigma)\left[\beta\sigma + 2\sqrt{\beta\sigma(2+\beta\sigma)}\right]} \simeq \begin{cases} \sqrt{3}\beta\sigma + \mathcal{O}(1), & \beta\sigma \gg 1 \\ (8\beta\sigma)^{1/4} + \mathcal{O}((\beta\sigma)^{3/4}), & \beta\sigma \ll 1 \end{cases}. \tag{B.32}$$

$q = 2$ **Case:**
In this case one will find seven distinct solutions. One solution is the trivial solution when $t = 0$, the other six are non-trivial but only one is real and positive for $\beta\sigma > 0$, it is given by:

$$t\sigma = (1+\beta\sigma)\left[1 - \frac{1}{(1+\beta\sigma)^3}\right]^{1/4} \simeq \begin{cases} \beta\sigma + \mathcal{O}(1), & \beta\sigma \gg 1 \\ (3\beta\sigma)^{1/4} + \mathcal{O}((\beta\sigma)^{3/4}), & \beta\sigma \ll 1 \end{cases}. \tag{B.33}$$

In both cases we can see that up to a pre-factor the local minimum before the ramp at low temperatures scales with β this is contrast to the high temperature case where it scales as $\beta^{1/4}$.

$q = 4$ **Case:**
In this case we will have two non-trivial real solutions which have closed form expressions. The exact expressions are complicated so we will not write them here, instead we will write the solutions as series expansion for small and large $\beta\sigma$. We start with the smaller solution which represents the initial dip in the form factor before the ramp given by:

$$t\sigma \simeq \begin{cases} \beta\sigma/\sqrt{3} + \mathcal{O}(1), \ \beta\sigma \gg 1 \\ (\beta\sigma)^{1/4} + \mathcal{O}((\beta\sigma)^{3/4}), \ \beta\sigma \ll 1 \end{cases} . \tag{B.34}$$

The next real solution corresponds to the small "kink" in the form factor that connects the ramp to the plateau which is also seen in GSE. The expression for the time when the kink occurs is well approximated in all temperature regimes by the following expression:

$$t\sigma \approx \sqrt{3}(1 + \beta\sigma). \tag{B.35}$$

Overall, we see that for $q = 1, 2, 4$ the inital dip before the plateau has the same temperature dependence up to an order one pre-factor. Furthermore, we are able to show that for the $q = 4$ case the form factor has an additional local maximum which represents the "kink" which connects the plateau to the ramp seen in Figure 3.9.

$q \gg 1$ **Case:**
We know that for very large values of q, the form factor exhibits an initial dip followed by oscillations before saturation to a plateau. In this case, we should expect to find more than one non-trivial extremal point which describe the peaks and troughs of the oscillations. In the case when $q \gg 1$, Eq. (B.31) at leading order will read:

$$\left[A^q - A^{-q}\right] \sin(q\theta) = 2\sin(\theta). \tag{B.36}$$

If we define $x = t\sigma/(1 + \beta\sigma)$ we can explicitly write:

$$\left[(1 + \beta\sigma)^q (1 + x^2)^{q/2} - (1 + \beta\sigma)^{-q}(1 + x^2)^{-q/2}\right] \sin\left[q \arctan(x)\right] = \frac{2x}{\sqrt{1 + x^2}}. \tag{B.37}$$

We can clearly see that the left hand side of Eq. (B.37) will diverge like $x^q \sin(q\pi/2)$ as $x \to \infty$. The left hand side saturates to a value of 2 in the $x \to \infty$ limit. This means that

there are a finite number of solutions for a given $q \gg 1$ - which is in agreement with the plots we have made. Clearly $x = 0$ is a solution, but we expect there to be more.

To understand how many solutions there are, we start by analyzing the number of roots (excluding $x = 0$) to the expression on the left hand side of Eq. (B.37). This is simply given by the roots of $\sin[q \arctan(x)]$ which occur when $q \arctan(x) = m\pi$ where $m \in \mathbb{N} \cup \{0\}$. Since $0 \leq \arctan(x) \leq \pi/2$, the number of zeros is controlled by q. In particular, we denote N_{root} as the number of zeros (excluding the zero at $x = 0$) we have:

$$N_{root} = \begin{cases} \frac{q}{2} - 1, \ q/2 \in \mathbb{N} \\ \lfloor \frac{q}{2} \rfloor, \ \text{otherwise} \end{cases} . \tag{B.38}$$

Now consider the right hand side of Eq. (B.37). Since the right-hand side is a monotonically increasing function which takes on values in the interval $(0, 2)$. It is not difficult to see that for a sufficiently large q there will be at least $N_{root} - 1$ non-trivial solutions to Eq. (B.37)[2]. Whether there is an additional solution depends on the limits as $x \to \infty$. In particular, one can argue that the number of solutions (excluding the $x = 0$ solution) is given by:

$$N_{sol.} = \begin{cases} N_{root}, \ \frac{N_{root}}{2} \in \mathbb{N} \\ N_{root} - 1, \ \frac{N_{root}}{2} \in (2\mathbb{N} + 1) \end{cases} . \tag{B.39}$$

Now that we have quantified the number of solutions we estimate that the solutions for sufficiently large q occur roughly at:

$$x_n = \frac{t_n \sigma}{1 + \beta\sigma} = \frac{n\pi}{q}, \ n = 0, 1, 2, 3, .., N_{sol.} \tag{B.40}$$

To illustrate how accurately this approximation captures the location of the extremal points of the form factor described by Eq. (3.35). We make Figure B.4, which depicts the averaged form factor with $q = 50$ and $\beta = 0.01$ with the red dots representing the value of the form factor at $t_n\sigma = (1 + \beta\sigma)n\pi/q = (1.01)\pi n/50$. We can see that our approximation for the location of local extrema representing the peaks and troughs of the regular decaying oscillation is not perfect but it does give a reasonable estimate. Similar plots can also be made at other temperatures as well.

Based on these results we conclude that the period of the oscillations in the form factor are roughly given by:

$$T \approx \frac{2\pi(1 + \beta\sigma)}{q\sigma}. \tag{B.41}$$

[2]By sufficiently large q, we mean that for a given $\beta\sigma$ we must have q such that the left hand side of Eq. (B.37) evaluated at $x = tan(\pi/(2q))$ be larger than 2. This roughly gives a condition that $q > \frac{\ln(2)}{\beta\sigma}$

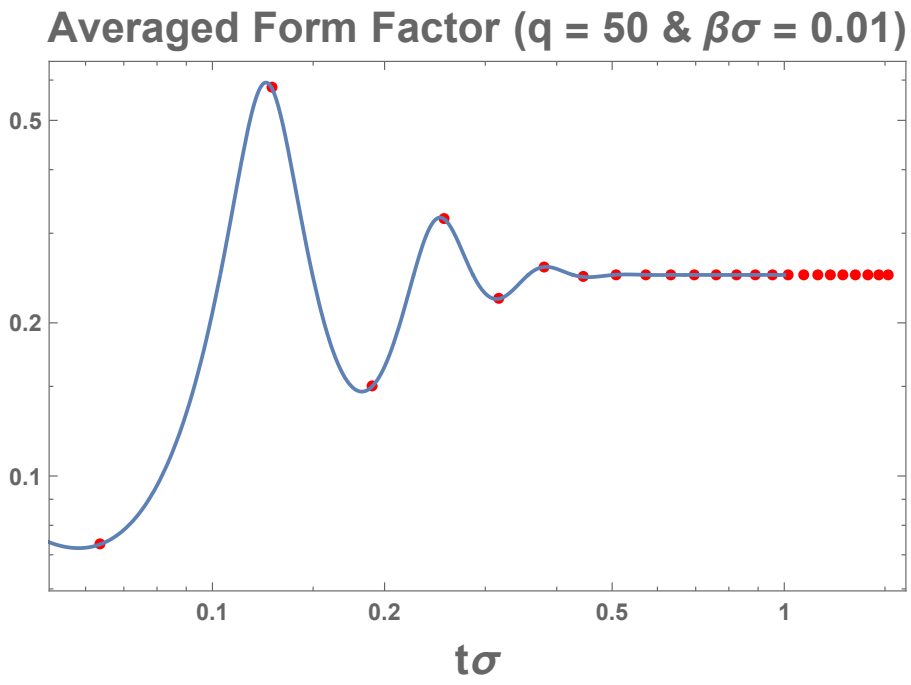

Figure B.4: We plot the expression of the form factor in Eq. (3.35) for $q = 50$, $\beta\sigma = 0.01$. The red dots indicate points on the form factor at $t_n\sigma = 1.01\pi n/50$. We can see that the points roughly occur local maxima and minima of the form factor.

B.5 Average Spectral Density For Gamma Distribution Spacing

In this section we compute the average spectral density for the Gamma Distribution spacing distribution given in Eq. (3.33). To begin, we can write the JPDF for the energy levels given as:

$$\begin{aligned} P(E_1,..,E_N) &= \prod_{k=1}^{N}\left[\Theta(E_k-E_{k-1})\frac{(E_k-E_{k-1})^q e^{-(E_k-E_{k-1})/\sigma}}{\Gamma(1+q)\sigma^{1+q}}\right] \\ &= \frac{e^{-(E_N-E_0)/\sigma}}{\left[\Gamma(1+q)\sigma^{1+q}\right]^N}\prod_{k=1}^{N}\Theta(E_k-E_{k-1})\left(E_k-E_{k-1}\right)^q. \end{aligned} \tag{B.42}$$

Using this we can write the average spectral density as:

$$\begin{aligned} \langle\rho(E)\rangle &= \int_{-\infty}^{\infty} dE_1\cdots dE_N P(E_1,..,E_N)\sum_{m=0}^{N}\delta(E-E_m) \\ \langle\rho(E)\rangle &= \delta(E-E_0)+\sum_{m=1}^{N}\int_{-\infty}^{\infty} dE_1\cdots dE_N\frac{e^{-(E_N-E_0)/\sigma}}{\left[\Gamma(1+q)\sigma^{1+q}\right]^N}\delta(E-E_m)\prod_{k=1}^{N}\Theta(E_k-E_{k-1})(E_k-E_{k-1})^q. \end{aligned} \tag{B.43}$$

With some work we can derive the following identities:

$$\begin{aligned} &\int_{-\infty}^{\infty} dE_1\cdots dE_{m-3}\prod_{k=1}^{m-2}\Theta(E_k-E_{k-1})(E_k-E_{k-1})^q \\ &= \frac{\sqrt{\pi}\Gamma(1+q)^{m-3}}{2^{2q+1}\Gamma(3/2+q)}\frac{\Gamma\left[2(1+q)\right]}{\Gamma\left[(m-2)(1+q)\right]}\Theta(E_{m-2}-E_0)(E_{m-2}-E_0)^{(m-2)q+(m-3)} \\ &= \frac{\Gamma(1+q)^{m-2}}{\Gamma\left[(m-2)(1+q)\right]}\Theta(E_{m-2}-E_0)(E_{m-2}-E_0)^{(m-2)q+(m-3)} \end{aligned} \tag{B.44}$$

$$\begin{aligned} &\int_{-\infty}^{\infty} dE_{m+2}\cdots dE_N e^{-(E_N-E_0)/\sigma}\prod_{k=m+2}^{N}\Theta(E_k-E_{k-1})(E_k-E_{k-1})^q \\ &= \left[\Gamma(1+q)\sigma^{1+q}\right]^{N-m-1} e^{-(E_{m+1}-E_0)/\sigma}. \end{aligned} \tag{B.45}$$

Using the identities above with some additional work one will find:

$$\langle\rho(E)\rangle = \delta(E-E_0)+\sum_{m=1}^{N}\left[\frac{(E-E_0)^{mq+m-1}}{\Gamma\left[m(1+q)\right]\sigma^{m(1+q)}}\right]\Theta(E-E_0)e^{-(E-E_0)/\sigma}. \tag{B.46}$$

This gives us the average spectral density given by Eq. (3.39). Furthermore, setting $q = 0$ we will recover the spectral density for the Poisson NNS model discussed in Section 3.3.2.

B.6 NNS Distribution for Oscillator with Chaotic Interactions 2×2 Case

We go over the calculation of the NNS distribution for the following matrix:

$$\mathcal{H} = \frac{\omega_0}{2}\begin{bmatrix} 0 & 0 \\ 0 & 1 \end{bmatrix} + \epsilon \begin{bmatrix} x_1 & x_3 + ix_4 \\ x_3 - ix_4 & x_2 \end{bmatrix}, \tag{B.47}$$

where the real entries are drawn from the following distributions: Where x_1, x_2, x_3, and x_4 are real random variables which follow the following distributions:

$$\begin{aligned} \mathcal{P}(x_1) &= \frac{1}{\sqrt{2\pi}} e^{-x_1^2/2} \\ \mathcal{P}(x_2) &= \frac{1}{\sqrt{2\pi}} e^{-x_2^2/2} \\ \mathcal{P}(x_3) &= \sqrt{\frac{1}{\pi}} e^{-x_3^2} \\ \mathcal{P}(x_4) &= \sqrt{\frac{1}{\pi}} e^{-x_4^2} \end{aligned} \tag{B.48}$$

.

We can compute the spacing distribution between the eigenvalues by evaluating the following integral:

$$\mathcal{P}(s) = \int_{-\infty}^{\infty} dx_1 \cdots dx_4 \mathcal{P}(x_1)\mathcal{P}(x_2)\mathcal{P}(x_3)\mathcal{P}(x_4)\delta\left(s - \frac{\omega_0}{2}\sqrt{\left(1 + \frac{2\epsilon(x_2 - x_1)}{\omega_0}\right)^2 + \frac{16\epsilon^2}{\omega_0^2}(x_3^2 + x_4^2)}\right). \tag{B.49}$$

We define the following change of variables:

$$\begin{aligned} x_1 &= \frac{z + r\cos\theta}{2\epsilon} + \frac{\omega}{2\epsilon} \\ x_2 &= \frac{z - r\cos\theta}{2\epsilon} \\ x_3 &= \frac{r\sin\theta\sin\phi}{2\epsilon} \\ x_4 &= \frac{r\sin\theta\cos\phi}{2\epsilon}. \end{aligned} \tag{B.50}$$

With these variables we have $dx_1dx_2dx_3dx_4 = \frac{r^2\sin\theta}{8\epsilon^4}drdzd\theta d\phi$ and the integral becomes:

$$\begin{aligned} \mathcal{P}(s) &= \frac{1}{16\pi^2\epsilon^4}\int_0^\infty dr\int_{-\infty}^\infty dz\int_0^\pi d\theta\int_0^{2\pi} d\phi r^2\sin\theta e^{-\frac{2(r^2+z^2)+2z\omega+\omega^2+2r\omega\cos(\theta)}{8\epsilon^2}}\delta(s-r) \\ &= \frac{s}{\sqrt{\pi}\epsilon\omega_0}\left(e^{\frac{\omega_0 s}{2\epsilon^2}} - 1\right)e^{-\frac{(2s+\omega_0)^2}{16\epsilon^2}}. \end{aligned} \tag{B.51}$$

This gives the result in Eq. (3.46).

B.7 Numerical Analysis in the Spread of Degenerate States

In this appendix, we go over numerical results which discuss the statistics of how the degenerate eigenvalues of the fermionic harmonic oscillator given in Eq. (3.56) split due to a perturbation by a random matrix in the GUE. The Hamiltonian in the basis of the unperturbed oscillator can be written as:

$$\frac{\mathcal{H}}{\omega_0} = \bigoplus_{p=0}^{N/2}\left[\left(p - \frac{N}{4}\right)\mathcal{I}(p)\right] + \frac{\epsilon}{\omega_0}\mathcal{H}_{GUE}, \tag{B.52}$$

where $I(p)$ is an identity matrix of size $\Omega(p)\times\Omega(p)$ (recall that $\Omega(p)$ is given by Eq. (3.57)) and $\mathcal{H}_{GUE}$ is a $2^{N/2}\times 2^{N/2}$ random matrix pulled from the Gaussian unitary ensemble (see footnote 25 for details of the variance of the Gaussian used for the matrix elements). We fix ϵ/ω_0 then we numerically compute the eigenvalues over r independent samples and collect

all these eigenvalues (there are $S = 2^{N/2} \times r$ number of them) and put them in an ordered set $\{E_i\}_{i=1}^{S}$ where $E_1 \leq E_2 \leq \cdots \leq E_S$. We define the following subsets labeled by p:

$$\begin{aligned} A_p &= \{E_k : k_{\min}(p) \leq k \leq k_{\max}(p)\} \\ k_{\min}(p) &= 1 + r \sum_{l=0}^{p-1} \Omega(l) \\ k_{\max}(p) &= r \sum_{l=0}^{p} \Omega(l), \end{aligned} \tag{B.53}$$

where $p = 0, 1, 2, .., N/2$. The set A_p simply partitions the original ordered set into subsets labeled by p which are of the size $|A_p| = r\Omega(p)$. The reason this is done can be illustrated by considering what happens when $\epsilon = 0$. In this case, there is no perturbation and the Hamiltonian is diagonal. If we took r samples of the exact same diagonal matrix and ordered all the eigenvalues in a list we would find there are exactly $|A_p| = r\Omega(p)$ eigenvalues with the value $E(p)$. Adding a small perturbation would lead to a small spreading in the eigenvalues within each degenerate sector so the set A_p is the set of eigenvalues that have "split" in the $p-th$ degenerate sector. We define the numerical width of the $p-th$ sector as:

$$\begin{aligned} W_{num}(p) &= \max(A_p) - \min(A_p) \\ \max(A_p) &= E_{k_{\max}(p)} \\ \min(A_p) &= E_{k_{\min}(p)}. \end{aligned} \tag{B.54}$$

The numerical average energy within the $p-th$ sector is given by:

$$\langle E(p) \rangle_{num} = \frac{1}{r} \sum_{i=k_{\min(p)}}^{k_{\max}(p)} E_i. \tag{B.55}$$

Applying this numerical procedure we obtain the following plots which compare various numerical and estimated quantities when $r = 100$ and $N = 22$.

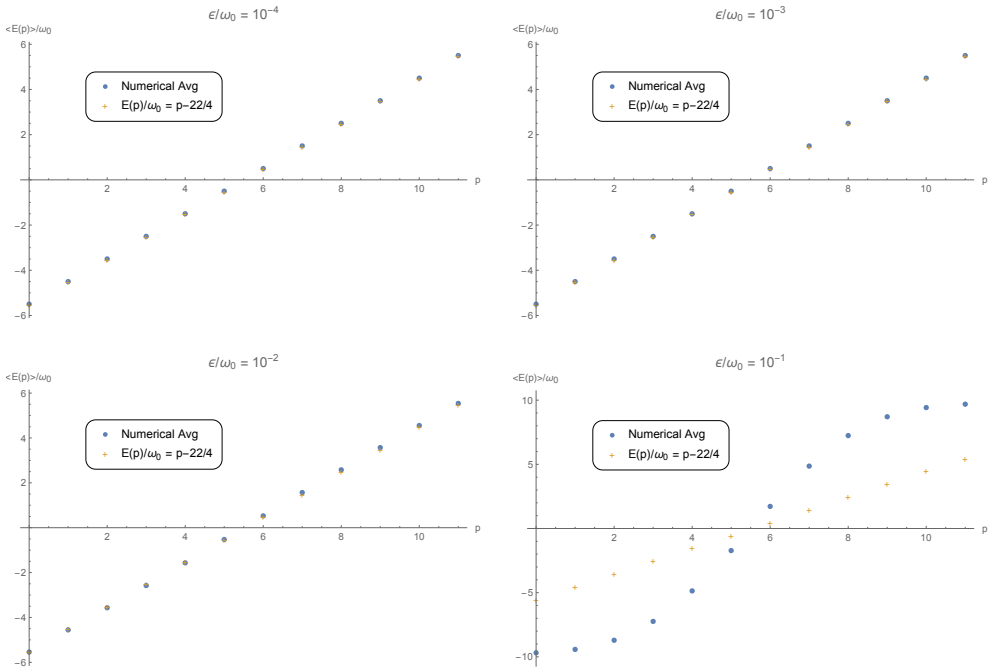

Figure B.5: Above are plots of the average energy within degenerate sectors labelled by p at various coupling regimes ranging from the weakly coupled regime with $\epsilon/\omega_0 = 10^{-4}$ to the strongly coupled regime with $\epsilon/\omega_0 = 10^{-1}$. The solid circles are numerical computations of the average and the "+" is the energy of the degeneracy sector in the free oscillator case.

We see that in the weakly coupled regime which is given by the top two plots of Figure B.5 the numerical average of the energies within the sector $p - th$ sector is close to the degenerate energy of the free oscillators which is consistent with predictions of first order degenerate perturbation theory. When $\epsilon/\omega_0 = 10^{-2}$ we can start to see small deviations in the average energy from the unperturbed energy. By the time we get to the strongly coupled regime where degenerate sectors strongly mix there are large deviations.

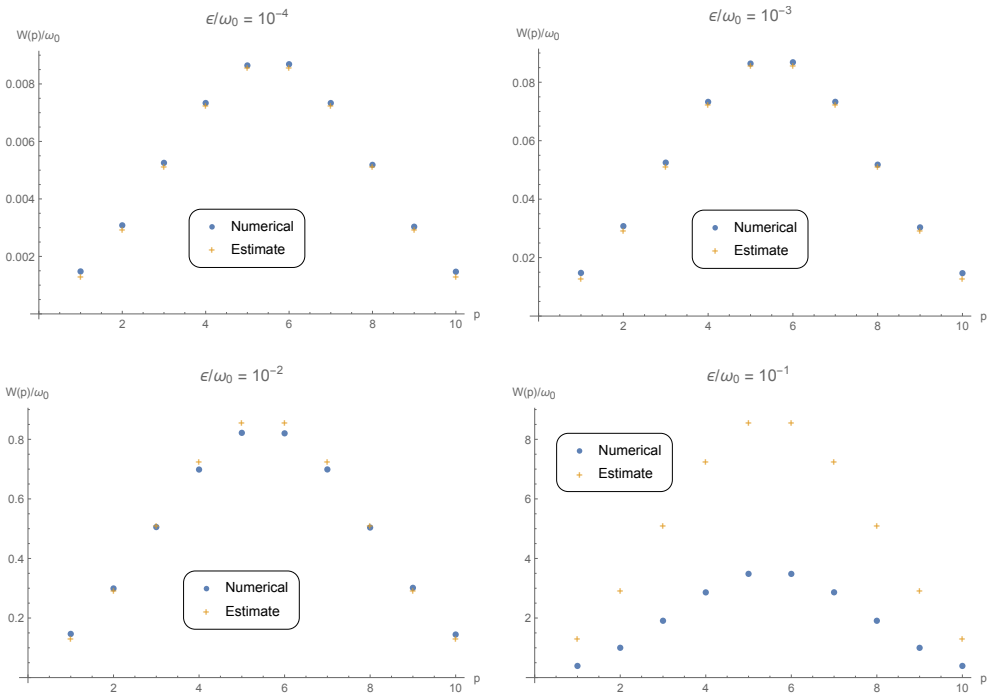

Figure B.6: Above are plots of the width in the spread of degenerate energy states within the p-th degenerate sector at various coupling regimes ranging from the weakly coupled regime with $\epsilon/\omega_0 = 10^{-4}$ to the strongly coupled regime with $\epsilon/\omega_0 = 10^{-1}$. The solid circles are numerical computations of the width and the "+" is the expectation of the width (Given by Eq. (3.63)) from first order degenerate perturbation theory.

In the weakly coupled regime which is given by the top two plots of Figure B.6, the numerical width of the spread in the energies within the $p-th$ sector is close to the estimate given by Eq. (3.63) which is obtained by applying first order degenerate perturbation theory. When $\epsilon/\omega_0 = 10^{-2}$, we can start to see small deviations from the estimate. By the time we get to the strongly coupled regime where degenerate sectors strongly mix there are large deviations.

Appendix C

Chapter 4 Appendix Materials

C.1 Numerical Analysis of Evaporation Rate Series for AdS Schwarzschild Black Hole

In this appendix we will numerically compute the following series for an AdS Schwarzschild black hole:

$$\begin{aligned}&\sum_{\ell=1}^{\infty} \ell^{d-2} \left[Li_2\left(e^{-x_{min,\ell}}\right) - x_{min,\ell} \ln\left(1-e^{-x_{min,\ell}}\right)\right] \\ &x_{min,\ell} = \sqrt{4\pi\left(2\pi(d-1) + \frac{4\pi L^2 \ell(\ell+d-2)}{dr_s^2 + (d-2)L^2}\right)\frac{\delta r}{r_s}}.\end{aligned} \tag{C.1}$$

To evaluate the series numerically we need to fix d, $\delta r/r_s$, and r_s/L. Once we do this we will compare the result to our approximated expression given by:

$$\begin{aligned}&\sum_{\ell=1}^{\infty} \ell^{d-2} \left[Li_2\left(e^{-x_{min,\ell}}\right) - x_{min,\ell} \ln\left(1-e^{-x_{min,\ell}}\right)\right] \\ &\approx d(d-2)! \left(\frac{r_s^2}{4\pi\beta\delta r}\right)^{\frac{d-1}{2}}.\end{aligned} \tag{C.2}$$

The approximated expression will differ from the numerical expression by a numerical pre-factor. In other words the numerical result can be written in the form:

$$\begin{aligned}&\sum_{\ell=1}^{\infty} \ell^{d-2} \left[Li_2\left(e^{-x_{min,\ell}}\right) - x_{min,\ell} \ln\left(1-e^{-x_{min,\ell}}\right)\right] \\ &= \mathcal{C}_d \left[d(d-2)! \left(\frac{r_s^2}{4\pi\beta\delta r}\right)^{\frac{d-1}{2}}\right],\end{aligned} \tag{C.3}$$

where $\mathcal{C}_d$ is a numerical pre-factor which will change with d, δr, and r_s/L. We summarize our results in tables C.1 - C.3. Each table fixes d and $\delta r/r_s$ to some fixed value (specified in the caption for each table). Within the table we vary the size of the black hole r_s/L (from 0 corresponding to an asymptotically flat black hole to 1000 corresponding to a very large AdS black hole) and numerically compute the series in Eq. (C.1). We also compute the value for series as determined by our approximation given in Eq. (C.2). We divide the numerical and approximate result to determine the pre-factor $\mathcal{C}_d$ that the two results differ by.

r_s/L	0	0.1	1	10	1000
Numerical	1.96×10^2	2.02×10^2	8.01×10^2	6.15×10^4	6.14×10^8
Approximation	1.89×10^2	1.95×10^2	7.59×10^2	5.72×10^4	5.70×10^8
$\mathcal{C}_3 = \frac{Numerical}{Approximation}$	1.04	1.04	1.06	1.08	1.08

Table C.1: $d = 3$ and $\delta r/r_s = 10^{-4}$

r_s/L	0	0.1	1	10	1000
Numerical	1.33×10^8	1.38×10^8	1.37×10^9	4.11×10^{13}	4.07×10^{23}
Approximation	1.47×10^8	1.53×10^8	1.45×10^9	4.12×10^{13}	4.05×10^{23}
$\mathcal{C}_6 = \frac{Numerical}{Approximation}$	0.91	0.90	0.95	1.00	1.01

Table C.2: $d = 6$ and $\delta r/r_s = 10^{-4}$

r_s/L	0	0.1	1	10	1000
Numerical	5.09×10^{17}	5.38×10^{17}	2.06×10^{19}	1.66×10^{27}	1.63×10^{45}
Approximation	5.98×10^{17}	6.32×10^{17}	2.30×10^{19}	1.69×10^{27}	1.63×10^{45}
$\mathcal{C}_{10} = \frac{Numerical}{Approximation}$	0.85	0.85	0.90	0.98	1.00

Table C.3: $d = 10$ and $\delta r/r_s = 10^{-4}$

C.2 Power Law Behaviour of Generalized Greybody Factor for Near Extremal BH

Here we present a way to get the power law behaviour for $\omega < \omega_{min,\ell}$ in Eq. (4.28). We do this by analyzing the near horizon solution of the wave equation for an extremal black hole. We will begin by considering modes with $\ell \geq 1$.

The first thing we do is recall that the potential needs to be written in the tortoise coordinate r_* which satisfies:

$$r_* = \int \frac{dr}{f(r)} \simeq \int \frac{dr}{f_1(r-r_s) + \frac{f_2}{2}(r-r_s)^2} = \frac{1}{f'(r_s)} \ln\left[\frac{(r-r_s)f''(r_s)}{2f'(r_s) + f''(r_s)(r-r_s)}\right] \leq 0, \tag{C.4}$$

where $f_n = f^{(n)}(r_s)$. We can easily invert this and find:

$$r - r_s = \frac{2f_1}{f_2(1-\exp(f_1 r_*))} \to -\frac{2}{r_* f''_{ext}(r_s)}, \tag{C.5}$$

where in the last expression we take the extremal limit where $f_1 \to 0$. Now that we have an expression for the near horizon tortoise coordinate we can analyze the wave equation which at leading order will read:

$$\frac{d^2\psi}{dr_*^2} + \left[\omega^2 - \frac{2\ell(\ell+d-2)}{r_s^2 f''_{ext}(r_s)}\frac{1}{r_*^2}\right]\psi = 0. \tag{C.6}$$

We can find the general solution to this equation can be written in terms of Bessel functions:

$$\begin{aligned} \psi(r_*) &= \sqrt{r_*}\left[AJ_{\nu_\ell}(\omega r_*) + BY_{\nu_\ell}(\omega r_*)\right] \\ \nu_\ell &= \frac{1}{2}\sqrt{1 + \frac{8\ell(\ell+d-2)}{r_s^2 f''_{ext}(r_s)}}. \end{aligned} \tag{C.7}$$

We want a solution that goes to zero at $r_* = 0$ this implies that $B = 0$ and we get the following solution:

$$\psi(r_*) = A\sqrt{r_*}J_\nu(\omega r_*). \tag{C.8}$$

One can easily see that this solution for very small r_* oscillates as a plane wave. However near the boundary it decays. It is the rate of decay that we are interested in. In particular, it is reasonable to assume that the shift from an oscillating function to a decaying function occurs near the classical turning point which is:

$$r_*^{tp}(\omega) = -\left[\frac{2\ell(\ell+d-2)}{\omega^2 r_s^2 f''_{ext}(r_s)}\right]^{1/2}. \tag{C.9}$$

Consider the ratio:

$$T^2 = \left|\frac{\psi(r_*)}{\psi(r_*^{tp})}\right|^2 = \left|\frac{r_*}{r_*^{tp}}\right|\left|\frac{J_\nu(\omega r_*)}{J_\nu(\omega r_*^{tp})}\right|^2, \tag{C.10}$$

where $r_*^{tp} \leq r_* \leq 0$. This gives a measure of how the amplitude of the solution decays in the non-classical region. We analyze the decay of the solution a distance $\delta r = r - r_s$ from the horizon in the classically forbidden region. To do this we need to consider $\omega \leq \omega_{min,\ell}$. We parameterize this in terms of $0 \leq \epsilon \leq 1$ and write $\omega = \epsilon\omega_{min,\ell}$. Then we can express r_*^{tp} as:

$$r_*^{tp}(\epsilon) = -\frac{2}{\epsilon\delta r f''_{ext}(r_s)}. \tag{C.11}$$

We also set r_* at the position of interest (i.e. where the absorbing surface is):

$$r_* = -\frac{2}{\delta r f''_{ext}(r_s)}. \tag{C.12}$$

Now we can express T^2 in terms of ϵ:

$$
\begin{aligned}
T^2(\epsilon) &= \epsilon \left| \frac{J_{\nu_\ell}(\alpha_\ell \epsilon)}{J_{\nu_\ell}(\alpha_\ell)} \right|^2 \\
\alpha_\ell &= \frac{-2\omega_{min,\ell}}{\delta r f''_{ext}(r_s)} = -\sqrt{\frac{2\ell(\ell+d-2)}{r_s^2 f''_{ext}(r_s)}} \\
\nu_\ell &= \sqrt{\frac{1}{4} + \alpha_\ell^2}.
\end{aligned}
\tag{C.13}
$$

We can do a series expansion of T^2 in α_ℓ to understand the power law behaviour we find:

$$
T^2 = \epsilon \left| \frac{J_{\nu_\ell}(\alpha_\ell \epsilon)}{J_{\nu_\ell}(\alpha_\ell)} \right|^2 \simeq \epsilon^{2\nu_\ell+1} \left[1 + \frac{\alpha_\ell^2(1-\epsilon^2)}{2(1+\nu_\ell)} + \mathcal{O}\left(\alpha_\ell^4\right) \right] \sim \epsilon^{2\nu_\ell+1}. \tag{C.14}
$$

We will use this behaviour to model the generalized greybody factor for $\omega < \omega_{min,\ell}$. So now we have the following for near extremal black holes:

$$
\gamma_\ell(\omega, \delta r) = \Theta(\omega - \omega_{min,\ell}) + \left(\frac{\omega}{\omega_{min,\ell}} \right)^{2\nu_\ell+1} \Theta\left(\omega_{min,\ell} - \omega\right). \tag{C.15}
$$

This gives the result in Eq. (4.28).

Now we will consider the $\ell = 0$ mode. In this case the leading order expansion of the effective potential near the horizon is:

$$
V_{\ell=0}(r) = V_0(r) = \frac{(d-1)\left[f''_{ext}(r_s)\right]^2}{4r_s}(r-r_s)^3 + \mathcal{O}\left((r-r_s)^4\right). \tag{C.16}
$$

Note that to capture the leading order behavior of the effective potential for $\ell = 0$ one must expand to third order. This is in contrast to the effective potential for $\ell \geq 1$ modes which. only required a second order expansion. As we will see this makes the $\ell = 0$ modes distinct from the higher order modes. With some work we can show that the wave equation near the horizon takes the form:

$$
\frac{d^2\psi}{dr_*^2} + \left[\omega^2 + \frac{2(d-1)}{r_s f''_{ext}(r_s)} \frac{1}{r_*^3} \right] \psi = 0. \tag{C.17}
$$

Unlike the $\ell \geq 1$ case we cannot find the general solution of this equation in a closed form. We instead opt to solve the equation in two regimes (close to the horizon and close to the conformal boundary) and then patch the solutions at the turning point of the potential.

Close to the horizon we have plane wave solutions. The outgoing plane wave normalized to one is given by:

$$\psi_I(r_*) = e^{i\omega r_*}. \tag{C.18}$$

In the classically forbidden region (where the amplitude of the solution will decay) we will have $\omega^2 \ll \frac{2(d-1)}{r_s f''_{ext}(r_s)} \frac{1}{r_*^3}$. So the solution can be roughly found by solving:

$$\frac{d^2\psi}{dr_*^2} + \frac{2(d-1)}{r_s f''_{ext}(r_s)} \frac{1}{r_*^3} \psi = 0. \tag{C.19}$$

The general solution will be given by Bessel functions of the first and second kind:

$$\begin{aligned} \psi_{II}(r_*) &= \frac{\sqrt{-r_*}}{\alpha} \left[c_1 J_1 \left(\frac{2i\alpha}{\sqrt{-r_*}} \right) + c_2 Y_1 \left(\frac{2i\alpha}{\sqrt{-r_*}} \right) \right] \\ \alpha &= \sqrt{\frac{2(d-1)}{r_s f''_{ext}(r_s)}}. \end{aligned} \tag{C.20}$$

Just like for the $\ell \geq 1$ modes we impose the boundary condition that the solution vanish at the conformal boundary located at $r_* = 0$. This gives the following solution the the forbidden region:

$$\psi_{II}(r_*) = \frac{A\sqrt{-r_*}}{\alpha} \left[J_1 \left(\frac{2i\alpha}{\sqrt{-r_*}} \right) + iY_1 \left(\frac{2i\alpha}{\sqrt{-r_*}} \right) \right]. \tag{C.21}$$

Patching the solutions in the two regions at the turning point r_*^{tp} by requiring $\psi_I(r_*^{tp}) = \psi_{II}(r_*^{tp})$ allows us to fix the constant A. To find the power law decay we analyze how the amplitude of the solution decays from the turning point to the screen in a similar manner to what we did for the $\ell \geq 1$ mode. In particular, the fraction of radiation that gets to the screen is given by:

$$\begin{aligned} T_0^2 &= \left| \frac{\psi_{II}(r_*^{screen})}{\psi_{II}(r_*^{tp})} \right|^2 \\ r_*^{screen} &= \frac{-2}{\delta r f''_{ext}(r_s)} \\ r_*^{tp}(\omega) &= -\left(\frac{2(d-1)}{\omega^2 r_s f''_{ext}(r_s)} \right)^{1/3}. \end{aligned} \tag{C.22}$$

We define $\omega = \epsilon\omega_{min,0}$ where $0 \leq \epsilon \leq 1$ and:

$$\begin{aligned}\omega_{min,0} &= \eta\frac{\delta r f''_{ext}(r_s)}{2}\\ \eta &= \left(\frac{(d-1)\delta r}{r_s}\right)^{1/2} \ll 1,\end{aligned} \tag{C.23}$$

$\omega_{min,0}$ is the minimal frequency in which waves would reach the screen without encountering the angular momentum barrier for $\ell = 0$. We can then write T_0^2 as:

$$T_0^2 = \epsilon^{2/3}\left|\frac{J_1(2i\eta) + iY_1(2i\eta)}{J_1(2i\eta\epsilon^{1/3}) + iY(2i\eta\epsilon^{1/3})}\right|^2 \simeq \epsilon^{4/3}\left[1 + \mathcal{O}\left(\eta^2\right)\right] \sim \epsilon^{4/3}. \tag{C.24}$$

So for the $\ell = 0$ mode the generalized greybody factor in our toy model will be:

$$\gamma_0(\omega, \delta r) = \Theta(\omega - \omega_{min,0}) + \left(\frac{\omega}{\omega_{min,0}}\right)^{4/3}\Theta(\omega_{min,0} - \omega). \tag{C.25}$$

C.3 Integrals Describing Evaporation rate in Near Extremal Regime

In this section we go over the assumptions to arrive at the series expression for the evaporation rate given by Eq. (4.30). We need to compute the integrals in Eq. (4.29).

We approximate the values of these integrals under the assumption that $\beta\omega_{min,\ell} \gg 1$ (i.e. we are sufficiently close to the extremal regime). Lets begin with the first term(s) in Eq. (4.29) which describes modes with $\omega \leq \omega_{min,\ell}$. The term(s) read:

$$\begin{aligned}&\frac{N_b}{2\pi}\sum_{\ell=1}^{\infty}\omega_{min,\ell}^2 N_\ell\int_0^1\frac{\epsilon^{2(\nu_\ell+1)}}{e^{\beta\omega_{min,\ell}\epsilon} - 1}d\epsilon = \frac{N_b}{2\pi}\sum_{\ell=1}^{\infty}\omega_{min,\ell}^2 N_\ell\int_0^1\frac{\epsilon^{2+\sqrt{1+4\alpha_\ell^2}}}{\exp\left(\frac{\beta\delta r f''_{ext}(r_s)\alpha_\ell\epsilon}{2}\right) - 1}d\epsilon\\ &= \frac{N_b\delta r^2\left[f''_{ext}(r_s)\right]^2}{8\pi}\sum_{\ell=1}^{\infty}N_\ell\int_0^1\frac{\alpha_\ell^2\epsilon^{2+\sqrt{1+4\alpha_\ell^2}}}{\exp\left(\frac{\beta\delta r f''_{ext}(r_s)\alpha_\ell\epsilon}{2}\right) - 1}d\epsilon.\end{aligned} \tag{C.26}$$

Note that the integrand will generally have a local maximum. In particular, as long as $\beta\delta r f''_{ext}(r_s)$ is sufficiently large (this is true when we are sufficiently close to extremality) we

are guaranteed to have a sharply peaked local maximum within the interval of integration. This means that we can easily extend the range of integration from $\epsilon \in (0,1)$ to $\epsilon \in (0,\infty)$ and still have a good estimate on the value of the integral. Such an integral can be done in full generality shown below:

$$\begin{aligned}&\int_0^1 \frac{\alpha_\ell^2 \epsilon^{2+\sqrt{1+4\alpha_\ell^2}}}{\exp\left(\frac{\beta\delta r f''_{ext}(r_s)\alpha_\ell \epsilon}{2}\right)-1} d\epsilon \approx \int_0^\infty \frac{\alpha_\ell^2 \epsilon^{2+\sqrt{1+4\alpha_\ell^2}}}{\exp\left(\frac{\beta\delta r f''_{ext}(r_s)\alpha_\ell \epsilon}{2}\right)-1} d\epsilon \\ &= \alpha_\ell^2 \left(\frac{\beta\delta r f''_{ext}(r_s)\alpha_\ell}{2}\right)^{-3-\sqrt{1+4\alpha_\ell^2}} \Gamma\left(3+\sqrt{1+4\alpha_\ell^2}\right) Li_{3+\sqrt{1+4\alpha_\ell^2}}(1)\,.\end{aligned} \tag{C.27}$$

Now we will deal with the second term(s) in Eq. (4.29) which describes modes with $\omega > \omega_{min,\ell}$ the terms read:

$$\begin{aligned}&\frac{N_b}{2\pi}\sum_{\ell=1}^\infty \omega_{min,\ell}^2 N_\ell \int_1^\infty \frac{\epsilon}{e^{\beta\omega_{min,\ell}\epsilon}-1} d\epsilon \\ &= \frac{N_b}{2\pi\beta^2}\sum_{\ell=1}^\infty N_\ell \left[Li_2\left(e^{-\beta\omega_{min,\ell}}\right) - \beta\omega_{min,\ell}\ln\left(1-e^{-\beta\omega_{min,\ell}}\right)\right].\end{aligned} \tag{C.28}$$

Combing these results give us the series representation of the evaporation rate given in Eq. (4.30).

C.4 The Contribution to Evaporation Rate of Tunneling vs Non-Tunneling modes in Near Extremal Regime

In this appendix we will discuss the relative size between the terms $S_{tun,\ell}$ and $S_{ntun,\ell}$ which are used to define the evaporation rate of a near extremal AdS RN black hole. The goal is to estimate the following ratio:

$$\begin{aligned}\frac{S_{ntun,\ell}}{S_{tun,\ell}} &= \frac{\left[Li_2\left(e^{-x_{min,\ell}}\right) - x_{min,\ell}\ln\left(1-e^{-x_{min,\ell}}\right)\right] x_{min,\ell}^{1+\sqrt{1+4\alpha_\ell^2}}}{\Gamma\left(3+\sqrt{1+4\alpha_\ell^2}\right) Li_{3+\sqrt{1+4\alpha_\ell^2}}(1)} \\ &\approx \frac{x_{min,\ell}^{2+\sqrt{1+4\alpha_\ell^2}} e^{-x_{min,\ell}}}{\Gamma\left(3+\sqrt{1+4\alpha_\ell^2}\right) Li_{3+\sqrt{1+4\alpha_\ell^2}}(1)},\end{aligned} \tag{C.29}$$

where in the last line we used $x_{min,\ell} \gg 1$ since we are in the near extremal regime. For a fixed ℓ we can see that the ratio $S_{ntun,\ell}/S_{tun,\ell} \ll 1$ due to the exponential suppression and it follows that $S_{ntun,\ell} \ll S_{tun,\ell}$ when we are sufficiently close to the extremal regime. This is why we use the approximation in Eq. (4.31) and ignore the modes that do not tunnel.

C.5 Analysis of the Evaporation Rates of Near Extremal Very Large AdS RN Black Holes

We discuss approximating the integrand in Eq. (4.33) which is given by:

$$\begin{aligned} I_\ell = &\left(\frac{\alpha_\ell r_s^2 f''_{ext}(r_s)}{(d-2)\sqrt{1+\frac{2r_s^2 f''_{ext}(r_s)\alpha_\ell^2}{(d-2)^2}}}\right)\left(\frac{d-2}{2}\left[-1+\sqrt{1+\frac{2r_s^2 f''_{ext}(r_s)\alpha_\ell^2}{(d-2)^2}}\right]\right)^{d-2} \\ &\times\left[\frac{\Gamma\left(3+\sqrt{1+4\alpha_\ell^2}\right) Li_{3+\sqrt{1+4\alpha_\ell^2}}(1)}{\left(\frac{\beta\delta r f''_{ext}(r_s)\alpha_\ell}{2}\right)^{1+\sqrt{1+4\alpha_\ell^2}}}\right]. \end{aligned} \tag{C.30}$$

When α_ℓ is close to zero one will find that the integrand initially grows. This growth will eventually slow down and stop when α_ℓ is sufficiently large and the integrand will decay. A conventional leading order expansion of the integrand in the small or large α_ℓ regime will not be able to capture this behavior. We make the following approximations, the product of the first two terms is approximated in the large α_ℓ regime to give:

$$\begin{aligned} &\left(\frac{\alpha_\ell r_s^2 f''_{ext}(r_s)}{(d-2)\sqrt{1+\frac{2r_s^2 f''_{ext}(r_s)\alpha_\ell^2}{(d-2)^2}}}\right)\left(\frac{d-2}{2}\left[-1+\sqrt{1+\frac{2r_s^2 f''_{ext}(r_s)\alpha_\ell^2}{(d-2)^2}}\right]\right)^{d-2} \\ &\approx \left(\frac{r_s^2 f''_{ext}(r_s)}{2}\right)^{\frac{d-1}{2}} \alpha_\ell^{d-2}. \end{aligned} \tag{C.31}$$

Even though this approximation is more accurate for larger α_ℓ one can plot the approximation and compare to the exact function and find reasonable agreement at small values of α_ℓ.

We approximate the terms in the second line with:

$$\left[\frac{\Gamma\left(3+\sqrt{1+4\alpha_\ell^2}\right) Li_{3+\sqrt{1+4\alpha_\ell^2}}(1)}{\left(\frac{\beta\delta r f''_{ext}(r_s)\alpha_\ell}{2}\right)^{1+\sqrt{1+4\alpha_\ell^2}}}\right] \approx \frac{\pi^4}{15}\left(\frac{\beta\delta r f''_{ext}(r_s)}{2}\right)^{-2-2\alpha_\ell^2}\alpha_\ell^{-2}. \tag{C.32}$$

Combining these gives:

$$I_\ell \approx \frac{\pi^4}{15}\left(\frac{r_s^2 f''_{ext}(r_s)}{2}\right)^{\frac{d-1}{2}}\left(\frac{\beta\delta r f''_{ext}(r_s)}{2}\right)^{-2-2\alpha_\ell^2}\alpha_\ell^{d-4}. \tag{C.33}$$

To get a sense of how the approximation compares to the full function we make various plots shown in Figure C.1 by fixing the values of $\frac{\beta\delta r}{r_s^2}$, $\frac{r_s}{L}$, and d. We can see that the approximation becomes worse as we increase d. However, even for larger values of d doing the integral of the approximated integrand will give a result that is off by a order one prefactor from the exact result. The approximation improves in the limit when $r_s/L \to \infty$ as we can see in the following plots in Figure C.2 where we increase r_s/L from 10^2 to 10^{50}:

C.6 Treating the $\ell = 0$ Mode in the Near Extremal Regime

Using the generalized greybody factor given by Eq. (C.25) the contribution to the evaporation rate of a near extremal AdS RN black hole is given by computing the following integrals:

$$\begin{aligned}\left.\frac{dM}{dt}\right|_{\ell=0} &= \frac{N_b}{2\pi}\left[\int_0^{\omega_{min,0}}\frac{\omega}{e^{\beta\omega}-1}\left(\frac{\omega}{\omega_{min,0}}\right)^{4/3}d\omega + \int_{\omega_{min,0}}^{\infty}\frac{\omega}{e^{\beta\omega}-1}d\omega\right] \\ &= \frac{N_b\omega_{min,0}^2}{2\pi}\left[\int_0^1\frac{\epsilon^{10/3}}{e^{\beta\omega_{min,0}\epsilon}-1}d\epsilon + \int_1^{\infty}\frac{\epsilon}{e^{\beta\omega_{min,0}\epsilon}-1}d\epsilon\right].\end{aligned} \tag{C.34}$$

Similar to the $\ell \geq 1$ modes, when $\beta\omega_{min,0} \gg 1$ we can extend the integration limits over the interval $(0,1)$ to $(0,\infty)$ without changing the value of the result. When we do this we will obtain the following evaporation rate from the $\ell = 0$ channel:

$$\left.\frac{dM}{dt}\right|_{\ell=0} = \frac{N_b}{2\pi\beta^2}\left[\frac{\Gamma\left(\frac{13}{3}\right)\zeta\left(\frac{13}{3}\right)}{\left(\beta\omega_{min,0}\right)^{7/3}} + Li_2\left(e^{-\beta\omega_{min,0}}\right) - \beta\omega_{min,0}\ln\left(1-e^{\beta\omega_{min,0}}\right)\right], \tag{C.35}$$

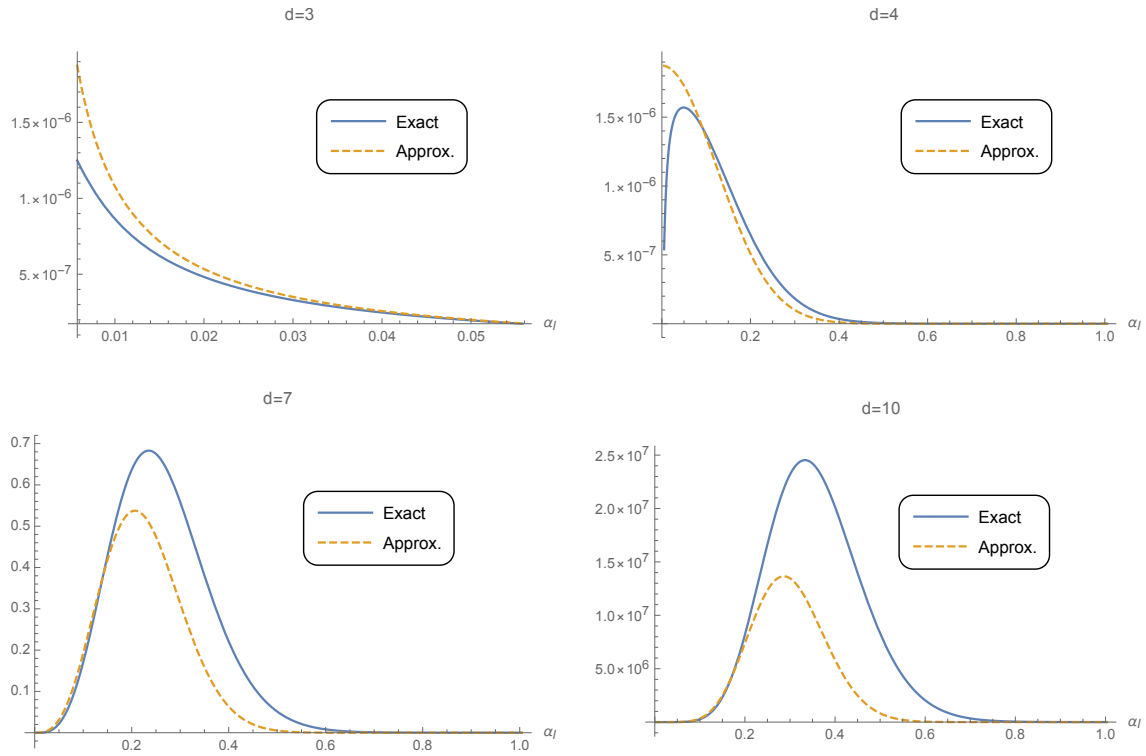

Figure C.1: $\frac{\beta\delta r}{r_s^2} = 100$ and $r_s/L = 100$.

where $\Gamma(13/3)\,\zeta(13/3) \approx 9.84$. Close to the extremal regime the primary contribution comes from the first term just like for modes $\ell \geq 1$. So we have:

$$\left.\frac{dM}{dt}\right|_{\ell=0} \approx \frac{N_b}{2\pi\beta^2}\Gamma(13/3)\,\zeta(13/3)\left[\left(\frac{(d-1)\delta r}{r_s}\right)^{1/2}\frac{\beta\delta r f''_{ext}(r_s)}{2}\right]^{-7/3}. \tag{C.36}$$

Now that we have the $\ell = 0$ contribution to the evaporation rate it is interesting to ask how large of an effect it has on the evaporation rate if we include it.

For large AdS black holes we estimated the evaporation rate contribution from modes with $\ell \geq 1$. We found that the evaporation rate went as β^{-4} (perhaps with some $\ln(\beta)$ dependence which we can ignore if β is sufficiently large.). If we look at the β dependence of the $\ell = 0$ contribution to the evaporation rate is it goes as $\beta^{-13/3}$. In the extremal limit when $\beta \to \infty$ the $\ell = 0$ mode's contribution to the evaporation rate will decay more quickly than the total contribution of the modes $\ell \geq 1$. So sufficiently close to the extremal

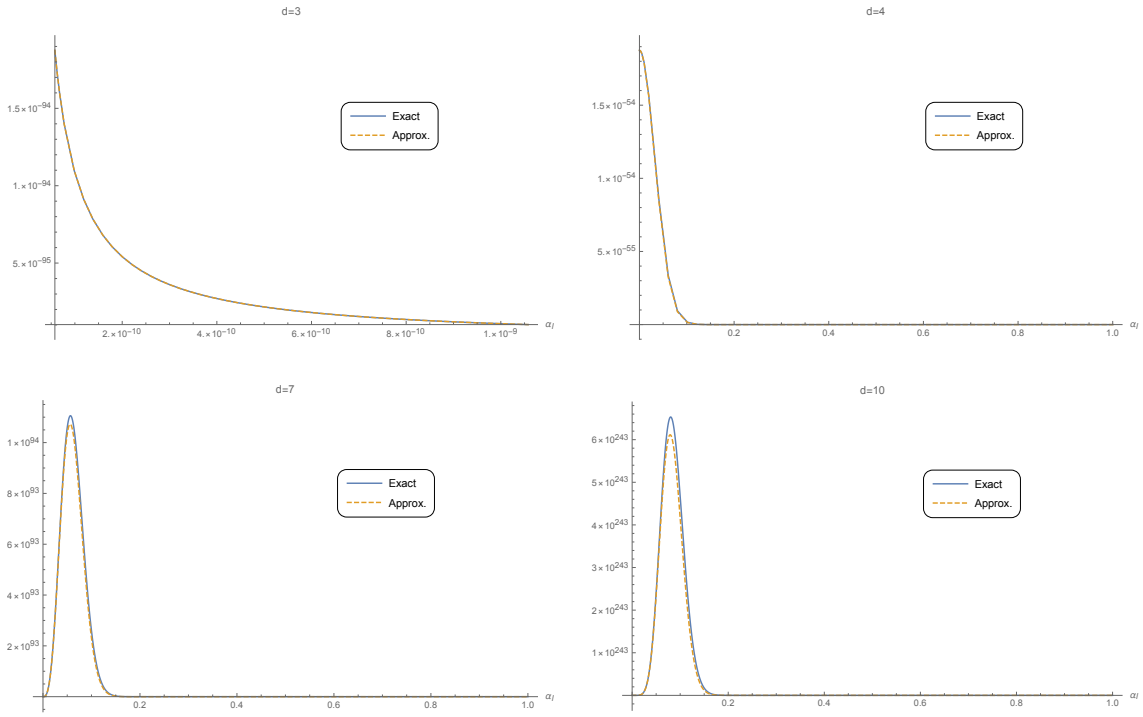

Figure C.2: $\frac{\beta\delta r}{r_s^2} = 100$ and $r_s/L = 10^{50}$.

regime for very large AdS black holes we can effectively ignore the contribution of the the $\ell = 0$ mode since it will be a sub-leading correction. This is also what happened in the case of AdS Schwarzschild black holes (assuming we placed the screen sufficiently close to the horizon).

For very small AdS black holes (or asymptotically flat black holes) we can consider the ratio between the $\ell = 1$ mode evaporation rate (given by Eq. (4.39)) and the $\ell = 0$ evaporation rate (given by Eq. (C.36)) which is given by:

$$\frac{\left.\frac{dM}{dt}\right|_{\ell=0}}{\left.\frac{dM}{dt}\right|_{\ell=1}} = \frac{\Gamma\left(13/3\right)\zeta\left(13/3\right)\left[(d-1)(d-2)^2\right]^{\frac{d-1}{d-2}}}{\left[(d-1)^{1/2}(d-2)^2\right]^{7/3}\Gamma\left(\frac{2(2d-3)}{d-2}\right)Li_{\frac{2(2d-3)}{d-2}}(1)}\left(\frac{r_s}{\delta r}\right)^{7/4}\left(\frac{r_s^2}{\beta\delta r}\right)^{\frac{d-8}{3(d-2)}} \sim \beta^{-\frac{d-8}{3(d-2)}}. \tag{C.37}$$

We can see that if $d < 8$ then $\ell = 0$ mode will dominate sufficiently close to the extremal regime and if $d > 8$ then the $\ell = 1$ mode will dominate sufficiently close to the extremal regime. Lets consider what happens when $d < 8$. For $\ell = 0$ mode we require $\beta\omega_{min,0} \gg 1 \Rightarrow \frac{\delta r}{r_s} \gg \left(\frac{r_s}{\beta}\right)^{2/3}$. We define Λ such that $\frac{\delta r}{r_s} = \Lambda \left(\frac{r_s}{\beta}\right)^{2/3}$ then the evaporation rate can be expressed as:

$$\frac{dM}{dt} \sim \frac{N_b}{\beta^2 \Lambda^{7/2}}. \tag{C.38}$$

Using this result we can express the information re-emergence time as:

$$t_{emerge} \sim \frac{\beta}{2\pi} \ln\left(\Lambda^{7/2} \frac{r_s^{d-1}}{\ell_p^{d-1}}\right). \tag{C.39}$$

We fix the β dependence of Λ by fixing the proper distance (which we denote as l_{prop}) between the screen and horizon. This means $\Lambda \sim \left(\frac{r_s}{\beta}\right)^{1/3} \left(\frac{l_{prop}}{r_s}\right)^2$. Then we find:

$$t_{emerge} \sim \frac{\beta}{2\pi} \left[\ln\left(\left(\frac{r_s}{\beta}\right)^{7/6} \frac{r_s^{d-1}}{\ell_p^{d-1} N_b}\right) + 2\ln\left(\frac{l_{prop}}{r_s}\right)\right]. \tag{C.40}$$

This shows that the even when $\ell = 0$ dominates we still get results for the information re-emergence time that are comparable to the results we obtained in cases where the $\ell = 1$ mode was dominant. The main change is the power that the combination r_s/β comes with, which is 7/6 rather than 1. As before, the sub-leading log term contains information about how far from the horizon the screen is placed. So we again get results consistent with known literature on the scrambling time of near extremal black holes.

C.7 Derivation of the Stress Energy Tensor of the Screen

In Section 4.4.1 we suggested that generalized greybody factors discussed in this paper can be understood in terms of a transmission coefficient for an effective potential given in Eq. (4.70). We stated that such a potential would be obtained by cutting off the geometry of the AdS black hole where the screen would be, we would then glue an exterior space which acts as a storage system for the radiation. By requiring this gluing to satisfy the Einstein field equations with some matter distribution, then there will generally be a singular matter distribution at the interface where the gluing occurs. In our setup the singular matter will

lie on a spherical shell where the screen would be. The problem of finding the stress energy tensor of such a shell is a well studied problem whose solution is stated in terms of Israel junction conditions [77] (see [119] for a review). The starting point is to write down the metrics both inside and outside the shell. We will utilize a hyperspherical coordinate system $x^\mu = (t, r, \phi^1, ..., \phi^{d-1})$. This coordinate sytem will be used both inside and outside the shell. In these coordinates the shell is at a fixed at $r = r_0 = const$. The metric inside the shell will be given by:

$$g^-_{\mu\nu} = -f_-(r)\delta^t_\mu\delta^t_\nu + f_-(r)^{-1}\delta^r_\mu\delta^r_\nu + r^2 g^\Omega_{IJ}\delta^I_\mu\delta^J_\nu, \tag{C.41}$$

where $I, J = 1, 2, ..., d-1$ are angular indices and g^Ω_{IJ} is the (diagonal) metric on a $d-1$ - unit sphere. The "$-$" sub-indices and super-indices indicate that we are dealing with tensors inside the shell ($r < r_0$). Analogously, we take the metric outside the shell to be:

$$\begin{aligned} g^+_{\mu\nu} &= -\Delta(r_0)f_+(r)\delta^t_\mu\delta^t_\nu + f_+(r)^{-1}\delta^r_\mu\delta^r_\nu + r^2 g^\Omega_{IJ}\delta^I_\mu\delta^J_\nu \\ \Delta(r_0) &= \frac{f_-(r_0)}{f_+(r_0)}, \end{aligned} \tag{C.42}$$

where the "$+$" sub-indices and super-indices indicate that we are dealing with tensors outside the shell ($r > r_0$). The additional time lapse constant $\Delta(r_0)$ is introduced so that the induced metric on both sides of the shell is the same in "natural" induced coordinates $y^a = (t, \phi^1, ..., \phi^{d-1})$. It is given as:

$$h_{ab} = \frac{\partial x^\mu}{\partial y^a}\frac{\partial x^\nu}{\partial y^b} g^\pm_{\mu\nu}\bigg|_{r=r_0} = \delta^\mu_a\delta^\nu_b g^\pm_{\mu\nu} = -f(r_0)\delta^t_a\delta^t_b + r_0^2 g^\Omega_{IJ}\delta^I_a\delta^J_b. \tag{C.43}$$

The stress energy tensor of the shell denoted S_{ab} is related to the discontinuity in the extrinsic curvature tensor and its trace on either side of the $r = r_0$ hypersurface. More specifically, we have[1]:

$$S_{ab} = -\frac{1}{8\pi}\left([K_{ab}] - [K]h_{ab}\right), \tag{C.44}$$

above the notation $[T]$ for any tensor T is defined as:

$$[T] = \lim_{r\to r_0} T^+ - \lim_{r\to r_0} T^-. \tag{C.45}$$

[1] In the formula below we assume that hypersurface is timelike.

So we need to calculate the extrinsic curvature on either side of the hypersurface, which is defined in terms of the covariant derivative of the normalized unit vector to the timelike hypersurface $r = r_0$:

$$K^{\pm}_{ab} = \delta^{\mu}_{a}\delta^{\nu}_{b}\nabla^{\pm}_{\mu}n^{\pm}_{\nu}. \tag{C.46}$$

Here, $\nabla^{\pm}_{\mu}$ is the covariant derivative with respect to the metrics, $g^{\pm}_{\mu\nu}$, on either side of the shell. The trace is simply given by:

$$K^{\pm} = h^{ab}K^{\pm}_{ab}. \tag{C.47}$$

The normal vector to a constant r hypersurface outside the shell is:

$$n^{+}_{\mu} = f_{+}(r)^{-1/2}\delta^{r}_{\mu}. \tag{C.48}$$

The normal vector to a constant r hypersurface inside the shell is:

$$n^{-}_{\mu} = f_{-}(r)^{-1/2}\delta^{r}_{\mu}. \tag{C.49}$$

Using these expressions we will find that:

$$\begin{aligned}
K^{+}_{ab} &= -\frac{1}{2}f_{-}(r_0)f_{+}(r_0)^{-1/2}f'_{+}(r_0)\delta^{t}_{a}\delta^{t}_{b} + r_0 f_{+}(r_0)^{1/2}g^{\Omega}_{IJ}\delta^{I}_{a}\delta^{J}_{b} \\
K^{-}_{ab} &= -\frac{1}{2}f_{-}(r_0)^{1/2}f'_{-}(r_0)\delta^{t}_{a}\delta^{t}_{b} + r_0 f_{-}(r_0)^{1/2}g^{\Omega}_{IJ}\delta^{I}_{a}\delta^{J}_{b} \\
K^{+} &= \frac{1}{2}f_{+}(r_0)^{-1/2}f'_{+}(r_0) + (d-1)r_0^{-1}f_{+}(r_0)^{1/2} \\
K^{-} &= \frac{1}{2}f_{-}(r_0)^{-1/2}f'_{-}(r_0) + (d-1)r_0^{-1}f_{-}(r_0)^{1/2}.
\end{aligned} \tag{C.50}$$

Using these expressions and plugging into Eq. (C.44) gives:

$$\begin{aligned}
16\pi S_{ab} = &-\frac{2(d-1)f_{-}(r_0)\left(f_{+}(r_0)^{1/2} - f_{-}(r_0)^{1/2}\right)}{r_0}\delta^{t}_{a}\delta^{t}_{b} \\
&+ \left[2(d-2)\left(f_{+}(r_0)^{1/2} - f_{-}(r_0)^{1/2}\right) + \frac{r_0 f'_{+}(r_0)}{f_{+}(r_0)^{1/2}} - \frac{r_0 f'_{-}(r_0)}{f_{-}(r_0)^{1/2}}\right] r_0 g^{\Omega}_{IJ}\delta^{I}_{a}\delta^{J}_{b}.
\end{aligned} \tag{C.51}$$

It is convenient to define the following basis on the shell:

$$\begin{aligned}\hat{e}_t^a &= \frac{\delta_t^a}{\sqrt{f_-(r_0)}} \\ \hat{e}_I^a &= \frac{\sqrt{g_\Omega^{II}}}{r_0}\delta_I^a,\end{aligned} \tag{C.52}$$

which allows us to write the inverse induced metric as:

$$h^{ab} = \eta^{cd}\hat{e}_c^a\hat{e}_d^b = -\hat{e}_t^a\hat{e}_t^b + \sum_{I=1}^{d-1}\hat{e}_I^a\hat{e}_I^b. \tag{C.53}$$

Using this basis we can see the stress energy tensor of the shell is that of a d - dimensional perfect fluid given by:

$$\begin{aligned}S^{ab} &= \rho\hat{e}_t^a\hat{e}_t^b + p\sum_I \hat{e}_I^a\hat{e}_I^b = (\rho+p)\,\hat{e}_t^a\hat{e}_t^b + ph^{ab} \\ \rho &= \frac{(d-1)\left(f_-(r_0)^{1/2} - f_+(r_0)^{1/2}\right)}{8\pi r_0} \\ p &= \frac{1}{16\pi r_0}\left[2(d-2)\left(f_+(r_0)^{1/2} - f_-(r_0)^{1/2}\right) + r_0\left(\frac{f_+'(r_0)}{f_+(r_0)^{1/2}} - \frac{f_-'(r_0)}{f_-(r_0)^{1/2}}\right)\right],\end{aligned} \tag{C.54}$$

where ρ is the energy density of the shell and p is the principle pressure. This completes our derivation of the stress energy tensor of a shell that allows for the gluing two spherically symmetric static spacetimes along the interface $r = r_0$. This will be used in the discussion of energy conditions of the shell.

C.8 Null Energy Condition of the Screen

In Appendix C.7, we derived a solution to the Einstein equation which represented the gluing of two different spherically symmetric solutions to the Einstein equation along a timelike hypersurface $r = r_0$ where our "absorptive" screen would be placed[2]. To have a consistent patching it is required that there be a thin shell of matter with a stress energy

[2]The reason for quotation marks is that the radiation is not actually absorbed by the screen, but rather leaks into the exterior flat or AdS space.

tensor given by Eq. (C.54). It is interesting to ask if such a shell will satisfy energy conditions.

In particular, we are interested in the null energy condition (NEC). The NEC states that for any future directed null vector k^μ one has:

$$T_{\mu\nu}k^\mu k^\nu \geq 0. \tag{C.55}$$

If we restrict ourselves to null vectors with no radial component then NEC simply becomes:

$$\rho + p \geq 0. \tag{C.56}$$

On the other hand, considering a purely radial null vector is more subtle since the rr component of the metric is discontinuous across the shell, and we should consider what happens on each side separately. The null vector will be given by:

$$k^\mu_\pm = c_\pm \left[\delta^\mu_t + \left(\frac{-g^\pm_{tt}}{g^\pm_{rr}} \right)^{1/2} \delta^\mu_r \right]. \tag{C.57}$$

If the radial null vector is to be future directed then $c_\pm \geq 0$. Since the stress energy tensor of the shell has no radial component we see that the null energy condition for a radial null vector becomes:

$$\rho \geq 0, \tag{C.58}$$

which is to say that the matter on the shell has a positive energy density. Now let us consider interior metric to be that of a Schwarzschild AdS black hole:

$$f_-(r) = 1 + \frac{r^2}{L_-^2} - \left(\frac{r_H}{r} \right)^{d-2} \left(1 + \frac{r_H^2}{L_-^2} \right). \tag{C.59}$$

The exterior metric will be chosen to be that of pure AdS[3]:

$$f_+(r) = 1 + \frac{r^2}{L_+^2}. \tag{C.60}$$

[3]The reader might be wondering why we choose pure AdS rather than flat space as we suggested in Section 4.4.1. The reason is that we want to have a well defined holographic description of the exterior system where the radiation is stored. The flat space limit can be obtained by sending L_+ to infinity. The advantage of using pure AdS rather than flat space from the beginning is that we can control how much separation there is between the shell and the exterior conformal boundary, the larger L_+ is the further we push the conformal boundary away from the screen.

Before analyzing whether it is possible to have $\rho \geq 0$ we will consider what happens to the energy density of the screen as we approach the horizon and the conformal boundary. At the horizon the the energy density of the screen takes on a negative value given by:

$$\rho(r_0 = r_H) = -\frac{d-1}{8\pi r_H}\sqrt{1+\frac{r_H^2}{L_+^2}}. \tag{C.61}$$

As the screen gets closer to the conformal boundary the energy density will saturate to the following constant:

$$\lim_{r_0\to\infty}\rho = \frac{d-1}{8\pi}\left(\frac{1}{L_-}-\frac{1}{L_+}\right). \tag{C.62}$$

From this we see that the radial NEC is always violated at the horizon but if $L_- \leq L_+$ then the radial NEC is satisfied as the screen approaches the conformal boundary. Now we will discuss the constraint of the energy density being non-negative. It will read:

$$\sqrt{1+\frac{r_0^2}{L_-^2}-\left(\frac{r_H}{r_0}\right)^{d-2}\left(1+\frac{r_H^2}{L_-^2}\right)} \geq \sqrt{1+\frac{r_0^2}{L_+^2}}. \tag{C.63}$$

Under the assumption that $r_0 > r_H$ we can square the expressions on both sides of the inequality to obtain the following simplified constraint:

$$\frac{1}{L_-^2}-\frac{1}{L_+^2}-\frac{1}{r_H^2}\left(\frac{r_H}{r_0}\right)^d\left(1+\frac{r_H^2}{L_-^2}\right) \geq 0. \tag{C.64}$$

We already know the radial NEC will be satisfied for a screen at the conformal boundary if $L_+ \geq L_-$. Furthermore, we also know that if screen is placed arbitrarily close to the horizon the radial NEC will be violated. From these considerations there must be a critical radius where the screen will saturate the radial NEC and the energy density will vanish. This is easily found and given by:

$$r_c = r_H\left(\frac{1+\frac{L_-^2}{r_H^2}}{1-\frac{L_-^2}{L_+^2}}\right)^{\frac{1}{d}}. \tag{C.65}$$

It is also interesting to consider how the energy density of the screen changes as we move the screen closer to the conformal boundary by considering $d\rho/dr_0 \geq 0$ for any radial coordinate outside the horizon. The expression for the derivative is given by:

$$\begin{aligned}\frac{d\rho}{dr_0} &= \frac{d-1}{8\pi r_0^2}\left[\frac{r_0 f_-'(r_0)}{2\sqrt{f_-(r_0)}} - \frac{r_0 f_+'(r_0)}{2\sqrt{f_+(r_0)}} - \sqrt{f_-(r_0)} + \sqrt{f_+(r_0)}\right] \\ &= \frac{(d-1)\xi(r_0)}{8\pi r_0^2\sqrt{f_-(r_0)f_+(r_0)}} \\ \xi(r_0) &= \sqrt{f_+(r_0)}\left(\frac{r_0 f_-'(r_0)}{2} - f_-(r_0)\right) + \sqrt{f_-(r_0)}\left(f_+(r_0) - \frac{r_0 f_+'(r_0)}{2}\right).\end{aligned} \tag{C.66}$$

The sign of the derivative depends on $\xi(r_0)$. By plugging in the expressions for $f_+(r_0)$ and $f_-(r_0)$ we will find that:

$$\begin{aligned}\xi(r_0) &= \sqrt{1+\frac{r_0^2}{L_+^2}}\left[-1+\frac{d}{2}\left(\frac{r_H}{r_0}\right)^{d-2}\left(1+\frac{r_H^2}{L_-^2}\right)\right] + \sqrt{1+\frac{r_0^2}{L_-^2}-\left(\frac{r_H}{r_0}\right)^{d-2}\left(1+\frac{r_H^2}{L_-^2}\right)} \\ &> \sqrt{1+\frac{r_0^2}{L_-^2}-\left(\frac{r_H}{r_0}\right)^{d-2}\left(1+\frac{r_H^2}{L_-^2}\right)} - \sqrt{1+\frac{r_0^2}{L_+^2}} = \frac{8\pi r_0\rho}{d-1}.\end{aligned} \tag{C.67}$$

We have a strict inequality since $r_0 < \infty$ (saturation occurs in limit as $r_0 \to \infty$):

$$\frac{d\rho}{dr_0} > \frac{\rho}{r_0\sqrt{f_+(r_0)f_-(r_0)}}. \tag{C.68}$$

This implies that at any point where the radial NEC is satisfied the energy density must increase within a neighborhood of that point. This is enough to show that for $r_0 \geq r_c$ the energy density must strictly increase. In Figure C.3 we plot of the energy density of the screen to illustrate the monotone increase of energy density.

Now that we have explored when the NEC is violated for radial null vectors we can move on to understanding the NEC for tangent null vectors (i.e. null vectors with no radial component). In this case we must understand the condition $\rho + p \geq 0$. Before doing this lets consider what happens to this combination as we approach the horizon and as we approach infinity. As we approach the horizon we have:

$$\lim_{r_0 \to r_H}(\rho + p) = -\infty. \tag{C.69}$$

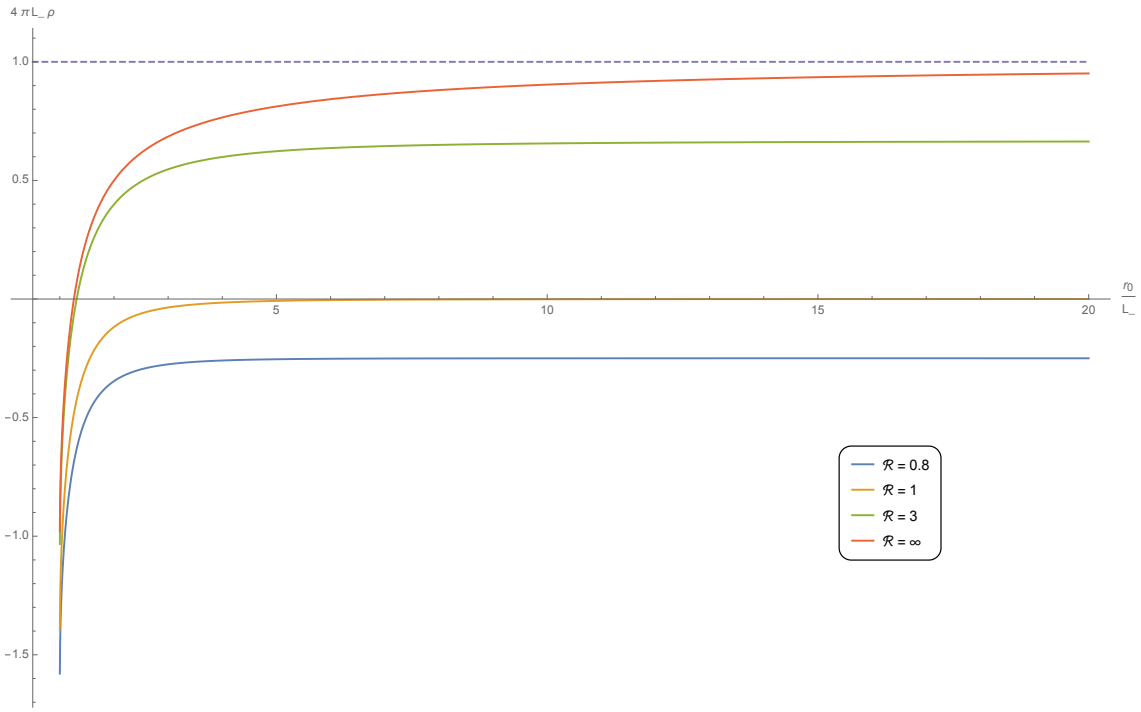

Figure C.3: Above is a plot of the energy density of the screen as a function of its placement for the case when $d = 3$ and $r_H/L_- = 1$. Each solid line is a plot of the energy density of the screen in units of the interior AdS radius, L_- for different choices of the ratio $\mathcal{R} = L_+/L_-$. We can see that all the lines start at $r_0/L_- = 1$ which is where the horizon of the black hole is. At $r_0/L_- = 1$ the energy density given by Eq. (C.61) and will be negative. All the lines then increase monotonically and will saturate to a value given by Eq. (C.62) at infinity. For cases when $\mathcal{R} < 1$ the energy density at the conformal boundary will saturate to a negative value. When $\mathcal{R} = 1$ the energy density is always negative and saturates to zero at the conformal boundary. When $\mathcal{R} > 1$ the energy density is positive if $r_0 > r_c$ where r_c is given by Eq. (C.65). The red curve corresponding to the limit when $\mathcal{R} = \infty$ represents the case when we patch a flat exterior metric at the screen interface and the dotted line is the value the energy density will saturate to at infinity. The main features of the energy density as illustrated in this plot remain intact if we consider higher dimensions and different values of r_H/L_-.

When we take the screen to infinity it can be shown that $\rho + p$ goes to zero with the

following leading order behaviour:

$$\rho + p = \frac{L_- - L_+}{8\pi r_0^2} + \mathcal{O}\left(\frac{1}{r_0^4}\right). \tag{C.70}$$

This means that if $L_+ > L_-$ then for sufficiently large r_0 the sum of the energy density and pressure is negative. If $L_+ < L_-$ the for sufficiently large r_0 the sum of the energy density and pressure is positive. Similar to the radial NEC, we see that there is a violation of the tangent NEC close to the horizon and a saturation at infinity. The divergent violation at the horizon comes from the pressure given by Eq. (C.54) due to the fact that $f_-(r_H) = 0$. Now that we understand what happens close to the horizon and infinity we will consider the constraint more generally. In terms of f_+ and f_-, it is given by the following inequality:

$$\rho + p = \frac{1}{16\pi r_0}\left[2\left(f_-(r_0)^{1/2} - f_+(r_0)^{1/2}\right) + r_0\left(\frac{f_+'(r_0)}{f_+(r_0)^{1/2}} - \frac{f_-'(r_0)}{f_-(r_0)^{1/2}}\right)\right] \geq 0. \tag{C.71}$$

It is difficult to make further progress analytically like we did for understanding the radial NEC. Therefore, we will resort to making plots for $\rho + p$ in Eq. (C.71) and make some general comments.

From Figure C.4 we can see that if $L_+ \geq L_-$ then the tangential NEC is violated for all $r_0 \in (r_H, \infty)$.

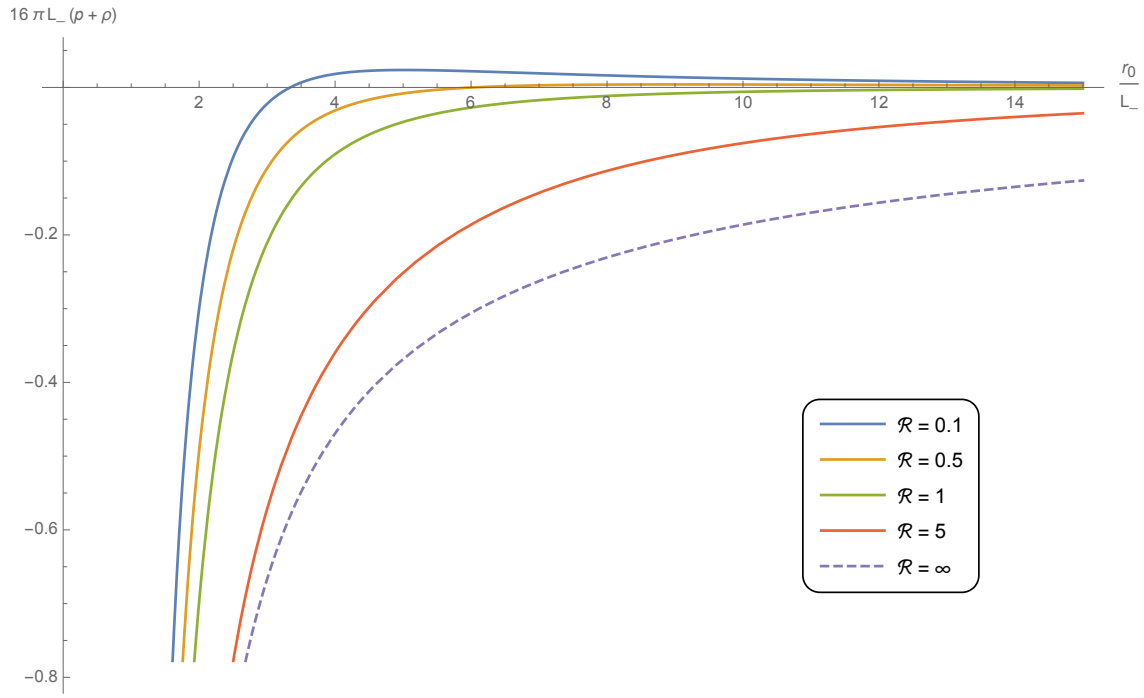

Figure C.4: Above is a plot of the sum of the energy density and pressure (i.e. $\rho+p$) of the screen as a function of its radial placement for the case when $d = 3$ and $r_H/L_- = 1$. Each solid line is a plot of the energy density of the screen in units of the interior AdS radius, L_-, for different choices of the ratio $\mathcal{R} = L_+/L_-$. For each line there is a divergence at $r_0/L_- = 1$ where the horizon of the black hole is. All the lines in the graph will saturate to a value of zero at infinity, however the way by which this is achieved is different depending on the value of $\mathcal{R}$. Lines with $\mathcal{R} < 1$ (blue and yellow line) actually cross the x-axis and then decrease and saturate to zero. Lines with $\mathcal{R} \geq 1$ (green, red, and dotted lines) stay below the x-axis and saturate to zero at infinity. This is consistent with the simple expressions we found in Eq. (C.69) and Eq. (C.70). The main features discussed remain intact in higher dimensions and for more general choices of r_H/L_-.

Appendix D

Chapter 5 Appendix Materials

D.1 Supplemental Calculations for Poincare AdS_3

D.1.1 Deriving General Solution for Extremal Curves in Poincare AdS_3

In this appendix we will find the general solution to the equations of motion that are obtain from the Lagrangian:

$$\mathcal{L} = \int L \frac{\sqrt{1 + \dot{z}^2 - \dot{t}^2}}{z}, \tag{D.1}$$

which we read off from the function given in Eq. (5.3). Since there is no explicit dependence on x there is a conserved Hamiltonian corresponding to x-translations which can be written as:

$$H_x = -\frac{L}{z\sqrt{1 + \dot{z}^2 - \dot{t}^2}}. \tag{D.2}$$

Furthermore, since there is no explicit time dependence we get the following equation for $\dot{t}$:

$$c_t = -\frac{L\dot{t}}{z\sqrt{1 + \dot{z}^2 - \dot{t}^2}}. \tag{D.3}$$

Combining D.2 and D.3 we will obtain the following equations for $t(x)$ and $z(x)$:

$$\begin{aligned} \dot{t} &= k \\ \dot{z}^2 &= \frac{L^2}{H_x^2 z^2} + k^2 - 1, \end{aligned} \tag{D.4}$$

where k, H_x are constants. The general solution to the equations above is:

$$\begin{aligned} t(x) &= kx + c_1 \\ z(x) &= \sqrt{\frac{L^2}{H_x^2(1-k^2)} - (1-k^2)(x+c_2)^2}. \end{aligned} \tag{D.5}$$

which is what we wrote in Eq. (5.4). In the special case where $k = 0$ the RT surface remains on a constant time slice and traces out a half circle in the bulk given by:

$$\begin{aligned} t(x) &= c_1 \\ z(x) &= \sqrt{\frac{L^2}{H_x^2} - (x+c_2)^2} \end{aligned} \tag{D.6}$$

It is straightforward to see that this is a half circle in the $z-x$ plane. It has a centre at $(t = c_1, x = -c_2, z = 0)$ with a radius $\frac{L}{|H_x|}$.

D.1.2 Analysis Of Extremal Curves in Poincare AdS_3

In Section 5.2.2 we wrote down equations for extremal RT curve trajectories that connected the boundary to the brane. In this subsection we will discuss why it is necessary for the quantity $-\Delta t^2 + \Delta x^2 + \Delta z^2 > 0$. We begin by noting that $z(x)$ describes conic sections in the $z-x$ plane which can be classified by the value of k summarized in the table below:

$\lvert k\rvert$	$z(x)$
0	circle
$0 < \lvert k\rvert < 1$	ellipse
1	parabola
$\lvert k\rvert > 1$	hyperbola

Lets consider the curve χ_1 described by the Eq. 5.8 in such a case we have the following:

$$\begin{aligned}\Delta t &= t_b - t_a \\ \Delta x &= a_1 + b_1 \sin\theta_0 \\ \Delta z &= b_1 \cos\theta_0\end{aligned} \tag{D.7}$$

Using this we can write the following expression for $z_1(x)$ in terms of the Δ's as follows:

$$z_1(x) = \sqrt{\frac{(x+a_1)\left[(x+a_1-\Delta x)(\Delta t^2 - \Delta x^2) + \Delta x \Delta z^2\right]}{\Delta x^2}} \tag{D.8}$$

We fix Δx and Δz and analyze χ_1 curve near $x = -a_1$ we have the following expansion:

$$z_1(x) = \sqrt{\frac{-\Delta t^2 + \Delta x^2 + \Delta z^2}{\Delta x}(x+a_1)} + \mathcal{O}((x+a_1)^{3/2}) \tag{D.9}$$

We can see that when $x > -a_1$ the expression is real only if $-\Delta t^2 + \Delta x^2 + \Delta z^2 > 0$. We can rewrite this and obtain the following bound for k_1:

$$\begin{aligned}|k_1| < |k_c| &= \sqrt{1 + \frac{\Delta z^2}{\Delta x^2}} = \frac{\sqrt{a_1^2 + b_1^2 + 2a_1 b_1 \sin\theta_0}}{a_1 + b_1 \sin\theta_0} \\ \Rightarrow |t_b - t_a| &< \sqrt{a_1^2 + b_1^2 + 2a_1 b_1 \sin\theta_0}\end{aligned} \tag{D.10}$$

Geometrically what occurs as $|k| \to |k_c|^-$ is that the hyperbola switches branches and the resulting branch does not connect to the boundary to the brane. An image would be good.

The condition that $-\Delta t + \Delta x^2 + \Delta z^2 > 0$ can also be interpreted as saying that the points on the boundary and brane are spacelike separated[1]. Furthermore, lets consider the sign of the norm of a tangent vector along any point on the curve. We have the following expression for the norm of the tangent vector:

$$\frac{L^2}{z_1^2}\left[-\left(\frac{dt_1^2}{dx}\right) + 1 + \left(\frac{dz_1^2}{dx}\right)\right] \tag{D.11}$$

The sign only depends on the expression in square brackets. With some work we will arrive at the following result:

$$-\left(\frac{dt_1}{dx}\right)^2 + 1 + \left(\frac{dz_1}{dx}\right)^2 = \frac{(-\Delta t^2 + \Delta x^2 + \Delta z^2)^2}{4(x+a_1)\left[(x+a_1)\Delta z^2 + (\Delta x - (x+a_1))\left(-\Delta t^2 + \Delta z^2 + \Delta x^2\right)\right]} \tag{D.12}$$

One can check that the signs of the expression above is non-negative as long as:

[1]Here when we say the two points are spacelike separated we mean that we consider lightcone from either of the two points. The we say another point is spacelke separated if it lies outside the bulk lightcone. The causal structure of vacuum AdS is the same as the causal structure of flat Minkowski.

- $-\Delta t^2 + \Delta x^2 + \Delta z^2 > 0$
- $-a_1 < x < -a_1 + \Delta x$

The first condition is equivalent to the bound $|k_1| < |k_c|$ and the second condition is simply describing the physically allowed region of the bulk. This shows that the condition that the point on the boundary be spacelike separated from the point on the brane (and vice-versa) implies that the tangent vector to the curve will also be spacelike.

D.1.3 Null Geodesics and Lightcones in Poincare AdS_3

In this subsection we will derive expressions for the trajectories of null geodesics in Poincare AdS_3. We begin with the Lagrangian which will give us the equations of motion that geodesics will satisfy:

$$\mathcal{L} = \frac{L^2}{z^2}\left[-\dot{t}^2 + \dot{z}^2 + \dot{x}^2\right]. \tag{D.13}$$

The associated equations of motion are given by:

$$\begin{aligned} \ddot{t} &= \frac{2\dot{t}\dot{z}}{z} \\ \ddot{x} &= \frac{2\dot{x}\dot{z}}{z} \\ \ddot{z} &= \frac{\dot{t}^2 + \dot{z}^2 - \dot{x}^2}{z} \end{aligned} \tag{D.14}$$

Since we want to deal with null geodesics this means:

$$\dot{t}^2 = \dot{z}^2 + \dot{x}^2 \tag{D.15}$$

The equation for z becomes:

$$\ddot{z} = \frac{2\dot{z}^2}{z} = 0 \Rightarrow z(\sigma) = \frac{c_2}{\sigma + c_1} \tag{D.16}$$

Plugging this into the x equation and solving we get:

$$x(\sigma) = \frac{c_3}{c_1 + \sigma} + c_4 \tag{D.17}$$

Finally we solve for t to get:

$$t(\sigma) = \frac{c_5}{c_1 + \sigma} + c_6 \tag{D.18}$$

The condition that we have null geodesics means that:

$$c_5^2 = c_3^2 + c_2^2 \tag{D.19}$$

We redefine $\sigma = \sigma(\lambda) = \left(\frac{\lambda+z_0}{c_2}\right)^{-1} - c_1$ and write the following general solution for null geodesics:

$$\begin{aligned} z(\lambda) &= \lambda + z_0 \\ x(\lambda) &= \frac{c_3}{c_2}\lambda + x_0 \\ t(\lambda) &= \frac{c_5}{c_2}\lambda + t_0 = \frac{\sqrt{c_3^2 + c_2^2}}{c_2}\lambda + t_0 \end{aligned} \tag{D.20}$$

These are just straight lines. We can consider an arbitrary point in the bulk (t_0, x_0, z_0) and find the equation of a lightcone from this point at a surface of the form $t_{l.c.} = t(x, z)$. We can do this by noting the following:

$$\begin{aligned} \lambda &= z - z_0 \\ x - x_0 &= \frac{c_3}{c_2}\lambda = \frac{c_3}{c_2}(z - z_0) \end{aligned} \tag{D.21}$$

Plugging this into the equation for $t(\lambda)$ gives:

$$(t - t_0)^2 = \lambda^2 + \left(\lambda\frac{c_3}{c_2}\right)^2 = (x - x_0)^2 + (z - z_0)^2 \tag{D.22}$$

We conclude a light cone centred at (t_0, x_0, z_0) has the equation:

$$|t(x, z) - t_0| = \sqrt{(x - x_0)^2 + (z - z_0)^2}. \tag{D.23}$$

This allows us to define causal relationships between points in the bulk.

D.1.4 Entanglement Wedges For Constant Time Intervals in Poincare AdS_3

An important fact about RT curves given in Eq. (D.6), which are anchored to constant time slice intervals on the boundary, is that they can be understood in terms of the intersection of certain lightcones whose apexes live on certain points on a conformal boundary (recall these

lightcones are described by the equation given in Eq. (D.23)). In particular, for the general solution given in Eq. (D.6) we can define two lightcones. One lightcone is generated by past directed null geodesics originating from from the point $(t_0 = c_1 + \frac{L}{|H_x|}, x_0 = -c_2, z = 0)$ given by:

$$t_{p.d.}(x, z) = c_1 + \frac{L}{|H_x|} - \sqrt{(x + c_2)^2 + z^2} \tag{D.24}$$

The other lightcone consists of future oriented null geodesics originating from the point $(t_0 = c_1 - \frac{L}{|H_x|}, x_0 = -c_2, z = 0)$ given by:

$$t_{f.d.}(x, z) = c_1 - \frac{L}{|H_x|} + \sqrt{(x + c_2)^2 + z^2} \tag{D.25}$$

The surfaces will intersect on the $t = c_1$ time slice along a curve we can find this curve by setting:

$$t_{p.d.}(x, z) = t_{f.d.}(x, z) \Rightarrow z = \sqrt{\frac{L^2}{H_x^2} - (x + c_2)^2} \tag{D.26}$$

This is precisely the RT curve anchored to a constant time boundary interval. The region enclosed by $t_{p.d.}$ and $t_{f.d.}$ is called the causal wedge we can express the null boundary of the causal wedge in the following compact notation:

$$\frac{L}{H_x} - |t - c_1| = \sqrt{(x + c_2)^2 + z^2}, \tag{D.27}$$

where $\frac{L}{H_x} - |t - c_1| \geq 0$. Points inside the causal wedge satisfy:

$$\frac{L}{H_x} - |t - c_1| > \sqrt{(x + c_2)^2 + z^2} \tag{D.28}$$

Since the boundary of the causal wedge contains the set of points in the RT curve we can conclude a well known that fact that in vacuum AdS the causal and entanglement wedges are the same. In particular for the specific case of the subregion A we have:

$$\begin{aligned} \frac{L}{|H_x|} &= \frac{a_2 - a_1}{2} \\ c_1 &= t_a \\ c_2 &= \frac{a_2 + a_1}{2}, \end{aligned} \tag{D.29}$$

which gives Eq. (5.10).

A similar game can also be played to understand the points contained in $\mathcal{W}_E(B)$. We appeal to the fact that, mathematically, there is nothing stopping us from continuing the section of the half circle describing $\chi_{dis.}(B)$ behind the brane all the way to the conformal boundary. Doing this will define a "virtual interval" that lies on a constant time slice $t = t_b$ behind the brane. The virtual interval associated with the brane interval B, denoted $\text{Vir}(B)$, is going to be equal to the following constant time slice interval on the boundary given by:

$$\begin{aligned}\text{Vir}(B) &= \{(t,x,z)|t = t_b, x \in [\frac{b_1+b_2}{2\sin\theta_0} - R_b, \frac{b_1+b_2}{2\sin\theta_0} + R_b], z = 0\}. \\ R_b &= \frac{\sqrt{b_1^2+b_2^2+2b_1b_2\cos(2\theta_0)}}{2\sin\theta_0}\end{aligned} \tag{D.30}$$

Clearly $\chi_{dis.}(B) \subseteq \chi_{dis.}(\text{Vir}(B))$ and we will also conclude that $\mathcal{W}_E(B) \subseteq \mathcal{W}_E(\text{Vir}(B))$. The expression for the null surface that bounds $\mathcal{W}_E(\text{Vir}(B))$ is given by Eq. (D.27) by setting:

$$\begin{aligned}\frac{L}{|H_x|} &= R_b = \frac{\sqrt{b_1^2+b_2^2+2b_1b_2\cos(2\theta_0)}}{2\sin\theta_0} \\ c_1 &= t_b \\ c_2 &= -\frac{b_1+b_2}{2\sin\theta_0}\end{aligned} \tag{D.31}$$

Finally we define $\mathcal{W}_E(B) = \mathcal{W}_E(\text{Vir}(B)) \cap \text{Phys}(AdS_3)$. Where $\text{Phys}(AdS_3)$ is the portion of the bulk spacetime which is not cutoff by the end-of-the-world brane. This essentially means that we can view $\mathcal{W}_E(B)$ as the piece cut out of the much larger entanglement wedge $\mathcal{W}_E(\text{Vir}(B))$. As shown in Figure 5.5.

D.1.5 Analysis of Naive Sufficient Condition for EWN (AdS_3)

In this Appendix we will derive a sufficient condition for entanglement wedge nesting to hold based on the criteria described in Eq. (5.13). We begin with the condition using χ_1 we have:

$$[|t_1(x) - t_b| + R_b]^2 - \left[x - \frac{b_1+b_2}{2\sin\theta_0}\right]^2 - z_1(x)^2 \leq 0 \tag{D.32}$$

On the χ_1 curve there is a relation between $|t_1(x) - t_b|$ and x given by:

$$x(\delta t_1) = b_1\sin\theta_0 - \frac{|t_1 - t_b|}{|k_1|} = b_1\sin\theta_0 - \frac{|\delta t_1|}{|k_1|} \tag{D.33}$$

We plug this into the inequality and simplify to obtain the following result:

$$\begin{aligned}&[|\delta t_1| + R_b]^2 - \left[b_1 \sin\theta_0 - \frac{|\delta t_1|}{|k_1|} - \frac{b_1+b_2}{2\sin\theta_0}\right]^2 - z_1\left(b_1\sin\theta_0 - \frac{|\delta t_1|}{|k_1|}\right)^2 \\ &= \frac{|\delta t_1|(a_1+b_1\sin\theta_0)}{|k_1|}\left[\left[|k_1| + \frac{R_b}{a_1+b_1\sin\theta_0}\right]^2 - \frac{\left(2a_1+\frac{b_1+b_2}{\sin\theta_0}\right)^2}{4(a_1+b_1\sin\theta_0)^2}\right] \leq 0\end{aligned} \tag{D.34}$$

So to satisfy the inequality we must require that:

$$|k_1| \leq -\frac{R_b}{a_1+b_1\sin\theta_0} + \frac{2a_1+\frac{b_1+b_2}{\sin\theta_0}}{2(a_1+b_1\sin\theta_0)} \tag{D.35}$$

Using a similar analysis for χ_2 one can also obtain another bound given as:

$$|k_2| \leq -\frac{R_b}{a_2+b_2\sin\theta_0} + \frac{2a_2+\frac{b_1+b_2}{\sin\theta_0}}{2(a_2+b_2\sin\theta_0)} \tag{D.36}$$

The stronger bound comes from our analysis using χ_1 and we are left with the following sufficient condition for entanglement wedge nesting:

$$|t_b - t_a| \leq a_1 + \frac{b_1+b_2-\sqrt{b_1^2+b_2^2+2b_1b_2\cos(2\theta_0)}}{2\sin\theta_0}, \tag{D.37}$$

which is what wrote in Eq. (5.14).

D.1.6 A Characterization of Causality in the 2D Boundary-Brane System

In this appendix we will discuss some basic aspects of causality in the 2D brane boundary system which we use in our discussion in Section 5.2.5. To begin we recall that the system we are considering is AdS_3 in Poincare coordinates which contains an end-of-the-world-brane. Recall the metric that we used is:

$$ds^2 = \frac{L^2}{z^2}\left[-dt^2+dx^2+dz^2\right] \tag{D.38}$$

The end-of-the-world brane is given by the surface that satisfies:

$$\begin{aligned}&z = \cot\theta_0 x \\ &x > 0,\end{aligned} \tag{D.39}$$

where $\theta_0 \in (0, \pi/2]$. What we refer to the as the "Boundary-Brane System" is a 2D system which consists of the union of the conformal boundary for $x < 0$ and the end-of-the-world brane for $x > 0$. We can characterize the system as the set of points in the bulk that satisfy:

$$z = \Theta(x) \cot \theta_0 x. \tag{D.40}$$

An alternate coordinate system which naturally foliates the bulk in terms of the end-of-the-world branes consists of a radial coordinate r and a angle θ which can be related to the (z, x) through the following transformation to polar coordinates:

$$\begin{aligned} z &= r \cos \theta \\ x &= r \sin \theta \end{aligned} \tag{D.41}$$

The metric now reads:

$$ds^2 = \frac{L^2}{\cos^2 \theta} \left[d\theta^2 + \frac{-dt^2 + dr^2}{r^2} \right] \tag{D.42}$$

Now the end-of-the-world brane is given by surfaces of constant θ. The brane boundary system is simply given by the union of the $\theta = -\pi/2$ slice and the $\theta = \theta_0$ slice. Since the 2D induced metric is conformally flat we know that null geodesics in the brane boundary system are very simple to analyze. In particular, if we started on the $t = t_a$ slice on the boundary at $(r = a_1)$ the null geodesics would get to $r = 0$ at time $t = t_a + a_1$. Then after that the time it takes to reach a point $r = b_1$ on the brane is:

$$t(b_1) - t_a = a_1 + b_1 \tag{D.43}$$

This is interesting because it naturally allows us to define what it means for two points on the brane boundary system to be timelike. In particular, if we have a point on the boundary with $r = a_1, t = t_a$ and another point on the brane at $r = b_1, t = t_b$ then:

- They are lightlike separated if $|t_b - t_a| = a_1 + b_1$
- They are timelike separated if $|t_b - t_a| > a_1 + b_1$
- They are spacelike separated if $|t_b - t_a| < a_1 + b_1$.

This would represent a natural way to define causal relationships if we are confined to do causal processes constrained within the 2D Boundary-Brane system.

Now lets consider a slightly different notion of causality which makes use of the signaling through the bulk. In this case we can consider a bulk light cone which starts at $(t = t_a, x = -a_1, z = 0)$. This lightcone is given by:

$$|t - t_a| = \sqrt{z^2 + (x + a_1)^2} \tag{D.44}$$

By projecting the bulk cone onto the 2D Boundary-Brane system we obtain the following curve:

$$|t(x) - t_a| = \sqrt{\Theta(x)\cot^2\theta_0 x^2 + (x+a_1)^2} = \begin{cases} x + a_1, & -a_1 < x < 0 \\ \sqrt{\cot^2\theta_0 x^2 + (x+a_1)^2}, & x \geq 0, \end{cases} \tag{D.45}$$

By plugging in $x = b_1 \sin\theta_0$ we obtain the following result:

$$|t(b_1\sin\theta_0) - t_a| = \sqrt{a_1^2 + b_1^2 + 2a_1 b_1 \sin\theta_0}. \tag{D.46}$$

This defines a new causal structure on the 2D Brane-Boundary system. Suppose we choose a point on the boundary at $r = a_1$ at time $t = t_a$ and another point on the brane at $r = b_1$ at time $t = t_b$ then:

- They are bulk lightlike separated if $|t_b - t_a| = \sqrt{a_1^2 + b_1^2 + 2a_1 b_1 \sin\theta_0}$
- They are bulk timelike separated if $|t_b - t_a| > \sqrt{a_1^2 + b_1^2 + 2a_1 b_1 \sin\theta_0}$
- They are bulk spacelike separated if $|t_b - t_a| < \sqrt{a_1^2 + b_1^2 + 2a_1 b_1 \sin\theta_0}$.

We can see that:

$$a_1 + b_1 \geq \sqrt{a_1^2 + b_1^2 + 2a_1 b_1 \sin\theta_0} \tag{D.47}$$

This suggests that certain causal ("local") processes in the bulk when projected onto the 2D Brane-Boundary system will appear non-causal ("non-local") when one tries to understand them solely in terms of causal relationships defined in the 2D Brane-Boundary system.

D.2 Supplemental Calculations for Planar BTZ Black Hole

D.2.1 Derivation of Thermal RT Surface (Planar BTZ Black Hole)

In this subsection we will derive the equations of motion to determine the thermal RT surface. We define the Lagrangian associated to the functional given in Eq. (5.34) below:

$$\mathcal{L}(t, \dot{t}, z, \dot{z}; x) = \frac{L}{z}\sqrt{-\tilde{f}(z)\dot{t}^2 + \frac{\dot{z}^2}{\tilde{f}(z)} + 1} \tag{D.48}$$

Since the Lagrangian no explicit x dependence so we can define a conserved Hamiltonian associated with x-translations given by:

$$\mathcal{H}_x = \dot{z}\frac{\partial \mathcal{L}}{\partial \dot{z}} + \dot{t}\frac{\partial \mathcal{L}}{\partial \dot{t}} - \mathcal{L} = -\frac{L^2}{z^2\mathcal{L}} \tag{D.49}$$

We have the following equation of motion for t:

$$\frac{\partial \mathcal{L}}{\partial \dot{t}} = c_t, \tag{D.50}$$

where c_t is constant. Plugging this into the Lagrangian we obtain the following expression for $\dot{t}$:

$$\dot{t} = -c_t \frac{\mathcal{L}z^2}{L^2\left(1-\frac{z^2}{z_+^2}\right)} = \frac{c_t}{\mathcal{H}_x\left(1-\frac{z^2}{z_+^2}\right)}. \tag{D.51}$$

Since $z < z_+$ we know that sign of the derivative will not change along the RT curve. Since we want to anchor the thermal RT surface to a constant time slice interval we must require that $c_t = 0$. This in turn means $\dot{t} = 0 \Rightarrow t(x) = t_{bdry}$. If we plug this back into the equation for $\mathcal{H}_x$ and rearrange for $\dot{z}$ we get:

$$\dot{z}^2 = \frac{\left(z_+^2 - z^2\right)\left(L^2 - \mathcal{H}_x^2 z^2\right)}{\mathcal{H}_x^2 z_+^2 z^2} \tag{D.52}$$

We can see that $\dot{z} = 0$ when $z = z_{tp} = L/|\mathcal{H}_x|$, this is the turning point for the RT curve where the derivative $\dot{z}$ goes to zero. We want an RT surface that starts at $x = -a$ extends into the bulk and then returns to the boundary at $x = a$. Rearranging the expression $\dot{z}$ we obtain the following integral equation for the "left portion" of the RT curve where $\dot{z} \geq 0$:

$$\int_{-a}^{x} dx = \int_0^{z(x)} \frac{z_+ z}{\sqrt{(z_+^2 - z^2)(z_{tp}^2 - z^2)}} dz \tag{D.53}$$

We can explicitly integrate each side of the expression and with some algebraic/trigonometric manipulations we arrive at the following result:

$$z_{left}(x) = \sqrt{z_+^2 - \left[z_+ \cosh\left(\frac{x+a}{z_+}\right) - z_{tp}\sinh\left(\frac{x+a}{z_+}\right)\right]^2} \tag{D.54}$$

By requiring that $z_{tp} = z(x_{tp})$ we obtain the following relation between x_{tp} and z_{tp}:

$$z_{tp} = z_+ \tanh\left(\frac{a + x_{tp}}{z_+}\right) \tag{D.55}$$

Plugging this back into the expression for $z_{left}(x)$ gives the following result:

$$z_{left}(x) = z_+ \sqrt{1 - \frac{\cosh^2\left(\frac{x-x_{tp}}{z_+}\right)}{\cosh^2\left(\frac{a+x_{tp}}{z_+}\right)}} \tag{D.56}$$

For the "right potion" of the RT curve we have to perform the following integrals:

$$\int_x^a dx = -\int_{z(x)}^0 \frac{z_+ z}{\sqrt{(z_+^2 - z^2)(z_{tp}^2 - z^2)}} dz = \int_0^{z(x)} \frac{z_+ z}{\sqrt{(z_+^2 - z^2)(z_{tp}^2 - z^2)}} dz \tag{D.57}$$

Its not hard to see based on our previous work on the left portion that the right portion of the RT curve will take the form:

$$z_{right}(x) = \sqrt{z_+^2 - \left[z_+ \cosh\left(\frac{a-x}{z_+}\right) - z_{tp} \sinh\left(\frac{a-x}{z_+}\right)\right]^2} \tag{D.58}$$

Once again, the requirement that $z_{tp} = z(x_{tp})$ gives:

$$z_{tp} = z_+ \tanh\left(\frac{a - x_{tp}}{z_+}\right). \tag{D.59}$$

Using this we can write:

$$z_{right}(x) = z_+ \sqrt{1 - \frac{\cosh^2\left(\frac{x-x_{tp}}{z_+}\right)}{\cosh^2\left(\frac{a-x_{tp}}{z_+}\right)}} \tag{D.60}$$

The condition that the two portions of the RT curves should be smoothly glued at $x = x_{tp}$ and $z = z_{tp}$ (i.e. $z_{left}(x_{tp}) = z_{right}(x_{tp})$) gives the following equation:

$$\sqrt{1 - \frac{\cosh^2\left(\frac{x-x_{tp}}{z_+}\right)}{\cosh^2\left(\frac{a-x_{tp}}{z_+}\right)}} = \sqrt{1 - \frac{\cosh^2\left(\frac{x-x_{tp}}{z_+}\right)}{\cosh^2\left(\frac{a+x_{tp}}{z_+}\right)}} \tag{D.61}$$

We can see that this requires the setting of $x_{tp} = 0$ as expected. So our final result for the thermal RT surface in Schwarzschild coordinates anchored to the endpoints of a constant

time slice interval on the boundary centred around $x = 0$ of size $2a$ is:

$$\begin{aligned} t(x) &= t_{bdry} \\ z(x) &= z_+ \sqrt{1 - \frac{\cosh^2\left(\frac{x}{z_+}\right)}{\cosh^2\left(\frac{a}{z_+}\right)}} \end{aligned} \tag{D.62}$$

This gives the result we wrote in Eq. (5.35).

From Schwarzschild to Kruskal Coordinates

Now that we have derived the thermal RT surface in Schwarzschild coordinates we can use the expression given for the thermal RT surface along with the transformations given in in Eq. (5.39). Lets begin by computing the thermal surface in the left exterior which is anchored to an interval on the boundary at time $t = t_L = t_{bdry}$. We have the following expressions for u and v:

$$\begin{aligned} v(x) &= \frac{\tau(x) - y(x)}{2} = \arctan\left[e^{-\frac{t_{bdry}}{z_+}} \sqrt{\frac{z_+ - z_L(x)}{z_+ + z_L(x)}}\right] \\ u(x) &= \frac{\tau(x) + y(x)}{2} = \arctan\left[-e^{\frac{t_{bdry}}{z_+}} \sqrt{\frac{z_+ - z_L(x)}{z_+ + z_L(x)}}\right] \\ z_L(x) &= z_+ \sqrt{1 - \frac{\cosh^2\left(\frac{x}{z_+}\right)}{\cosh^2\left(\frac{a}{z_+}\right)}} \end{aligned} \tag{D.63}$$

With these expressions we can write the following:

$$\begin{aligned}
\sin\left(\tau(x)\right) = \sin\left[v(x)+u(x)\right] &= -\sqrt{\frac{(z_L^2-z_+^2)\sinh^2\left(\frac{t_{bdry}}{z_+}\right)}{z_L^2\sinh^2\left(\frac{t_{bdry}}{z_+}\right)-z_+^2\cosh^2\left(\frac{t_{bdry}}{z_+}\right)}} \\
&= -\frac{\cosh\left(\frac{x}{z_+}\right)\sinh\left(\frac{t_{bdry}}{z_+}\right)}{\sqrt{\cosh^2\left(\frac{a}{z_+}\right)+\cosh^2\left(\frac{x}{z_+}\right)\sinh^2\left(\frac{t_{bdry}}{z_+}\right)}} \\
\sin\left(y(x)\right) = \sin\left[u(x)-v(x)\right] &= -\frac{\cosh\left(\frac{t_{bdry}}{z_+}\right)\cosh\left(\frac{x}{z_+}\right)}{\sqrt{\cosh^2\left(\frac{a}{z_+}\right)+\cosh^2\left(\frac{x}{z_+}\right)\sinh^2\left(\frac{t_{bdry}}{z_+}\right)}}
\end{aligned} \tag{D.64}$$

This gives Eq. (5.40).

Next we proceed with writing the thermal RT surface anchored to a constant time slice interval $t = t_{Br}$ on an end-of-the-world brane in the right exterior. We have the following expressions for u and v in the right exteriors:

$$\begin{aligned}
v(x) &= \frac{\tau(x)-y(x)}{2} = \arctan\left[-e^{-\frac{t_{Br}}{z_+}}\sqrt{\frac{z_+-z_R(x)}{z_++z_R(x)}}\right] \\
u(x) &= \frac{\tau(x)+y(x)}{2} = \arctan\left[e^{\frac{t_{Br}}{z_+}}\sqrt{\frac{z_+-z_R(x)}{z_++z_R(x)}}\right] \\
z_R(x) &= z_+\sqrt{1-\frac{\cosh^2\left(\frac{x}{z_+}\right)}{\cosh^2\left(\frac{a}{z_+}\right)}\left(1-\frac{z_{Br}^2}{z_+^2}\right)}
\end{aligned} \tag{D.65}$$

With similar manipulations as before we find that a thermal RT surface in the right exterior anchored to a constant time slice interval ($t = t_{Br}$) centred around $x = 0$ of length $2a$ is

given by:

$$\begin{aligned}
\sin\left(\tau(x)\right) = \sin[v(x)+u(x)] &= \frac{\sqrt{1-\frac{z_{Br}^2}{z_+^2}}\cosh\left(\frac{x}{z_+}\right)\sinh\left(\frac{t_{Br}}{z_+}\right)}{\sqrt{\cosh^2\left(\frac{a}{z_+}\right)+\left(1-\frac{z_{Br}^2}{z_+^2}\right)\cosh^2\left(\frac{x}{z_+}\right)\sinh^2\left(\frac{t_{Br}}{z_+}\right)}} \\
\sin(y(x)) = \sin[u(x)-v(x)] &= \frac{\sqrt{1-\frac{z_{Br}^2}{z_+^2}}\cosh\left(\frac{x}{z_+}\right)\cosh\left(\frac{t_{Br}}{z_+}\right)}{\sqrt{\cosh^2\left(\frac{a}{z_+}\right)+\left(1-\frac{z_{Br}^2}{z_+^2}\right)\cosh^2\left(\frac{x}{z_+}\right)\sinh^2\left(\frac{t_{Br}}{z_+}\right)}}
\end{aligned} \tag{D.66}$$

This gives the expressions in Eq. (5.41). We can check that the following identities hold:

$$\begin{aligned}
\frac{\cos^2\left(y(\pm a)\right)}{\cos^2\left(\tau(\pm a)\right)} &= \frac{z_{Br}^2}{z_+^2} \\
\frac{\sin(y(x))+\sin(\tau(x))}{\sin(y(x))-\sin(\tau(x))} &= e^{\frac{2t_{Br}}{z_+}}
\end{aligned} \tag{D.67}$$

which is exactly what we would expect from the coordinate transformations given in Eq. (5.28).

D.2.2 Derivation of Connected RT Surface (Planar BTZ Black Hole)

Derivation in Kruskal Coordinates:

We will go over the derivation of finding the connected RT surface that connects the brane and boundary intervals that are placed in the same position in the "x-direction" (i.e. brane and boundary intervals have endpoints that are located at the same x-coordinate location). The connected RT surface will consist of two line segments that go through the black hole horizon and connect the endpoints of the intervals on the brane and boundary which may exist on different time slices. To obtain such line segments we must extremize the functional given in Eq. (5.42). The Lagrangian associated to the functional is:

$$\mathcal{L} = \frac{\sqrt{L^2\left(-\dot{\tau}^2+1\right)+\frac{r_+^2}{L^2}\cos^2\tau\dot{x}^2}}{\cos y}. \tag{D.68}$$

Since there is no explicit x-dependence we have that:

$$\frac{\partial \mathcal{L}}{\partial \dot{x}} = c_x \tag{D.69}$$

where c_x is constant. Plugging in the actual Lagrangian gives the following expression for $\dot{x}$:

$$\dot{x} = c_x \frac{L^2}{r_+^2} \frac{\cos^2 y}{\cos^2 \tau} \mathcal{L} \tag{D.70}$$

We can see that within the bulk geometry a spacelike RT surface will have a derivative that is monotonic for $c_x \neq 0$. However, we also know that we must require the RT curve to start and end at the same x-coordinate. This is only possible if $c_x = 0$. Therefore, we restrict ourselves to the set of RT surfaces with $\dot{x} = 0$. This means we need to deal with a much simpler Lagrangian:

$$\mathcal{L} = L \frac{\sqrt{1 - \dot{\tau}^2}}{\cos y}, \tag{D.71}$$

which is what we wrote in Eq. (5.43). Since we no longer have any explicit τ dependence on the Lagrangian we have another conserved quantity namely:

$$c_\tau L = \frac{\partial \mathcal{L}}{\partial \dot{\tau}} \tag{D.72}$$

The extra factor L is just a convenient normalization. Plugging in the appropriate Lagrangian gives:

$$\dot{\tau} = \pm \frac{1}{\sqrt{1 + \frac{1}{c_\tau^2 \cos^2 y}}} \tag{D.73}$$

The sign of the solution above is determined by $\text{sign}(\tau_{Br} - \tau_{bdry})$. In particular, when $\tau_{Br} - \tau_{bdry} > 0$ we have that:

$$\int_{\tau_{bdry}}^{\tau(y)} d\tau = \int_{-\pi/2}^{y} \frac{dy'}{\sqrt{1 + \frac{1}{c_\tau^2 \cos^2 y'}}} \tag{D.74}$$

The integrals can be done explicitly to obtain:

$$\tau(y) - \tau_{bdry} = \arctan \left[\frac{c_\tau \sin y'}{\sqrt{1 + c_\tau^2 \cos^2 y'}} \right] \Bigg|_{-\pi/2}^{y} \tag{D.75}$$

Using the relation between arcsin and arctan allows us to write:

$$\tau(y) - \tau_{bdry} = \arcsin\left[\frac{c_\tau}{\sqrt{1+c_\tau^2}}\sin y\right] + \arcsin\left[\frac{c_\tau}{\sqrt{1+c_\tau^2}}\right] \tag{D.76}$$

This gives us the expression for the connected RT surface in Eq. (5.44). Note that in general that $\text{sign}(c_\tau) = \text{sign}(\tau_{Br} - \tau_{bdry})$. We can see for a fixed τ_{bdry} the value of c_τ fixes where in time the connected surface connects to the brane.

Connected Surface in Schwarzschild Coordinates:

Now that we have obtained an expression for the connected RT curve in Kruskal coordinates we can express it in the right exterior in Schwarzschild coordinates with the help of the coordinate transformations given in Eq. (5.28). Since we are interested analyzing entanglement wedge nesting in the right exterior in Schwarzschild coordinates. We will find it convenient to use the following expression for the connected surface in Kruskal coordinates:

$$\begin{aligned}\tau(y) &= \tau_{Br} + \arcsin(c_t \sin y) - \arcsin(c_t \sin y_{Br}) = \tau_* + \arcsin(c_t \sin y)\\ c_t &= \frac{c_\tau}{\sqrt{1+c_\tau^2}}\end{aligned} \tag{D.77}$$

The connected RT surface ends on a brane located at $y = y_{Br}$ where $0 \leq y_{Br} \leq \pi/2$ and at $\tau = \tau_{Br}$ where $|\tau_{Br}| \leq y_{Br}$. Recall the following relation between Kruskal and Schwarzschild coordinates. We have:

$$\begin{aligned}t &= \frac{L^2}{2r_+}\ln\left[\frac{\sin y + \sin\tau}{\sin y - \sin\tau}\right]\\ r &= r_+\frac{\cos\tau}{\cos y}\end{aligned} \tag{D.78}$$

We can invert the relations above to obtain the following:

$$\begin{aligned}\sin y &= \pm\frac{1}{\sqrt{1+\frac{1}{\left(\frac{r^2}{r_+^2}-1\right)\cosh^2\left(\frac{r_+ t}{L^2}\right)}}}\\ \sin\tau &= \pm\frac{\tanh\left(\frac{r_+ t}{L^2}\right)}{\sqrt{1+\frac{1}{\left(\frac{r^2}{r_+^2}-1\right)\cosh^2\left(\frac{r_+ t}{L^2}\right)}}} \Rightarrow \cos\tau = \frac{\sqrt{\frac{r^2}{r^2-r_+^2}}}{\cosh\left(\frac{r_+ t}{L^2}\right)\sqrt{1+\frac{1}{\left(\frac{r^2}{r_+^2}-1\right)\cosh^2\left(\frac{r_+ t}{L^2}\right)}}}\end{aligned} \tag{D.79}$$

where the "+" is for the right exterior, the "−" is for the left exterior. We focus on the right exterior and take the "+" sign. From the equation of the connected surface we have that:

$$c_t \sin y = \sin(\tau - \tau_*) = \cos\tau_* \sin\tau - \sin\tau_* \cos\tau. \tag{D.80}$$

Now we plug in the expressions we had for $\sin\tau$ and $\sin y$ in Eq. (D.79) into Eq. (D.80) to obtain:

$$\begin{aligned} c_t &= \pm \cos\tau_* \tanh\left(\frac{r_+ t}{L^2}\right) - \sin\tau_* \frac{\sqrt{\frac{r^2}{r^2 - r_+^2}}}{\cosh\left(\frac{r_+ t}{L^2}\right)} \\ \Rightarrow c_t \cosh\left(\frac{r_+ t}{L^2}\right) &= \pm \cos\tau_* \sinh\left(\frac{r_+ t}{L^2}\right) - \sin\tau_* \sqrt{\frac{r^2}{r^2 - r_+^2}} \end{aligned} \tag{D.81}$$

Rearranging the expression above and recalling that $z = L^2/r$, we obtain the following expression for the connected RT surface in the right exterior in Schwarzschild coordinates:

$$\begin{aligned} \left(\frac{z}{z_+}\right)^2 &= 1 - \frac{\sin^2\tau_*}{\left[\cos\tau_* \sinh\left(\frac{r_+ t}{L^2}\right) - c_t \cosh\left(\frac{r_+ t}{L^2}\right)\right]^2} \\ &= 1 - \frac{\sin^2\tau_*}{\left[A\cosh\left(\frac{r_+ \Delta t}{L^2}\right) + B\sinh\left(\frac{r_+ \Delta t}{L^2}\right)\right]^2} \\ A &= \cos\tau_* \sinh\left(\frac{r_+ t_{Br}}{L^2}\right) - c_t \cosh\left(\frac{r_+ t_{Br}}{L^2}\right) \\ B &= \cos\tau_* \cosh\left(\frac{r_+ t_{Br}}{L^2}\right) - c_t \sinh\left(\frac{r_+ t_{Br}}{L^2}\right) \\ \Delta t &= t - t_{Br} \end{aligned} \tag{D.82}$$

An important point to note in the expression above is the issue of the sign of Δt. In particular, depending on the precise value of c_t the surface would extend away from the brane toward positive t or negative t. For example, if c_t was fixed such that the connected surface moves toward larger $t > t_{Br}$ then we certainly cannot have $\Delta t < 0$ (at least in a arbitrarily small neighborhood of the brane). So the central question is how to understand if we should be in the case where $\Delta t > 0$ or $\Delta t < 0$ for a given c_t. At first glance this may appear to be a rather complicated issue due to the expressions we wrote. However, there is a useful "trick" we can use to circumvent this problem.

To begin we do an expansion around the $\Delta t = 0$ (near the brane) to get:

$$\left(\frac{z}{z_+}\right)^2 = \left[1 - \frac{\sin^2\tau_*}{A^2}\right] + \frac{2r_+\sin^2\tau_*}{A^2L^2}\frac{B}{A}\Delta t \tag{D.83}$$

One can check that the zeroth order term will evaluate to:

$$1 - \frac{\sin^2\tau_*}{A^2} = \frac{\cos^2 y_{Br}}{\cos^2\tau_{Br}} = \frac{z_{Br}^2}{z_+^2}. \tag{D.84}$$

This makes sense since $\Delta t = 0$ should place us on the brane. Now lets focus on the linear order term. The linear order term will dictate if the brane is moving above or below the $t = t_{Br}$. In particular we want to z to increase so the surface moves outward away from the brane this means the linear term should have an overall positive sign. This in turn means that we must require that $\text{sign}(B/A) = \text{sign}(\Delta t)$. With the identity we showed for the zeroth order term we are able to write:

$$\left(\frac{z}{z_+}\right)^2 = 1 - \frac{1 - \frac{z_{Br}^2}{z_+^2}}{\left[\cosh\left(\frac{r_+\Delta t}{L^2}\right) + \frac{B}{A}\sinh\left(\frac{r_+\Delta t}{L^2}\right)\right]^2} \tag{D.85}$$

Now we have a precise characterization of how the value of c_t affects if $\Delta t > 0$ or if $\Delta t < 0$. In particular if $B/A > 0 \Rightarrow \Delta t > 0$ and if $B/A < 0 \Rightarrow \Delta t < 0$. We can "automate/circumvent" these cases by strictly dealing with the following expression involving absolute values:

$$\left(\frac{z}{z_+}\right)^2 = 1 - \frac{1 - \frac{z_{Br}^2}{z_+^2}}{\left[\cosh\left(\frac{r_+|\Delta t|}{L^2}\right) + \left|\frac{B}{A}\right|\sinh\left(\frac{r_+|\Delta t|}{L^2}\right)\right]^2} \tag{D.86}$$

This precisely gives us the expression for the connected surface in Schwarzschild coordinates in the right exterior given in Eq. (5.45).

Useful Properties of "B/A":

It is worthwhile to take the time to more carefully understand the properties of the ratio B/A. We can explicitly write it as follows in terms of c_t, y_{Br}, and τ_{Br}:

$$\frac{B}{A} = \frac{c_t\cos^2 y_{Br}\tan\tau_{Br} - \sin y_{Br}\sqrt{1 - c_t^2\sin^2 y_{Br}}}{\cos\tau_{Br}\left(c_t\sin y_{Br} - \tan\tau_{Br}\sqrt{1 - c_t^2\sin^2 y_{Br}}\right)} \tag{D.87}$$

Since we want to strictly consider intervals on the brane in the right exterior we must require that $|\tau_{Br}| < y_{Br}$ we also note that $|c_t| < 1$. With this we have the following properties of B/A:

- $\lim_{c_t \to -1}(B/A) \geq 0$.
- $\lim_{c_t \to 1}(B/A) \leq 0$.
- B/A is singular at $c_t = c_0 = \frac{\sin \tau_{Br}}{\sin y_{Br}}$.
- $\frac{d}{dc_t}\left(\frac{B}{A}\right)$ is non-negative (i.e. monotonically increasing as c_t increases) when $c_t \neq c_0$.

With the properties listed above we can easily deduce that $B/A \geq 0$ when $-1 < c_t < c_0$ and $B/A \leq 0$ when $c_0 < c_t < 1$. So the sign of B/A swaps at $c_t = c_0$. One can easily check that the point of sign swapping occurs exactly when the connected extremal surface passes through the bifurcate horizon at $\tau = y = 0$. These facts will become very important when we discuss sufficient conditions for entanglement wedge nesting.

D.2.3 Null Geodesics and Lightcones for Planar BTZ Background

In this appendix we will derive expressions the null geodesics propagating in the exterior spacetime of a planar BTZ black hole in Schwarzschild coordinates. The equations of motion for the geodesics will be obtained from the following Lagrangian (where we parameterize the geodesics trajectories using $z = \frac{L^2}{r}$):

$$\begin{aligned} \mathcal{L} &= \frac{L^2}{z^2}\left[-\tilde{f}(z)\dot{t}^2 + \frac{1}{\tilde{f}(z)} + \dot{x}^2\right] \\ \tilde{f}(z) &= 1 - \frac{z^2}{z_+^2}. \end{aligned} \tag{D.88}$$

Using the fact that the the Lagrangian has no explicit x or t dependence we have the following conserved quantities:

$$\begin{aligned} -\frac{\tilde{f}(z)}{z^2}\dot{t} &= a_t \\ \frac{\dot{x}}{z^2} &= a_x \end{aligned} \tag{D.89}$$

Dividing one equation by the other and squaring gives:

$$\left(\frac{\tilde{f}(z)\dot{t}}{\dot{x}}\right)^2 = \alpha^2, \tag{D.90}$$

where α is some constant. Finally we can use the condition for having a null geodesic (i.e. $\mathcal{L}=0$) to obtain the following first order equations that can be easily integrated:

$$\begin{aligned}\frac{dx}{dz} &= \pm\frac{1}{\sqrt{\alpha^2-\tilde{f}(z)}} \Rightarrow x-x_0 = \pm z_+ \text{arctanh}\left[\frac{z}{z_+\sqrt{\alpha^2-1+\frac{z^2}{z_+^2}}}\right]\Bigg|_{z_0}^{z} \\ \frac{dt}{dz} &= \frac{\pm\alpha}{\tilde{f}(z)\sqrt{\alpha^2-\tilde{f}(z)}} \Rightarrow t-t_0 = \pm z_+ \text{arctanh}\left[\frac{z\alpha}{z_+\sqrt{\alpha^2-1+\frac{z^2}{z_+^2}}}\right]\Bigg|_{z_0}^{z}\end{aligned} \tag{D.91}$$

In the special case where we choose a point $(t_0, x_0, z_0=0)$ we can use the expression above to obtain we have a fairly simple expression for the lightcone:

$$\begin{aligned}\left(\frac{t(x,z)-t_0}{z_+}\right)^2 &= \text{arctanh}^2\left[\frac{\sqrt{z^2+(z_+^2-z^2)\tanh^2\left(\frac{x-x_0}{z_+}\right)}}{z_+}\right] \\ &= \text{arctanh}^2\left[\sqrt{1-\frac{1-\frac{z^2}{z_+^2}}{\cosh^2\left(\frac{x-x_0}{z_+}\right)}}\right].\end{aligned} \tag{D.92}$$

For more general cases the expression will be much more complicated and we will not explicitly write it here (nor will we require it in our discussions).

D.2.4 Entanglement Wedges For Constant Time Intervals in BTZ Background

An important fact about the thermal RT curves given in Eq. (5.35), which are anchored to constant time slice intervals on the boundary, is that they can be understood in terms of the intersection of certain lightcones whose apexes live on certain points on a conformal boundary (recall these lightcones are described by the equation given in Eq. (D.92)). In particular, for the thermal RT surface given in Eq. (5.35) we can define two lightcones. One lightcone is generated by past directed null geodesics originating from from the point $(t_0 = t_{bdry}+a, x_0=0, z=0)$ given by:

$$t_{p.d.}(x,z) = t_{bdry}+a-z_+\text{arctanh}\left[\sqrt{1-\frac{1-\frac{z^2}{z_+^2}}{\cosh^2\left(\frac{x}{z_+}\right)}}\right] \tag{D.93}$$

The other lightcone consists of future oriented null geodesics originating from the point $(t_0 = t_{bdry} - a, x_0 = 0, z = 0)$ given by:

$$t_{f.d.}(x,z) = t_{bdry} - a + z_+ \text{arctanh}\left[\sqrt{1 - \frac{1-\frac{z^2}{z_+^2}}{\cosh^2\left(\frac{x}{z_+}\right)}}\right] \tag{D.94}$$

The surfaces will intersect along a curve on the constant time slice $t = t_{bdry}$ we can find this curve by setting:

$$t_{p.d.}(x,z) = t_{f.d.}(x,z) \Rightarrow z = z_+\sqrt{1 - \frac{\cosh^2\left(\frac{x}{z_+}\right)}{\cosh^2\left(\frac{a}{z_+}\right)}}, \tag{D.95}$$

This is precisely the RT curve anchored to a constant time boundary interval. The region enclosed by $t_{p.d.}$ and $t_{f.d.}$ is called the causal wedge we can express the null boundary of the causal wedge in the following compact notation:

$$a - |t - t_{bdry}| = z_+ \text{arctanh}\left[\sqrt{1 - \frac{1-\frac{z^2}{z_+^2}}{\cosh^2\left(\frac{x}{z_+}\right)}}\right] \tag{D.96}$$

where $a - |t - t_{bdry}| \geq 0$, which is what we wrote in Eq. (5.46). Points inside the causal wedge satisfy:

$$a - |t - t_{bdry}| > z_+ \text{arctanh}\left[\sqrt{1 - \frac{1-\frac{z^2}{z_+^2}}{\cosh^2\left(\frac{x}{z_+}\right)}}\right] \tag{D.97}$$

Since the boundary of the causal wedge contains the set of points in the RT curve we can conclude a well known that fact that in the BTZ black hole background the causal and entanglement wedges are the same. We give an example of what it may look like in Figure 5.7.

For a constant time slice on the Brane in the BTZ background we take a similar approach to as we did in Appendix D.1.4 for Poincare AdS_3. For the interval on the brane A_{Br} we continue it past the brane and allow it to end on the boundary this defines a new

constant time slice interval, the "virtual interval", denoted $\mathrm{Vir}(A_{Br})$ which is defined as follows:

$$\begin{aligned}\mathrm{Vir}(A_{Br}) &= \{(t,x,z)|t=t_{Br}, x\in[-a',a'], z=0\}\\ a' &= z_+ \mathrm{arccosh}\left[\frac{\cosh\left(\frac{a}{z_+}\right)}{\sqrt{1-\frac{z_{Br}^2}{z_+^2}}}\right].\end{aligned} \tag{D.98}$$

With this we clearly see that $\mathcal{W}_E(A_{Br}) \subseteq \mathcal{W}_E(\mathrm{Vir}(A_{Br}))$. In particular, we can see that $\mathcal{W}_E(A_{Br}) = \mathcal{W}_E(\mathrm{Vir}(A_{Br})) \cap \mathrm{Phys}(BTZ)$. Where $\mathrm{Phys}(BTZ)$ is the portion of the bulk BTZ spacetime which is not cut off by the end-of-the-world brane. We can explicitly write an inequality (which is in Eq. (5.48)) which characterizes the set of points in $\mathcal{W}_E(A_{Br})$:

$$\begin{aligned}a'-|t-t_{Br}| &> z_+ \mathrm{arctanh}\left[\sqrt{1-\frac{1-\frac{z^2}{z_+^2}}{\cosh^2\left(\frac{x}{z_+}\right)}}\right]\\ a' &= z_+ \mathrm{arccosh}\left[\frac{\cosh\left(\frac{a}{z_+}\right)}{\sqrt{1-\frac{z_{Br}^2}{z_+^2}}}\right].\end{aligned} \tag{D.99}$$

Where it is implicitly understood that we only keep points that are not cutoff by the end-of-the-world brane. In Figure 5.8 we given an example of what $\mathcal{W}_E(A_{Br})$ might look like.

D.2.5 Analysis of Naive Sufficient Condition for EWN (Planar BTZ)

In this appendix we will manipulate the constraint given by Eq. (5.50) to obtain the inequality given in Eq. (5.51).

We begin by defining $\Delta t = t_\chi - t_{Br}$ and then we rearrange the inequality to obtain the following:

$$\frac{z_\chi^2}{z_+^2} \geq 1 - \frac{\cosh^2\left(\frac{a}{z_+}\right)}{\cosh^2\left(\frac{a'+|\Delta t|}{z_+}\right)} \tag{D.100}$$

Now we have the following identity which comes from a trig expansion:

$$\cosh\left(\frac{a'+|\Delta t|}{z_+}\right)=\frac{\cosh\left(\frac{a}{z_+}\right)\cosh\left(\frac{|\Delta t|}{z_+}\right)+\sinh\left(\frac{|\Delta t|}{z_+}\right)\sqrt{\sinh^2\left(\frac{a}{z_+}\right)+\frac{z_{Br}^2}{z_+^2}}}{\sqrt{1-\frac{z_{Br}^2}{z_+^2}}} \tag{D.101}$$

Using this we obtain the following expression:

$$\begin{aligned}\frac{z_\chi^2}{z_+^2}&\geq 1-\frac{1-\frac{z_{Br}^2}{z_+^2}}{\left[\cosh\left(\frac{|\Delta t|}{z_+}\right)+\sinh\left(\frac{|\Delta t|}{z_+}\right)\sqrt{\tanh^2\left(\frac{a}{z_+}\right)+\frac{z_{Br}^2}{z_+^2\cosh^2\left(\frac{a}{z_+}\right)}}\right]^2}\\ \frac{z_\chi^2}{z_+^2}&\geq 1-\frac{1-\frac{z_{Br}^2}{z_+^2}}{\left[\cosh\left(\frac{|\Delta t|}{z_+}\right)+\sinh\left(\frac{|\Delta t|}{z_+}\right)\sqrt{1-\frac{1-\frac{z_{Br}^2}{z_+^2}}{\cosh^2\left(\frac{a}{z_+}\right)}}\right]^2}\end{aligned} \tag{D.102}$$

Next we plug in the explicit expression for z_χ from Eq. (5.45) and with some simple algebraic manipulations we arrive at the following simple constraint:

$$\left|\frac{B}{A}\right|\geq\sqrt{1-\frac{1-\frac{z_{Br}^2}{z_+^2}}{\cosh^2\left(\frac{a}{z_+}\right)}}. \tag{D.103}$$

This gives us Eq. (5.51). It is useful to note that when $c_t=0$ we have:

$$\begin{aligned}&\left|\frac{B}{A}\right|^2\Big|_{c_t=0}-\left(1-\frac{1-\frac{z_{Br}^2}{z_+^2}}{\cosh^2\left(\frac{a}{z_+}\right)}\right)=\left|\frac{\sin y_{Br}}{\sin\tau_{Br}}\right|^2-\left(1-\frac{1-\frac{z_{Br}^2}{z_+^2}}{\cosh^2\left(\frac{a}{z_+}\right)}\right)\\ &\geq\left|\frac{\sin y_{Br}}{\sin\tau_{Br}}\right|^2-1\geq 0,\end{aligned} \tag{D.104}$$

as long as $|\tau_{Br}|<y_{Br}$, which it is. So we can see that EWN is always satisfied in our setup when $c_t=0$.

We argued in Section 5.3.4 that to translate the constraint above to a constraint on c_t simply requires us to find the appropriate solutions to:

$$\left|\frac{B}{A}\right| = \Xi = \sqrt{1 - \frac{1 - \frac{z_{Br}^2}{z_+^2}}{\cosh^2\left(\frac{a}{z_+}\right)}}. \tag{D.105}$$

The solutions to this equation will determine the endpoints on an interval in the c_t parameter space over which EWN is satisfied. In particular, the parameter space over which EWN holds will take the form $c_t \in [c_-, c_+]$ where $c_- \leq 0$ and $c_+ \geq 0$. For $c_- \leq 0$ we need to solve:

$$\frac{B}{A} = \Xi \tag{D.106}$$

We can write the equation above as follows:

$$\begin{aligned} &\frac{X\cos^2 y_{Br}\sin\tau_{Br} - \sqrt{1-X^2}\sin^2 y_{Br}\cos\tau_{Br}}{X\cos\tau_{Br} - \sqrt{1-X^2}\sin\tau_{Br}} = \Xi\sin y_{Br}\cos\tau_{Br} \\ &X = c_t\sin y_{Br} \end{aligned} \tag{D.107}$$

The relevant solution is given by:

$$c_t = c_- = -\left[1 + \frac{\left[\cos(2\tau_{Br}) - \cos(2y_{Br})\right]\left[\Xi^2\cos^2\tau_{Br} - \cos^2 y_{Br}\right]}{2\cos^2\tau_{Br}\left(\sin y_{Br} - \Xi\sin\tau_{Br}\right)^2}\right]^{-\frac{1}{2}} \tag{D.108}$$

and for c_+ we need to solve:

$$\frac{B}{A} = -\Xi, \tag{D.109}$$

which is the same equation as Eq. (D.107) with an added minus sign on the right-hand side. The relevant solution is given by:

$$c_t = c_+ = \left[1 + \frac{\left[\cos(2\tau_{Br}) - \cos(2y_{Br})\right]\left[\Xi^2\cos^2\tau_{Br} - \cos^2 y_{Br}\right]}{2\cos^2\tau_{Br}\left(\sin y_{Br} + \Xi\sin\tau_{Br}\right)^2}\right]^{-\frac{1}{2}} \tag{D.110}$$

This gives us the bounds given in Eq. (5.52). It is not difficult to see from Figure 5.9 that to get the tightest bound we need to move the horizontal line representing the value of Ξ upwards. The highest it will go is when $a \to \infty \Rightarrow \Xi \to 1$ in that case we obtain the following results for $c_\pm$:

$$c_\pm = \pm\frac{1}{\sqrt{1 + \left(\frac{\sin\tau_{Br} \mp \sin y_{Br}}{\cos\tau_{Br}}\right)^2}} \tag{D.111}$$

These are the bounds in Eq. (5.53).